

A Statistical Mechanical Approach of Self-Organization of a Quantised Vortex Gas in a Two-Dimensional Superfluid



Davide Maestrini

School of Mathematics, UEA
Norwich, NR7 4TJ, England.

A thesis submitted to the University of East Anglia for the degree of

Doctor of Philosophy

September 2016

© This copy of the thesis has been supplied on condition that anyone who consults it is understood to recognise that its copyright rests with the author and that use of any information derived there from must be in accordance with current UK Copyright Law. In addition, any quotation or extract must include full attribution.

Contents

1	Introduction	1
1.1	Superfluidity and Bose-Einstein Condensates	1
1.2	The role of the dimensionality in Bose-Einstein Condensates	2
1.3	Fluid-Dynamics Approach to Bose-Einstein Condensates	4
1.4	Three-Dimensional and Two-Dimensional Classical Turbulence	5
1.5	Statistical Mechanics of Point Vortices	6
1.6	Three-Dimensional and Two-Dimensional Quantum Turbulence	10
1.7	Statistical Mechanics of Quantised Point Vortices	12
1.8	Thesis Outline	13
2	Gross-Pitaevskii Theory and Point Vortex Model	14
2.1	Weakly Interacting Bose Gas	14
2.2	Vortex Solutions	17
2.3	Hydrodynamic Formulation of Bose-Einstein Condensates	19
2.4	Two Dimensional Flows in Unbounded Domains	23
2.4.1	Point Vortex Decomposition	25
2.4.2	Point Vortex Approximation of the Gross-Pitaevskii Equation .	28
2.4.3	Lamb-Oseen Vortex	31
2.5	Domains with Boundaries	34
2.5.1	Vortex near a corner	36
2.5.2	Vortex in a box	38
2.5.3	Angular Momentum	40
3	Statistical Mechanics of point vortices	43
3.1	Essentials of Thermodynamics	44
3.2	Entropy from Statistical Mechanics	49
3.2.1	Microcanonical Ensemble and Negative Temperature	51
3.3	Maximum Entropy Principle and Boltzmann-Poisson Equation	60

CONTENTS

4 Mean-Field Theory of Vortex Gas in Bounded Geometries	67
4.1 Boltzmann-Poisson Equation of Two-Species Neutral Vortex Gas	68
4.2 Linear Theory	72
4.3 Non-Trivial Solutions Of The Boltzmann-Poisson Equation	78
4.4 Solutions of the Boltzmann-Poisson Equation in the Squared Domain .	85
4.5 Solutions of the Boltzmann-Poisson Equation in the Rectangular Domain	88
4.6 Solutions of the Boltzmann-Poisson as a Function of the Aspect Ratio .	90
4.7 Role of the Angular Momentum	91
5 Point Vortex Dynamics in the Square and the Rectangle	93
5.1 Point Vortex Dynamics	95
5.1.1 Dynamics in the Square	96
5.1.2 Dynamics in the Rectangle	101
5.2 Angular Momentum	105
5.2.1 Angular Momentum in the Square	106
5.2.2 Angular Momentum in the Rectangle	107
5.3 Entropy analysis for the point vortex dynamics	108
5.3.1 Generating the ensembles	110
5.3.2 Lamb-Oseen Vortex in a Box	115
5.3.3 Entropy Evaluation	126
5.3.4 Entropy Comparison	131
5.4 Analysis of the Angular Momentum	138
5.5 Annihilation with the Boundaries	141
6 Gross-Pitaevskii Simulations in the Square and the Rectangle	146
6.1 Gross-Pitaevskii Equation in Two Dimensions	146
6.2 Dynamics in the Square	148
6.3 Dynamics in the Rectangle	151
7 Conclusions	156

Abstract

In this work the relaxation of a two-dimensional Bose-gas from a non-equilibrium initial condition consisting of vortices and antivortices is studied. To focus on the role of the vortex excitations on the time evolution of the system, a point vortex model is used. The relaxation of the vortex gas is seen to lead to clustering of like-signed vortices that can be explained in terms of negative temperature states. The nature of the Coulomb interactions between vortices, precludes a well-defined thermodynamic limit. The large scale flow structures, therefore, strongly depend on the shape of the geometry. These structures can be explained in terms of a maximum entropy principle for the vortex gas that leads to the Boltzmann-Poisson equation. For a square region, the maximum entropy configuration corresponds to a monopole. This configuration results in the spontaneous acquisition of angular momentum by the flow. However, by stretching the square domain into a rectangle, the configuration which maximises the entropy switches to a dipole where like-signed vortices tend to equally occupy the two halves of the domain. In this case, the mean flow has zero angular momentum. A direct qualitative and quantitative comparison between the predictions of the Boltzmann-Poisson equation and dynamical simulations of a point vortex model are presented. In particular, we show that vortex-antivortex annihilation results in evaporative heating of the vortex gas and the subsequent migration of the system into the negative temperature regime. Moreover, the study is extended to the dynamics of quantised vortices in the same confined geometries in a two-dimensional Bose-Einstein condensate described by the Gross-Pitaevskii equation. Despite the coexistence of phonons with vortex excitations that interact together, the above predictions continue to apply in this more realistic model of a two-dimensional superfluid.

Acknowledgements

First and foremost, I want to thank my supervisor Hayder Salman for his constant support and help: (almost) 24 hours per day, (for sure) 7 days a week. He has taught me a priceless lesson: how hard it can be doing good research.

I would like also to thank Davide Proment and Miguel Onorato for their support before and throughout these four years of Ph.D.

Last but not least, I am very grateful to "il tecnico" Alberto: thank you very much for your help.

E poi che la sua mano a la mia puose
con lieto volto, ond' io mi confortai,
mi mise dentro a le segrete cose.

Inferno, III, 19-21

And when his hand he had stretch'd forth
To mine, with pleasant looks, whence I was cheer'd,
Into that secret place he led me on.

Inferno, III, 18-20

List of Figures

2.1	Padè approximation of a vortex profile $f(\eta)$ solution of Eq. (2.23) for $k = 1$	19
2.2	Vorticity and velocity profile for a Lamb-Oseen vortex.	34
2.3	The grey area represents the domain \mathcal{D} . Along the boundary $\partial\mathcal{D}$ the u component must vanish.	35
2.4	The system composed by a vortex in proximity of a corner: the shaded area is the domain where the <i>real</i> vortex is placed while the other vortices outside the domain are the <i>images</i> . The red vortices have positive circulation while the blue have negative circulation.	37
2.5	Each corner can be represented by adding three images per each corner: however, this is not sufficient to ensure the streamfunction to be constant along the walls and on each of the four corners. If C_0 is the reference cell which needs to be mimic then other cells C_j , $j = 1, \dots, 8$, which contain the images, must be placed around C_0	38
2.6	Only an infinite set of images can mimic the presence of a box (shaded area) with impenetrable walls.	39
3.1	The configurations on the sides have same entropy but different energies. There must exist a configuration at intermediate energy which maximises the entropy S	46
3.2	In the configuration on the left (<i>a</i>), vortices are close to their images: this configuration has a lower energy with respect to the one on the right (<i>c</i>) where point vortices with the same circulation cluster together. The energy of the system represented in the centre, lies in between the energies of the previous two configurations. The reference cell is surrounded by copies of it which contain the images.	48

LIST OF FIGURES

3.3	Temperature T and inverse temperature β in unit of the Boltzmann constant k_B as a function of the energy E for a system of point vortices in a box.	49
3.4	Three particles in a box: the macrostate is defined by saying that two particles in the box are red and one is blue. Each particle is located in a specific position in the box: this identifies the microstate. If the two red particles are swapped (figure on the right), the macrostate is the same. However, the microstate has changed.	50
3.5	Figure (a) on the left: structure function $\Omega'(E, N, \mathcal{D})$ (blue) and the portion of the phase space $\Omega(E, N, \mathcal{D})$ (green) defined by Eq. (3.17). Figure (b) on the right: temperature T as a function of the energy E . The trend of the graph of the temperature here presented is different from the graph presented in Fig. (3.3) due to the presence of two maxima in the structure function.	54
3.6	Figure (a) on the left: structure function $\Omega'(E, N, \mathcal{D})$ (blue) and the portion of the phase space $\Omega(E, N, \mathcal{D})$ (green) defined by Eq. (3.17). Figure (b) on the right: temperature T as a function of the energy E . The trend of the graph of the temperature presented is similar to the one presented in Fig. (3.3) due to the presence of a single maximum in the structure function.	55
3.7	Statistical weights in the square: dependence on the total energy and total energy per vortex are considered on the left and the right panels respectively.	56
3.8	Constraints on the positions of point vortices: Fig. a) on the left δ_B (green shaded region) imposes a minimum distance between a vortex and its closest images with opposite circulation. In Fig. b) on the right the constraint δ_V can affect also vortices with same circulation within the considered domain (upper right).	57
3.9	Statistical weights in the square with sides $L_x = L_y = 2$ for different values of δ_B and δ_V as indicated above each figure.	58
3.10	Statistical weights in the rectangle with aspect ratio $\Lambda = 1.5$ for different values of δ_B and δ_V as indicated above each figure.	59

LIST OF FIGURES

4.1	Contour plots for the solutions $\Psi_{2,1}$ (Fig. <i>a</i>)), $\Psi_{2,2}$ (Fig. <i>b</i>)) and $\Psi_{2,1} + \Psi_{2,2}$ (Fig. <i>c</i>)) of the homogeneous Helmholtz equation (4.28) in the square: they will be called <i>monopole</i> , <i>quadrupole</i> and <i>diagonal dipole</i> respectively. The blue and the red lines correspond to negative and positive values of the streamfunction.	74
4.2	On the left the function $f(\lambda^2; n, m, 1)$ given by Eq. (4.41) for the particular case of $L_x = L_y = 2$ and $\Lambda = 1$: among all zeros, the most relevant is the first one which corresponds to $\lambda^2 \sim 11.5$. On the right, the trend of the function $f(\lambda^2; n, m, \Lambda)$ in the vicinity of the first zero for different values of the aspect ratio Λ indicated in the legend.	77
4.3	Contour plots of the streamfunction Ψ given by Eq. (4.41) for values of λ^2 which correspond to the first three zeros of $f(\lambda^2; n, m, 1)$ indicated in Fig.(4.2) on the left. The values of λ^2 are indicated above each figure. .	78
4.4	Comparison of the linear entropy given by Eq. (4.27) for different solutions of the linearised BP equation (4.22). By increasing the aspect ratio of the domain, the entropy of the monopole decreases while the entropy of the dipole increases. For small values of the aspect ratio Λ the monopole is dominant but for larger values of Λ the dipole configuration has a higher entropy. The entropies of the quadrupole and the diagonal dipole are not relevant for this linear analysis. The inset figures are the streamfunction for the monopole, dipole, diagonal dipole and quadrupole for $\Lambda = 1$ and $\Lambda = 1.5$. The blue and red contour lines represent the negative and the positive values of the streamfunction respectively. . .	79
4.5	Chebyshev nodes in the interval $[-1, 1]$: the nodes are more dense near the endpoints.	85
4.6	Branches related to the solutions of Eq. (4.46) for different values of $\tilde{\lambda}^2$ in the square with $L_x = L_y = 2$. The monopole (green curve) has the highest entropy followed by the diagonal dipole (red curve). Values of $\tilde{\lambda}^2$ are indicated at the beginning and at the end of each branch and each circle refers to an increment of 0.5 in its value.	86
4.7	Contour plots for the dipole <i>a</i>), the diagonal dipole <i>b</i>), and for the monopole <i>c</i>). These solutions have been obtained by solving the BPE for $\tilde{\lambda}^2 = 9$: the blue line corresponds to a region where the streamfunction is negative while the red lines represents a region where the streamfunction is positive.	87

LIST OF FIGURES

4.8	Variation of error as a function of $\tilde{\lambda}^2$ for different solution branches in the squared domain. The error increases as $\tilde{\lambda}^2$ decreases: this is due to the localised solution to the BP equation for small values of $\tilde{\lambda}^2$	88
4.9	Branches related to the solutions of the Eq. (4.46) for different values of $\tilde{\lambda}^2$ in the rectangle with aspect ratio $\Lambda = 1.5$: the higher value for the entropy is achieved by the dipole (blue curve).	89
4.10	Variation of error as a function of $\tilde{\lambda}^2$ for different solution branches in the rectangular domain. The error increases as $\tilde{\lambda}^2$ decreases: this is due to the localised solution to the BPE for small values of $\tilde{\lambda}^2$	90
4.11	Branches related to the solutions of the BP equation (4.17) as a function of the aspect ratio Λ for the dipole <i>a</i>) and for the monopole <i>b</i>) for different values of the parameter $\tilde{\lambda}^2$. In Fig. <i>c</i>) the graphs presented in <i>a</i>) and <i>b</i>) are compared.	91
5.1	Figures <i>a</i>) and <i>b</i>) show two configurations at τ_1 and τ_2 respectively and the resulting ensemble is given by Fig. <i>c</i>) on the right: the red and blue circles represent the vortices with positive and negative circulation respectively.	95
5.2	Statistical weights in the square for neutral systems of point vortices composed of a different total number of vortices N : the vertical dotted line represents the energy of the initial configuration. On the left the configuration (upper figure) in which the red and the blue circles represent the vortices with positive and negative circulation respectively. The figure below is the corresponding contour plot for the streamfunction per vortex ψ/N . All the random configurations have been generated by imposing a minimum distance $\delta_V = 0.08$ between each vortex and a minimum distance $\delta_B = 0.12$ between the vortices and the boundaries. .	97
5.3	Number of vortices as a function of time in the square. The contour plots represent the streamfunction per vortex ψ/N for three different time intervals during the dynamics. Indicated below each inset is the interval used to generate the averaged streamfunctions while the number of positive and negative vortices used in the averaging is indicated above each inset.	98

LIST OF FIGURES

5.4	Contour plots of the streamfunction per vortex ψ/N evaluated over different time intervals in the square: the total number of vortices used in the averaging in each case and the interval from which the plots have been evaluated are indicated above each figure. All plots were generated from a total of $N^+ = N^- = 264$ vortices. The colors of the contour plots refer to the same colorbar as in Fig. (5.3) and Fig. (5.2).	99
5.5	Contour plots of the streamfunction per vortex ψ/N evaluated over different time intervals in last part of the dynamics in the square: the total number of vortices used in the averaging in each case and the interval from which the plots have been evaluated are indicated above each figure. All plots were generated from a total of $N^+ = N^- = 252$ vortices. The colors of the contour plots refer to the same colorbar as in Fig. (5.3) and Fig. (5.2).	100
5.6	Statistical weights in the rectangle for neutral systems composed of different number of vortices N : the vertical dotted line represents the energy of the initial configuration. On the left the configuration (upper figure) in which the red and the blue circles represent the positive and negative vortices. The figure below is the corresponding contour plot for the streamfunction per vortex ψ/N . All the random configurations have been generated by imposing a minimum distance $\delta_V = 0.08$ between each vortex and a minimum distance $\delta_B = 0.12$ between the vortices and the boundaries.	101
5.7	Number of vortices as a function of time in the rectangle. The contour plots represent the streamfunction per vortex ψ/N for four different time intervals during the dynamics. Indicated below each inset is the interval used to generate the averaged streamfunctions while the number of positive and negative vortices used in the averaging is indicated above each inset.	102
5.8	Contour plots of the streamfunction per vortex ψ/N evaluated over different time intervals in the rectangle: the total number of vortices used in the averaging in each case and the interval from which the plots have been evaluated are indicated above each figure. The colors of the contour plots refer to the same colorbar as in Fig. (5.3) and Fig. (5.2).	103
5.9	From the top to the bottom: total angular momentum L , volume term L_V and boundary term L_B evaluated in the square during the dynamics. The red dotted line represents the zero.	106

LIST OF FIGURES

5.10 Graph of the total angular momentum L as a function of time in the square: the inset figures are the streamfunction per vortex ψ/N for different time intervals generated during the dynamics. The interval from which the plots have been evaluated are indicated above each figure. The red dotted line represents the zero.	107
5.11 From the top to the bottom: total angular momentum L , volume term L_V and boundary term L_B in the rectangle. The red dotted line represents the zero.	108
5.12 Graph of the total angular momentum L as a function of time in the rectangle: the inset figures are the streamfunction per vortex ψ/N for different time intervals generated during the dynamics. The interval from which the plots have been evaluated are indicated above each figure. The red dotted line represents the zero.	109
5.13 Ensembles for the dipole (<i>a</i>), diagonal dipole (<i>b</i>) and monopole (<i>c</i>) in the square: the number of vortices in each ensemble is $N = 8580$, $N = 8360$ and $N = 8502$ respectively. The red and the blue dots represent the vortices with positive and negative circulation respectively.	111
5.14 On the left, positions of the vortices at initial time $\tau = 20$: the yellow and orange circles represent a positive and two negative vortices respectively. In the centre, the position of the vortices after $\Delta\tau = 0.005$ (upper figure) and after $\Delta\tau = 0.025$ (lower figure). On the right, the resulting ensembles: in the lower image the separation between the vortices at time τ_1 and τ_2 is enough to avoid spatial correlations which will affect the resulting vorticity fields. In the upper image the separation of the vortices is not enough to avoid any spatial correlation.	112
5.15 Mean distance between two instantaneous configurations of vortices for the dipole, diagonal dipole and monopole in the square: each dot in the above figures represents the separation $ \Delta z $ of each vortex after an amount of time $\Delta\tau$. In the case of the dipole $\Delta\tau = 0.009$, for the diagonal dipole $\Delta\tau = 0.0185$ and for the monopole $\Delta\tau = 0.025$. The red and the blue dots represent the positive and negative vortices respectively.	114
5.16 Ensembles for the monopole (<i>a</i>) and the dipole (<i>b</i>) in the rectangle: the number of vortices in each ensemble are $N = 8022$ and $N = 8086$ respectively. The red and the blue dots represent the vortices with positive and negative circulation respectively.	115

LIST OF FIGURES

5.17 Mean separation between two instantaneous configurations of vortices for the monopole and the dipole in the rectangle: each dot in the above figures represents the separation $ \Delta z $ of each vortex after an amount of time $\Delta\tau$. In the case of the monopole $\Delta\tau = 0.012$ and for the dipole $\Delta\tau = 0.025$. The red and the blue dots represent the positive and negative vortices respectively.	116
5.18 Configuration which automatically satisfies the boundary conditions given by (5.11): the real vortex v_1 and its three images v_2 , v_3 and v_4 which made up a periodic cell. The two sets of images continue along the x and the y directions by periodically repeating this periodic cell. If v_1 has positive circulation then so does the image v_3 while the other two vortices have a negative circulation.	120
5.19 Positive (left) and negative (right) circulation for the initial condition as a function of the number of modes m and n and for different meshgrids indicated in the legend. The size of the Gaussian kernel is $\sigma = 0.05$	124
5.20 Configuration at initial time (on the left) and at later time $\tau = 20$ (on the right): the asymmetric distribution of vortices in the latter configuration causes more loss in the positive circulation (see Fig. (5.21) on the right) due to the positions of the positive vortices near the boundary.	125
5.21 Positive and negative circulation for the initial condition (on the left) and at later time $\tau = 20$ (on the right) as a function of the radius σ . The positive circulation in the figure on the right decreases more rapidly as σ increases, due to the positions of the positive vortices being located close to the boundaries. The configurations at the initial time and at $\tau = 20$ are shown in Fig. (5.20).	125
5.22 On the left, the absolute value of the entropy per number of vortices $ S/N $ as a function of σ . Results correspond to the dipole in the square generated from different ensembles (each with different amount of vortices indicated in the legend) presented in a log log scale. On the right the results are presented for the range of the values of the parameter σ for which the entropy remains almost constant.	128

LIST OF FIGURES

5.23 On the left, the absolute value of the entropy per number of vortices $ S/N $ as a function of σ . Results correspond to the diagonal dipole in the square generated from different ensembles (each with different amount of vortices indicated in the legend) presented in a log log scale. On the right the results are presented for the range of the values of the parameter σ for which the entropy remains almost constant.	128
5.24 On the left, the absolute value of the entropy per number of vortices $ S/N $ as a function of σ . Results correspond to the monopole in the square generated from different ensembles (each with different amount of vortices indicated in the legend) presented in a log log scale. On the right the results are presented for the range of the values of the parameter σ for which the entropy remains almost constant.	129
5.25 On the left, the absolute value of the entropy per number of vortices $ S/N $ as a function of σ . Results correspond to the monopole in the rectangle for different ensembles (each with different amount of vortices indicated in the legend) in a log log scale. On the right the values of the parameter σ for which the entropy remains almost constant.	130
5.26 On the left, the absolute value of the entropy per number of vortices $ S/N $ as a function of σ . Results correspond to the dipole in the rectangle for different ensembles (each with different amount of vortices indicated in the legend) in a log log scale. On the right the values of the parameter σ for which the entropy remains almost constant.	131
5.27 Non dimensional energy \hat{E}_σ (blue curve) as a function of the parameter σ and its mean value \bar{E} (red dotted line) for the dipole (left), diagonal dipole (centre) and the monopole (right) in the square.	133
5.28 Energy-entropy comparison between the results obtained from the solutions of the BP equation and those obtained from the ensembles (PV) in the square. Included on the right three magnified plots for the dipole (d), the diagonal dipole (c) and the monopole (b): in each figure each marker represents the energy \hat{E}_σ and the entropy \hat{S}_σ for each value of the parameter σ	134
5.29 Non dimensional energy \hat{E}_σ (blue curve) as a function of the parameter σ and its mean value \bar{E} (red dotted line) for the monopole (left), and the dipole (right) in the rectangle. In the legend the mean values are indicated.	136

LIST OF FIGURES

5.30 Energy-entropy comparison between the results obtained from the solutions of the BP equation and those obtained from the ensembles (PV) in the rectangle. On the right two magnified plots for the monopole c) and the dipole b): in each figure each marker represents the energy \hat{E}_σ and the entropy \hat{S}_σ for each value of the parameter σ	137
5.31 Non-dimensional normalised angular momentum associated to the ensembles in the square: the dipole (left), the diagonal dipole (centre) and monopole (right). The blue dotted lines represent the mean value of each configuration and the green dotted line the values of \hat{L} associated to the solutions of the BP equation. In the case of the monopole there are two values: one related to the solution for $\tilde{\lambda}^2 = 9$ and the other one for $\tilde{\lambda}^2 = 8.5$	140
5.32 Non-dimensional normalised angular momentum associated to the ensembles in the rectangle: the monopole (left) and the dipole (right). The blue dotted lines represent the mean value of each configuration and the green dotted line the values of \hat{L} associated to the solutions of the BP equation.	142
5.33 Normalised number of positive (blue curve) and negative (green curve) vortices in the square a) and in the rectangle b). The normalisation is given by the initial number of vortices $N^\pm = 60$. The red curve represents the polarisation $P(N^+, N^-)$ and the black dashed line represents the zero. The inset figures show the vortex positions and the corresponding streamfunction ψ . Above each configuration the number of positive and negative vortices are indicated.	144
5.34 Total angular momentum in the square (blue curve) and in the rectangle (green curve).	144
6.1 Initial condition for the GP simulation in the square: Fig. a) is the density field $ \phi ^2$ and, b) is the corresponding pseudo-vorticity field ω_{ps} . The red and blue dots represent the vortices and antivortices, respectively.	149
6.2 Number of vortices (blue curve), antivortices (green curve) and polarisation (red curve) as a function of time τ in units of t_v during the GP simulation in the square. The discrepancy in the number of positive and negative vortices gives raise to a negative polarisation P	150

LIST OF FIGURES

- 6.3 Averaged streamfunction per total number of vortices $\psi/(N^+ + N^-)$ in the square for three configurations in which the system is found during the dynamics. For the dipole *a*) the averaging interval corresponds to $\tau \in [11.5t_v - 12.95t_v]$, for the diagonal dipole *b*) it corresponds to $\tau \in [10.06t_v - 10.49t_v]$, and for the monopole *c*) it corresponds to $\tau \in [18.4t_v - 18.7t_v]$ 150
- 6.4 Initial condition for the GP simulation in the rectangle with aspect ratio $\Lambda = 1.5$: Fig. *a*) is the density field $|\phi|^2$ and, *b*) is the corresponding pseudo-vorticity field ω_{ps} . The red and blue dots represent the vortices and antivortices, respectively. 151
- 6.5 Number of vortices (blue curve), antivortices (green curve) and polarisation (red curve) as a function of time τ in units of t_v during the GP simulation in the rectangle. The discrepancy in the number of positive and negative vortices gives raise to a negative polarisation P 152
- 6.6 Averaged streamfunctions per total number of vortices $\psi/(N^+ + N^-)$ in the rectangle during the first half of the GP simulation. Both images show the presence of a monopole at different stage during the dynamics. The averaging interval of the configuration *a*) corresponds to $\tau \in [2.44t_v - 2.58t_v]$ while for *b*) it corresponds to $\tau \in [6.61t_v - 6.84t_v]$ 153
- 6.7 Averaged streamfunctions $\psi/(N^+ + N^-)$ in the rectangle during the GP simulations in the second half of the dynamics: on the left the dipole configuration and on the right the monopole is caused by a strongly polarised system. The averaging interval of the configuration *a*) corresponds to $\tau \in [8.77t_v - 9.2t_v]$ while for *b*) it corresponds to $\tau \in [12.65.61t_v - 13.23t_v]$ when the system is strongly polarised. 153
- 6.8 Graph of the total angular momentum L as a function of time τ in unit of t_v in the square and in the rectangle: the inset figures are the streamfunction per vortex $\psi/(N^+ + N^-)$ for different instantaneous configurations during the dynamics. Figures *a*) and *c*) show the streamfunction in the square of an asymmetric and symmetric configuration during the dynamics, respectively. Figures *b*) and *d*) show the streamfunction of a symmetric and an asymmetric configuration in the rectangle, respectively. The colors of the contour plots refer to the same colorbar shown in Fig. (6.6) and the red dotted line represents the zero. 154

Chapter 1

Introduction

1.1 Superfluidity and Bose-Einstein Condensates

In 1908 ${}^4\text{He}$ was liquefied by K. Onnes in his laboratory in Leiden at the temperature of 4.125K and pressure of 1 atm. Moreover, he tried to solidify ${}^4\text{He}$ by lowering the temperature keeping the external pressure at 1 atm. After attempting to do so over a three years period, he was not able to achieve the solid phase of ${}^4\text{He}$. However, during the experiments he noticed that the liquid helium had a strange behaviour when the temperature was lowered below $T_\lambda = 2.18\text{K}$ called the *lambda point*. When the temperature was just above T_λ the liquid helium was boiling like the water near to its boiling point. When the temperature was exactly T_λ , the bubbling immediately stopped and the surface of the liquid was still even if the temperature was lowered further towards the absolute zero. The experiments showed the presence of two different liquid phases which were called He-I, above T_λ , and He-II, below T_λ . Around the *lambda point*, analysis of the density and the heat capacity of the liquid helium showed even stranger results. As the temperature was lowered, the density increased as expected. However, what was unexpected, was that below T_λ the density started to decrease. Even more surprisingly, around T_λ , the heat capacity assumed very large values. The dramatic change in the properties of liquid helium in the passage from He-I to He-II are now understood and they can be explained in terms of a second order phase transition [55]. In 1937 two independent groups, one in Cambridge led by J.F. Allen and D. Misner, and the other one in Moscow led by P. Kapitza, revealed the amazing property that He-II can flow without friction [3]. This peculiar characteristic convinced Kapitza to coin the term *superfluidity* and to call the second liquid phase of helium, the *superfluid* phase. Therefore, if $T > T_\lambda$, liquid helium is in a normal fluid with viscosity and if $T < T_\lambda$ it is a superfluid with a viscosity which is of the order of 10^{-9} P1 [49].

The very first progress in the understanding of superfluidity dates back to 1938 when F. London had the revolutionary idea to focus on the constituents of ^4He . Each atom of ^4He is made of two electrons, two protons and two neutrons and therefore, it is a boson. London had the idea to associate the superfluidity to the Bose-Einstein condensation (BEC) theorized in 1924 by S. Bose [17] and A. Einstein [41]. Although liquid helium and BECs are very different, London tried to connect them. An important difference between them is that the latter involves weakly interacting gases while the former is a strongly correlated system. An exhaustive theory to describe these strong interactions is missing and, at the moment, there are only phenomenological models [35]. In 1995, after seventy years from its prediction, the first BEC was created by E.A. Cornell, E. Wieman [5] and W. Ketterle [36] who used a gas of ^{87}Rb atoms cooled down to 170 nK ($1n\text{K}=10^{-9}\text{K}$). Around the same year the existence of a condensate in superfluid helium by neutron scattering [52] confirmed the idea proposed by London. This result fully established an intimate connection between superfluidity and BECs. After the first realisation of BEC with ^{87}Rb atoms, other atoms such ^{85}Rb [34], ^{41}K [81], ^4He [99], ^{174}Yb [113], ^{133}Cs [118], ^{52}Cr [51], ^{84}Sr [111], ^{86}Sr [110], ^{40}Ca [64], ^{164}Dy [70] have been used to achieve the condensation. In general, the phenomenon of the BEC is a phase transition which can occur with different species of atoms with integer spin when they are cooled below a critical temperature T_C .

1.2 The role of the dimensionality in Bose-Einstein Condensates

In general, in a three dimensional system, a phase transition is associated with the emergence of a long-range order (LRO) below a critical temperature $T_C > 0$: this corresponds to the emergence of an order parameter due to a spontaneous breaking of some continuous symmetry of the Hamiltonian [55]. Examples of such phase transitions are given by the spin chains [88] and BECs [89]. In the first example, below a critical temperature T_C all the spins tend to be aligned along the same direction and, as a consequence, the system acquires a non-zero value of the magnetisation. In the second case, the order parameter, given by the macroscopic complex wave function for the condensate ϕ [126], appears when bosons are cooled below the critical temperature T_{BEC} which is the highest temperature at which a macroscopic number of bosons will occupy the lowest energy level. This temperature can be evaluated by considering the total number of bosons N with mass m distributed over the energy states ϵ with the

chemical potential $\mu = 0$ [91],

$$N = \int_0^{+\infty} n(\epsilon) g_3(\epsilon) d\epsilon, \quad (1.1)$$

where $g_3(\epsilon)$ is the density of states in a three dimensional box with sides L and $n(\epsilon)$ is the Bose-Einstein distribution

$$g_3(\epsilon) = 2\pi \left(\frac{L}{\pi\hbar} \right)^3 (2m)^{3/2} \sqrt{\epsilon}, \quad n(\epsilon) = \frac{1}{e^{\beta(\epsilon-\mu)} - 1}, \quad (1.2)$$

where β is the inverse temperature of the system, $h = 6.626070040(81) \times 10^{-34} Js$ is the Planck's constant and $\hbar = h/2\pi$ is the reduced Planck's constant. By substituting Eqs. (1.2) into Eq. (1.1), it is possible to find that the temperature T_{BEC} at which the condensation occurs is given by

$$T_{BEC} \approx \frac{h^2}{2m\pi k_B} \left(\frac{N}{V\zeta(\frac{3}{2})} \right)^{3/2}, \quad (1.3)$$

where $k_B = 1.3806488(13) JK^{-1}$ is the Boltzmann constant, $\zeta(3/2) \approx 2.612$ is the values of the Riemann zeta function $\zeta(z)$ for $z = 3/2$, N is the total number of particles in the volume V . It has to be noticed that in Eq. (1.1) a key role is played by the density of states $g_3(\epsilon)$ which depends on the dimensionality of the considered space. In general, the dimensionality of a system is very important to a phase transition to occur: a phase transition which involves a spontaneous symmetry breaking is impossible in the thermodynamic limit in one and two-dimensional infinite systems with short range interactions at any non-zero temperature [78]. Therefore, in 1D and 2D, true LRO does not occur in the ideal Bose gas, where there are no interactions between the particles, or weakly interacting infinite uniform Bose gases. However, BECs are created in laboratories in a confined region of the space and this is the reason why the above results do not hold and they can exist in lower spatial dimensions. The trapping potential changes the shape of the density of states and hence, condensation can occur. In particular, it has been shown by Bagnato [9] that an ideal BEC can occur in one dimensional systems if the confining potential $U(x) \sim x^n$ and $n < 2$, and in two dimensions if $U(x, y) \sim x^n + y^m$ and $n^{-1} + m^{-1}$ is finite. In addition, the condensation can occur in low dimensions also for a weakly interacting Bose gas [10].

1.3 Fluid-Dynamics Approach to Bose-Einstein Condensates

When all the bosons are in the condensed state, it is possible to adopt the *Hartree* or mean-field approximation which permits to write the N -body wavefunction which describes all the bosons as a product of N single-particle wavefunction [91]. This single-particle wavefunction is called the *condensate wavefunction* or *macroscopic wavefunction* and is indicated by $\phi(\mathbf{x})$ where \mathbf{x} is the position vector. Moreover, in this approximation the dynamics of a BECs is well described by the so called Gross-Pitaevskii (GP) equation [53] given by

$$i\hbar \frac{\partial \phi(\mathbf{x}, t)}{\partial t} = -\frac{\hbar^2}{2m} \nabla^2 \phi(\mathbf{x}, t) + V_{ext}(\mathbf{x}, t)\phi(\mathbf{x}, t) + g|\phi(\mathbf{x}, t)|^2\phi(\mathbf{x}, t), \quad (1.4)$$

where \mathbf{x} is the position vector, $V_{ext}(\mathbf{x}, t)$ is a confining external potential which can depend on both space \mathbf{x} and time t , and $g = 4\pi\hbar a_s/m$ is the coupling constant proportional to the scattering length a_s of two interacting bosons. The presence of the above equation makes atomic BECs easier to investigate than liquid helium. As previously said, the external potential is an essential ingredient for the condensation, but in the following it will be set to zero. The physical content of Eq. (1.4) is revealed by considering the Madelung transformation [92]

$$\phi(\mathbf{x}, t) = \sqrt{n(\mathbf{x}, t)}e^{i\theta(\mathbf{x}, t)}, \quad (1.5)$$

which maps the dynamics of a condensate into the continuity equation

$$\frac{\partial \rho}{\partial t} + \nabla \cdot (\rho \mathbf{v}) = 0, \quad \mathbf{v} = \frac{\hbar}{m} \nabla \theta(\mathbf{x}, t), \quad \rho = mn(\mathbf{x}, t), \quad (1.6)$$

and a classical Euler equation for an inviscid and irrotational fluid

$$\frac{\partial \mathbf{v}}{\partial t} + (\mathbf{v} \cdot \nabla) \mathbf{v} = -\frac{g}{m^2} \nabla \rho + \frac{\hbar^2}{2m^2} \nabla \left[\frac{\nabla^2 \sqrt{\rho}}{\sqrt{\rho}} \right], \quad (1.7)$$

where the additional last term, called *quantum pressure*, reveals the quantum nature of the system. It follows that the dynamics of a condensate can be expressed in terms of the local condensate density ρ and the superfluid velocity, \mathbf{v} . This representation provides a *hydrodynamical formulation* of BECs and allows connections to be made between classical fluids and quantum fluids. In particular, one of the problems of key interest is the analogy between turbulence in classical fluids and quantum fluids.

Therefore, in the following, a briefly review on the key features of classical turbulence before discussing open problems in quantum turbulence will be given.

1.4 Three-Dimensional and Two-Dimensional Classical Turbulence

Turbulence was recognised as an important behaviour of fluids more than five hundred years ago by Leonardo da Vinci. He described it as follows

“...the smallest eddies are almost numberless, and large things are rotated only by large eddies and not by small ones, and small things are turned by small eddies and large.”

Since then, there seems to have been no substantial progresses in the understanding of turbulence until the first half of the 19th Century when C. L. Navier and G. G. Stokes presented an equation, the Navier-Stokes equation [11], for the dynamics of all fluid flows including those that are in a turbulent state. This system of non-linear partial differential equation admits few exact solutions under some hypothesis which sometimes can oversimplify the problem. In 1922, L.F. Richardson [97] provided an intuitive characterisation of turbulence

“Big whorls have little whorls, which feed on their velocity; and little whorls have lesser whorls, and so on to viscosity.”

In a physical description, if energy is injected in a three dimensional system, it spontaneously flows towards the small scales (large wave numbers). At sufficiently small scales, viscosity becomes important and it dissipates the energy into heat. This mechanism, called *Richardson cascade*, is also known as a *direct cascade* and, in homogeneous systems, is associated with the conservation of the energy on intermediate scale, the inertial range.

Important progress in the understanding of classical turbulence was made by A.N. Kolmogorov in 1941 [109] who proposed a method to evaluate the energy spectrum of a turbulent flow. His result is based on a dimensional analysis and it leads to the conclusion that the energy spectrum in the inertial range is given by $E(k) \sim k^{-5/3}$, where k is the magnitude of the three-dimensional wavenumber vector \mathbf{k} . On the other hand, two-dimensional systems have been widely investigated by R. H. Kraichnan [65] and G. K. Batchelor [11] and they exhibit a different behaviour. When the energy is injected at intermediate scale, it flows towards larger scales (small wave numbers) and

leads to the formation of large eddies. This flow of energy that is opposite to the three-dimensional case and is called an *inverse energy cascade*. The contrasting behaviour between 2D and 3D arises because for an ideal inviscid fluid in 2D there is an additional invariant (constant of motion) called the enstrophy that is defined as

$$\mathcal{E} = \frac{1}{2} \int |\boldsymbol{\omega}|^2 d^2 \mathbf{x}. \quad (1.8)$$

The presence of an additional invariant associated with the enstrophy, also leads to a *direct cascade* for the enstrophy which exhibits a spectrum given by $E(k) \sim k^{-3}$ and it is associated with the stretching of the large patches of vortices. Experimental evidences of these cascades have been reported in [23]. From now on, if not explicitly specified, a two-dimensional system is considered.

1.5 Statistical Mechanics of Point Vortices

The first explanation on the formation of large clusters in two-dimensional fluid dynamics was given by Onsager in 1949 [90] when he published a seminal work on the study on two-dimensional hydrodynamic turbulence by using a statistical mechanical approach. In his work, he used the so called *point vortex model* [86] (PVM) which was introduced by H. L. F. von Helmholtz in 1858. In this model, a vortex located in \mathbf{x}_0 has vorticity given by

$$\omega(\mathbf{x}) = \gamma \delta(\mathbf{x} - \mathbf{x}_0), \quad (1.9)$$

where γ is its circulation which is defined as

$$\gamma = \oint_C \mathbf{v} \cdot d\mathbf{l}, \quad (1.10)$$

where C is a closed path which encloses the vortex, \mathbf{v} is the velocity field generated by the vortex and $d\mathbf{l}$ is the infinitesimal displacement along the path C . Onsager noticed that a two-dimensional system composed by point vortices (PVs) in a bounded domain \mathcal{D} can admit a negative absolute temperature. From a statistical mechanical point of view, the temperature of a system is defined as

$$\frac{1}{T} = \left(\frac{\partial S}{\partial E} \right)_{\mathcal{D}}, \quad (1.11)$$

where S is the entropy of the system, E its energy and the subscript \mathcal{D} means that the partial differentiation is performed keeping the area \mathcal{D} constant. If the entropy

of a system is an increasing function of the energy, then the temperature is always positive. However, in the case of PVs, the entropy can be a decreasing function of the energy E and in this case the PVs with same circulation tend to cluster together forming large coherent structures. This is exactly the scenario described by the inverse energy cascade: the energy flows from small scales, when vortices are separated, to large scales, where vortices of the same sense of rotation tend to gather together. The formation of these eddies, in Onsager's model, is a direct consequence of the fact that a two-dimensional confined system with area \mathcal{D} has a finite phase space. This can be immediately seen by looking at the equation of motions for a system composed of N point vortices with circulation γ_k , $k = 1, \dots, N$, given by [86]

$$\dot{x}_k = \frac{1}{\gamma_k} \frac{\partial \mathcal{H}}{\partial y_k}, \quad \dot{y}_k = -\frac{1}{\gamma_k} \frac{\partial \mathcal{H}}{\partial x_k}, \quad (1.12)$$

where \mathcal{H} is the Hamiltonian (interaction energy) of the system. Clearly these equations are written in Hamiltonian form, and it is immediate to conclude that the phase space is finite and it is given by \mathcal{D}^N . This profound connection between statistical mechanics and hydrodynamics suggested that a fully and consistent theory based on statistical mechanics was necessary to describe the two-dimensional turbulence. In 1973, G. Joyce and D. Montgomery [60] developed a statistical theory for a two-dimensional electrostatic guiding plasma based on the maximum entropy principle. The possibility of using this theory for the PVM is given by the fact that the Hamiltonian in both systems is of the same form [86]. They found that the configurations which maximise the entropy (statistical equilibrium) correspond to solutions of the so called Boltzmann-Poisson (BP) equation. This is a second order non-linear differential equation for the stream-function $\psi(\mathbf{x})$ of the flow related to the vorticity by $\nabla^2 \psi(\mathbf{x}) = -\omega(\mathbf{x})$. Moreover, in perfect agreement with Onsager, they found that the BP equation has non-trivial solutions only if the temperature of the system is negative and these solutions correspond to configurations in which PVs cluster together and form large eddies.

The statistical theory of point vortices in confined geometries was fully developed by Y. B. Pointin and S. Lundgren [93, 71] in 1976 and 1977. Their main aim was to understand how the geometry modifies the formation of the large coherent structures and for this reason they investigated the circular domain and the square. In particular, they wanted to establish if the configurations which maximise the entropy depended on the shape of the domain. They noticed that in the circular domain, the positive and negative vortices tend to cluster in two separate clusters forming a dipole. In the case of the square, the most probable configuration corresponds to vortices with one charge

occupying the centre of the domain and the vortices of the other charge occupying the four corners. Moreover, they also investigated the most probable configuration in a rectangular geometry [71] and they found that for values of the aspect ratio $\Lambda = L_x/L_y$ greater than a critical value $\Lambda_C = 1.122$ the most probable configuration is no longer the monopole but the dipole. In this second scenario, the vortices will share equally the rectangular domain by forming two large eddies. Their work fully established that the statistical equilibrium is determined by the shape of the container. A deeper insight about the differences between the circular domain and the square/rectangle is that the circular geometry the total angular momentum L of the system is a constant of motion. The conservation of the angular momentum imposes a strong constraint on the vortex dynamics. However, the angular momentum is not a constant of motion if the PVs are confined in a square or, more in general, in a rectangular geometry.

A possible way to test these assertions is to investigate the dynamics of PVs with the PVM in a confined geometry. This can be done by solving the equation of motion (1.12), where the Hamiltonian \mathcal{H} needs to be specified for the respective geometries. A possible method to evaluate the Hamiltonian for the PVM in bounded geometries is the so called *method of images* [86]: in this method, the PVs are placed in strategic positions outside the domain in order to ensure that a zero normal velocity is satisfied at the boundary. In 1941 C.C. Lin [69] showed that using such an approach any boundary condition can be satisfied. In the case of a circular geometry the Hamiltonian \mathcal{H} can be easily derived [86] and the dynamics in such a geometry has been studied by Y. B. Pointin [93] and it agrees with the prediction given of the statistical theory. However, the study of the vortex dynamics in the square and in the rectangle was not considered since the Hamiltonian for such domains was only derived in 1989 by L. J. Campbell [24]. A numerical method to solve the Euler equations was developed by J. P. Christensen [32] in 1969 and he revealed that in the square the statistical equilibrium is associated to the monopole while for the rectangle with aspect ratio $\Lambda > \Lambda_C$ the dipole is the maximum entropy configuration. Although in 1990 the Hamiltonian in the rectangle and in the square was known, L.J. Campbell and K. O’Neil [25] investigated the vortex dynamics in these geometries by using the random walk method. They also noticed that a possible mechanism to increase the energy of the system was to introduce in the dynamics an annihilation parameter between the positive and the negative vortices. Their motivation was to use this to represent the effects of diffusion.

The realisation that statistical mechanical approaches could be applied to fluid dynamics through the PVM stimulated interest in decaying turbulence in classical fluids and in particular in two-dimensional Navier-Stokes flows in confined geometries [33],

[21], [74], [27], [104], [61], [82], [62], [30]. A striking result has been obtained by H. C. Clercx *et al.* [33] in 1998: by studying the two-dimensional turbulence in a squared container with rigid boundaries, they discovered that the high entropy state is given by the monopole and which has a non-zero angular momentum. In other words, a two-dimensional classical fluid in a squared container whose dynamics is governed by the Navier-Stokes equations will spontaneously evolve towards a monopole configuration which carries a non-zero angular momentum. On the other hand, as a direct consequence of the results obtained by S. Lundgren [71], the dynamics in a rectangular container must evolve towards the maximum entropy configuration, the dipole, which has zero angular momentum. In 2009, J. B. Taylor *et al.* [114] numerically solved the Boltzmann-Poisson equation in the square and in two different rectangular geometries with different aspect ratio showing the maximum entropy configurations in these geometries. Moreover, in the case of the square, the associated emergence of non-zero angular momentum is driven by the shape of the container rather than the energy of the system: this reinforces the fact that the acquisition of angular momentum by a system can be understood in terms of the statistical theory of PVs in two dimensions. Similarly conclusions were obtained by Esler *et al.* in 2015 [43] in more complicated geometries such as the *Neumann ovals*. These studies demonstrate the role played by the geometry in the dynamics of PVs and the importance of a statistical approach in the description of these systems. The sensitivity of the emergent flows to the shape of the domain is due to the lack of a well-defined thermodynamic limit. This limit, in which the number of constituents N and the area of the domain \mathcal{D} go to infinity while their ratio N/\mathcal{D} is held constant, is a standard assumption in statistical mechanics in order to obtain quantities which do not depend on the number of constituents or on the shape of the container. However, due to the long range interaction for the PVM, the influence of the domain is an inescapable characteristic as $N \rightarrow \infty$ [43].

Although the statistical properties of hydrodynamic turbulence can be described by using the PVM, classical fluids do not represent the natural application of the PVM. When a vortex in a superfluid is considered, it has a vorticity of the form given by Eq. (1.9) and a circulation as given by Eq. (2.37). A peculiarity of vortices in superfluids is that their circulation is quantised [47], [90] and is given by $\gamma = \hbar/m$ [92] where m is the mass of the single condensate boson. This peculiar property makes a vortex in a superfluid a well-defined object with a well-defined circulation. Vortices in superfluids represent the most appropriate system in which the PVM can be applied. Quantised vortices have been experimentally detected and recorded with a photographic technique in liquid helium by E. J. Yarmchuk *et al.* in 1979 [121] and, in BECs, by Neely *et al.*

in 2010 [85].

1.6 Three-Dimensional and Two-Dimensional Quantum Turbulence

While CT is associated with continuous distributions of vorticity, QT deals with a collection of vortices with quantised circulation that closely resemble point vortices [92]. In three dimensions, these structures are vortex lines and in two dimensions, they are point vortices. Before the realisation of BEC in 1995 [73], liquid helium was the only quantum fluid in which it was possible to study QT. Although both support superfluidity, the vortices in these two systems have different sizes: a vortex in superfluid 4He has a characteristic radius $r_{He} \sim \text{\AA}$ [39], while in a BEC $r_{BEC} \sim \mu\text{m}$ [59]. As a consequence, it is easier to detect a vortex during an experiment in a BEC rather than in liquid helium. Moreover, from an experimental point of view, 4He does not offer the possibility to change parameters such as the interaction strength between the atoms of helium nor its density.

All these problems are absent in BECs: they provide very flexible systems to work with due to their compressibility, to the tunable interatomic interactions, to the large number of experimental methods to generate superfluid flows and furthermore, due to the presence of a well established microscopic theory. In fact, all the dynamics of a BEC at zero temperature can be well described by the GP equation presented in Chapter 2. Therefore, QT can be studied by creating vortex lines in three-dimensional BECs and quantum vortices in two-dimensional BECs and investigating their dynamics, their mutual interactions and their interactions with the condensate. All these interactions are well modelled by the GP equation in the limit of zero temperature. However, if the condensate is at non-zero temperature, other models are necessary [13], [94]. These models are important since the incompressible energy of a BEC is radiated by emission of sound and then dissipated with the interactions with the thermal cloud [1].

All these considerations seem to lead to the conclusion that BECs provide a suitable environment in which QT can be studied. However, the most natural questions to raise at this stage are the following: "how can quantum vortices be created and detected in a BEC?" Quantum vortices can be created in a BEC by phase imprinting [67, 54], by transfer of orbital angular momentum to the condensate [120] or by laser stirring [85]. As to their detection, interferometric techniques have been used to detect the position and the winding number of the vortices [75], [31], [58] while sequential images

taken during their dynamics [4], [85], [48], [79] have also been used. Therefore, all the ingredients for the study of QT are present and the immediate comparison between CT and QT is to find the presence of a direct cascade in a three dimensional BEC. Evidence of a direct energy cascade was found by J. Maurer [76] in 1998 and by M. Kobayashi [72] in 2005. Such direct cascade was also found in other quantum fluids like ^4He by T. Araki [112] in 2002 and in ^3He by D. I. Bradley [19] in 2006.

Regarding two-dimensional systems, various attempts have been made to make a connection between CT and QT from a numerical point of view. The energy flux from small scales to large scales have been demonstrated by Yatsuyanagi *et al.* [122] in 2005 but, in 2009, R. Numasato *et al.* [87] concluded that an inverse energy cascade is not a necessary feature of two-dimensional QT. However, the presence of an inverse energy cascade in BECs has been found in various geometries [84], [6],[108],[95]. In all these works, the authors focused on the analysis of the energy spectrum during the decay of quantum turbulence, but other possible ways to quantify the clustering in a BEC based on the Ripley's function [98] have been proposed by A. White [119]. Only recently A.S. Bradley and B.P. Anderson in 2012 [18] fully established a link between the two-dimensional CT and two-dimensional QT.

In order to compare CT to QT, the role of the annihilation of quantum vortices with opposite circulation needs to be understood: this mechanism has been investigated in detail by several authors [83], [66]. An important progress in the modelling of the dynamics of quantum vortices in BECs has been made by Simula *et al.* [107] in 2014 by using the PVM and adding to it an annihilation parameter δ_{run} : PVs with opposite circulation whose mutual distance is less than δ_{run} are removed from the system. This artefact mimics the pair annihilation which is naturally present in a BEC but is absent in the PVM since this model conserves the total number of vortices. A similar approach has been used by T. Billam *et al.* [14] in a doubly periodic domain. The idea of introducing an annihilation parameter, dates back to 1990 when L.J. Campbell and K. O'Neil [25] noticed that this mechanism can increase the energy per vortex of the system and leads to clustering. It results in evaporative heating (the inverse of evaporative cooling) in which coldest constituents are removed from the system, and these constituents are represented by the vortex-antivortex pairs. Since the annihilation process increases the energy per vortex, the systems migrates into the negative temperature regime, and Onsager's statistical theory could now be applied to the quantised vortex gas. More recently, in 2016, X. Yu *et al.* [125] successfully applied a statistical theory based on point vortices to describe the formation of large coherent structures in a circular domain. In the case of a finite temperature BEC, the vortex dynamics can

be modelled by using the so called *dissipative* PVM [7], which takes into account the interactions between the vortices and the condensate. However, these works focused on the doubly periodic domain or on the circular region in which the total angular momentum is a constant of motion. As already pointed out in the case of CT, the role played by the geometry is fundamental in the long term dynamics of the system. In particular, the differences in the long term dynamics of quantum vortices in the square and the rectangle, for our knowledge, have never been investigated with the PVM.

1.7 Statical Mechanics of Quantised Point Vortices

It is clear that the dynamics of quantised vortices in a BEC can be investigated with the PVM. However, a systematic description in the square and the rectangle are missing and this is the first aim of this thesis: to investigate in depth the dynamics of PVs in these confining geometries in which, due to the absence on the constraint on the angular momentum, a spontaneous acquisition of angular momentum could occur. Moreover, due to the nature of quantised vortices, it is natural to apply statistical theories based on the PVM to the study of QT.

The problem of applying statistical methods to the analysis of a BEC in real experiments has been carried out in 2011 by Yefsah *et al.* [123]. However, a mean-field theory based on the PVM is missing in the literature: this theory is the key to understand and to predict the formation of large coherent structures in two-dimensional QT. Therefore, the second aim of the thesis is to develop a mean-field theory of quantised point vortices in a two-dimensional system and to compare the results obtained from the dynamical descriptions of the system with the PVM. In particular, a mean-field theory based on the microcanonical approach will be developed in a generic confined domain \mathcal{D} and applied to a squared and rectangular domain. The choice of these geometries is also reinforced by the possibility of creating BECs in uniform potential optical traps which allow the study of the dynamics of quantised vortices in geometries like the square and the rectangle [50]. This fact emphasizes the utility of using the PVM to model the dynamics of quantised vortices in such domain. An additional aim of this thesis, is to make a quantitative connection between the mean-field theory and the dynamics described with the PVM. Indeed, such detailed comparisons are completely missing in the literature even in studies motivated by CT. Finally, testing these theories against predictions obtained with the GP model of a superfluid has not been considered to date. We will therefore culminate the findings of our results with the PVM and the statistical approach to compare these against a more realistic microscopic model in the

form of the GP equation.

Summarising, this thesis will investigate the dynamics of point vortices in the square and the rectangle, will show how to develop and apply a mean-field theory to such systems and how it is possible to make a quantitative comparison between these two approaches.

1.8 Thesis Outline

This thesis is organised into six Chapters and a brief description on the contents of each Chapter is given below. In Chapter 2, a brief introduction to BECs and the derivation of the GP equation will be provided. Moreover, the hydrodynamic approach to BECs will be given and, the PVM will be presented as a possible way to describe the dynamics of quantised vortices in BECs. The PVM will be fully developed in the case of unbounded and bounded domains. In Chapter 3 a review of classical and statistical thermodynamics will be given and in particular, the concept of the negative temperatures will be discussed in the context of the point vortex model and fully explained. By applying the maximum entropy principle to a system composed of point vortices, the BP equation will be derived. In Chapter 4 the BP equation for a neutral system of point vortices is solved numerically in a square and a rectangle and the solutions obtained are classified in terms of their energy and entropy. This will allow the classification of the configurations of point vortices according to whether they correspond to local or global maxima of the entropy in both geometries. In Chapter 5 the dynamics of point vortices in the square and the rectangle will be investigated in depth. In particular, several aspects of the dynamics will be considered. In the first part, a qualitative analysis of the dynamics of point vortices is presented. This will reveal good agreement with the statistical predictions presented in Chapter 4. A description of the dynamics based on the analysis of the angular momentum is also given. In this Chapter, a method that allows direct quantitative comparison between predictions of the PVM and the statistical theory of Chapter 4, is also developed. To our knowledge such a thorough validation between direct dynamical simulations and results of the BP equation has not been performed before. In Chapter 6 the dynamics of quantised vortices is investigated by numerically solve the GP equation in a squared domain and in a rectangle. This study will show good agreement with the results presented in Chapter 5.

Chapter 2

Gross-Pitaevskii Theory and Point Vortex Model

2.1 Weakly Interacting Bose Gas

In nature there are two kind of particles: bosons and fermions. If a system is composed of N identical particles each of mass m then, according to Quantum Mechanics, it is described by the N body wave function

$$\Psi(\mathbf{x}_1, \mathbf{x}_2, \dots, \mathbf{x}_N), \quad (2.1)$$

where \mathbf{x}_i is the position of the i -th particle, $i = 1, 2, \dots, N$. The wave functions which describe bosons and fermions have different behaviour if two particles are swapped. In particular for bosons the wave function has to be symmetric under permutation of any two identical particles

$$\Psi(\dots, \mathbf{x}_i, \dots, \mathbf{x}_j, \dots) = \Psi(\dots, \mathbf{x}_j, \dots, \mathbf{x}_i, \dots), \quad (2.2)$$

while for fermions the wave function is asymmetric under the same permutation

$$\Psi(\dots, \mathbf{x}_i, \dots, \mathbf{x}_j, \dots) = -\Psi(\dots, \mathbf{x}_j, \dots, \mathbf{x}_i, \dots). \quad (2.3)$$

In this work the former kind of particles are considered and, hereafter, it will be understood that the particles which are being studied are bosons. The wave function $\Psi(\mathbf{x}_1, \mathbf{x}_2, \dots, \mathbf{x}_N)$ satisfies the Schrödinger equation

$$\hat{H}\Psi(\mathbf{x}_1, \mathbf{x}_2, \dots, \mathbf{x}_N) = E\Psi(\mathbf{x}_1, \mathbf{x}_2, \dots, \mathbf{x}_N), \quad (2.4)$$

where

$$\hat{H} = -\frac{\hbar^2}{2m} \sum_{i=1}^N \nabla_i^2 + \frac{1}{2} \sum_{i,j=1}^N V_{int}(\mathbf{x}_i - \mathbf{x}_j), \quad (2.5)$$

is the Hamiltonian operator of the system and $V_{int}(\mathbf{x}_i - \mathbf{x}_j)$ is the interaction potential between particles. In Eq. (2.5) the factor $1/2$ in the second summation avoids the over counting of interaction between pairs. When the number of particles is large, solving the Schrödinger equation for all particles with a suitable initial condition, is very complicated and for this reason a quantum field theory approach is more suitable. In a second quantization framework ¹, the wave function is replaced by the field operators $\hat{\Psi}^\dagger(\mathbf{x})$ and $\hat{\Psi}(\mathbf{x})$ which create and annihilate a particle at position \mathbf{x} respectively and which satisfy the following commutation rules at equal time

$$[\hat{\Psi}(\mathbf{x}'), \hat{\Psi}^\dagger(\mathbf{x})] = \delta(\mathbf{x} - \mathbf{x}'), \quad [\hat{\Psi}^\dagger(\mathbf{x}'), \hat{\Psi}^\dagger(\mathbf{x})] = [\hat{\Psi}(\mathbf{x}'), \hat{\Psi}(\mathbf{x})] = 0. \quad (2.6)$$

where $[\hat{A}, \hat{B}] = \hat{A}\hat{B} - \hat{B}\hat{A}$, and δ is the Dirac delta function. The Hamiltonian operator (2.5), in the second quantisation formalism, becomes [92]

$$\begin{aligned} \hat{H} = & \int d^3\mathbf{x} \hat{\Psi}^\dagger(\mathbf{x}, t) \left[-\frac{\hbar^2}{2m} \nabla^2 + V_{ext}(\mathbf{x}, t) \right] \Psi(\mathbf{x}, t) \\ & + \frac{1}{2} \int d^3\mathbf{x} \int d^3\mathbf{x}' \hat{\Psi}^\dagger(\mathbf{x}, t) \hat{\Psi}^\dagger(\mathbf{x}', t) V_{int}(\mathbf{x}', \mathbf{x}) \hat{\Psi}(\mathbf{x}, t) \hat{\Psi}(\mathbf{x}', t). \end{aligned} \quad (2.7)$$

where $V_{ext}(\mathbf{x}, t)$ is an external potential and $d^3\mathbf{x} = dx dy dz$. If the considered system consists of a dilute gas then the interactions between bosons are dominated by two-body collisions and hence, the interaction potential can be written as [92]

$$V_{int}(\mathbf{x}, \mathbf{x}') = g\delta(\mathbf{x} - \mathbf{x}') = \frac{4\pi\hbar^2 a_s}{m} \delta(\mathbf{x} - \mathbf{x}'), \quad (2.8)$$

where g is the coupling constant and a_s is the s-wave scattering length. In a d -dimensional space the units of the field operators $\hat{\Psi}$ and $\hat{\Psi}^\dagger$ can be obtained from Eq. (2.6) and are given by $[\hat{\Psi}] = [\hat{\Psi}^\dagger] = \ell^{-d/2}$ which reduces to $[\hat{\Psi}] = [\hat{\Psi}^\dagger] = \ell^{-3/2}$ in the three dimensional case. Replacing the interaction potential (2.8) into Eq. (2.7)

¹For a complete and formal definition see [45].

gives

$$\begin{aligned}\hat{H} = & \int d^3\mathbf{x} \hat{\Psi}^\dagger(\mathbf{x}, t) \left[-\frac{\hbar^2}{2m} \nabla^2 + V_{ext}(\mathbf{x}, t) \right] \hat{\Psi}(\mathbf{x}, t) \\ & + \frac{g}{2} \int d^3\mathbf{x} \hat{\Psi}^\dagger(\mathbf{x}, t) \hat{\Psi}^\dagger(\mathbf{x}, t) \hat{\Psi}(\mathbf{x}, t) \hat{\Psi}(\mathbf{x}, t).\end{aligned}\quad (2.9)$$

The time evolution of the operator $\hat{\Psi}$ is governed by the Heisenberg equation [45]

$$i\hbar \frac{\partial \hat{\Psi}(\mathbf{x}, t)}{\partial t} = [\hat{\Psi}(\mathbf{x}, t), \hat{H}], \quad (2.10)$$

and by using the commutation relations (2.6)

$$\begin{aligned}[\hat{\Psi}(\mathbf{x}, t), \hat{H}] &= -\frac{\hbar^2}{2m} \nabla^2 \hat{\Psi}(\mathbf{x}, t) + V_{ext}(\mathbf{x}, t) \hat{\Psi}(\mathbf{x}, t) \\ &+ \frac{g}{2} \int d^3\mathbf{x}' [\hat{\Psi}(\mathbf{x}, t), \hat{\Psi}^\dagger(\mathbf{x}', t) \hat{\Psi}^\dagger(\mathbf{x}', t) \hat{\Psi}(\mathbf{x}', t) \hat{\Psi}(\mathbf{x}', t)] \\ &= \left[-\frac{\hbar^2}{2m} \nabla^2 + V_{ext}(\mathbf{x}, t) + g \hat{\Psi}^\dagger(\mathbf{x}, t) \hat{\Psi}(\mathbf{x}, t) \right] \hat{\Psi}(\mathbf{x}, t).\end{aligned}\quad (2.11)$$

Therefore, the time derivative of the operator $\hat{\Psi}(\mathbf{x}, t)$ given by Eq. (2.10) becomes

$$i\hbar \frac{\partial \hat{\Psi}(\mathbf{x}, t)}{\partial t} = \left[-\frac{\hbar^2}{2m} \nabla^2 + V_{ext}(\mathbf{x}, t) + g \hat{\Psi}^\dagger(\mathbf{x}, t) \hat{\Psi}(\mathbf{x}, t) \right] \hat{\Psi}(\mathbf{x}, t). \quad (2.12)$$

If the temperature of the system is sufficiently low, by using the *Bogoliubov ansatz* [15]

$$\hat{\Psi}(\mathbf{x}, t) = \phi(\mathbf{x}, t) + \delta\hat{\phi}(\mathbf{x}, t), \quad (2.13)$$

the wave function can be split into a mean-field term which has non zero mean value $\langle \phi(\mathbf{x}, t) \rangle \neq 0$ which represents the vacuum expectation values of the operator $\hat{\Psi}(\mathbf{x}, t)$ and a term which has a zero mean value $\langle \delta\hat{\phi}(\mathbf{x}, t) \rangle = 0$ and it represents the quantum fluctuations. This assumption is justified if the lowest energy states are macroscopically occupied and hence the system can be described by the classical field $\phi(\mathbf{x}, t)$ and the fluctuations around it. By substituting (2.13) into Eq. (2.9), the Hamiltonian \hat{H} gives will consist of five terms [94]: a leading order term H_0 which involves only the complex wave function $\phi(\mathbf{x}, t)$ and other four terms which involve both $\phi(\mathbf{x}, t)$ and the operator $\delta\hat{\phi}(\mathbf{x}, t)$. In the $T = 0$ limit, the non condensate contribution $\delta\hat{\phi}$ can be set equal to

zero and hence $\hat{H} \approx H_0$, and hence, Eq. (2.12) becomes

$$i\hbar \frac{\partial \phi(\mathbf{x}, t)}{\partial t} = -\frac{\hbar^2}{2m} \nabla^2 \phi(\mathbf{x}, t) + V_{ext}\phi(\mathbf{x}, t) + g|\phi(\mathbf{x}, t)|^2\phi(\mathbf{x}, t), \quad (2.14)$$

which is known as *Gross-Pitaevskii* equation. Hereafter, the Gross-Pitaevskii equation will be referred as GP equation. The normalization condition on the wave function is given by

$$\int |\phi(\mathbf{x}, t)|^2 d^3\mathbf{x} = N, \quad (2.15)$$

where N is the total number of bosons in the condensate.

2.2 Vortex Solutions

In this section a gas in an unbounded domain is considered, hence in the GP equation (2.14) $V_{ext} = 0$ and a particular solution of the equation will be investigated. Therefore a coordinate system (r, θ, z) can be used and it will be assumed that the solution does not depend on the z -coordinate. This assumption is justified since a ground states solution, corresponding to a straight vortex line, is considered. The GP equation assumes a simple form if the time and spatial dependence of the wavefunction can be factorized as

$$\phi(\mathbf{x}, t) = \phi(\mathbf{x}) \exp\left(\frac{-i\mu t}{\hbar}\right), \quad (2.16)$$

where μ is the chemical potential, which represents the energy associated with the addition of one boson to the condensate. By substituting (2.16) into Eq. (2.14) the following time-independent GP can be obtained

$$\left(-\frac{\hbar^2}{2m} \nabla^2 - \mu + g|\phi(\mathbf{x})|^2\right) \phi(\mathbf{x}) = 0. \quad (2.17)$$

In cylindrical coordinates the wavefunction $\phi(\mathbf{x})$ can be written as

$$\phi(r, \theta) = e^{ik\varphi} F(r), \quad k = \pm 1, \pm 2, \dots, \quad (2.18)$$

and hence, Eq. (2.17) becomes

$$-\frac{\hbar^2}{2m} \frac{1}{r} \frac{d}{dr} \left(r \frac{dF}{dr} \right) + \frac{\hbar^2}{2m} \frac{k^2}{r^2} F(r) + gF^3(r) - \mu F(r) = 0. \quad (2.19)$$

At a point located far away from the vortex line, the density must be equal to the uniform value n_∞ while at the centre of the vortex line it must approach to zero. This is due to the fact that the second term of Eq. (2.19) is singular in $r = 0$ and hence $F(r) = 0$ if $r = 0$ avoids singularities in Eq. (2.19). Therefore,

$$F(r) \rightarrow \sqrt{n_\infty} \quad \text{if } r \rightarrow +\infty, \quad F(r) \rightarrow 0 \quad \text{if } r \rightarrow 0 \quad (2.20)$$

and the wave function can be written as $F(r) = \sqrt{n_\infty}f(r)$, and Eq. (2.19) becomes

$$-\sqrt{n_\infty} \frac{\hbar^2}{2m} \frac{1}{r} \frac{d}{dr} \left(r \frac{df}{dr} \right) + \sqrt{n_\infty} \frac{\hbar^2}{2m} \frac{k^2}{r^2} f(r) + gn_\infty^{3/2} f^3(r) - \mu \sqrt{n_\infty} f(r) = 0. \quad (2.21)$$

As $r \rightarrow +\infty$ the first two terms of the above equation vanish, leading to

$$\mu = gn_\infty, \quad (2.22)$$

which gives the relation between the chemical potential μ , the density of particles n_∞ and the coupling constant g . Equation (2.21) reduces to

$$\frac{1}{\eta} \frac{d}{d\eta} \left(\eta \frac{df}{d\eta} \right) + \left(1 - \frac{k^2}{\eta^2} \right) f(\eta) - f^3(\eta) = 0, \quad (2.23)$$

if the following dimensionless quantities are introduced

$$\eta \equiv \frac{r}{\xi}, \quad \xi \equiv \frac{\hbar}{\sqrt{2mgn_\infty}}, \quad (2.24)$$

where ξ is called the *healing length*. The healing length is the characteristic length where the kinetic term and the non linear term of the GP equation compete,

$$\frac{\hbar^2}{2m\xi^2} = gn_\infty, \quad (2.25)$$

and it represents the distance over which the wave function tends to its bulk value when a localized perturbation occurs. Fig. (2.1) shows the vortex profile $f(\eta)$ written in terms of a Padè approximation [12] for $k = 1$. At this stage, a vortex in a BEC seems to be only characterised by a region of the space where the density goes to zero. This is not the full story and, in order to understand the real nature of a vortex in a BEC, it is convenient to write the so called *hydrodynamic formulation* of a BEC.

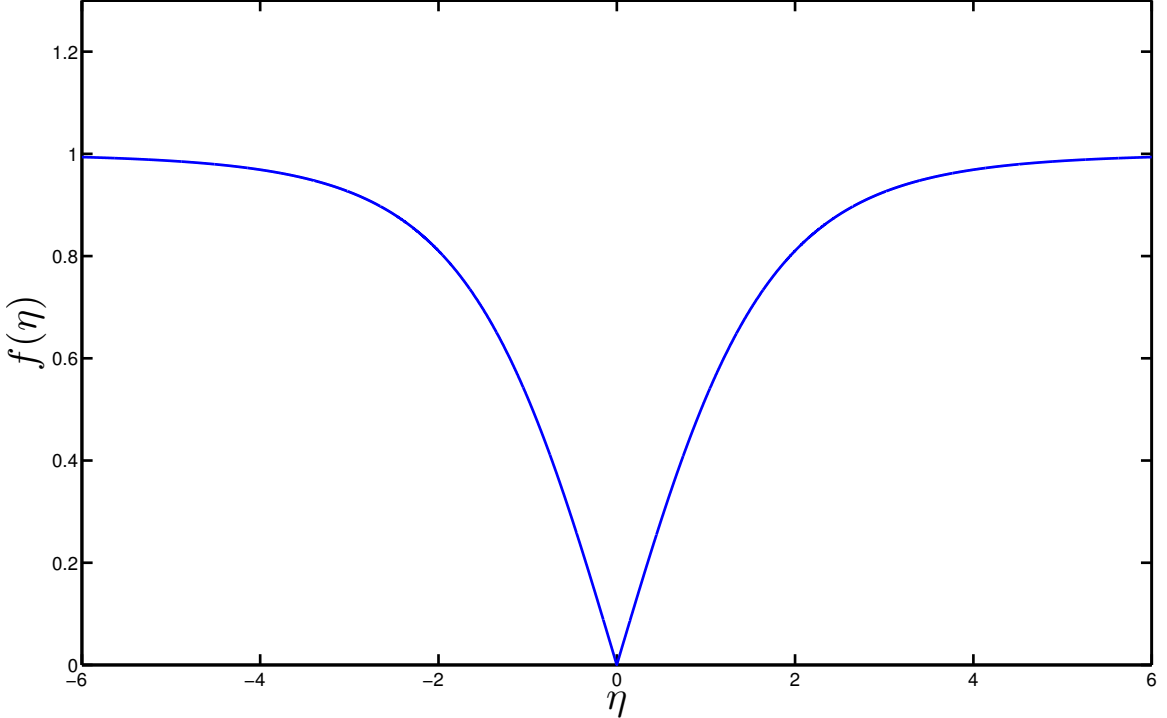


Figure 2.1: Padé approximation of a vortex profile $f(\eta)$ solution of Eq. (2.23) for $k = 1$.

2.3 Hydrodynamic Formulation of Bose-Einstein Condensates

In this section, the hydrodynamics approach to BECs will be explained. In the following, for simplicity the spatial and time dependence (\mathbf{x}, t) of the wave function will be understood. By multiplying the GP equation (2.14) by ϕ^* and by considering the complex conjugate of this quantity the following equations can be obtained

$$\begin{aligned} i\hbar\phi^*\frac{\partial\phi}{\partial t} &= -\frac{\hbar^2}{2m}\phi^*\nabla^2\phi + V_{ext}|\phi|^2 + g|\phi(\mathbf{x}, t)|^4, \\ -i\hbar\phi\frac{\partial\phi^*}{\partial t} &= -\frac{\hbar^2}{2m}\phi\nabla^2\phi^* + V_{ext}|\phi|^2 + g|\phi(\mathbf{x}, t)|^4. \end{aligned} \quad (2.26)$$

Subtracting them

$$i\hbar\left(\phi^*\frac{\partial\phi}{\partial t} + \phi\frac{\partial\phi^*}{\partial t}\right) = -\frac{\hbar^2}{2m}(\phi^*\nabla^2\phi - \phi\nabla^2\phi^*), \quad (2.27)$$

which assumes the form

$$\frac{\partial n}{\partial t} + \nabla \cdot (n\mathbf{v}) = 0, \quad (2.28)$$

where the particle density n , and the velocity field of the condensate \mathbf{v} are given by

$$n \equiv \phi\phi^* = |\phi|^2, \quad \mathbf{v} \equiv \frac{\hbar}{2mi} \left(\frac{\phi^*\nabla\phi - \phi\nabla\phi^*}{|\phi|^2} \right). \quad (2.29)$$

Instead of using the density of particles n , it is useful to define the mass density $\rho \equiv m|\phi|^2$ for which Eq. (2.28) becomes

$$\frac{\partial\rho}{\partial t} + \nabla \cdot (\rho\mathbf{v}) = 0. \quad (2.30)$$

Hence the GP equation has the form of a continuity equation for the mass density ρ . The total mass M of the condensate is simply given by integrating the mass density over the total volume

$$\int \rho d^3\mathbf{x} = \int m|\phi|^2 d^3\mathbf{x} = m \int |\phi|^2 d^3\mathbf{x} = mN = M. \quad (2.31)$$

A complete description of a BEC from a fluid dynamics point of view is obtained by writing the complex function ϕ in the magnitude-phase representation

$$\phi(\mathbf{x}, t) = \sqrt{n(\mathbf{x}, t)} e^{i\varphi(\mathbf{x}, t)}, \quad (2.32)$$

also known as Madelung transformation. Since

$$\begin{aligned} \nabla\phi &= \nabla\sqrt{n}e^{i\varphi} + \sqrt{n}i\nabla\varphi e^{i\varphi}, \\ \nabla\phi^* &= \nabla\sqrt{n}e^{-i\varphi} - \sqrt{n}i\nabla\varphi e^{-i\varphi}, \end{aligned} \quad (2.33)$$

the velocity field becomes

$$\mathbf{v} = \frac{\hbar}{2mi} \left(\frac{\phi^*\nabla\phi - \phi\nabla\phi^*}{|\phi|^2} \right) = \frac{\hbar}{2mi} \frac{2ni\nabla\varphi}{n} = \frac{\hbar}{m}\nabla\varphi, \quad (2.34)$$

which reveals an interesting property of condensates: $\nabla \times \mathbf{v} = \mathbf{0}$. Hence, the flow is irrotational which is a typical characteristic of superfluids. It is now possible to deeply understand the nature of a vortex in a BEC and in a superluid by evaluating the integrated change in the phase

$$\Delta\varphi = \oint_C \nabla\varphi \cdot d\mathbf{l}, \quad (2.35)$$

where $d\mathbf{l} = dr\mathbf{u}_r + rd\theta\mathbf{u}_\theta$ is the infinitesimal displacement along the curve C which encloses a vortex. Assuming the values of the wavefunction ϕ_{in} and ϕ_{fin} at the initial and final points of the curve $C_{in} \equiv C_{fin}$, to be equal (single-valued wavefunction), it implies

$$\Delta\varphi = 2\pi k, \quad k = \pm 1, \pm 2 \dots \quad (2.36)$$

Therefore, a vortex in a BEC is not only a region in which the density goes to zero, but most importantly, it is a phase defect of the condensate. The evaluation of the circulation is straightforward and is given by

$$\gamma = \oint_C \mathbf{v} \cdot d\mathbf{l} = \frac{\hbar}{m} k, \quad k = \pm 1, \pm 2 \dots \quad (2.37)$$

where C is a curve which encloses the singularity and \mathbf{v} is given by Eq. (2.34). If the curve C does not enclose any singularity, then Stoke's theorem can be applied and

$$\gamma = \oint_C \mathbf{v} \cdot d\mathbf{l} = \int_A \nabla \times \mathbf{v} \cdot d\mathbf{A}, \quad (2.38)$$

where A is a surface with boundary C and $d\mathbf{A}$ is the surface normal. Since the flow is irrotational, the circulation is identically zero. However, Stoke's theorem does not hold if C encloses a vortex and hence, a fluid can be irrotational and still carry circulation: in this case the velocity field is irrotation except at the position of the vortex in which all the circulation is squeezed. Equation (2.37) reveals an important property of quantum fluids: the circulation is quantized and the quantum of circulation is given by \hbar/m . This property is not true in classical fluids where the circulation can assume any continuous value. If the velocity field generated by a single vortex $\mathbf{v} = v_r\mathbf{u}_r + v_\theta\mathbf{u}_\theta$ has no component along \mathbf{u}_r , Eq. (2.37) gives

$$\gamma = \oint_C \mathbf{v} \cdot d\mathbf{l} = 2\pi r v_\theta, \quad v_\theta = \frac{\gamma}{2\pi r}, \quad (2.39)$$

which is the azimuthal velocity around the singularity which is singular at the position of the vortex. To conclude the hydrodynamic formulation of BEC, the Madelung transformation (2.32) is now substituted into the GP equation (2.14) where, without loss of generality, the external potential V_{ext} is set equal to zero. Equating both the real and the imaginary parts of the left and right hand sides, leads to the following two

equations

$$\Re e : -\hbar \frac{\partial \theta}{\partial t} \sqrt{n} = -\frac{\hbar^2}{2m} \nabla^2 \sqrt{n} + \frac{\hbar^2}{2m} \sqrt{n} |\nabla \varphi|^2 + gn\sqrt{n}, \quad (2.40)$$

$$\Im m : \hbar \frac{\partial \sqrt{n}}{\partial t} = -\frac{\hbar^2}{2m} \sqrt{n} \nabla^2 \varphi - \frac{\hbar^2}{m} \nabla \sqrt{n} \cdot \nabla \varphi. \quad (2.41)$$

For points where $n \neq 0$, the gradient of Eq. (2.40) gives

$$-m \frac{\partial \mathbf{v}}{\partial t} = -\frac{\hbar^2}{2m} \nabla \left[\frac{\nabla^2 \sqrt{n}}{\sqrt{n}} \right] + \frac{1}{2} \nabla |\mathbf{v}|^2 + g \nabla n, \quad (2.42)$$

where Eq. (2.34) has been used. The second term on the right hand side can be written by using the following vectorial identity $\nabla |\mathbf{v}|^2 = 2\mathbf{v} \times (\nabla \times \mathbf{v}) + 2(\mathbf{v} \cdot \nabla)\mathbf{v}$ which gives

$$-m \frac{\partial \mathbf{v}}{\partial t} = -\frac{\hbar^2}{2m} \nabla \left[\frac{\nabla^2 \sqrt{n}}{\sqrt{n}} \right] + \mathbf{v} \times (\nabla \times \mathbf{v}) + (\mathbf{v} \cdot \nabla)\mathbf{v} + g \nabla n, \quad (2.43)$$

and since $\nabla \times \nabla \varphi = 0$,

$$\frac{\partial \mathbf{v}}{\partial t} + (\mathbf{v} \cdot \nabla)\mathbf{v} = -\frac{g}{m^2} \nabla \rho + \frac{\hbar^2}{2m^2} \nabla \left[\frac{\nabla^2 \sqrt{\rho}}{\sqrt{\rho}} \right]. \quad (2.44)$$

where $\rho = mn(\mathbf{x}, t)$ is the mass density. If the last term in the above equation is neglected, the above equation is similar to the Euler equation for an ideal fluid. It should be notice that the Euler equation contains the term $\mathbf{v} \times (\nabla \times \mathbf{v})$ which in this case is identically zero. The last term is the *quantum pressure* which reveals the quantum nature of the system and it vanishes if $\hbar \rightarrow 0$. If the imaginary part (2.41) is considered, by writing

$$\frac{1}{2} \frac{\partial n}{\partial t} = -\frac{\hbar}{2m} n \nabla^2 \varphi - \frac{\hbar}{2m} \nabla n \cdot \nabla \varphi = -\frac{1}{2} \nabla \cdot (n\mathbf{v}), \quad (2.45)$$

and noting that

$$\nabla n = \nabla(\sqrt{n})^2 = 2\sqrt{n} \nabla \sqrt{n} \quad , \quad \frac{\partial n}{\partial t} = \frac{\partial}{\partial t}(\sqrt{n})^2 = 2\sqrt{n} \frac{\partial \sqrt{n}}{\partial t}. \quad (2.46)$$

the continuity equation (2.28)

$$\frac{\partial n}{\partial t} + \nabla \cdot (n\mathbf{v}), \quad (2.47)$$

is recovered which can be multiplied by the mass of each boson m in order to get Eq. (2.30). This shows that the GP equation contains two fundamental equations of fluid

dynamics: the continuity equation (2.47) and the Euler equation (2.44) except for the quantum pressure term.

2.4 Two Dimensional Flows in Unbounded Domains

In this section a brief introduction on two dimensional fluid dynamics will be given. A two-dimensional flow is described by a velocity field

$$\mathbf{u} = \mathbf{u}(\mathbf{x}, t) = u\mathbf{i} + v\mathbf{j}, \quad (2.48)$$

where the component w along the \mathbf{k} direction is zero. The density of the fluid $\rho(\mathbf{x}, t)$ will in general be a function of space and time and the conservation of the mass implies that the density must satisfy the continuity equation (2.30). If the density does not change in time and space the flow is said to be incompressible and hence, the continuity equation (2.30) becomes

$$\nabla \cdot \mathbf{u} = 0. \quad (2.49)$$

Hereafter, the density will be assumed to be constant in space and time. The vorticity field $\boldsymbol{\omega}$ is defined as the curl of the velocity field \mathbf{u}

$$\boldsymbol{\omega} = \nabla \times \mathbf{u}, \quad (2.50)$$

whose magnitude acts as a measure of the *local* rotation of fluid elements. It has to be emphasized that the vorticity has nothing directly to do with any global rotation of the fluid: in fact a fluid can undergo rigid rotation but have zero vorticity. The incompressibility condition given by (2.49) imposes the existence of a function ψ called *vector potential*, such that

$$\mathbf{u} = \nabla \times \psi, \quad (2.51)$$

where the dependence of the spatial variables is understood. By inserting (2.51) into (2.50), the vorticity becomes

$$\boldsymbol{\omega} = -\nabla^2 \psi + \nabla(\nabla \cdot \psi). \quad (2.52)$$

the vector potential is not unique: in fact, for any smooth scalar field χ , it is possible to define $\psi' = \psi + \nabla \chi$ which still satisfy Eq. (2.49). This gauge freedom can be used

to fix the gauge $\nabla \cdot \psi = 0$ which will simplify Eq. (2.52) into

$$\omega = -\nabla^2 \psi. \quad (2.53)$$

In a two dimensional flow, the vorticity (2.50) has a non-zero component only along \mathbf{k} and hence also the vector potential is non-zero only along the same direction and it can be written $\psi = \psi \mathbf{k}$. As a consequence, Eq. (2.53) reduces to a scalar equation

$$\omega = -\nabla^2 \psi, \quad (2.54)$$

where ψ is called *streamfunction*. Moreover, by inserting $\psi = \psi \mathbf{k}$ into (2.51), the velocity becomes

$$\mathbf{u} = \nabla \times \psi = \nabla \psi \times \mathbf{k} + \psi \nabla \times \mathbf{k} = \nabla \psi \times \mathbf{k} = \frac{\partial \psi}{\partial y} \mathbf{i} - \frac{\partial \psi}{\partial x} \mathbf{j}, \quad (2.55)$$

and hence, by comparison with Eq. (2.48)

$$u = \frac{\partial \psi}{\partial y}, \quad v = -\frac{\partial \psi}{\partial x}. \quad (2.56)$$

In order to understand the importance of the streamfunction, the concept of a streamline needs to be introduced. A *streamline* is defined as a line that is everywhere tangent to the instantaneous velocity field. Hence, if $d\mathbf{x} = dx\mathbf{i} + dy\mathbf{j}$ is the element of length along the streamline, then the cross product between $d\mathbf{x}$ and \mathbf{u} must vanish,

$$\mathbf{u} \times d\mathbf{x} = (udx - vdy)\mathbf{k} = \mathbf{0}, \quad (2.57)$$

which defines the equation of a streamline. The variation of the streamfunction $d\psi(x, y)$ along a streamline is given by

$$d\psi = \frac{\partial \psi}{\partial x} dx + \frac{\partial \psi}{\partial y} dy = -vdx + udy = 0, \quad (2.58)$$

where in the last equality Eq. (2.57) has been used. This shows the important property that along a streamline the streamfunction is constant.

For a fluid with constant density ρ , described by a velocity field \mathbf{u} , it is possible to define its kinetic energy by

$$E_{kin} = \frac{\rho}{2} \int |\mathbf{u}|^2 d^2 \mathbf{x}, \quad (2.59)$$

where $d^2\mathbf{x} = dx dy$, and the integral is extended to the unbounded domain. Integrating by parts and assuming that the streamfunction goes to zero at infinity, Eq. (2.59) becomes

$$E_{kin} = \frac{\rho}{2} \int |\nabla \psi| \cdot |\nabla \psi| d^2\mathbf{x} = -\frac{\rho}{2} \int \psi \nabla^2 \psi d^2\mathbf{x}, \quad (2.60)$$

Recalling Eq. (2.54), the final expression for the kinetic energy is given by

$$E_{kin} = \frac{\rho}{2} \int \psi(\mathbf{x}) \omega(\mathbf{x}) d^2\mathbf{x}. \quad (2.61)$$

Another important physical quantity related to a fluid is given by the angular momentum \mathbf{L} : for a fluid with density ρ it is given by

$$\mathbf{L} = \int (\mathbf{x} - \mathbf{x}_c) \times \rho \mathbf{u} d^2\mathbf{x} \quad (2.62)$$

where \mathbf{x}_c is the reference position about which the angular momentum needs to be evaluated and the integral is extended to the considered domain. It is clear that the angular momentum has a non-zero component only along the \mathbf{k} direction since $\mathbf{x} - \mathbf{x}_c$ and \mathbf{u} do not have component along \mathbf{k} .

Sometimes, it is useful to express the velocity and the vorticity fields in polar coordinates (r, θ) and, in this case, the radial and azimuthal components of the velocity are given by

$$u_r = \frac{1}{r} \frac{\partial \psi}{\partial \theta}, \quad u_\theta = -\frac{\partial \psi}{\partial r}. \quad (2.63)$$

Expressing Eq. (2.54) in polar coordinates, the vorticity is given by

$$\omega = -\frac{1}{r} \frac{\partial}{\partial r} \left(r \frac{\partial \psi}{\partial r} \right) - \frac{1}{r^2} \frac{\partial^2 \psi}{\partial \theta^2}. \quad (2.64)$$

2.4.1 Point Vortex Decomposition

In the previous section a description of a fluid flow in terms of the velocity field has been provided and important physical quantities such as the kinetic energy and the angular momentum have been introduced. As stated at the end of §(??), the velocity field \mathbf{u} can be obtained once the vorticity field $\boldsymbol{\omega}$ is given. Hence, the first step is to define the vorticity field $\boldsymbol{\omega}$ for the flow.

The simplest model for a flow containing vorticity is the so called *point vortex model* and it was introduced by Helmholtz [56] in 1858: in this model, the vorticity of a single vortex with circulation γ_0 located at the point $\mathbf{x} = \mathbf{x}_0$, is represented by the Dirac's

delta function

$$\omega_0(\mathbf{x}) = \gamma_0 \delta(\mathbf{x} - \mathbf{x}_0). \quad (2.65)$$

In other words, the vorticity source is concentrated at the point $\mathbf{x} = \mathbf{x}_0$ it has infinite intensity but a finite circulation. Since the Eq. (2.54) is linear, for a distribution of N vortices it is possible to invoke the principle of superposition. Hence, labelling each point vortex by a subscript j , the total vorticity for such a system is given by

$$\omega(\mathbf{x}) = \sum_{j=1}^N \omega_j(\mathbf{x}) = \sum_{j=1}^N \gamma_j \delta(\mathbf{x} - \mathbf{x}_j), \quad (2.66)$$

where \mathbf{x}_j and γ_j are the position and the circulation of j -th vortex respectively.

The streamfunction for a single vortex with strength γ_0 placed at $\mathbf{x} = \mathbf{x}_0$ can be evaluated by solving Eq. (2.54) with (2.65) on the left hand side,

$$\nabla^2 \psi_0 = -\gamma_0 \delta(\mathbf{x} - \mathbf{x}_0), \quad (2.67)$$

whose solution ² is given by

$$\psi_0(\mathbf{x}) = -\frac{\gamma_0}{2\pi} \log |\mathbf{x} - \mathbf{x}_0|. \quad (2.68)$$

The presence of a single vortex generates a velocity field whose components are given by (2.56)

$$u_0(x, y) = \frac{\partial \psi}{\partial y} = -\frac{\gamma_0}{2\pi} \frac{y - y_0}{(x - x_0)^2 + (y - y_0)^2}, \quad (2.69)$$

$$v_0(x, y) = -\frac{\partial \psi}{\partial x} = \frac{\gamma_0}{2\pi} \frac{x - x_0}{(x - x_0)^2 + (y - y_0)^2}. \quad (2.70)$$

Notice that the velocity field is undefined at $(x, y) = (x_0, y_0)$ where the vortex is located and since a point vortex does not induce velocity on itself, the position of an isolated point vortex does not change in time. For a distribution of N vortices located at \mathbf{x}_i with strength γ_i , the principle of superposition can be invoked. Therefore, the streamfunction is given by

$$\psi(\mathbf{x}) = \sum_{i=1}^N \psi_i(\mathbf{x}) = -\frac{1}{2\pi} \sum_{i=1}^N \gamma_i \log |\mathbf{x} - \mathbf{x}_i|, \quad (2.71)$$

²For details see Appendix §(??)

and the components of the velocity are given by

$$u(x, y) = \sum_{i=1}^N u_i(x, y) = \sum_{i=1}^N \frac{\gamma_i}{2\pi} \frac{y - y_i}{(x - x_i)^2 + (y - y_i)^2}, \quad (2.72)$$

$$v(x, y) = \sum_{i=1}^N v_i(x, y) = - \sum_{i=1}^N \frac{\gamma_i}{2\pi} \frac{x - x_i}{(x - x_i)^2 + (y - y_i)^2}, \quad (2.73)$$

for $(x, y) \neq (x_i, y_i)$, $i = 1, \dots, N$. In this case, the velocity field is not defined in all the positions $(x, y) = (x_i, y_i)$, $i = 1, \dots, N$ in which vortices are located. If N vortices are present in a flow, the velocity at the position (x_j, y_j) where a vortex is located, is given by evaluating the velocity field generated by the $N-1$ vortices except from the j -th vortex at the position $(x, y) = (x_j, y_j)$, hence

$$u_j \equiv u(x_j, y_j) = \sum_{\substack{i=1 \\ i \neq j}}^N \frac{\gamma_i}{2\pi} \frac{y_j - y_i}{(x_j - x_i)^2 + (y_j - y_i)^2}, \quad (2.74)$$

$$v_j \equiv v(x_j, y_j) = - \sum_{\substack{i=1 \\ i \neq j}}^N \frac{\gamma_i}{2\pi} \frac{x_j - x_i}{(x_j - x_i)^2 + (y_j - y_i)^2}, \quad (2.75)$$

where the terms $j = i$ have been removed in order to avoid the contribution of the j -th vortex. Since the velocity of a single vortex evaluated at the position of the vortex is not defined, hence, also its kinetic energy is singular: in fact, assuming a constant density ρ , the kinetic energy is given by substituting Eq. (2.65) and Eq. (2.68) into Eq. (2.61)

$$E_{kin} = \frac{\rho}{2} \int \psi_0(\mathbf{x}) \omega_0(\mathbf{x}) d^2\mathbf{x} = - \frac{\rho \gamma_0^2}{4\pi} \int \log |\mathbf{x} - \mathbf{x}_0| \delta(\mathbf{x} - \mathbf{x}_0) d^2\mathbf{x}, \quad (2.76)$$

which diverges since the presence of Dirac's delta function imposes $\mathbf{x} = \mathbf{x}_0$. This divergent quantity is called the *selfinteraction* and, in this model, it is not a well defined quantity. For a distribution of N vortices, the kinetic energy will be given by two contributions: the first is given by all the selfinteractions terms and the second contribution is given by all the interactions between all the other vortices. The selfinteraction terms will be neglected and the term which involves all the interactions between the vortices will be called *Hamiltonian* and it will be denoted by the letter \mathcal{H} . Therefore, when a distribution of N vortices is considered, the kinetic energy is given by inserting (2.71)

and (2.66) into (2.61)

$$E_{kin} = -\frac{\rho}{4\pi} \sum_{i,j=1}^N \gamma_i \gamma_j \log |\mathbf{x}_i - \mathbf{x}_j| = \mathcal{H} + \mathcal{H}_\infty, \quad (2.77)$$

where a factor $1/2$ has been introduced in order not to double count the interactions. \mathcal{H} represents the regular part and \mathcal{H}_∞ the self interaction terms

$$\mathcal{H} = -\frac{\rho}{4\pi} \sum_{\substack{i,j=1 \\ i \neq j}}^N \gamma_i \gamma_j \log |\mathbf{x}_i - \mathbf{x}_j|, \quad \mathcal{H}_\infty = -\frac{\rho}{4\pi} \lim_{\epsilon \rightarrow 0} \sum_{i=1}^N \gamma_i^2 \log |\epsilon|. \quad (2.78)$$

By knowing the Hamiltonian of the system, the components of the velocity can be recovered by evaluating the following terms

$$\dot{x}_j = \frac{1}{\gamma_j} \frac{\partial \mathcal{H}}{\partial y_j}, \quad \dot{y}_j = -\frac{1}{\gamma_j} \frac{\partial \mathcal{H}}{\partial x_j}. \quad (2.79)$$

At this stage it is useful to notice that in the above equations the position coordinates play the role of canonically conjugate coordinates for the Hamiltonian system given by \mathcal{H} as defined in (2.78). This is a crucial property of a two dimensional system: the *phase space* coincides with the physical space and this important fact plays a fundamental role in the study of these systems using a statistical mechanical approach. More details are given in Chapter §3.

2.4.2 Point Vortex Approximation of the Gross-Pitaevskii Equation

The GP equation (2.14) can also be derived [92] by evaluating

$$i\hbar \frac{\partial \phi}{\partial t} = \frac{\delta H_{GP}}{\delta \phi^*}, \quad (2.80)$$

where H_{GP} is the energy functional defined as

$$H_{GP} = \int d^3\mathbf{x} \left[\frac{\hbar^2}{2m} |\nabla \phi(\mathbf{x}, t)|^2 + V_{ext} |\phi(\mathbf{x}, t)|^2 + \frac{g}{2} |\phi(\mathbf{x}, t)|^4 \right]. \quad (2.81)$$

Following [18], the two dimensional GP energy functional H_{GP} can be decomposed as the sum of the following four terms

$$E_K = \frac{1}{2} \int \rho(\mathbf{x}, t) |\mathbf{v}(\mathbf{x}, t)|^2 d^3\mathbf{x}, \quad (2.82)$$

$$E_V = \frac{1}{m} \int \rho(\mathbf{x}, t) V_{ext}(\mathbf{x}, t) d^3\mathbf{x}, \quad (2.83)$$

$$E_I = \frac{g}{2m^2} \int \rho^2(\mathbf{x}, t) d^3\mathbf{x}, \quad (2.84)$$

$$E_Q = \frac{\hbar^2}{2m^2} \int \nabla \sqrt{\rho(\mathbf{x}, t)} |^2 d^3\mathbf{x}. \quad (2.85)$$

where $\rho(\mathbf{x}, t) = mn(\mathbf{x}, t)$ is the density, V_{ext} is the external potential and g is the coupling constant defined by Eq. (2.8). These terms are the component of the total energy H decomposed into the kinetic energy E_K , the potential energy E_V , the interaction energy E_I and the quantum pressure energy E_Q . When the flow is described on lengthscales larger than the healing length, the density can be approximated as $\rho(\mathbf{x}, t) \approx \rho_0 + \epsilon \tilde{\rho}(\mathbf{x}, t)$ where $\epsilon \ll 1$. Then at leading order E_I is constant and E_Q is zero. If the external potential is zero, then also E_V is zero and the relevant term in the energy functional H_{GP} is the kinetic energy term E_K . A three-dimensional system containing N straight vertical vortex lines can be reduced to a planar distribution of N point vortices if the variable along the \mathbf{k} direction is set to be constant. In this case, the kinetic energy E_K of a planar distribution of vortices becomes

$$E_K = \frac{1}{2} \int \rho(\mathbf{x}, t) |\mathbf{v}(\mathbf{x}, t)|^2 d^2\mathbf{x}, \quad (2.86)$$

and it presents both infrared and ultraviolet divergence. In order to regularised E_K , a multiply connected domain \mathcal{A} which contains N vortices each with circulation γ_k is considered. The domain \mathcal{A} is assumed to be bounded by a circle with radius R in which small circles \mathcal{C}_k with radius r_k ($k = 1, \dots, N$) around each vortex have been removed. The radius r_k of each circle is small but still large compared to the healing length ξ defined by Eq. (2.24). At leading order, the kinetic term E_K can be written as follows

$$E_K = \frac{\rho_0}{2} \int_{\mathcal{A}} |\mathbf{v}|^2 d^2\mathbf{x} = \frac{\rho_0}{2} \int_{\mathcal{A}} (\mathbf{v} \times \nabla \psi) \cdot \mathbf{k} d^2\mathbf{x}, \quad (2.87)$$

where ψ is the streamfunction given by Eq. (2.71) related to the components of the velocity \mathbf{v} by Eq. (2.56). Since $\nabla \times (\mathbf{v}\psi) = \psi \nabla \times \mathbf{v} + \mathbf{v} \times \nabla \psi$, and the fluid is irrotational

in the multiple connected domain, the above equation becomes

$$E_K = \frac{\rho_0}{2} \int_{\mathcal{A}} \nabla \times (\mathbf{v}\psi) \cdot d\mathbf{S} = \frac{\rho_0}{2} \oint_{\mathcal{C}} \psi \mathbf{v} \cdot d\mathbf{l} + \frac{\rho_0}{2} \oint_{\mathcal{C}_k} \psi \mathbf{v} \cdot d\mathbf{l}, \quad (2.88)$$

where $d\mathbf{S} = \mathbf{k}d^2\mathbf{x}$ and the Stokes' theorem has been applied. In Eq. (2.88) $d\mathbf{l}_k = (dr_k, r_k d\theta)$ is the infinitesimal displacement along each curve \mathcal{C}_k and $d\mathbf{l} = (dr, rd\theta)$ along \mathcal{C} . Along the curve \mathcal{C} distant R from the vortices, the velocity field and the streamfunction ψ can be approximated by replacing all the vortices by a single vortex with circulation equal to the sum of the circulations of all vortices, hence

$$v_\theta = \frac{\gamma_{tot}}{2\pi R}, \quad \psi(R) = -\frac{\gamma_{tot}}{2\pi} \log R, \quad \gamma_{tot} = \sum_{k=1}^N \gamma_k, \quad (2.89)$$

where Eqs. (2.39) and (2.71) have been used. Substituting these two quantities into the integral along \mathcal{C} in Eq. (2.88) gives

$$\frac{\rho_0}{2} \oint_{\mathcal{C}} \psi \mathbf{v} \cdot d\mathbf{l} = -\frac{\rho}{4\pi} \gamma_{tot}^2 \log R. \quad (2.90)$$

The second integral of (2.88) along the curves \mathcal{C}_k can be regularised by assuming that on the circle the streamfunction given by Eq. (2.71) is nearly constant and it is given by

$$\psi(\mathbf{x}_k) = -\frac{1}{2\pi} \sum_{\substack{j=1 \\ j \neq k}}^N \gamma_j \log |\mathbf{x}_k - \mathbf{x}_j|. \quad (2.91)$$

In fact, since the velocity around each circle \mathcal{C}_k is given by $v_\theta = \gamma_k/2\pi r_k$, the last term of Eq. (2.88) becomes

$$\frac{\rho_0}{2} \oint_{\mathcal{C}_k} \psi \mathbf{v} \cdot d\mathbf{l} = -\frac{\rho_0}{4\pi} \sum_{\substack{j,k=1 \\ j \neq k}}^N \gamma_j \gamma_k \log |\mathbf{x}_k - \mathbf{x}_j|, \quad (2.92)$$

which is the regularised interaction energy. The first integral given by Eq. (2.90) is constant and it does not contribute to the dynamics. On the other hand, the integral given by (2.92) depends on the mutual distance $|\mathbf{x}_k - \mathbf{x}_j|$ and it contributes to the dynamics. The term of the kinetic energy E_K given by Eq. (2.92) is equivalent to the regular term of the Hamiltonian \mathcal{H} for the point vortex model given by Eq. (2.78). This ensures the possibility of studying the dynamics of quantum vortices in a BEC described by the GP equation (2.14) by using the point vortex model approach where

the equation of motions are given by Eq. (2.79).

2.4.3 Lamb-Oseen Vortex

The vorticity defined by the point vortex model is very useful for a mathematical purpose, but it is not suitable for numerical purposes due to the presence of the delta function. For this reason a continuum representation of vorticity from superfluid point vortices can be introduced by considering the so called *Lamb-Oseen vortex* as an exact solution of the Navier-Stokes equation. This vorticity field is a way to regularising point vortices that will be used in this work later. Since it arises as an exact solution of the Navier-Stokes equation for the vorticity, a brief introduction to the Navier-Stokes equation for an incompressible fluid in three spatial dimension will be given, and subsequently a two dimensional case is considered.

The Navier-Stokes equation for a three dimensional velocity field \mathbf{u} with density ρ is given by [86]

$$\frac{\partial \mathbf{u}}{\partial t} + (\mathbf{u} \cdot \nabla) \mathbf{u} = -\frac{1}{\rho} \nabla p + \nu \nabla^2 \mathbf{u}, \quad (2.93)$$

where p is the pressure field and ν is the viscosity of the fluid. By using the following identities

$$(\mathbf{u} \cdot \nabla) \mathbf{u} = \frac{1}{2} \nabla |\mathbf{u}|^2 - \mathbf{u} \times (\nabla \times \mathbf{u}), \quad (2.94)$$

$$\nabla^2 \mathbf{u} = -\nabla \times \nabla \times \mathbf{u} + \nabla (\nabla \cdot \mathbf{u}), \quad (2.95)$$

Eq. (2.93) can be written as

$$\frac{\partial \mathbf{u}}{\partial t} + \frac{1}{2} \nabla |\mathbf{u}|^2 + \boldsymbol{\omega} \times \mathbf{u} = -\frac{1}{\rho} \nabla p - \nu \nabla \times \nabla \times \mathbf{u}, \quad (2.96)$$

where the incompressibility condition (2.49) has been applied. Taking the curl of this equation and noticing that the divergence of a curl and the curl of a gradient are trivially zero, gives

$$\frac{\partial \boldsymbol{\omega}}{\partial t} + \nabla \times (\boldsymbol{\omega} \times \mathbf{u}) = \nu \nabla^2 \boldsymbol{\omega}. \quad (2.97)$$

By using the following identity

$$\nabla \times (\boldsymbol{\omega} \times \mathbf{u}) = (\mathbf{u} \cdot \nabla) \boldsymbol{\omega} - (\boldsymbol{\omega} \cdot \nabla) \mathbf{u} + \boldsymbol{\omega} (\nabla \cdot \mathbf{u}) - \mathbf{u} (\nabla \cdot \boldsymbol{\omega}), \quad (2.98)$$

and noticing that the last two terms vanish, the Navier-Stokes equation for the vorticity

finally becomes

$$\frac{\partial \boldsymbol{\omega}}{\partial t} + (\mathbf{u} \cdot \nabla) \boldsymbol{\omega} - (\boldsymbol{\omega} \cdot \nabla) \mathbf{u} = \nu \nabla^2 \boldsymbol{\omega}. \quad (2.99)$$

This equation holds for a three dimensional flow, and if a two dimensional flow is considered, it can be simplified since the last term on the left hand side vanishes

$$\frac{\partial \boldsymbol{\omega}}{\partial t} + (\mathbf{u} \cdot \nabla) \boldsymbol{\omega} = \nu \nabla^2 \boldsymbol{\omega}. \quad (2.100)$$

In addition, for a two dimensional flow, the vorticity $\boldsymbol{\omega}$ becomes a scalar function perpendicular to the plane where the dynamics occurs so that $\boldsymbol{\omega} = (0, 0, \omega(x, y))$. Hence, the above vectorial equation becomes

$$\frac{\partial \omega}{\partial t} + (\mathbf{u} \cdot \nabla) \omega = \nu \nabla^2 \omega. \quad (2.101)$$

By using a polar coordinate system and by assuming $\mathbf{u} = (0, u_\theta, 0)$ and $\boldsymbol{\omega} = (0, 0, \omega(r))$ the Navier-Stokes equation becomes the heat equation for the vorticity ω

$$\frac{\partial \omega}{\partial t} = \nu \nabla^2 \omega. \quad (2.102)$$

Equation (2.102) is a diffusive equation which depends on the viscosity ν which determines the size of the viscous vortex core. Before solving Eq. (2.102) it is important to clarify what Eq. (2.102) represents. If a single vortex with strength γ_0 is placed somewhere in a two dimensional space the above equation represents the evolution in time of the vorticity field due to the viscosity represented by the parameter ν . If the vortex is assumed to be placed at the origin, at some initial time, the vorticity is given by

$$\omega(\mathbf{x}, t = 0) = \gamma_0 \delta(\mathbf{x}), \quad (2.103)$$

which is the required initial condition. By inserting the inverse Fourier transform of the vorticity field

$$\omega(\mathbf{x}, t) = \frac{1}{2\pi} \int_{-\infty}^{+\infty} \int_{-\infty}^{+\infty} \tilde{\omega}(\mathbf{k}, t) e^{i\mathbf{k} \cdot \mathbf{x}} dk_x dk_y, \quad \mathbf{k} = (k_x, k_y), \quad (2.104)$$

into Eq. (2.102) the problem is reduced to solving

$$\frac{\partial \tilde{\omega}}{\partial t} = -\nu |\mathbf{k}|^2 \tilde{\omega}, \quad (2.105)$$

which can be integrated to obtain

$$\tilde{\omega}(\mathbf{k}, t) = A e^{-\nu|\mathbf{k}|^2 t}, \quad (2.106)$$

where A needs to be determined by imposing the initial condition described in (2.103). In particular, the Fourier transform of the initial condition is given by

$$A = \tilde{\omega}(\mathbf{k}, t=0) = \frac{1}{2\pi} \int_{-\infty}^{+\infty} \int_{-\infty}^{+\infty} \gamma_0 \delta(\mathbf{x}) e^{-i\mathbf{k}\cdot\mathbf{x}} dx dy = \frac{\gamma_0}{2\pi}. \quad (2.107)$$

The vorticity field is therefore given by evaluating the inverse Fourier transform of the above quantity

$$\omega(\mathbf{x}, t) = \frac{\gamma_0}{4\pi^2} \int_{-\infty}^{+\infty} \int_{-\infty}^{+\infty} e^{-\nu|\mathbf{k}|^2 t} e^{i\mathbf{k}\cdot\mathbf{x}} d\mathbf{k}, \quad (2.108)$$

which is a Gaussian integral of the form

$$\int_{-\infty}^{+\infty} \int_{-\infty}^{+\infty} e^{-\alpha|\mathbf{k}|^2 + \beta \cdot \mathbf{k}} d\mathbf{k} = \frac{\pi}{\alpha} e^{|\beta|^2 / 4\alpha}. \quad (2.109)$$

By comparison $\alpha = \nu t$ and $\beta = i\mathbf{x}$, and finally the vorticity is

$$\omega(\mathbf{x}, t) = \frac{\gamma_0}{4\pi\nu t} e^{-|\mathbf{x}|^2 / 4\nu t}, \quad (2.110)$$

which can be written as a function of the distance r ,

$$\omega(r, t) = \frac{\gamma_0}{4\pi\nu t} e^{-r^2 / 4\nu t}. \quad (2.111)$$

In the case of a point vortex the value of the circulation in a circle of radius $r > 0$ is always γ_0 : in the Lamb-Oseen vortex, this is not valid anymore. The value of the circulation in a circle of radius r and at time t is given by

$$\gamma_0(r, t) = \int_0^r \omega(\xi, t) 2\pi \xi d\xi = \gamma_0 \left[-e^{-\xi^2 / 4\nu t} \right]_0^r = \gamma_0 \left(1 - e^{-r^2 / 4\nu t} \right), \quad (2.112)$$

therefore, the value of the circulation depends on the distance r at which the integral (2.112) is evaluated and on time t . For a point vortex, the radial and the azimuthal component of the velocity are given by substituting (2.68) into (2.63) with $\mathbf{x}_0 = (0, 0)$

$$u_r = 0, \quad u_\theta = \frac{\gamma_0}{2\pi r} \quad (2.113)$$

and hence, the velocity profile of the Lamb-Oseen vortex is given by substituting γ_0 in

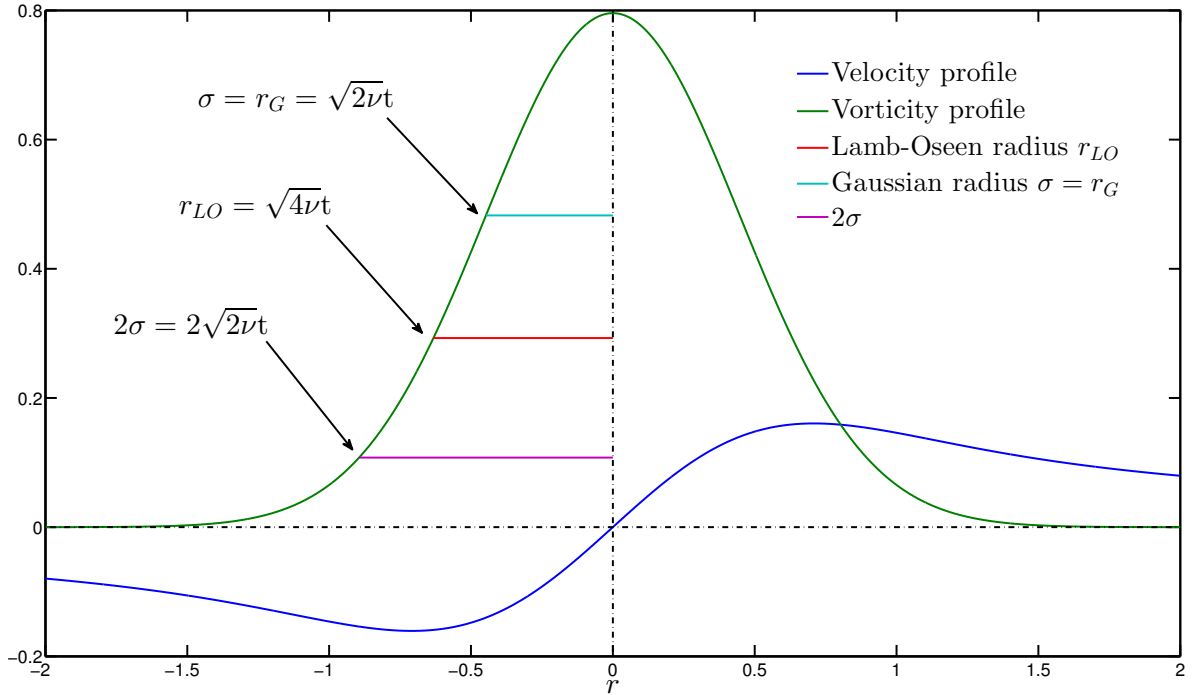


Figure 2.2: Vorticity and velocity profile for a Lamb-Oseen vortex.

the (2.113) with $\gamma_0(r, t)$ given by (2.112)

$$u_\theta(r, t) = \frac{\gamma_0}{2\pi r} \left(1 - e^{-r^2/4\nu t} \right). \quad (2.114)$$

The velocity and vorticity profiles for a Lamb-Oseen vortex as a function of the distance r from the core of the vortex are shown in Fig.(2.2): in this case $\gamma_0 = 1$ and $\nu = 0.1$. Fig.(2.2) shows also that for the Lamb-Oseen vortex, the velocity field is not singular, and this allows also the evaluation of the kinetic energy for a single vortex.

2.5 Domains with Boundaries

In the previous section a flow in an unbounded case has been described. However, experiments and physical systems are typically bounded, hence it is extremely important to develop a theory for finite size systems. Since the velocity field generated by a distribution of point vortices requires the knowledge of the streamfunction ψ , its role is crucial to investigate their dynamics. The Eq. (2.71) for the streamfunction is valid when an unbounded domain is considered, but its validity ceases in the presence of a finite domain of a solid boundary. Hereafter, a general domain \mathcal{D} with boundary $\partial\mathcal{D}$

will be considered. The domain \mathcal{D} could be a closed, simply or multiply connected region in the plane, or it could be an unbounded region with a solid boundary.

Intuitively, a solid boundary does not allow the fluid to penetrate it: this condition is satisfied if the normal component of velocity is zero on the boundary

$$\mathbf{u} \cdot \mathbf{n}|_{\partial\mathcal{D}} = 0, \quad (2.115)$$

where \mathbf{n} is the normal to the boundary. An example is shown in Fig.(2.3) where a vertical solid wall is considered: the normal \mathbf{n} to the boundary has component $(-1, 0)$ and the condition (2.115) imposes the component of the velocity in the x -direction to be zero, and the velocity can be only tangential to the boundary. In the presence of a boundary it is possible to define two kinds of Green's function, depending on whether the boundary condition is imposed on the function G or on its derivative. The *Green's function of the first kind* is defined as the solution of the following boundary problem

$$\nabla^2 G_I(\mathbf{x}, \mathbf{x}_i) = -\delta(\mathbf{x} - \mathbf{x}_i), \quad \mathbf{x} \in \mathcal{D}, \quad (2.116)$$

$$G_I(\mathbf{x}, \mathbf{x}_i) = 0, \quad \mathbf{x} \in \partial\mathcal{D}. \quad (2.117)$$

hence, the boundary conditions apply to the function G (Dirichlet boundary condition).

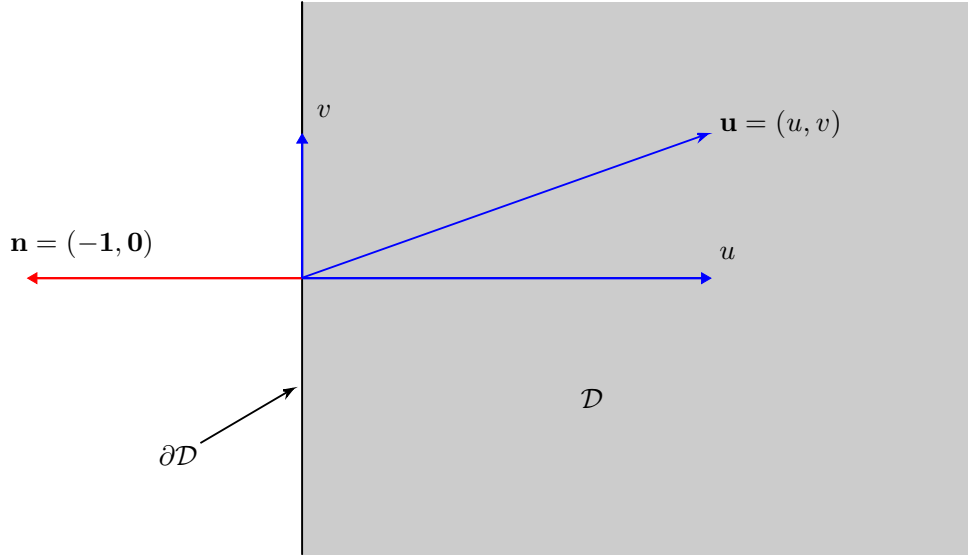


Figure 2.3: The grey area represents the domain \mathcal{D} . Along the boundary $\partial\mathcal{D}$ the u component must vanish.

The *Green's function of the second kind* is defined as the solution of the following

boundary problem

$$\nabla^2 G_{II}(\mathbf{x}, \mathbf{x}_i) = -\delta(\mathbf{x} - \mathbf{x}_i), \quad \mathbf{x} \in \mathcal{D}, \quad (2.118)$$

$$\frac{\partial G_{II}}{\partial \mathbf{n}}(\mathbf{x}, \mathbf{x}_i) = 0, \quad \mathbf{x} \in \partial \mathcal{D}. \quad (2.119)$$

As already stated, in the presence of a solid boundary the fluid cannot penetrate it, and hence, the velocity of the fluid must be parallel to the boundary. This condition implies that the boundary is a streamline for the flow as explained in §(2.4), and it requires a constant value of the streamfunction on $\partial \mathcal{D}$. As a consequence, the most natural choice is the Green's function of the first kind G_I .

As a first step, G_I can be decomposed into the sum of the fundamental solution $G(\mathbf{x}, \mathbf{x}_i)$ in the unbounded plane and an additional function G_H which is harmonic in \mathcal{D} but can have an unknown number of singularities, labelled by α , outside \mathcal{D}

$$G_I(\mathbf{x}) = \sum_i G(\mathbf{x}, \mathbf{x}_i) + \sum_\alpha G_H(\mathbf{x}, \mathbf{x}_\alpha). \quad (2.120)$$

The purpose of this additional function is to impose the right boundary conditions, since they are not satisfied by the fundamental solution. The number of singularities is not known a priori and it depends on the specific boundary conditions. Since $G_I(\mathbf{x}, \mathbf{x}_i)$ has to be zero on the boundary, then

$$\sum_i G(\mathbf{x}, \mathbf{x}_i) = - \sum_\alpha G_H(\mathbf{x}, \mathbf{x}_\alpha), \quad \mathbf{x} \in \partial \mathcal{D}. \quad (2.121)$$

This method is called *method of images* and the singularities are vortices with various strengths placed in particular positions outside the domain in order to satisfy the boundary conditions. It has to be noticed that finding $\sum_i G(\mathbf{x}, \mathbf{x}_i)$ is not simple, but it has been shown by Lin [69] that such a function always exists. In particular, for domains with certain symmetries, it is straightforward to construct the additional function G_H . In the following, two examples are presented: the first one is the procedure to construct the streamfunction for a single vortex in the vicinity of a corner (see §(2.5.1)). This example is preparatory for the case of a system of vortices contained in a box with sides L_x and L_y (see §(2.5.2)).

2.5.1 Vortex near a corner

The first example is given by a single vortex of strength γ located at (x_1, y_1) near two hard walls which form a corner as shown in Fig.(2.4). The boundary conditions

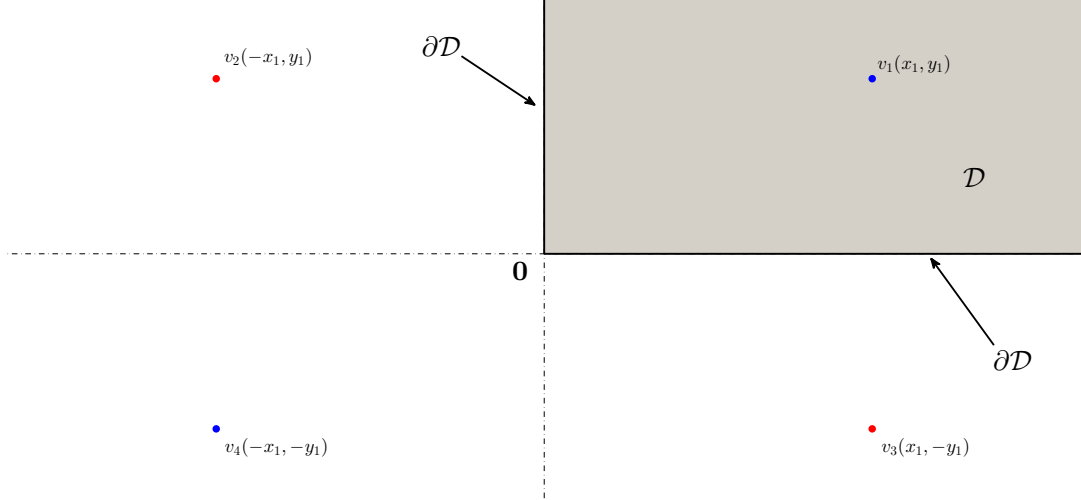


Figure 2.4: The system composed by a vortex in proximity of a corner: the shaded area is the domain where the *real* vortex is placed while the other vortices outside the domain are the *images*. The red vortices have positive circulation while the blue have negative circulation.

which need to be imposed are such that the Green's function of the first kind is zero if evaluated along the walls and at the corner which is the origin. It is easy to show [86] that G_I which satisfies the required boundary conditions is given by

$$\begin{aligned} G_I(\mathbf{x}) &= G(\mathbf{x}, \mathbf{x}_1) + \sum_{\alpha} G_H(\mathbf{x}, \mathbf{x}_{\alpha}) \\ &= -\frac{1}{2\pi} \log |\mathbf{x} - \mathbf{x}_1| \\ &\quad + \frac{1}{2\pi} \log |\mathbf{x} - \mathbf{x}_1^*| + \frac{1}{2\pi} \log |\mathbf{x} + \mathbf{x}_1^*| - \frac{1}{2\pi} \log |\mathbf{x} + \mathbf{x}_1|, \end{aligned} \quad (2.122)$$

where the first term represents the fundamental solution $G(\mathbf{x}, \mathbf{x}_1)$ and the other three terms represent $G_H(\mathbf{x}, \mathbf{x}_{\alpha})$, $\alpha = 1, 2, 3$. The fundamental solution is the contribution in the absence of the boundary and the other three terms ensure the Green's function $G_I(\mathbf{x})$ to vanish along the two walls. The fundamental solution represent a vortex located at (x_1, y_1) which is the only singularity in the domain \mathcal{D} . Outside the domain, three images are required to represent the effect of the corner: the first two are placed at $(-x_1, y_1)$ and $(x_1, -y_1)$ with opposite circulation $-\gamma$, and the third image is placed at $(-x_1, -y_1)$ with the same circulation γ . The streamfunction is obtained by simply

multiplying each term by the respective circulation and hence,

$$\begin{aligned}\psi(\mathbf{x}) = & -\frac{\gamma}{2\pi} \log |\mathbf{x} - \mathbf{x}_1| \\ & + \frac{\gamma}{2\pi} \log |\mathbf{x} - \mathbf{x}_1^*| + \frac{\gamma}{2\pi} \log |\mathbf{x} + \mathbf{x}_1^*| - \frac{\gamma}{2\pi} \log |\mathbf{x} + \mathbf{x}_1|. \quad (2.123)\end{aligned}$$

2.5.2 Vortex in a box

The previous example provides a starting point to understand how to model a system composed by vortices in a generic rectangular domain. If a single vortex is in the box, each corner is emulated by the presence of three vortices as described in the previous example (see Fig.(2.4)).

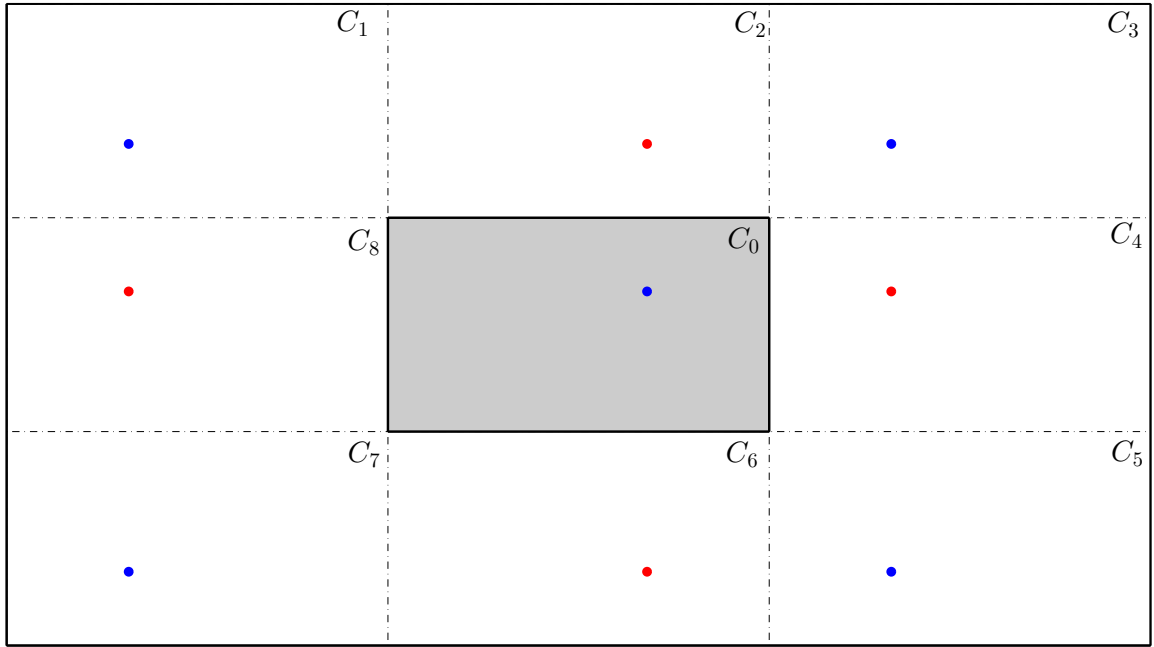


Figure 2.5: Each corner can be represented by adding three images per each corner: however, this is not sufficient to ensure the streamfunction to be constant along the walls and on each of the four corners. If C_0 is the reference cell which needs to be mimicked then other cells C_j , $j = 1, \dots, 8$, which contain the images, must be placed around C_0 .

The bottom right corner can be represented by the images located in the cells C_6 , C_7 and C_8 . The upper left corner by the images in the cells C_8 , C_1 and C_2 . The upper right corner by the images in the cells C_2 , C_3 and C_4 and finally the lower right corner by the images in the cells C_4 , C_5 and C_6 . However, the presence of the additional charges for each corner do not impose the right boundary conditions for the other corners. This problem can be solved only by adding an infinite set of images along both directions

as shown in Fig.(2.6). This fact has an immediate consequence: an infinite number of

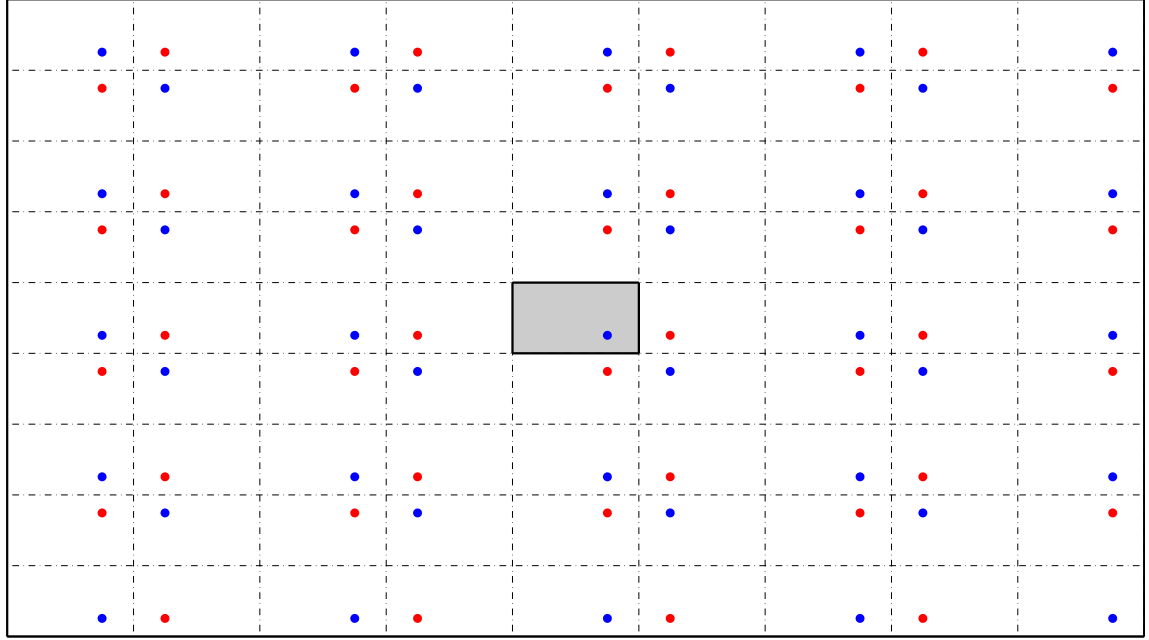


Figure 2.6: Only an infinite set of images can mimic the presence of a box (shaded area) with impenetrable walls.

terms are required to construct the streamfunction for a single vortex in the box. By considering Eq. (2.78) it immediately follows that an infinite set of vortices will have an infinite amount of energy. However, the infinite summation of all the interactions can be regularised and it will give a compact form for the Hamiltonian \mathcal{H} . In particular the Hamiltonian for N vortices with circulation γ_i located at (x_i, y_j) in a box with sides L_x and L_y , and aspect ratio $\Lambda = L_x/L_y$ is given by

$$\mathcal{H} = \frac{\rho}{4\pi} \left[\sum_{i=1}^N \gamma_i^2 b(x_i, y_i, \Lambda) + \sum_{i=1}^{N-1} \sum_{j=i+1}^N \gamma_i \gamma_j h(x_i, x_j, y_i, y_j, \Lambda) \right], \quad (2.124)$$

where the two functions $h(x_i, x_j, y_i, y_j, \Lambda)$ and $b(x_i, y_i)$ are defined as

$$\begin{aligned} h(x_i, x_j, y_i, y_j, \Lambda) &\equiv f(|x_i - x_j|, |y_i - y_j|, \Lambda) - f(|x_i - x_j|, L_y - y_i - y_j, \Lambda) \\ &\quad - f(L_x - x_i - x_j, |y_i - y_j|, \Lambda) + f(L_x - x_i - x_j, L_y - y_i - y_j, \Lambda), \\ b(x_i, y_i) &\equiv \frac{1}{2} [-f(2L_x - 2x_i, 0, \Lambda) + f(2L_x - 2x_i, L_y - 2y_i, \Lambda) - f(0, 2L_y - 2y_i, \Lambda)], \end{aligned} \quad (2.125)$$

and the additional function $f(x, y, \Lambda)$ is given by

$$f(x, y, \Lambda) = \left\{ \frac{2\pi}{\Lambda} \left[y(y-1) + \frac{1}{6} \right] - \log \prod_{k=-\infty}^{+\infty} \zeta(k, x, y, \Lambda) \right\}, \quad (2.126)$$

where

$$\zeta(k, x, y, \Lambda) = 1 - 2 \cos \left(\frac{2\pi x}{L_x} \right) e^{-\frac{2\pi|y+k|}{\Lambda}} + e^{-\frac{4\pi|y+k|}{\Lambda}}. \quad (2.127)$$

For a complete derivation, see Appendix§(??). The Hamiltonian (2.124) relies on the knowledge of the energy of two infinite arrays of vortices, along the x and the y directions which has been derived by Campbell [24] in 1989. Due to Eq. (2.61), the streamfunction is given by

$$\psi(x, y) = \frac{\rho}{2\pi} \sum_{j=1}^N \frac{\gamma_j}{2} h(x, x_j, y, y_j, \Lambda), \quad (2.128)$$

where $h(x, x_j, y, y_j, \Lambda)$ is given by Eq. (2.125).

2.5.3 Angular Momentum

The angular momentum of a fluid with constant density ρ measured with respect to a point $\mathbf{x}_c = (x_c, y_c)$ is defined as

$$\mathbf{L} = \rho \int_{\mathcal{D}} (\mathbf{x} - \mathbf{x}_c) \times \mathbf{u} dx dy, \quad (2.129)$$

where \mathbf{x} is the position vector, \mathbf{u} is the velocity field and \mathcal{D} is the surface of the system delimited by a regular curve $\partial\mathcal{D}$. The angular momentum is perpendicular to the plane where the dynamics occurs, therefore from now on only its magnitude L will be considered. The magnitude of \mathbf{L} can be evaluated by using (2.56)

$$\mathbf{u} = (u, v) = \left(\frac{\partial \psi}{\partial y}, -\frac{\partial \psi}{\partial x} \right), \quad \mathbf{x} - \mathbf{x}_c = (x - x_c, y - y_c), \quad (2.130)$$

for which

$$L = -\rho \int_{\mathcal{D}} \left[(x - x_c) \frac{\partial \psi}{\partial x} + (y - y_c) \frac{\partial \psi}{\partial y} \right] dx dy, \quad (2.131)$$

which can be written as

$$L = -\frac{\rho}{2} \int_{\mathcal{D}} \nabla \psi \cdot \nabla h dx dy, \quad (2.132)$$

where $h(x, y) \equiv (x - x_c)^2 + (y - y_c)^2$. For any smooth functions f and g , $\nabla \cdot [f \nabla g] = \nabla f \cdot \nabla g + f \nabla^2 g$ and the above becomes

$$L = -\frac{\rho}{2} \int_{\mathcal{D}} \nabla \cdot [h \nabla \psi] dx dy + \frac{\rho}{2} \int_{\mathcal{D}} h \nabla^2 \psi dx dy = L_B + L_V. \quad (2.133)$$

Therefore, the angular momentum with respect to the point (x_0, y_0) of a fluid in a bounded domain \mathcal{D} , is given by the sum of two terms: a volume term L_V which involves the vorticity $\omega = -\nabla^2 \psi$ of the distribution and a boundary term L_B which involves the value of the velocity field on the boundaries. These two terms are respectively

$$L_V = -\frac{\rho}{2} \int_{\mathcal{D}} \omega [(x - x_c)^2 + (y - y_c)^2] dx dy, \quad (2.134)$$

and, after applying the divergence theorem,

$$L_B = -\frac{\rho}{2} \oint_{\partial \mathcal{D}} [(x - x_c)^2 + (y - y_c)^2] (-v, u) \cdot d\mathbf{n}, \quad (2.135)$$

where $d\mathbf{n}$ is the normal vector to the boundary \mathcal{D} . The vorticity in the point vortex model is given by (2.65) and hence the volume term L_V simply becomes

$$L_V = -\frac{\rho}{2} \sum_{i=1}^N \gamma_i [(x_i - x_c)^2 + (y_i - y_c)^2], \quad (2.136)$$

where (x_i, y_i) and γ_i are the position and the circulation of the i -th vortex. It is evident that the boundary term L_B depends on the considered geometry: it can be evaluated by knowing a parametrisation for the boundary $\partial \mathcal{D}$ and the components u and v of the velocity field on $\partial \mathcal{D}$. However, the total angular momentum can be evaluated indirectly by inserting Eq. (2.56) into (2.129)

$$L = \int_{\mathcal{D}} \rho |(\mathbf{x} - \mathbf{x}_c) \times \mathbf{v}| dx dy = -\rho \int_{\mathcal{D}} \left[(x - x_c) \frac{\partial \psi}{\partial x} + (y - y_c) \frac{\partial \psi}{\partial y} \right] dx dy. \quad (2.137)$$

integrating by parts once, with the boundary condition $\psi = 0$ on $\partial \mathcal{D}$, gives

$$L = 2\rho \int_{\mathcal{D}} \psi dx dy. \quad (2.138)$$

Hence the boundary term can be evaluated from

$$L_B = 2\rho \int_{\mathcal{D}} \psi dx dy - L_V, \quad (2.139)$$

where L_B is given by (2.134). It is useful to normalise the angular momentum L with the maximum angular momentum L_{max} which the system will have if it rotates as a solid body. In particular, the moment of inertia \mathcal{I} of a rectangular body with density ρ is

$$\mathcal{I} = \rho \frac{L_x L_y (L_x^2 + L_y^2)}{12}, \quad (2.140)$$

and, assuming that the system rotates at angular velocity Ω and its total energy E is purely rotational, then

$$E = \frac{1}{2} \mathcal{I} \Omega^2, \quad (2.141)$$

from which

$$\Omega = \sqrt{\frac{2E}{\mathcal{I}}}. \quad (2.142)$$

Therefore, the maximum angular momentum is given by

$$L_{max} = \mathcal{I} \Omega = \sqrt{2E\mathcal{I}}. \quad (2.143)$$

Chapter 3

Statistical Mechanics of point vortices

“The formation of large, isolated vortices is an extremely common, yet spectacular phenomenon in unsteady flow. Its ubiquity suggests an explanation on statistical grounds.”

Onsager, 1949

Anyone who wants to analyse the properties of matter in a real problem might want to start by writing down the fundamental equations and then try to solve them mathematically. Although there are people who try to use such an approach, these people are the failures in this field...

With these words, in 1963, Richard Feynman [46] was referring to the necessity of using a statistical approach when systems composed of a large number of constituents (atoms, molecules, ...) are considered. In particular, for such a system, it is difficult to apply the traditional approach in order to determine the dynamics of each constituent: solving the equation of motion with the appropriate boundary conditions will be impossible for a system which consists of a number of particles of the order of Avogadro’s number ($\sim 10^{23}$) such as a liquid or a gas. Rather than focusing on the individual motion of particles a statistical mechanical approach aims to make predictions about emergent macroscopic measures that arise from the collective behaviour of the constituents particles. Since the system is composed of large number of particles, statistical arguments become very effective. In this chapter a brief overview on thermodynamics and statistical mechanics will be given. For a complete and more exhaustive

approach see [96] or [8]. In particular in §(3.1) the concept of temperature and entropy will be introduced. Moreover, considerations will be given on how particular systems can admit *negative* temperature states. The concept of negative temperature has a particular interpretation which will be explained in detail. In §(3.2) the entropy will be re-interpreted in a statistical sense: this will provide the possibility to investigate systems composed of point vortices and to determine the range of energies for which positive and negative temperatures occur. Finally, in §(3.3) an important equation, called the *multi-species Boltzmann-Poisson* equation, for a system composed of a total of N constituents will be derived. This is a time independent, second order, non linear, partial differential equation that describes maximum entropy states of a system. Moreover, the expression for the entropy S as a function of the N constituents, the domain \mathcal{D} and the energy E will be given explicitly. Knowledge of the expression for S provides the possibility to classify different solutions of the *Boltzmann-Poisson equation*, but this task will be discussed in the next chapter when the equation will be solved numerically.

3.1 Essentials of Thermodynamics

A *thermodynamic system* is a region of the universe characterised by a set of *thermodynamic variables* which are experimentally measurable. The set of thermodynamic variables is divided into two subsets: *extensive* and *intensive*. Extensive variables (e.g., volume V , total mass m , total internal energy E , ...) depend on the size of the system, while intensive variables (e.g., temperature T , pressure p , density ρ , specific heat C , etc.) do not scale with the size of the system. If all thermodynamic variables are constant in time an *equilibrium state* emerges. In order for equilibrium to be established, three conditions must be satisfied:

- *mechanical equilibrium*: there are no moments of force,
- *thermal equilibrium*: there are no heat fluxes,
- *chemical equilibrium*: there are no chemical reactions.

The evolution of a system from an initial equilibrium state to a final equilibrium state is called a *transformation* and it is governed by the following laws of thermodynamics:

- *Zeroth Law*

Any thermodynamic system has a state function called *absolute temperature* T . If two systems are in thermal equilibrium with a third system, they must be in thermal equilibrium with each other and have the same temperature T ,

- *First Law*

Any thermodynamic system in equilibrium has a state function called *internal energy* E which is constant if the system is isolated. If the system interacts with another system then the variation of internal energy must satisfy the following conservation law

$$dE = \delta Q - \delta W, \quad (3.1)$$

where δQ is the heat added to (or absorbed by) the system and δW is the work done by the system,

- *Second Law*

In any thermodynamic system there exists a state function called *entropy* S with the following properties

- if an isolated system reaches equilibrium, then

$$dS \geq 0. \quad (3.2)$$

- if the system is not isolated and a transformation at temperature T occurs, then

$$dS = \frac{\delta Q}{T}, \quad (3.3)$$

where δQ is the infinitesimal heat exchanged during the transformation.

- *Third Law*

It is impossible for any process to reduce the temperature T of a system to a zero value in a finite number of operations.

The work done by the system, due to a change in its volume V is given by $\delta W = pdV$ where p is the pressure, therefore the entropy is

$$dS = \frac{\delta Q}{T} = \frac{dE + \delta W}{T} = \frac{dE + pdV}{T}, \quad (3.4)$$

If an isochoric process is considered, so that the volume V remains constant, then it is possible to define the temperature as follows

$$\frac{1}{T} = \left(\frac{\partial S}{\partial E} \right)_V, \quad (3.5)$$

where the subscript V means that the partial differentiation has been evaluated at constant volume. The entropy can be any function of the internal energy E : in particular the definition does not require S to increase monotonically with respect to E and it can also decrease as E increases. It is clear from the second law of thermodynamics that the change in entropy can be defined when a transformation occurs, however, there are different ways to define it. Historically Boltzmann associated entropy to the logarithm of the number of possible configurations that the constituents of a given system can be arranged into. In what follows, the idea of Boltzmann will be introduced and explained with an example. For this purpose, a system composed of N magnets will be considered. Each magnet can have two possible configurations with respect to the orientation of its magnetic moment, each one with different energies E_\uparrow and E_\downarrow , such that $E_\uparrow > E_\downarrow$. In the presence of a strong magnetic field all the magnets will point in the same direction. Clearly, the configuration where all the magnets are pointing down (\downarrow) has lower energy than the configuration where all magnets are pointing up (\uparrow). In the case of a magnetic field pointing down, there is only one possible configuration and the energy is fixed to NE_\downarrow . By switching off the magnetic field, some magnets will switch orientation and the energy of the system will increase. As a consequence, also so of configurations in which the system can be arranged for a given energy increases. If the external magnetic field is now switched on and it points to the north, all the magnets will orientate along the same direction. The energy of the system reaches its maximum value $NE_\uparrow > NE_\downarrow$ and in this case there is only one possible configuration in which the system can be found. The configurations where all the magnets have the same direction can be obtained in only one arrangement: all the magnets are pointing up or down (see Fig. (3.1)). According to the idea of Boltzmann, the entropy is proportional to the

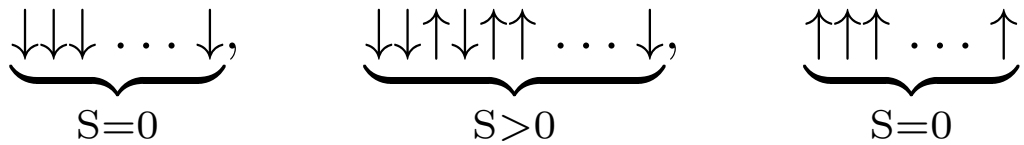


Figure 3.1: The configurations on the sides have same entropy but different energies. There must exist a configuration at intermediate energy which maximises the entropy S .

logarithm of the number arrangements W , therefore

$$W = 1^N = 1, \quad S \sim \log W = 0. \quad (3.6)$$

If the magnets are pointing randomly, then the total number of arrangements W and the entropy of the system are given by

$$W = 2^N, \quad S \sim \log W > 0. \quad (3.7)$$

Therefore, there must be a value of the energy $E = \tilde{E}$ at which the entropy reaches its maximum and then it diminishes as E increases. For energies $E < \tilde{E}$ the temperature of the system is positive since $\partial S/\partial E > 0$ while for configurations for which $E > \tilde{E}$ the temperature is negative since $\partial S/\partial E < 0$. It has to be noticed that the critical energy \tilde{E} for which $\partial S/\partial E = 0$ corresponds to an infinite temperature. This example suggests that there is a connection between the total number of arrangements of all the constituents and the probability of the system to be found in that particular configuration, and this will be discussed later in §3.2. It suggests that there is a connection between disorder and entropy: more precisely if a system reaches an equilibrium configuration, then the entropy reaches a maximum which is not necessarily a global maximum. In what follows, the same idea will be applied to a system composed of point vortices: as a first step it is important to investigate the Hamiltonian of the system and understand which are the configuration of vortices with higher and lower energies. In the point vortex model, as discussed in §(2), the energy depends on the mutual distance between the vortices. Moreover, in the presence of boundaries, the energy depends also on the distance between the vortices and their images. The interaction energy (Hamiltonian \mathcal{H}) between point vortices in an unbounded domain is given by

$$\mathcal{H} = -\frac{1}{4\pi} \sum_{\substack{j,i=1 \\ j \neq i}}^N \gamma_i \gamma_j \log |\mathbf{x}_i - \mathbf{x}_j|, \quad (3.8)$$

and it is clear that $-\log |\mathbf{x}_i - \mathbf{x}_j| \rightarrow +\infty$ when $|\mathbf{x}_i - \mathbf{x}_j| \rightarrow 0$. Hence, the product $\gamma_i \gamma_j$ determines the lower and higher energy configurations. Lower energy configurations are realized when vortices with opposite value of the circulation are close, and higher energy configurations are achieved when vortices with the same circulation cluster together. Since bounded domains are considered in this work, the first configuration can be obtained in two different ways: the first one is when vortices are close to their images which replicate the presence of the boundaries while the second is when vortices with opposite circulation are close together. On the other hand, high energy states, correspond to configurations where the point vortices are clustered together (see Fig. (3.2)). The configurations where vortices are perfectly mixed and not too close to the

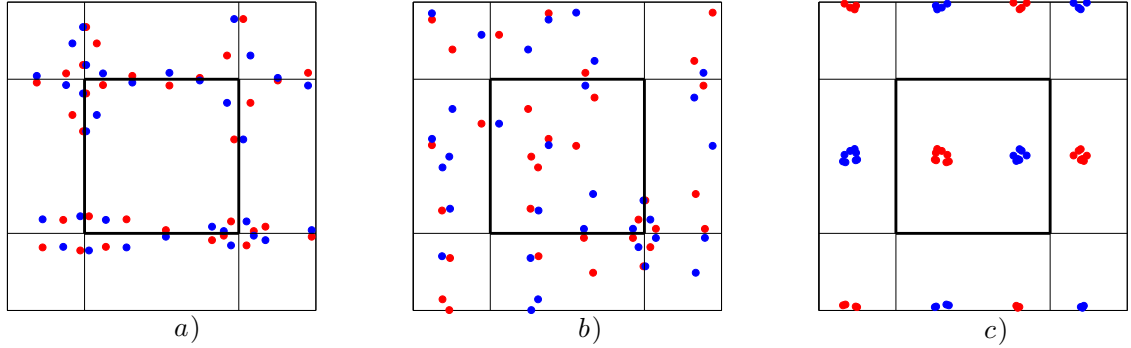


Figure 3.2: In the configuration on the left (a)), vortices are close to their images: this configuration has a lower energy with respect to the one on the right (c)) where point vortices with the same circulation cluster together. The energy of the system represented in the centre, lies in between the energies of the previous two configurations. The reference cell is surrounded by copies of it which contain the images.

boundary are the intermediate energy states. Of course this types of configuration can be recovered in far more ways than the other two cases. Therefore, an analogous behaviour observed in the magnets is recovered: low and high energy states correspond to minima of the entropy while intermediate states correspond to configurations with higher entropy. An example of a possible graph of the temperature T and the inverse temperature β as a function of energy E for the system above described is given by Fig. (3.3). The inverse temperature β lies in the range $+\infty < \beta < -\infty$ and concepts such as *hotter* and *colder* configurations can also be extended to negative temperature regimes: a body A at temperature T_A is *hotter* than a body B at temperature T_B if the heat flows from A to B if they are brought into thermal contact. A body A at temperature T_A is *colder* than a body B at temperature T_B if the heat flows from B to A if they are brought into thermal contact. With this convention the first and the second law of thermodynamics can be used for system with absolute positive and negative temperature while the third law needs to be modified as follows:

- *modified Third Law*[96]

It is impossible for any process to reduce the temperature of a system to absolute zero for positive temperature or to raise the temperature of a system to absolute zero for negative temperature in a finite number of operations.

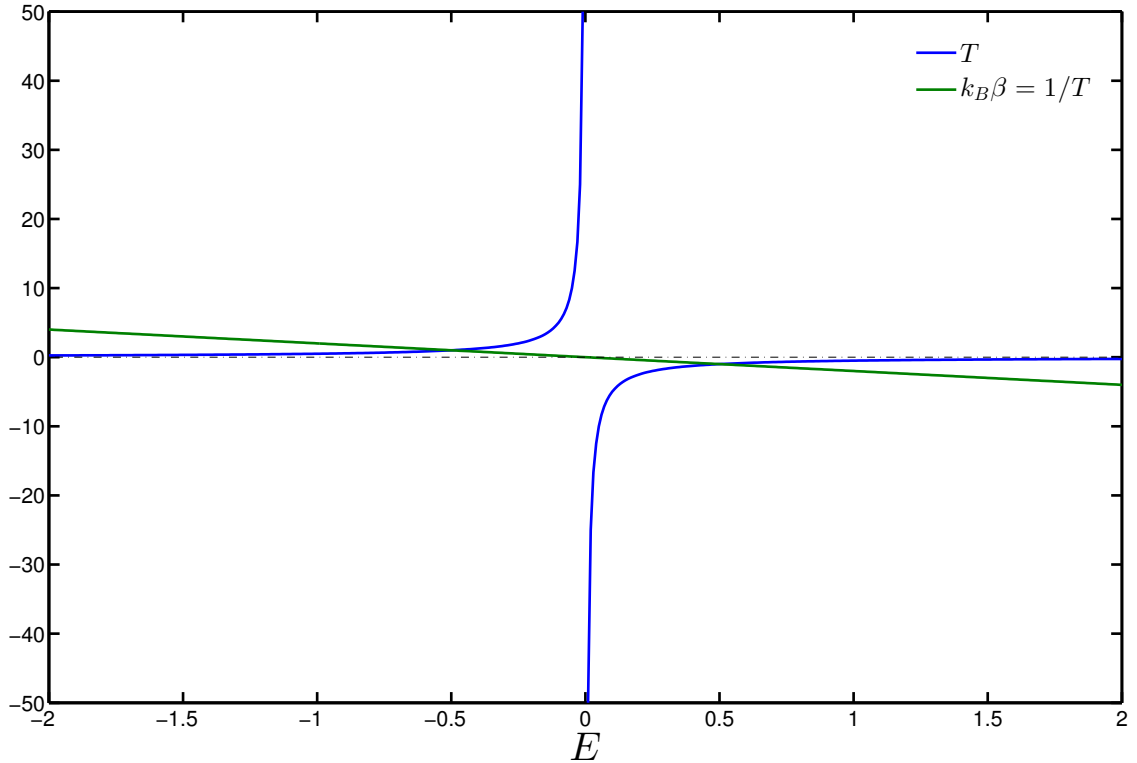


Figure 3.3: Temperature T and inverse temperature β in unit of the Boltzmann constant k_B as a function of the energy E for a system of point vortices in a box.

3.2 Entropy from Statistical Mechanics

The outcome of an uncertain experiment that depends on an inherent random elements is given in terms of the *probability* of occurrence of a particular outcome. For example, in the case of fair die, the prediction that a particular outcome is observed can be based on the assumption of equal *a priori* probability postulate is assumed: namely, the probability that any of the six faces of a die land uppermost is equally likely. This postulate does not contradict the laws of physics and is the basic assumption to Statistical Thermodynamics. Now consider any system with N constituents (atoms, electrons, vortices,...) which can be described by specifying some macroscopically measurable independent parameters like the volume V , the total internal energy E , the pressure p , and other physical quantities. A macroscopic state or *macrostate* can be defined by specifying the values of these parameters and any other conditions to which the system is subject. For example, for an isolated system, a macrostate is defined by fixing the total volume V and the total internal energy E . From a microscopic point of view there are many different configurations of the N constituents which do not change the macrostate. These different configurations are called *microstates*. All

microstates appear as all different possible ways the system can achieve a particular macrostate (see Fig. 3.4). The key assumption of Statistical Thermodynamics is the “equal *a priori* probability”: in other words, all microstates are equally probable. On the other hand, this assumption does not hold for the macrostates. In particular the probability to find a system in a particular macrostate is proportional to the number of microstates which can give rise to it. It is a common experience that isolated systems can evolve in time until they reach the macrostate which corresponds to the equilibrium: this macrostate corresponds to microstates with the highest number of possible configurations that coincide with a given macrostate.

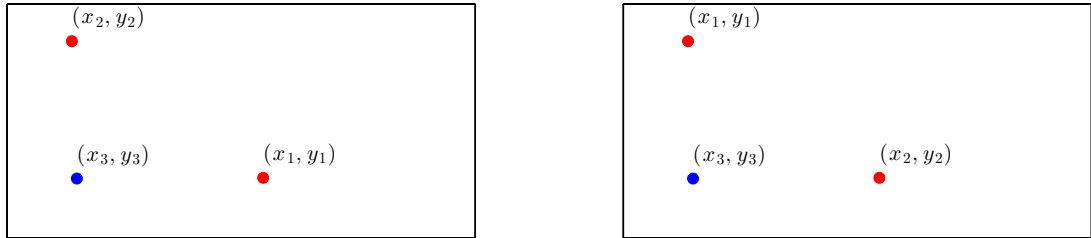


Figure 3.4: Three particles in a box: the macrostate is defined by saying that two particles in the box are red and one is blue. Each particle is located in a specific position in the box: this identifies the microstate. If the two red particles are swapped (figure on the right), the macrostate is the same. However, the microstate has changed.

The above definition can now be applied to a system A composed of N_A particles and occupying a volume V_A and a system B with N_B constituents and volume V_B . In the following, $W_A(E_A)$ denotes the number of microstates of A in the range $[E_A, E_A + \delta E_A]$ and $W_B(E_B)$ the number of microstates of B in the range $[E_B, E_B + \delta E_B]$. If brought into thermal contact, the systems will exchange energy until they reach equilibrium. The system composed of the two systems is isolated, therefore the total energy

$$E = E_A + E_B, \quad (3.9)$$

is constant. For this latter system, the number of microstates is given by

$$W(E) = W_A(E_A)W_B(E_B) = W_A(E_A)W_B(E - E_A), \quad (3.10)$$

which achieves a maximum when

$$\frac{\partial W}{\partial E_A} = W_B(E_B) \frac{\partial W_A}{\partial E_A} - W_A(E_A) \frac{\partial W_B}{\partial E_B} = 0, \quad (3.11)$$

or similarly

$$\beta(E_A) = \beta(E_B), \quad (3.12)$$

where we have introduced

$$\beta(E_j) = \frac{\partial \log W_j}{\partial E_j}, \quad j = A, B. \quad (3.13)$$

The above quantity has the dimension of a reciprocal energy, therefore Eq. (3.5) is recovered by defining the entropy

$$S = k_B \log W(E, N, V), \quad (3.14)$$

where the log is the natural logarithm in base e . Equation(3.14) is called *Boltzmann's relation* and it represents the connection between thermodynamics and statistical mechanics. There are three different ensembles which can be used to describe the dynamics of a system by using the Statistic Thermodynamics: the difference between them is related to the quantities which are conserved by the system. They are the *Microcanonical*, the *Canonical* and the *Grand Canonical* ensemble. In the Grand Canonical ensemble both energy E and number of particles N can change. The Canonical ensemble approach can be used if the energy can vary but the total number of particles is fixed: this approach is useful to describe system which are in thermal equilibrium with a heat bath and the energy between them can be exchanged. Finally the Microcanonical ensemble applies when the total number of the particle and the energy of the system are both constant. The choice of ensemble is a delicate matter for systems with long-range interaction like the point vortex model because it can lead to ensemble inequivalence [42], [22]. Therefore, in the following a microcanonical ensemble approach where the total energy E , the total number of constituent N and the volume V are fixed will be considered. Moreover, since two dimensional systems are investigated, the area \mathcal{D} will be used instead of the volume V .

3.2.1 Microcanonical Ensemble and Negative Temperature

As pointed out at the end of the last section, the most suitable ensemble for the point vortex model from a statistical point of view, is the microcanonical ensemble. The reason is because this ensemble describes systems where the number of constituent N and the total energy E are constant in time. This is certainly the case of the point vortex model which has been introduced in the previous chapter. As was discussed in §3.1, the point vortex has the property that the entropy decreases as the system increases

its energy, and hence the temperature of the vortex distribution can be negative in the sense discussed in section §3.1. However, a more rigorous approach to define a system which admits negative temperature states will now be explained. This is based on a seminal work done by Onsager in 1949 [90] in where the main ingredient is the boundedness of the phase space.

As described in §2 the equation of motion for a two dimensional system composed by N point vortices each with circulation γ_k , $k = 1 \dots N$, are given by the Hamilton's equation

$$\gamma_k \dot{x}_k = \frac{\partial \mathcal{H}}{\partial y_k}, \quad \gamma_k \dot{y}_k = -\frac{\partial \mathcal{H}}{\partial x_k}, \quad (3.15)$$

where \mathcal{H} is the Hamiltonian which, in the point vortex model, depends on the mutual distance between vortices and on the particular considered geometry. The position coordinates $(x_1, x_2, \dots, x_N, y_1, y_2, \dots, y_N)$ act as the canonically conjugated variables, and define the so called *phase space* which, for the point vortex system, coincides with the two-dimensional physical space. It follows that, for unbounded geometries, the phase space will in general be unbounded. However, in particular circumstances the phase space can be bounded even if the physical space is unbounded. This arises, for example, when all vortices have the same circulation. In particular for two point vortices with equal circulation, the vortices rotate around each other and in this case, although the physical space is unbounded, the phase space remains bounded. The dynamics of N point vortices vortices is described by the equations of motion (3.15). Hence the dynamics occurs on a isosurface where the energy is constant. Let us denote $\Omega(E, N, \mathcal{D})$ the portion of the phase space which corresponds to all positions that N point vortices can occupy with energy less than E within a domain \mathcal{D}

$$\Omega(E, N, \mathcal{D}) = \int_{-\infty}^E \Omega'(\tilde{E}, N, \mathcal{D}) d\tilde{E}. \quad (3.16)$$

The function $\Omega'(\tilde{E}, N, \mathcal{D})$ is also known as the *structure function*[63]. This is a monotonically increasing function of the energy such that

$$\lim_{E \rightarrow -\infty} \Omega(E, N, \mathcal{D}) = 0, \quad \lim_{E \rightarrow +\infty} \Omega(E, N, \mathcal{D}) = \mathcal{D}^N, \quad (3.17)$$

and hence, the function $\Omega'(\tilde{E}, N, \mathcal{D}) > 0$. The constraints (3.17) impose the following condition on $\Omega'(\tilde{E}, N, \mathcal{D})$

$$\lim_{\tilde{E} \rightarrow \pm\infty} \Omega'(\tilde{E}, N, \mathcal{D}) = 0^+. \quad (3.18)$$

Combining this with the fact that the function Ω' is positive, imposes that it has at least one maximum at some value \mathcal{E} , or in other words

$$\Omega''(\mathcal{E}, N, \mathcal{D}) = 0. \quad (3.19)$$

Once these quantities are known, the temperature T of the system can be immediately defined

$$\frac{1}{T} \equiv \frac{\Omega''(E, N, \mathcal{D})}{\Omega'(E, N, \mathcal{D})} = \frac{\partial}{\partial E} \log \Omega'(E, N, \mathcal{D}), \quad (3.20)$$

and by comparison with Eq. (3.14) it follows that the structure function is proportional to the number of microstates [8]

$$\Omega'(E, N, \mathcal{D}) \sim W(E, N, \mathcal{D}). \quad (3.21)$$

The number of maxima of Ω' is an important issue: Fig. (3.5) shows a distribution with two maxima and, as a consequence, it is not possible to see a similar trend in the graph of the temperature as a function of the energy E as the one presented in Fig. (3.3).

A similar graph for the temperature to the one presented in Fig. (3.3) can be obtained if the function $\Omega'(E, N, \mathcal{D})$ has a unique maximum and this is the case shown in Fig. (3.6). The presence of a single maximum in the entropy is the case of a system composed by point vortices. In order to demonstrate this peculiarity, in the following, focus will be given to two specific domains: a square with sides $L_x = L_y = 2$ and a rectangular region, with the same area of the previous one, characterised by an aspect ratio $\Lambda = L_x/L_y = 1.5$. Moreover, a neutral gas composed by an equal number of vortices (positive charge) and antivortices (negative charge) will be considered. The existence of negative temperature states in the case of point vortices can be demonstrated numerically by noticing that the curve $W(E)$ represents the distribution of configurations as a function of the energy E . Therefore, the curves can be generated by evaluating the energy of a large number of random neutral configurations of N vortices and constructing the related histograms. The energy E and the energy per vortex E/N of the system are evaluated by using Eq. (2.124). The weight functions are then evaluated from the histograms $\{W_i\}$ by using a normalised Gaussian kernel [106] such that

$$W(E) = \frac{1}{M} \sum_{i=1}^{N_b} \frac{W_i}{\sqrt{2\pi}\sigma} \exp(-(E - E_i)^2/2\sigma^2), \quad (3.22)$$

where σ is the kernel width, $N_b = 50$ is the total number of bins and W_i is the number

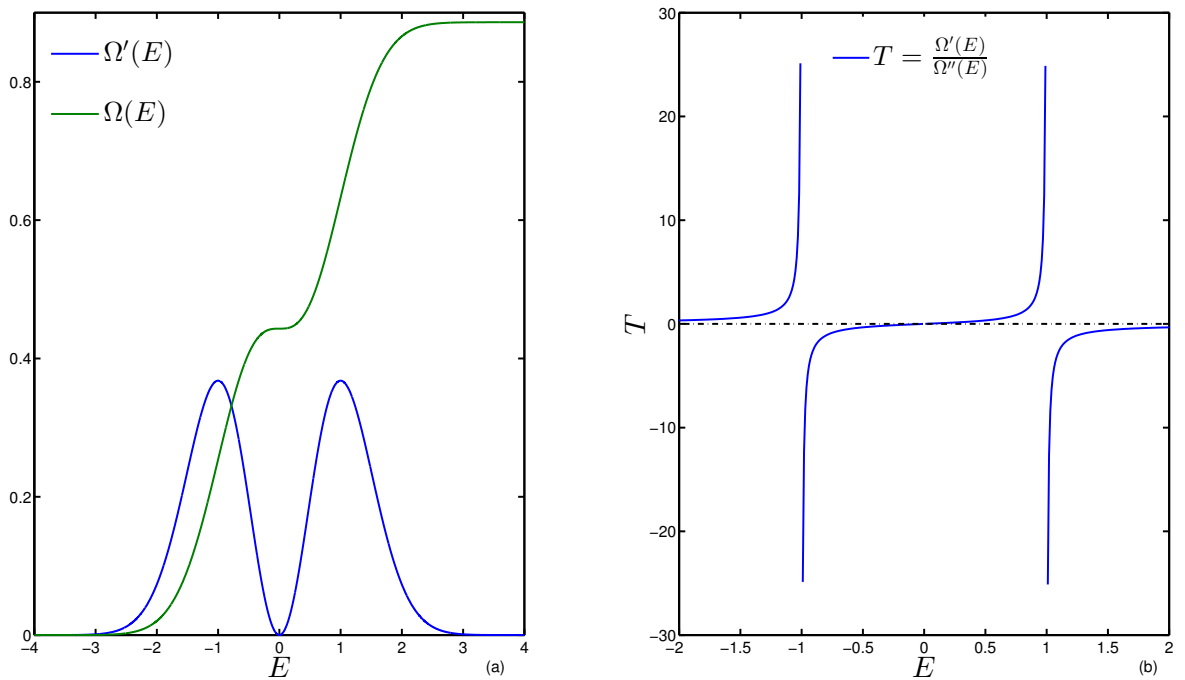


Figure 3.5: Figure (a) on the left: structure function $\Omega'(E, N, \mathcal{D})$ (blue) and the portion of the phase space $\Omega(E, N, \mathcal{D})$ (green) defined by Eq. (3.17). Figure (b) on the right: temperature T as a function of the energy E . The trend of the graph here presented is different from the graph presented in Fig. (3.3) due to the presence of two maxima in the structure function.

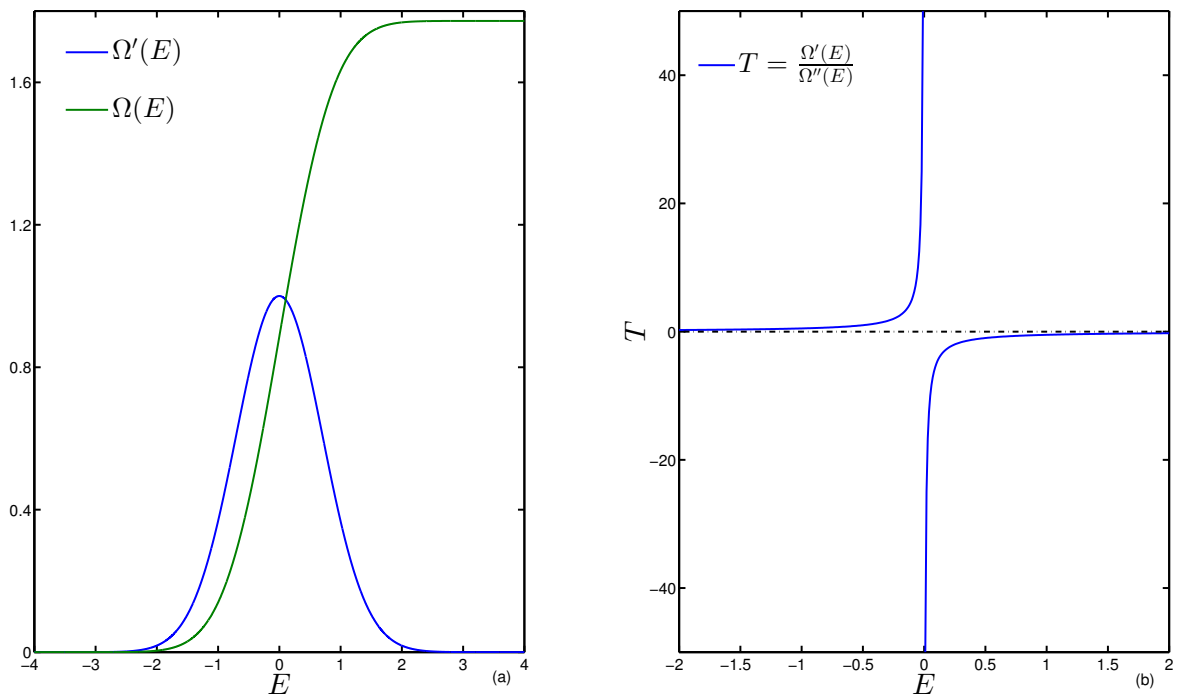


Figure 3.6: Figure (a) on the left: structure function $\Omega'(E, N, \mathcal{D})$ (blue) and the portion of the phase space $\Omega(E, N, \mathcal{D})$ (green) defined by Eq. (3.17). Figure (b) on the right: temperature T as a function of the energy E . The trend of the graph of the temperature presented is similar to the one presented in Fig. (3.3) due to the presence of a single maximum in the structure function.

of realization with energy lying within the interval $(E, E + \Delta E)$. The value of the kernel width σ needs to be imposed in order to obtain smooth statistical weights. For the distribution generated by considering the total energy E and the energy per vortex E/N the values of the kernel width are $\sigma = 0.35$ and $\sigma = 0.01$, respectively. A total of $M = 100000$ are used. The results are shown in Fig. (3.7) for systems composed of different numbers of vortices $N = 10, 20, 40, 80$ and 160 . Plots showing the dependence on both the total energy (left) and interaction energy per vortex (right) are included. In both cases the distributions show a single maximum and hence the existence of

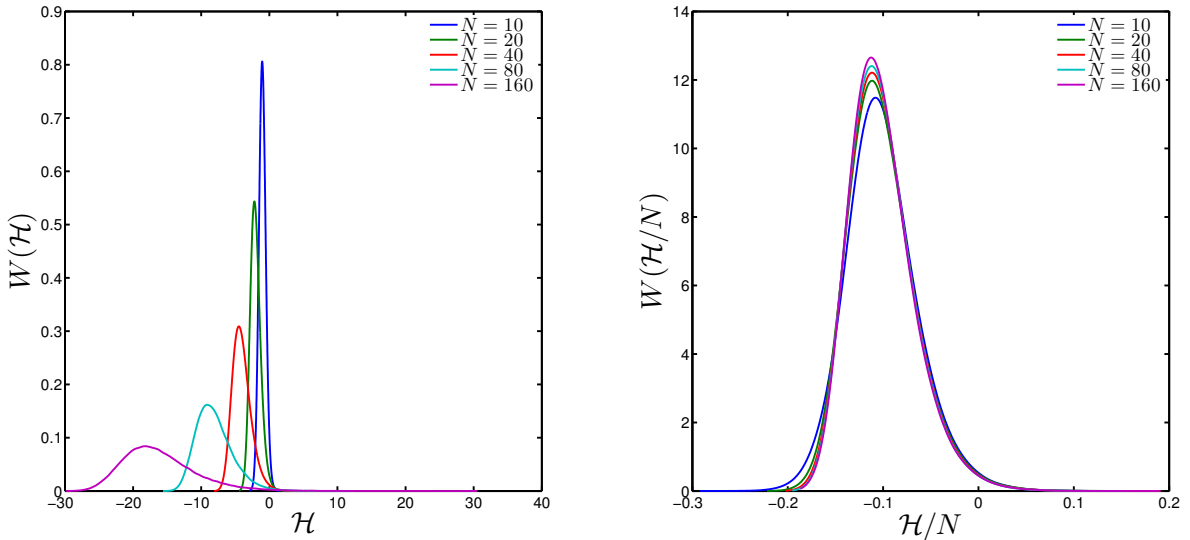


Figure 3.7: Statistical weights in the square: dependence on the total energy and total energy per vortex are considered on the left and the right panels respectively.

negative temperature states. When the dependence on energy E is considered, the maxima of the statistical weights are shifted to lower energies with increasing number of vortices: in terms of the statistical thermodynamics, this is equivalent to saying that more macrostates are accessible. In contrast, the distributions showing the dependence on the energy per vortex E/N , tend to converge to a limiting distribution: this feature has already been pointed out by Campbell *et al.* [25] also for a non neutral distribution of vortices and by Esler *et al.* [44] in different confining geometries. In particular, in [44] an explicit expression for the limiting distribution was obtained. Figure (3.7) shows the existence of negative temperature states for which the temperature presents the same features shown in Fig. (3.6) since all the distributions have a single maximum. Due to physical reasons that will be widely discussed in §(5), the statistical weights have also been generated by imposing two additional constraints δ_V and δ_B on the position of vortices: the first one imposes a minimum distance between vortices within

the domain and the second one imposes a minimum distance between vortices and the boundaries. Imposing a minimum distance between vortices within the domain prevents configurations where the energy will be too high or too low due to clustering of opposite signed or like-signed vortices (see Fig. (3.8) on the right). The constraint on the boundary, on the other hand, excludes very low energy contributions from vortices and their images (see Fig. (3.8) on the left). As a consequence, the difference between the distributions where vortices are free to occupy any positions and these cases is given by a reduced range of energies and more peaked distributions.

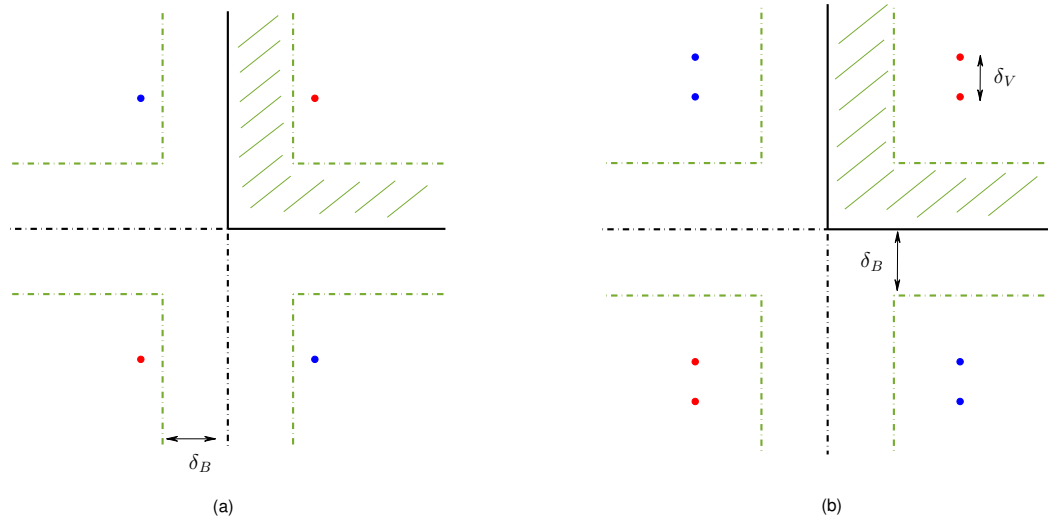


Figure 3.8: Constraints on the positions of point vortices: Fig. a) on the left δ_B (green shaded region) imposes a minimum distance between a vortex and its closest images with opposite circulation. In Fig. b) on the right the constraint δ_V can affect also vortices with same circulation within the considered domain (upper right).

This analysis has been carried out in the square and in the rectangle with aspect ratio $\Lambda = 1.5$ and the results are shown in Figs. (3.9) and (3.10), respectively. One can see that in both cases the effects of the constraints are more important when a large number of vortices is considered since the constraints introduce an effective packing factor in the problem. Although the distributions have different behaviours from those presented in Fig. (3.7), the qualitative features persist and it is still possible to define the regions where the tangent to the curves is positive and negative.

These preliminary results are important to determine when a given configuration of point vortices is in the positive or negative temperature regime. This will be relevant in Chapter (5) when the dynamics of point vortices will be studied and the transition between positive and negative states investigated. In the next section a mean-field theory based on a statistical approach will be presented and the *multi-species Boltzmann-*

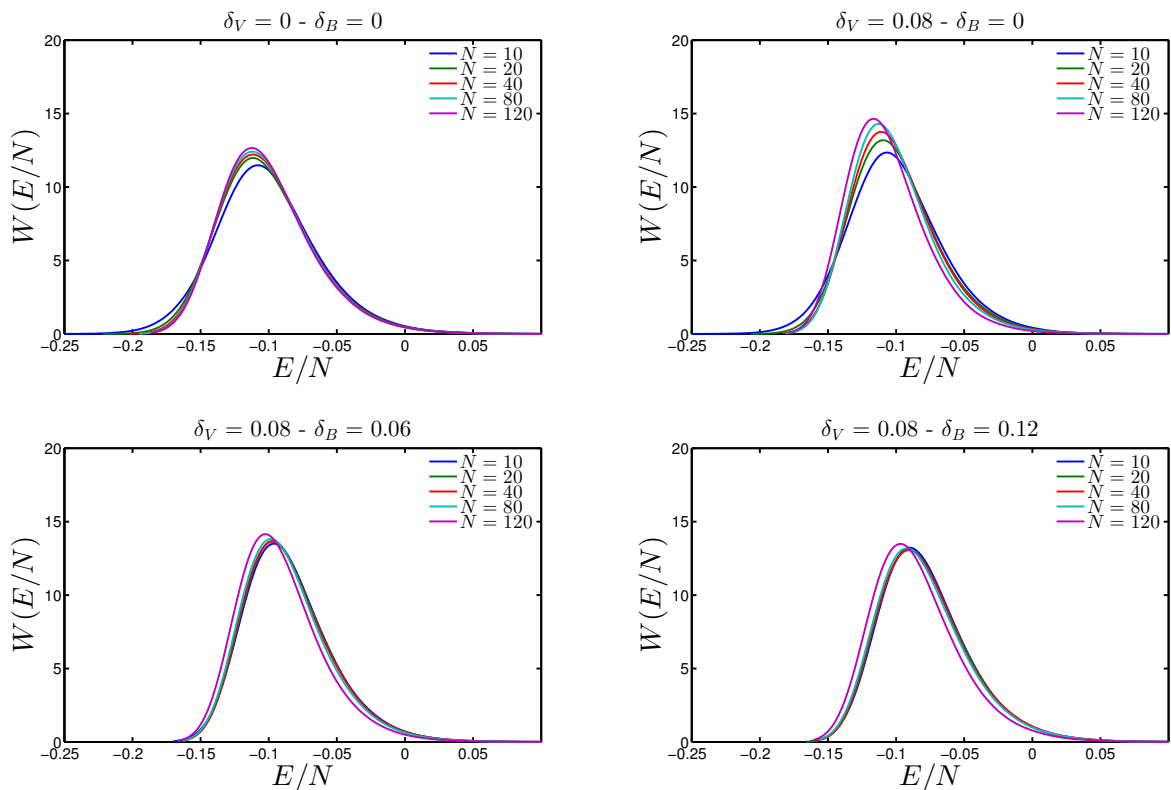


Figure 3.9: Statistical weights in the square with sides $L_x = L_y = 2$ for different values of δ_B and δ_V as indicated above each figure.

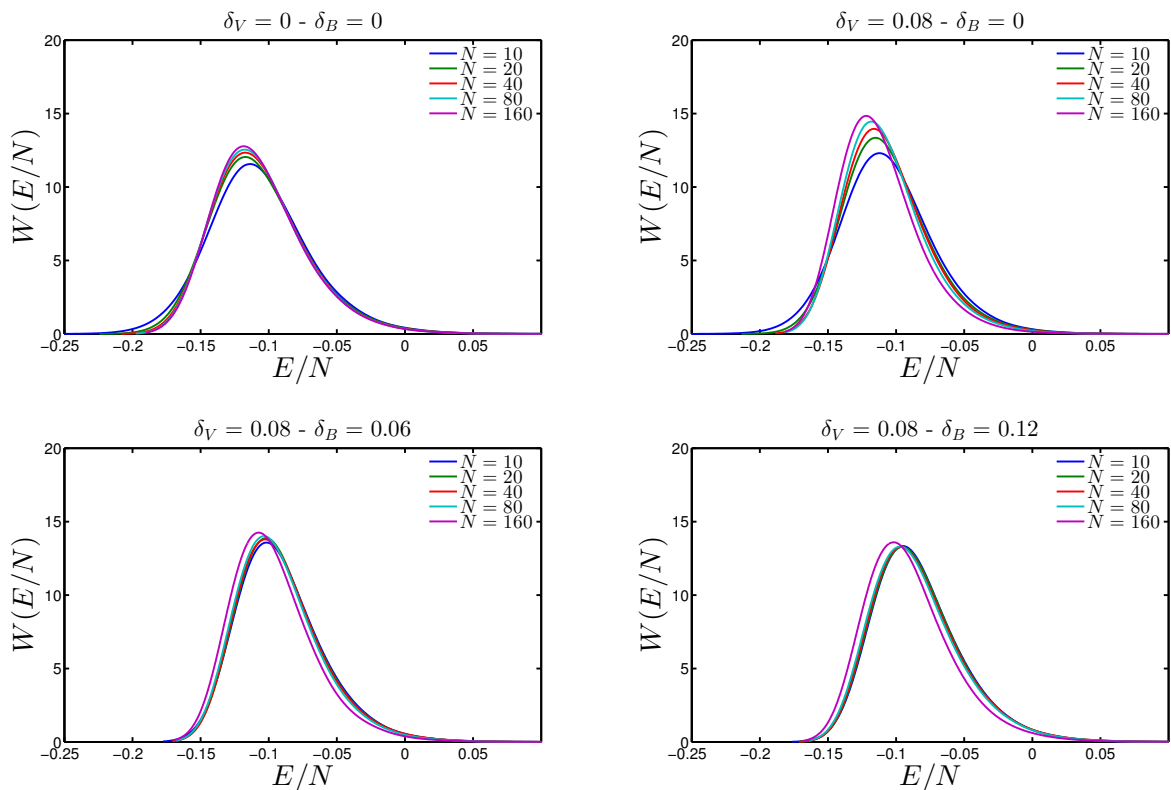


Figure 3.10: Statistical weights in the rectangle with aspect ratio $\Lambda = 1.5$ for different values of δ_B and δ_V as indicated above each figure.

Poisson equation will be derived. This is a fundamental equation which connects the fluid dynamics to the Statistical Mechanics since its solutions represent configuration of point vortices which maximise the entropy of the system.

3.3 Maximum Entropy Principle and Boltzmann-Poisson Equation

In this section the most probable vorticity distribution in a generic planar domain with area \mathcal{D} , subject to some constraints, will be derived following a statistical approach. This derivation follows the idea given by Chavanis in [30]. Consider a system of N point vortices divided in species with different circulations $\pm\gamma_a$, where the subscript a will be used to denote the different species of vortices. If N_a represents the number of vortices of each species, then the total number of vortices, the total circulation and the total vorticity are given by

$$N = \sum_a N_a, \quad \Gamma = \sum_a \Gamma_a = \sum_a N_a \gamma_a, \quad \omega(x, y) = \sum_a \omega_a(x, y) \quad (3.23)$$

where Γ_a and $\omega_a(x, y)$ represent the total circulation and the total vorticity given by all the vortices of species a . The total circulation can be expressed as follows

$$\Gamma = \int_{\mathcal{D}} \omega(x, y) dx dy = \sum_a \int_{\mathcal{D}} \omega_a(x, y) dx dy, \quad (3.24)$$

or

$$\Gamma = \sum_a N_a \gamma_a = \sum_a \int_{\mathcal{D}} \gamma_a n_a(x, y) dx dy, \quad (3.25)$$

where $n_a(x, y)$ is the number density of vortices of species a . Combining Eqs. (3.25) and (??), the vorticity of each species can be expressed as

$$\omega_a(x, y) = \gamma_a n_a(x, y). \quad (3.26)$$

For brevity, explicit dependence on the arguments x and y will be dropped. The PVM, as already mentioned, is a model which conserves the total energy given by Eq. (2.124) and the number of vortices of each species N_a . The latter can be expressed in terms of the conservation of the total circulation or the circulation of each species a . Therefore,

the following two quantities are conserved

$$E = \frac{\rho}{2} \int_{\mathcal{D}} \omega \psi dx dy, \quad \Gamma_a = \int_{\mathcal{D}} n_a \gamma_a dx dy = \int_{\mathcal{D}} \omega_a dx dy, \quad (3.27)$$

where $\psi(x, y)$ is the streamfunction associated with the vorticity field. It is important to note that there can be other conserved quantities depending on the considered domain \mathcal{D} . For example in [93] and [107], a circular geometry was considered and in this case the angular momentum L is an additional conserved quantity.

The domain \mathcal{D} is now divided into a very large number of small cells (each of size h^2 say) which can contain an arbitrary large number of point vortices and each of these cells is labelled by the index i . For a given distribution of point vortices in the total domain \mathcal{D} , a microstate is defined when the positions of all point vortices in each cell are defined, while a macrostate is specified by the number of point vortices of each species in each cell. Swapping the positions of two point vortices of the same species will change the microstate, but will not change the macrostate (see Fig. (3.4)). Given the above definition for the macrostate, the set of numbers of vortices of species a in each cell will be denoted by $\{N_{i,a}\}$. The vorticity of each species a in the $i - th$ cell, due to the $N_{i,a}$ point vortices, is then given by

$$\omega_{i,a} = \gamma_a n_{i,a} = \gamma_a \frac{N_{i,a}}{h^2}. \quad (3.28)$$

The total number of configurations, or microstates, corresponding to the macrostate $\{N_{i,a}\}$ is given by [55]

$$W(\{N_{i,a}\}) = \prod_a \prod_i \frac{N_a!}{N_{i,a}!}, \quad (3.29)$$

where N_a is the number of vortices of each species a . This can be obtained by remembering that the possible ways of choosing k objects out of m is given by the binomial coefficient

$$\binom{m}{k} = \frac{m!}{k!(m-k)!}. \quad (3.30)$$

In the considered case, $k = N_{i,a}$ represents the number of vortices in the $i - th$ cell, and $m = \sum_i N_{i,a} = N_a$ is the total number of vortices of species a . Therefore, the number of ways of putting $N_{1,a}$ vortices in the first cell, $N_{2,a}$ in the second cell, $N_{3,a}$ in the third cell, ..., with the constraint

$$\sum_i N_{i,a} = N_a, \quad (3.31)$$

is given by

$$\begin{aligned}
 W(\{N_{i,a}\}) &= \binom{N_a}{N_{1,a}} \binom{N_a - N_{1,a}}{N_{2,a}} \binom{N_a - N_{1,a} - N_{2,a}}{N_{3,a}} \cdots \binom{N_a - N_{1,a} \cdots N_{i-1,a}}{N_{i,a}} \\
 &= \frac{N_a!}{N_{1,a}!(N_a - N_{1,a})!} \frac{(N_a - N_{1,a})!}{N_{2,a}!(N_a - N_{1,a} - N_{2,a})!} \cdots \\
 &= \frac{N_a!}{N_{1,a}!N_{2,a}!N_{3,a}! \cdots N_{i,a}!} = \prod_i \frac{N_a!}{N_{i,a}!}.
 \end{aligned} \tag{3.32}$$

Finally, since the system is composed of a species of point vortices, the final result is

$$W(\{N_{i,a}\}) = \prod_a \prod_i \frac{N_a!}{N_{i,a}!}. \tag{3.33}$$

By using the *Boltzmann relation* given by Eq. (3.14), the entropy S is related to the number of microstates by the following

$$S[\omega_a] = k_B \log W(\{N_{i,a}\}). \tag{3.34}$$

Substituting Eq. (3.33) into Eq. (3.34) gives

$$\begin{aligned}
 S &= k_B \log \left(\prod_a \prod_i \frac{N_a!}{N_{i,a}!} \right) = k_B \sum_a \log N_a! + k_B \sum_a \log \prod_i \frac{1}{N_{i,a}!} \\
 &= k_B \sum_a \log N_a! - k_B \sum_a \sum_i \log N_{i,a}!
 \end{aligned} \tag{3.35}$$

Using the *Stirling approximation*

$$\begin{aligned}
 S &= k_B \sum_a \log N_a! - k_B \sum_a \sum_i \log N_{i,a}! \\
 &\sim k_B \sum_a \{N_a \log N_a - N_a\} - k_B \sum_a \sum_i \{N_{i,a} \log N_{i,a} - N_{i,a}\} \\
 &= k_B \sum_a N_a \log N_a - k_B \sum_a \sum_i N_{i,a} \log N_{i,a}.
 \end{aligned} \tag{3.36}$$

By inserting Eq. (3.28) in the above equation, the entropy becomes

$$\begin{aligned} S &= k_B \sum_a N_a \log N_a - k_B \sum_a \sum_i \frac{\omega_{i,a}}{\gamma_a} h^2 \log \left(\frac{\omega_{i,a} h^2}{\gamma_a} \right) \\ &= k_B \sum_a N_a \log N_a - k_B \sum_a \sum_i \frac{\omega_{i,a}}{\gamma_a} h^2 \log \left(\frac{\omega_{i,a} \mathcal{D}}{\gamma_a} \right) - k_B \sum_a \sum_i \frac{\omega_{i,a}}{\gamma_a} h^2 \log \frac{h^2}{\mathcal{D}} \\ &= k_B \sum_a N_a \log N_a - k_B \sum_a \sum_i \frac{\omega_{i,a}}{\gamma_a} h^2 \log \left(\frac{\omega_{i,a} \mathcal{D}}{\gamma_a} \right) - k_B \sum_a \frac{\omega_a}{\gamma_a} h^2 \log \frac{h^2}{\mathcal{D}}, \end{aligned} \quad (3.37)$$

where \mathcal{D} has been added in order to ensure dimensionless quantities in the logarithmic terms. If the continuum limit is considered

$$\sum_i \xrightarrow[h \rightarrow 0]{} \frac{1}{h^2} \int dx dy, \quad (3.38)$$

by neglecting the last divergent term, the above equation can be written as

$$\begin{aligned} S &= k_B \sum_a N_a \log N_a - k_B \sum_a \frac{1}{h^2} \int_{\mathcal{D}} \frac{\omega_a}{\gamma_a} h^2 \log \left(\frac{\omega_a \mathcal{D}}{\gamma_a} \right) dx dy \\ &= k_B \sum_a N_a \log N_a - k_B \sum_a \frac{1}{h^2} \int_{\mathcal{D}} \frac{\omega_a}{\gamma_a} h^2 \log \left(\frac{N_a \omega_a \mathcal{D}}{\gamma_a N_a} \right) dx dy. \end{aligned} \quad (3.39)$$

The last term of the above Eq. can be manipulated as follows

$$- k_B \sum_a \log N_a \int_{\mathcal{D}} \frac{\omega_a}{\gamma_a} dx dy - k_B \sum_a \int_{\mathcal{D}} \frac{\omega_a}{\gamma_a} \log \left(\frac{\omega_a \mathcal{D}}{\gamma_a N_a} \right) dx dy,$$

which gives

$$- k_B \sum_a N_a \log N_a - k_B \sum_a \int_{\mathcal{D}} \frac{\omega_a}{\gamma_a} \log \left(\frac{\omega_a \mathcal{D}}{\gamma_a N_a} \right) dx dy, \quad (3.40)$$

where Eq. (3.26) has been used. Finally, by inserting Eq. (3.40) into (3.39), the Boltzmann entropy as a function of the vorticity of each species a is given by

$$S[\omega_a] = -k_B \sum_a \int_{\mathcal{D}} \frac{\omega_a}{\gamma_a} \log \left(\frac{\omega_a \mathcal{D}}{\gamma_a N_a} \right) dx dy. \quad (3.41)$$

The next step is to find the most probable vorticity. This corresponds to the vorticity distribution which maximises the entropy subject to the constraints that the total number of vortices N and the total energy E are conserved. The first condition is equivalent to the conservation of the total circulation for each species of vortices. This

is a maximization problem which can be solved with the Lagrange multipliers method: in this case the Lagrange multipliers are the inverse temperature β and the chemical potentials μ_a of each species of vortices. The critical points of the Boltzmann entropy are determined by solving the following equation

$$\delta S - \beta \delta E - \sum_a \mu_a \delta \Gamma_a = 0, \quad (3.42)$$

with respect to ω_a . Inserting the variations of the entropy (3.41), the energy and the total circulation for each specie of vortices (3.27), gives

$$-\int_{\mathcal{D}} \sum_a \left[\frac{1}{\gamma_a} \log \left(\frac{\omega_a \mathcal{D}}{N_a \gamma_a} \right) + \frac{1}{\gamma_a} + \mu_a + \rho \beta \psi \right] \delta \omega_a dx dy = 0. \quad (3.43)$$

and hence, the vorticity which maximize the entropy is given by

$$\omega_a = \frac{N_a}{\mathcal{D}} \gamma_a A_a e^{-\rho \beta \gamma_a \psi}, \quad (3.44)$$

where the quantity $A_a = \exp(-1 - \mu_a \gamma_a)$ must be determined by the conservation of the total circulation of each species Γ_a . Imposing this constraint leads to

$$\Gamma_a = N_a \gamma_a = \int_{\mathcal{D}} \omega_a dx dy = \frac{1}{\mathcal{D}} \int_{\mathcal{D}} N_a \gamma_a A_a e^{-\rho \beta \gamma_a \psi} dx dy, \quad (3.45)$$

and hence

$$A_a = \mathcal{D} \left(\int_{\mathcal{D}} e^{-\rho \beta \gamma_a \psi} dx dy \right)^{-1}. \quad (3.46)$$

The terms A_a represent the spatial distribution of vortices. Finally, the total vorticity is given by

$$\omega = \sum_a \omega_a(x, y) = \sum_a \frac{N_a}{\mathcal{D}} \gamma_a A_a e^{-\rho \beta \gamma_a \psi}, \quad (3.47)$$

where A_a is given by (3.46). On the other hand, the vorticity must satisfy Eq. (2.54), therefore the streamfunction and the vorticity are related by the so called *multi-species Boltzmann-Poisson* (MSBP) equation

$$\nabla^2 \psi = - \sum_a \frac{N_a}{\mathcal{D}} \gamma_a A_a e^{-\rho \beta \gamma_a \psi}. \quad (3.48)$$

If in the above equation the terms A_+ and A_- are considered equal, then Eq. (3.48) reduces to the *Sinh-Poisson* equation which has been studied by many authors [60],

[115], [77] [124]. However, there is no fundamental reason in the assumption $A_+ = A_-$ and hence, it is important to study the full MSBP equation [30]. A numerical analysis on the solutions of the Sinh-Poisson equation can be found in [16] and [77], while analytic solutions can be found in [115]. If the inverse temperature β is positive, then the only real solution to the MSBP equation is given by $\psi(x, y) = \text{const.}$ and therefore, the solution is given by a uniform spatial distribution [115]. This means that for states with positive temperature the most probable configurations have uniform spatial distribution of vortices. Systems for which $\beta > 0$ have been widely studied by Hückel and Debye [38]. However, if $\beta < 0$ different type of solutions can be found [28], [114]. These solutions have a nonuniform spatial distribution and this is a peculiarity of negative temperature states. Therefore, the nontrivial solutions to the MSBP equation (3.48) are related to the emergence of nontrivial flows associated to the formation of large clusters of vortices. In two-dimensional systems, the equation (2.67) implies a Coulomb type interactions given by Eq. (3.8). Because of the long-range interaction between vortices, the equilibrium states are strongly influenced by the confining geometry and this causes different spatial distribution of vortices which depends on the shape of the container [44], [25], [93]. For a complete and exhaustive description on the thermodynamics of long-range interactions systems see [29]. Moreover, the MSBP equation is based on the principle of maximum entropy, which is a general and universal law, and for this reason it arises in other fields such as biophysics [37], chemistry [38], electrochemistry [116] and stellar systems [29] where systems are composed of a large number of constituents. Finally, the entropy S is therefore given by substituting Eq. (3.44) into Eq. (3.41)

$$\begin{aligned}
 S &= -k_B \sum_a \int_{\mathcal{D}} \frac{\omega_a}{\gamma_a} \log (A_a e^{-\rho\beta\gamma_a\psi}) dx dy \\
 &= -k_B \sum_a \log A_a \int_{\mathcal{D}} n_a dx dy + k_B \sum_a \int_{\mathcal{D}} \omega_a \rho \beta \psi dx dy \\
 &= -k_B \sum_a N_a \log A_a + 2k_B \beta E,
 \end{aligned} \tag{3.49}$$

where A_a is given by Eq. (3.46). It should be noted that Eqs.(3.48) and (3.49) are valid for any generic domain \mathcal{D} . However, as mentioned in section §(3.2.1) in this work a neutral system of point vortices in two particular geometries will be investigated: a square with sides $L_x = L_y = 2$ and a rectangular region with aspect ratio $\Lambda = L_x/L_y = 1.5$. Therefore, the MSBP equation in the case of two species of vortices will be considered and numerically solved in these regions. Moreover, these solutions will be classified by their energy E and entropy S . Details as such an analysis are presented

in the next Chapter.

Chapter 4

Mean-Field Theory of Vortex Gas in Bounded Geometries

In the previous chapter the vorticity which maximises the entropy and the multi-species Boltzmann-Poisson (MSBP) equation have been derived for a system composed of different species of point vortices in a generic domain \mathcal{D} . The MSBP equation is a second order, time independent, non linear partial differential equation for the streamfunction ψ , whose solutions represent stationary configurations for the entropy S . In general, for a given value of $\beta < 0$ several solutions can exist for ψ . Physically this is because the equation admits solutions that are all local entropy maximisers. However, a solution ψ can correspond to a global maximum of the entropy. Moreover, because of the long-range nature of the Coulomb interactions, these solutions can also depend on the geometry \mathcal{D} . In this chapter and in the rest of the work the case of systems composed of two species of vortices will be considered: the resulting MSBP equation will be simply called Boltzmann-Poisson (BP) equation where the fact that it is written for two species will be understood. The aims of this chapter are to provide a procedure which allows for the classification of the solutions of the BP equation in terms of their energy and entropy and to develop an iterative algorithm to find the solutions of the BP equation. The last part of the chapter will focus on the classification of the solutions in two specific domains: a squared region and a rectangular domain with aspect ratio $\Lambda = 1.5$, and finally the role of the angular momentum of the system in these geometries will be discussed.

In §4.1 the MSBPE will be written for a system of two species of point vortices, and a procedure to classify the solutions of the BP equation will be provided. This procedure requires knowledge of the solution ψ of the BP equation and one important quantity which can be determined from it: the non-dimensional energy from which also

the non-dimensional entropy can be derived. In §4.2 the linear analysis to the BPE will be performed. This analysis will reveal the presence of two important classes of solutions: the first class is composed by the functions whose mean value is non-zero while the solutions in the second class have zero mean value. In the same section the peculiar behaviour of the entropy of these two classes with respect to the aspect ratio Λ of the rectangular domain \mathcal{D} will be explained. In §4.3 an iterative algorithm which converges to non-trivial solutions of the BPE will be described. In §4.4 and §4.5 classification for the solutions of the BP equation in the square and the rectangle with aspect ratio $\Lambda = 1.5$ will be presented. This classification improves the work done by Taylor *et al.* [114] and gives predictions on the dynamics of point vortices which will be presented in §5. In fact in [114] only two type of solutions to the BP equation have been considered, the so called *monopole* and *dipole*. However, an important type of solution is given by the *diagonal dipole*. This type of solution will be considered in §4.4 and this will give the possibility to explain the behaviour of the dynamics of point vortices which will be presented in the next Chapter. Finally, in §4.7, the ability of a neutral vortex gas to spontaneously acquire a nonzero angular momentum L will be discussed.

4.1 Boltzmann-Poisson Equation of Two-Species Neutral Vortex Gas

In the previous chapter the MSBP equation has been derived by imposing the maximum entropy principle. The solution of this equation is the streamfunction ψ which is related to the distribution of different species of point vortices, where each species is identified by the value of the circulation of the vortices. Motivated by applications to quantum fluids where stable vortices typically have a quantised circulation that is equal in magnitude and opposite in sign, from now on a system composed of two species of vortices with circulation $\pm\gamma$ will be considered. In this section, a method to classify the solutions of the BP equation in terms of the non-dimensional energy \hat{E} and the non-dimensional entropy per vortex \hat{S} will be presented. These two quantities can both be determined from knowledge of the solution ψ of the BP equation which can be obtained by applying the algorithm developed in §4.3.

Introducing the spatial average over the domain \mathcal{D} of a generic scalar function f defined on \mathcal{D}

$$\langle f \rangle \equiv \frac{1}{\mathcal{D}} \int_{\mathcal{D}} f(x, y) dx dy, \quad (4.1)$$

the MSBP equation (3.48) can be written as follows

$$\nabla^2 \psi = - \sum_a \frac{N_a}{\mathcal{D}} \gamma_a \frac{e^{-\rho\beta\gamma_a\psi}}{\langle e^{-\rho\beta\gamma_a\psi} \rangle}, \quad (4.2)$$

where ψ is the streamfunction that is related to the vorticity according to Eq. (2.54). In particular, for a neutral gas composed of $N_+ = N_- = N/2$ vortices each with circulation $+\gamma$ and $-\gamma$ respectively, the above equation becomes

$$\nabla^2 \psi = - \frac{N\gamma}{2\mathcal{D}} \left[\frac{e^{-\rho\beta\gamma\psi}}{\langle e^{-\rho\beta\gamma\psi} \rangle} - \frac{e^{\rho\beta\gamma\psi}}{\langle e^{\rho\beta\gamma\psi} \rangle} \right], \quad (4.3)$$

and the entropy given by Eq. (3.49) reduces to

$$S = - \frac{Nk_B}{2} \log (A_+ A_-) + 2k_B\beta E, \quad (4.4)$$

where the averaged terms A_{\pm} is given by

$$A_{\pm} = \mathcal{D} \left(\int_{\mathcal{D}} e^{\mp\rho\beta\gamma\psi} dx dy \right)^{-1}, \quad (4.5)$$

and the energy E is given by Eq. (2.61). Therefore, in order to evaluate the entropy S and the energy E for a distribution of N vortices in a domain \mathcal{D} , the streamfunction ψ , and the correspondent inverse temperature β are needed. The streamfunction ψ can be determined by solving the BP equation as will be discussed in §4.3. The value of the inverse temperature β can be expressed as a function of the energy E : for example Edwards *et al.* [40] obtained a useful approximation for β in terms of E for a doubly periodic domain while Esler *et al.* [44] considered the von Neumann oval. Rather, in this work the BP equation is solved numerically. To proceed a dimensionless streamfunction $\Psi = \rho\beta\gamma\psi$ is defined for which Eq. (4.3) becomes

$$\nabla^2 \Psi = - \frac{N\gamma^2\rho\beta}{2\mathcal{D}} \left[\frac{e^{-\Psi}}{\langle e^{-\Psi} \rangle} - \frac{e^{\Psi}}{\langle e^{\Psi} \rangle} \right]. \quad (4.6)$$

In the next section it will be shown that, in order to have non trivial solutions, the inverse temperature β is a non-positive quantity and hence, it is possible to define a positive constant λ^2

$$\lambda^2 = - \frac{N\gamma^2\rho\beta}{\mathcal{D}}, \quad (4.7)$$

from which the BPE becomes

$$\nabla^2 \Psi = -\frac{\lambda^2}{2} \left[\frac{e^\Psi}{\langle e^\Psi \rangle} - \frac{e^{-\Psi}}{\langle e^{-\Psi} \rangle} \right]. \quad (4.8)$$

In terms of the new dimensionless streamfunction Ψ , the averaged terms A_{\pm} are simply given by

$$A_{\pm} = \mathcal{D} \left(\int_{\mathcal{D}} e^{\mp \Psi} dx dy \right)^{-1}. \quad (4.9)$$

The expression for the energy becomes

$$E = -\frac{\rho}{2} \frac{1}{\rho^2 \beta^2 \gamma^2} \int_{\mathcal{D}} \Psi \nabla^2 \Psi dx dy = \frac{\tilde{E}}{\rho \beta^2 \gamma^2}, \quad (4.10)$$

where \tilde{E} is a dimensionless energy such that

$$\tilde{E} = -\frac{1}{2} \int_{\mathcal{D}} \Psi \nabla^2 \Psi dx dy. \quad (4.11)$$

The entropy S , evaluated with the nondimensional streamfunction Ψ , becomes

$$S = -\frac{Nk_B}{2} \log (A_+ A_-) + 2k_B \frac{\tilde{E}}{\rho \beta \gamma^2}. \quad (4.12)$$

The expression for the energy in Eq. (4.11) does not depend on the number of vortices, however, the entropy S still contains the dependence on the number N . When N is sufficiently large, it can be shown [93], that the energy is proportional to the square of the number of vortices, $E \sim \rho N^2 \gamma^2$. Therefore, an alternative expression for the dimensionless energy, denoted \hat{E} and also used by Taylor *et al.* [114], can be defined by

$$\hat{E} \equiv \frac{E}{4\rho N^2 \gamma^2} = -\frac{\beta E}{4N\mathcal{D}\lambda^2}. \quad (4.13)$$

Substituting Eq. (4.10) into the above expression and by using the definition of λ^2 gives

$$\hat{E} = -\frac{\tilde{E}}{4N\mathcal{D}\rho\beta\gamma^2\lambda^2} = \frac{\tilde{E}}{4\mathcal{D}^2\lambda^4}, \quad (4.14)$$

which can be substituted into Eq. (4.12) to obtain

$$S = -\frac{Nk_B}{2} \log (A_+ A_-) + 2k_B \frac{4\mathcal{D}^2\lambda^4}{\rho\beta\gamma^2} \hat{E}. \quad (4.15)$$

Finally, by using the definition of λ^2 given by Eq. (4.7) a nondimensional entropy per vortex \hat{S} can be defined as follows

$$\frac{S}{Nk_B} \equiv \hat{S} = -\frac{1}{2} \log(A_- A_+) - \frac{8\hat{E}\mathcal{D}^2\lambda^4}{\mathcal{D}\lambda^2} = -\frac{1}{2} \log(A_+ A_-) - 8\mathcal{D}\lambda^2\hat{E}. \quad (4.16)$$

All these quantities can be evaluated by knowing the streamfunction Ψ and the correspondent inverse temperature λ^2 . Therefore, by starting from the BP equation, the following steps can be applied to classify its solutions in terms of the energy and entropy in a generic domain \mathcal{D} :

- Fix a value for the positive constant λ^2 .

- Solve the BPE

$$\nabla^2\Psi + \frac{\lambda^2}{2} \left[\frac{e^\Psi}{\langle e^\Psi \rangle} - \frac{e^{-\Psi}}{\langle e^{-\Psi} \rangle} \right] = 0, \quad (4.17)$$

for the specific value of λ^2 and obtain the solution Ψ .

- Evaluate the averaged terms

$$A_\pm = \mathcal{D} \left(\int_{\mathcal{D}} e^{\mp\Psi} dx dy \right)^{-1}. \quad (4.18)$$

- Evaluate the energy \tilde{E} and \hat{E}

$$\tilde{E} = \frac{\lambda^2}{4} \int_{\mathcal{D}} \Psi \left[\frac{e^\Psi}{\langle e^\Psi \rangle} - \frac{e^{-\Psi}}{\langle e^{-\Psi} \rangle} \right] dx dy, \quad \hat{E} = \frac{\tilde{E}}{4\mathcal{D}^2\lambda^4}. \quad (4.19)$$

- Evaluate the entropy per vortex \hat{S} in unit of k_B

$$\hat{S} = -\frac{1}{2} \log(A_+ A_-) - 8\mathcal{D}\lambda^2\hat{E}. \quad (4.20)$$

This procedure requires the solution Ψ to the BP equation for a given value of the parameter λ^2 , and this is the aim of §4.3. Therefore, before considering the BP equation it is useful to first consider the *linearised Boltzmann-Poisson* equation, which is the result of the linearisation of the BP equation.

4.2 Linear Theory

In the previous section, a procedure for classifying the solutions Ψ of the BP equation in terms of energy and entropy has been explained for a given value of the parameter λ^2 . In this section the BP equation given by Eq. (4.17) will be linearised about the state with zero mean flow i.e. $\Psi = 0$ and the linearised theory will be studied. This will reveal that in the BP equation the inverse temperature β is negative. Moreover, it will reveal the presence of two distinct families of solutions Ψ : those for which $\langle \Psi \rangle = 0$ and those for which $\langle \Psi \rangle \neq 0$. The distinction between the two cases depends on the fact that the former correspond to solutions with a vanishing net angular momentum whereas the latter have a non-zero angular momentum. The importance of these two classes of solution is due to the fact that, depending on the aspect ratio Λ of the rectangular region, either one can be a global maximiser of the entropy. The linear analysis of the BP equation has been previously performed by Chavanis *et al.* in [28] where the authors studied the linear theory in bounded geometries with and without constraints on the angular momentum L and on the total circulation of the system. In particular the authors investigated the squared and rectangular geometry characterised by the aspect ratio Λ . They confirmed the prediction given by Lundgren *et al.* [71] on the presence of a critical aspect ratio $\Lambda \sim 1.122$ such that the high entropy states for $\Lambda < \Lambda_c$ are achieved by a configuration in which vortices of one sign are in the centre and the vortices with opposite sign are near the corners. However, for aspect ratio $\Lambda > \Lambda_c$ the most probable configuration consist in a configuration where the vortices occupy the one half of the rectangle. The linear analysis which is now performed is a particular case of the more general approach presented by Chavanis *et al* in [28].

The sign of the factor in front of the squared brackets in Eq. (4.6) depends on the inverse temperature β . Since the linearisation is around $\Psi = 0$, the following Taylor expansions for the dimensionless streamfunction Ψ is considered

$$\exp(\pm\epsilon\Psi) \sim 1 \pm \epsilon\Psi + \mathcal{O}(\epsilon^2), \quad \langle \exp(\pm\epsilon\Psi) \rangle \sim 1 \pm \epsilon\langle \Psi \rangle + \mathcal{O}(\epsilon^2), \quad (4.21)$$

where $\epsilon \ll 1$, can be substitute in the BP equation. Considering the leading order terms, leads to

$$\nabla^2\Psi = -\frac{N\gamma^2\rho\beta}{\mathcal{D}} (\langle \Psi \rangle - \Psi), \quad (4.22)$$

which is the *linearized Boltzmann-Poisson* equation. Multiplying both sides by $-\Psi/2$

and integrating over the domain \mathcal{D} gives

$$\begin{aligned} -\frac{1}{2} \int_{\mathcal{D}} \Psi \nabla^2 \Psi dx dy &= \frac{N\gamma^2\rho\beta}{2\mathcal{D}} \left[\langle \Psi \rangle \int_{\mathcal{D}} \Psi dx dy - \int_{\mathcal{D}} \Psi^2 dx dy \right] \\ &= \frac{N\gamma^2\rho\beta}{2} [\langle \Psi \rangle^2 - \langle \Psi^2 \rangle] = -\frac{N\gamma^2\rho\beta}{2} \text{Var}(\Psi), \end{aligned} \quad (4.23)$$

where $\text{Var}(\Psi) = \langle \Psi^2 \rangle - \langle \Psi \rangle^2$ is the variance of Ψ . The left hand side of the above equation is the energy of the system given by Eq. (2.60) where the density $\rho = 1$. Since the energy and $\text{Var}(\Psi)$ are non-negative quantities, the inverse temperature β must be negative. If the inverse temperature is positive, then the only possible solution is given by the trivial case $\Psi(x, y) = 0$ everywhere. This shows that non trivial solutions to the BPE exist if the temperature of the system is negative. Hence, it is possible to define a positive quantity

$$\lambda^2 = -\frac{N\gamma^2\rho\beta}{\mathcal{D}}, \quad (4.24)$$

from which Eq. (4.22) becomes

$$\nabla^2 \Psi + \lambda^2 \Psi = \lambda^2 \langle \Psi \rangle. \quad (4.25)$$

The averaged terms A_{\pm} in the linear approximation (4.21) become

$$A_{\pm} \sim \mathcal{D} \left(\int_{\mathcal{D}} [1 \pm \epsilon \Psi + \mathcal{O}(\epsilon^2)] dx dy \right)^{-1} \sim 1, \quad (4.26)$$

and therefore, the entropy given by Eq. (4.4) simplifies to [114]

$$S = 2k_B \beta E = -2k_B \frac{\lambda^2 \mathcal{D}}{N\gamma^2\rho} E. \quad (4.27)$$

The above equation reveals an important property: in the linear approximation, the parameter λ^2 is a direct measure of the relative entropy of different solutions the linear BP equation with the same energy E . This is true only for the linearised BPE: for the full nonlinear BP equation the expression for the entropy given by Eq. (4.20) needs to be considered.

In the following the linear equation (4.25) will be solved and, since the linear theory is being considered, knowledge of λ^2 leads to the evaluation of the entropy for solutions of the linearised BP equation. In order to solve the inhomogeneous linear BP equation

(4.25) it is convenient to find the solutions to the homogeneous problem

$$\nabla^2 \Psi + \lambda^2 \Psi = 0, \quad (4.28)$$

in the rectangular domain given by $0 \leq x \leq L_x$ and $0 \leq y \leq L_y$ with $\Psi = 0$ on the boundaries in order to satisfy the boundary conditions (2.115). By using the method of separation of variables, the eigenfunctions and the eigenvalues of Eq. (4.28) are given by

$$\Psi_{n,m}(x, y) = \sin\left(\frac{n\pi}{L_x}x\right) \sin\left(\frac{m\pi}{L_y}y\right), \quad \lambda_{n,m}^2 = \pi^2 \left(\frac{n^2}{L_x^2} + \frac{m^2}{L_y^2}\right), \quad (4.29)$$

where n, m are positive integers. The eigenfunctions and the eigenvalues in a generic rectangular domain with aspect ratio $\Lambda = L_x/L_y > 1$ are given by

$$\Psi_{n,m}(x, y; \Lambda) = \sin\left(\frac{n\pi}{\sqrt{\Lambda}L_x}x\right) \sin\left(\frac{m\pi\sqrt{\Lambda}}{L_y}y\right), \quad \lambda_{n,m}^2 = \pi^2 \left(\frac{n^2}{\Lambda L_x^2} + \frac{\Lambda m^2}{L_y^2}\right), \quad (4.30)$$

where the sides L_x and L_y are changed into $\sqrt{\Lambda}L_x$ and $L_y/\sqrt{\Lambda}$, respectively. The case $\Lambda = 1$ reduces to a square and if $\Lambda > 1$ the square is stretched into a rectangle for which $L_x > L_y$. This transformation changes the shape of the domain keeping the area $\mathcal{D} = L_x L_y$ constant. The number of zeros of the above function along both directions x and y depends on the integers n and m respectively: in order to have $\langle \Psi \rangle = 0$, n and m can not be both odd. Figure (4.1) shows contour plots of the streamfunction $\Psi_{2,1}$ (Fig. a)) called *dipole*, $\Psi_{2,2}$ (Fig. b)) called *quadrupole* and for the superposition $\Psi_{2,1} + \Psi_{1,2}$ (Fig. c)) called *diagonal dipole*. The general solution to the homogeneous

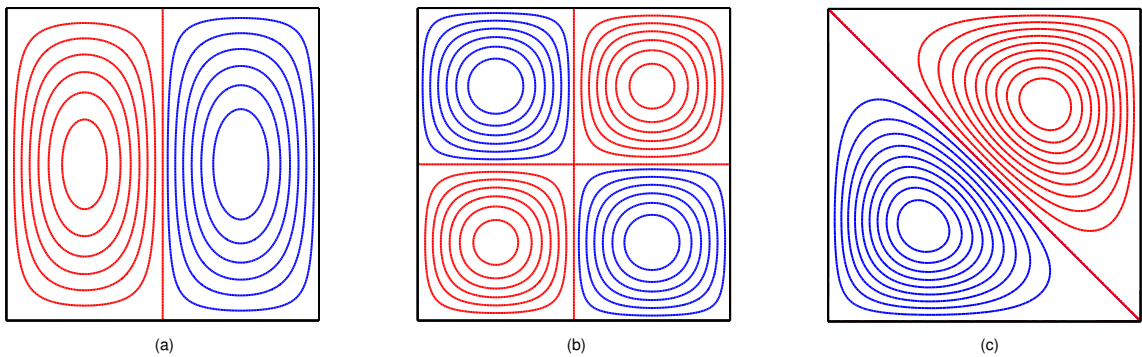


Figure 4.1: Contour plots for the solutions $\Psi_{2,1}$ (Fig. a)), $\Psi_{2,2}$ (Fig. b)) and $\Psi_{2,1} + \Psi_{1,2}$ (Fig. c)) of the homogeneous Helmholtz equation (4.28) in the square: they will be called *monopole*, *quadrupole* and *diagonal dipole* respectively. The blue and the red lines correspond to negative and positive values of the streamfunction.

linear BP equation (4.28) is then given by the principle of superposition

$$\Psi(x, y; \Lambda) = \sum_{m=1}^{+\infty} \sum_{n=1}^{+\infty} A_{mn} \sin\left(\frac{n\pi}{\sqrt{\Lambda}L_x}x\right) \sin\left(\frac{m\pi\sqrt{\Lambda}}{L_y}y\right), \quad (4.31)$$

where A_{mn} are normalization constants. The solution to the inhomogeneous equation (4.25) can now be found by finding the constants $A_{n,m}$ such that the inhomogeneous BP equation (4.25) is satisfied. Inserting Eq. (4.31) into the left hand side of Eq. (4.25) gives

$$\sum_{m,n} A_{mn} \left[\lambda^2 - \frac{n^2\pi^2}{\Lambda L_x^2} - \frac{m^2\pi^2\Lambda}{L_y^2} \right] \sin\left(\frac{n\pi}{\sqrt{\Lambda}L_x}x\right) \sin\left(\frac{m\pi\sqrt{\Lambda}}{L_y}y\right). \quad (4.32)$$

Multiplying the above quantity by two generic elements of the basis $\sin\left(n'\pi x/\sqrt{\Lambda}L_x\right)$ identified by an index n' and $\sin\left(m'\pi\sqrt{\Lambda}y/L_y\right)$ identified by an index m' and integrating with respect to x and y gives

$$A_{m',n'} \left[\lambda^2 - \frac{n'^2\pi^2}{\Lambda L_x^2} - \frac{m'^2\Lambda\pi^2}{L_y^2} \right] \frac{L_x L_y}{4}, \quad (4.33)$$

where the following property has been used

$$\int_0^L \sin\left(\frac{n\pi}{L}x\right) \sin\left(\frac{n'\pi}{L}x\right) dx = \frac{L}{2}\delta_{n,n'}.$$

The right hand side of Eq. (4.25) becomes

$$\lambda^2 \langle \Psi \rangle \int_0^{\sqrt{\Lambda}L_x} \int_0^{L_y/\sqrt{\Lambda}} \sin\left(\frac{n'\pi}{\sqrt{\Lambda}L_x}x\right) \sin\left(\frac{m'\pi\sqrt{\Lambda}}{L_y}y\right) dx dy, \quad (4.34)$$

which is

$$\lambda^2 \langle \Psi \rangle \frac{L_x L_y}{m' n' \pi^2} \left[(-1)^{n'} - 1 \right] \left[(-1)^{m'} - 1 \right], \quad (4.35)$$

due to the equality

$$\int_0^L \sin\left(\frac{n'\pi}{L}x\right) dx = -\frac{L}{n'\pi} \left[(-1)^{n'} - 1 \right]. \quad (4.36)$$

Therefore, in order to have a non-zero value, the integers m' and n' must be odd.

Combining Eqs. (4.33) and (4.35) gives

$$A_{m,n} \left[\lambda^2 - \frac{n^2\pi^2}{\Lambda L_x^2} - \frac{m^2\pi^2\Lambda}{L_y^2} \right] \frac{L_x L_y}{4} = \lambda^2 \langle \Psi \rangle \frac{4L_x L_y}{mn\pi^2}, \quad (4.37)$$

which allows for the evaluation of the coefficients $A_{m,n}$ given by

$$A_{m,n} = \lambda^2 \langle \Psi \rangle \frac{16}{mn\pi^2} \frac{1}{\lambda^2 - n^2\pi^2/\Lambda L_x^2 - m^2\pi^2\Lambda/L_y^2}. \quad (4.38)$$

This expression for the coefficients can be substituted into Eq. (4.31) to obtain the general solution to the inhomogeneous Helmholtz equation (4.25) for which $\langle \Psi \rangle \neq 0$

$$\Psi(x, y; \Lambda) = \frac{16\lambda^2 \langle \Psi \rangle}{\pi^2} \sum_{m=1}^{+\infty}' \sum_{n=1}^{+\infty}' \frac{\sin(n\pi x/\sqrt{\Lambda}L_x) \sin(m\pi\sqrt{\Lambda}y/L_y)}{mn(\lambda^2 - n^2\pi^2/\Lambda L_x^2 - m^2\pi^2\Lambda/L_y^2)}, \quad (4.39)$$

where the summations with the apostrophe means that only the odd integers are considered. The integral of the streamfunction Ψ over the domain \mathcal{D} is given by

$$\int_0^{\sqrt{\Lambda}L_x} \int_0^{L_y/\sqrt{\Lambda}} \Psi dx dy = \frac{16\lambda^2 \langle \Psi \rangle}{\pi^4} \sum_{m=1}^{+\infty}' \sum_{n=1}^{+\infty}' \frac{4L_x L_y}{m^2 n^2 (\lambda^2 - n^2\pi^2/\Lambda L_x^2 - m^2\pi^2\Lambda/L_y^2)}, \quad (4.40)$$

where the equality (4.36) has been used. Therefore, by using the definition of spatial average (4.1), the parameter λ^2 must satisfy the following equation

$$f(\lambda^2; n, m, \Lambda) = 0, \quad (4.41)$$

where the function $f(\lambda^2; n, m, \Lambda)$ is defined as follows

$$f(\lambda^2; n, m, \Lambda) = \frac{64\lambda^2}{\pi^4} \sum_{n=1}^{+\infty}' \sum_{m=1}^{+\infty}' \frac{1}{m^2 n^2 (\lambda^2 - n^2\pi^2/\Lambda L_x^2 - m^2\pi^2\Lambda/L_y^2)} - 1. \quad (4.42)$$

The number of zeros of the solution Ψ given by Eq. (4.39), are related to the solution of the Eq. (4.41). Figure (4.2) *a*) shows the graph of the function $f(\lambda^2; n, m, 1)$ for the particular case $\Lambda = 1$: it can be noted that the function does not have zeros for negative values of λ^2 but only for positive values of λ^2 . The zeros of the function $f(\lambda^2; n, m, 1)$ have been numerically evaluated by solving Eq. (4.41) and the first three are given by $\lambda^2 = 11.5287$, $\lambda^2 = 38.634$ and $\lambda^2 = 47.177$. For these values of λ^2 , the solutions Ψ given by Eq. (4.39) in the case of $\Lambda = 1$, are presented in Fig. (4.3). Since the entropy $S \sim -\lambda^2$, the higher entropy is achieved for small values of the parameter λ^2 and hence,

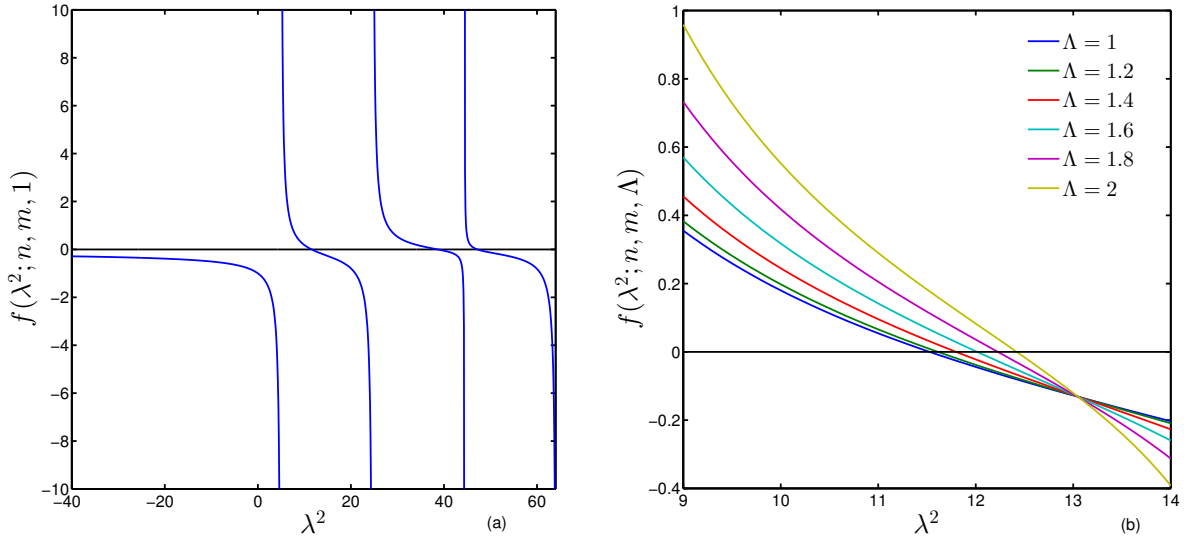


Figure 4.2: On the left the function $f(\lambda^2; n, m, 1)$ given by Eq. (4.41) for the particular case of $L_x = L_y = 2$ and $\Lambda = 1$: among all zeros, the most relevant is the first one which corresponds to $\lambda^2 \sim 11.5$. On the right, the trend of the function $f(\lambda^2; n, m, \Lambda)$ in the vicinity of the first zero for different values of the aspect ratio Λ indicated in the legend.

the relevant zero is the first one about $\lambda^2 \sim 11.5287$. This value of λ^2 corresponds to a streamfunction Ψ with the fewer number of zeros as shown in Fig. (4.3). For larger values of the parameter λ^2 the streamfunction Ψ presents more zeros (see Fig (4.3) b) and c)) and these configurations have lower entropy. Figure (4.2) on the right, shows the trend of the function $f(\lambda^2; n, m, \Lambda)$ in the vicinity of the first zero as a function of Λ : the value of the first zero is shifted to the right as Λ increases. As a consequence, for these family of solutions, the entropy S decreases as Λ increases. The linearised BP equation (4.25) allows the identification of two different types of solution: the first type is composed of solutions for which $\langle \Psi \rangle = 0$ given by Eq. (4.31) and the second for which $\langle \Psi \rangle \neq 0$ given by (4.39). The relation between the parameter λ^2 and the entropy S of these two types will be investigated by comparing the zeros of $f(\lambda^2; n, m, \Lambda)$ given by Eq. (4.41) and the values of $\lambda_{n,m}^2$ given by the second of Eq. (4.29) for the dipole, the diagonal dipole and the quadrupole. The zeros of $f(\lambda^2; n, m, \Lambda)$ are numerically evaluated by using the software Mathematica. The eigenvalues for the dipole and the quadrupole are given by

$$\lambda_{2,1}^2(\Lambda) = \pi^2 \left(\frac{4}{\Lambda L_x^2} + \frac{\Lambda}{L_y^2} \right), \quad \lambda_{2,2}^2(\Lambda) = 4\pi^2 \left(\frac{1}{\Lambda L_x^2} + \frac{\Lambda}{L_y^2} \right), \quad (4.43)$$

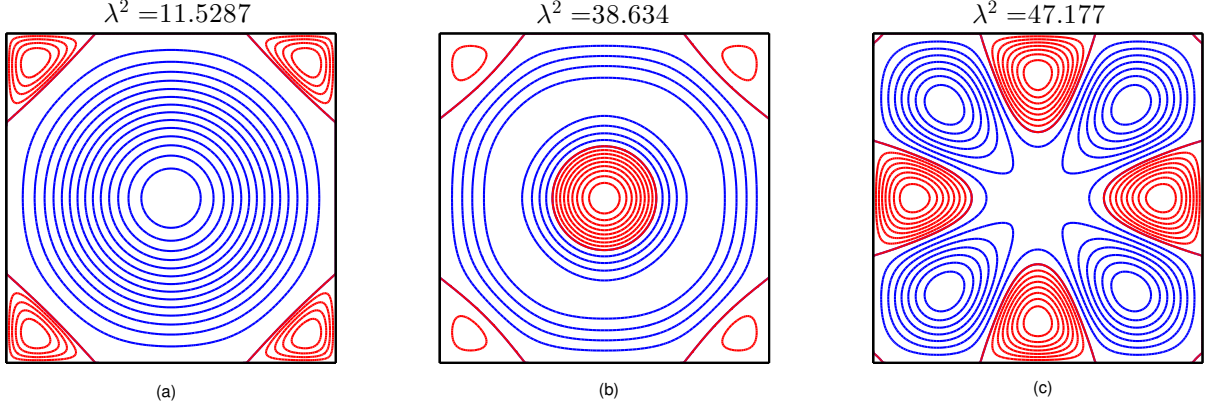


Figure 4.3: Contour plots of the streamfunction Ψ given by Eq. (4.41) for values of λ^2 which correspond to the first three zeros of $f(\lambda^2; n, m, 1)$ indicated in Fig.(4.2) on the left. The values of λ^2 are indicated above each figure.

and for the diagonal dipole

$$\lambda_{2,1}^2(\Lambda) + \lambda_{1,2}^2(\Lambda) = \pi^2 \left(\frac{4}{\Lambda L_x^2} + \frac{\Lambda}{L_u^2} \right) + \pi^2 \left(\frac{1}{\Lambda L_x^2} + \frac{4\Lambda}{L_u^2} \right). \quad (4.44)$$

Figure (4.4) shows how the entropy (λ^2) for the different types of flow varies as a function of the aspect ratio Λ . The four curves correspond to a monopole, dipole, diagonal dipole and quadrupole. The inset figures show the streamfunction for these four kind of solutions in the square ($\Lambda = 1$) and in the rectangle with aspect ratio $\Lambda = 1.5$. The configurations which play an important role are the dipole and the monopole: the quadrupole and the diagonal dipole have a very low entropy compared with the other two configurations. The linear theory shows that for low aspect ratio, the monopole configuration has higher entropy while for high aspect ratio the dipole has higher entropy. The critical value of the aspect ratio has been evaluated by [71] and it is $\Lambda_c = 1.122$.

4.3 Non-Trivial Solutions Of The Boltzmann-Poisson Equation

The BP equation is a non-linear, second order, partial differential equation which admits $\Psi = 0$ as a trivial solution. In §(4.2) it was shown that non-trivial solutions exist if the inverse temperature β is negative. In this section an iterative algorithm

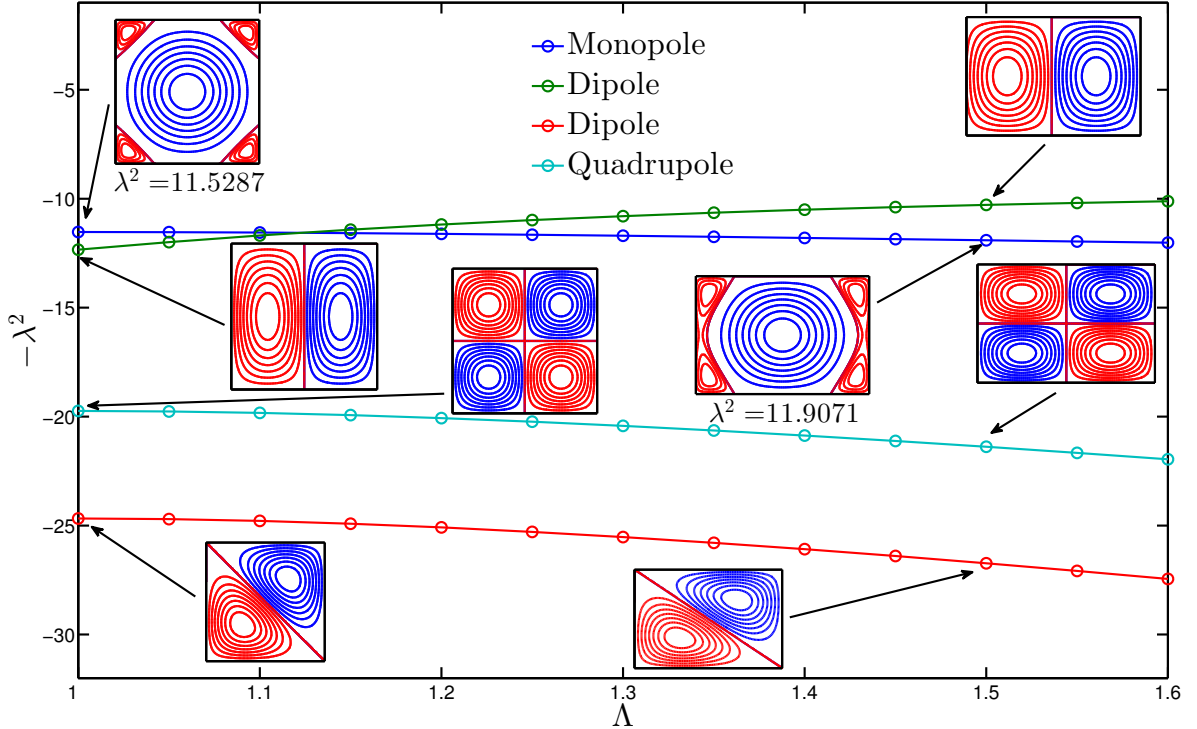


Figure 4.4: Comparison of the linear entropy given by Eq. (4.27) for different solutions of the linearised BP equation (4.22). By increasing the aspect ratio of the domain, the entropy of the monopole decreases while the entropy of the dipole increases. For small values of the aspect ratio Λ the monopole is dominant but for larger values of Λ the dipole configuration has a higher entropy. The entropies of the quadrupole and the diagonal dipole are not relevant for this linear analysis. The inset figures are the streamfunction for the monopole, dipole, diagonal dipole and quadrupole for $\Lambda = 1$ and $\Lambda = 1.5$. The blue and red contour lines represent the negative and the positive values of the streamfunction respectively.

which converges to a non trivial solutions Ψ of the equation

$$\nabla^2 \Psi + \frac{\lambda^2}{2} \left[\frac{e^\Psi}{\langle e^\Psi \rangle} - \frac{e^{-\Psi}}{\langle e^{-\Psi} \rangle} \right] = 0, \quad \Psi = 0, \quad \text{on } \partial\mathcal{D}, \quad (4.45)$$

will be presented. The algorithm is an extension of the method developed by McDonald [77] for solving the Sinh-Poisson equation. To enhance the numerical stability of the iterative algorithm the above form of the BP equation is rewritten in the form

$$\nabla^2 \Psi + \tilde{\lambda}^2 \left[\sqrt{\frac{a_-}{a_+}} e^\Psi - \sqrt{\frac{a_+}{a_-}} e^{-\Psi} \right] = 0, \quad (4.46)$$

where

$$\tilde{\lambda}^2 = \frac{2\lambda^2}{\sqrt{a_+ a_-}}, \quad a_\pm = \langle e^{\pm\Psi} \rangle. \quad (4.47)$$

The fist step of the algorithm is to start with an initial guess $\varphi(x, y)$ which approximates the exact solution Ψ of the BP equation. A residual function $R(x, y)$ can be defined as

$$R(x, y) = \left(\nabla^2 \varphi + \tilde{\lambda}^2 \left[\sqrt{\frac{a_-}{a_+}} e^\varphi - \sqrt{\frac{a_+}{a_-}} e^{-\varphi} \right] \right) / (\varphi, \varphi), \quad (4.48)$$

where (f, g) is the inner product of two real functions f and g defined by

$$(f, g) = \int_{\mathcal{D}} f(x, y) g(x, y) dx dy. \quad (4.49)$$

The residual function $R(x, y)$ represents the discrepancy between the exact solution Ψ and the trial solution φ . Following McDonald, the denominator (φ, φ) is included in the definition of $R(x, y)$ to ensure the algorithm converges to a non-trivial solution for the streamfunction Ψ . A variation in the trial function $\varphi(x, y)$ corresponds to a change in $R(x, y)$ given by

$$\delta R(x, y) = \frac{\nabla^2 \delta \varphi + \tilde{\lambda}^2 \delta [\dots] - 2(\delta \varphi, \varphi) R(x, y)}{(\varphi, \varphi)}, \quad (4.50)$$

where $\delta(\varphi, \varphi) = (\delta \varphi, \varphi) + (\varphi, \delta \varphi) = 2(\delta \varphi, \varphi)$ and $[\dots]$ corresponds to the terms in the squared brackets in Eq. (4.48). Since

$$\begin{aligned} \delta \sqrt{\frac{a_i}{a_j}} &= \frac{1}{2} \sqrt{\frac{a_j}{a_i}} \left[\frac{a_j \delta a_i - a_i \delta a_j}{a_j^2} \right], \quad i = \pm, j = \mp, \\ \delta a_\pm &= \delta \langle e^{\pm \varphi} \rangle = \pm \langle e^{\pm \varphi} \delta \varphi \rangle, \end{aligned} \quad (4.51)$$

the variation of the terms contained in the square brackets becomes

$$\begin{aligned}
 \delta[\dots] &= \delta \sqrt{\frac{a_-}{a_+}} e^\varphi + \sqrt{\frac{a_-}{a_+}} e^\varphi \delta\varphi - \delta \sqrt{\frac{a_+}{a_-}} e^{-\varphi} + \sqrt{\frac{a_+}{a_-}} e^{-\varphi} \delta\varphi \\
 &= -\frac{1}{2} \sqrt{\frac{a_+}{a_-}} \left(\frac{\langle e^{-\varphi} \delta\varphi \rangle}{a_+} + \frac{a_- \langle e^\varphi \delta\varphi \rangle}{a_+^2} \right) e^\varphi + \sqrt{\frac{a_-}{a_+}} e^\varphi \delta\varphi \\
 &\quad -\frac{1}{2} \sqrt{\frac{a_-}{a_+}} \left(\frac{\langle e^\varphi \delta\varphi \rangle}{a_-} + \frac{a_+ \langle e^{-\varphi} \delta\varphi \rangle}{a_-^2} \right) e^{-\varphi} + \sqrt{\frac{a_+}{a_-}} e^{-\varphi} \delta\varphi \\
 &= \mathcal{L}[\varphi, \delta\varphi] + h(\varphi) \delta\varphi,
 \end{aligned} \tag{4.52}$$

where the operator \mathcal{L} , which depends on the functions φ and $\delta\varphi$, is given by

$$\begin{aligned}
 \mathcal{L}[\varphi, \delta\varphi] = & -\frac{1}{2} \frac{\langle e^{-\varphi} \delta\varphi \rangle}{\sqrt{a_+ a_-}} e^\varphi - \frac{1}{2a_+} \sqrt{\frac{a_-}{a_+}} \langle e^\varphi \delta\varphi \rangle e^\varphi \\
 & -\frac{1}{2} \frac{\langle e^\varphi \delta\varphi \rangle}{\sqrt{a_+ a_-}} e^{-\varphi} - \frac{1}{2a_-} \sqrt{\frac{a_+}{a_-}} \langle e^{-\varphi} \delta\varphi \rangle e^{-\varphi},
 \end{aligned} \tag{4.53}$$

and

$$h(\varphi) = \sqrt{\frac{a_-}{a_+}} e^\varphi + \sqrt{\frac{a_+}{a_-}} e^{-\varphi}. \tag{4.54}$$

Inserting these quantities into Eq. (4.50) gives

$$\delta R(x, y) = \frac{\nabla^2 \delta\varphi + \tilde{\lambda}^2 h(\varphi) \delta\varphi - \tilde{\lambda}^2 \mathcal{L}[\varphi, \delta\varphi] - 2(\delta\varphi, \varphi)R(x, y)}{(\varphi, \varphi)}. \tag{4.55}$$

Hence, $\delta\varphi$ is evaluated by requiring $\delta R = -R$ such that

$$\nabla^2 \delta\varphi + \tilde{\lambda}^2 h(\varphi) \delta\varphi - \tilde{\lambda}^2 \mathcal{L}[\varphi, \delta\varphi] - 2(\delta\varphi, \varphi)R(x, y) = -(\varphi, \varphi)R(x, y). \tag{4.56}$$

Writing the variation $\delta\varphi$ as a product of a constant α and an unknown function $v(x, y)$ which goes to zero on the boundary

$$\delta\varphi(x, y) = \alpha v(x, y), \quad \alpha = \frac{(\varphi, \varphi)}{2(v, \varphi) - (\varphi, \varphi)}, \tag{4.57}$$

will simplify the fourth term of the above equation. Therefore, by inserting $(\varphi, \varphi)R(x, y) = 2\alpha R(x, y)(v, \varphi) - \alpha(\varphi, \varphi)R(x, y)$ into Eq. (4.56) gives

$$\nabla^2 v(x, y) + \tilde{\lambda}^2 h(\varphi) v(x, y) - \tilde{\lambda}^2 \mathcal{L}[\varphi, v] = (\varphi, \varphi)R(x, y). \tag{4.58}$$

CHAPTER 4. MEAN-FIELD THEORY OF VORTEX GAS IN BOUNDED GEOMETRIES

Since the operator \mathcal{L} is linear, it is possible to introduce a new operator \mathcal{F} such that $\mathcal{L}[\varphi, v] = \mathcal{F}[\varphi]v(x, y)$ and hence, Eq. (4.58) becomes

$$\left[\nabla^2 + \tilde{\lambda}^2 h(\varphi) - \tilde{\lambda}^2 \mathcal{F}[\varphi] \right] v(x, y) = (\varphi, \varphi) R(x, y). \quad (4.59)$$

By defining \mathcal{Z} the operator in the square brackets,

$$\mathcal{Z} \equiv \nabla^2 + \tilde{\lambda}^2 h(\varphi) - \tilde{\lambda}^2 \mathcal{F}[\varphi], \quad (4.60)$$

then the function $v(x, y)$ is given by the product of its inverse and the right hand side of the above equation

$$v(x, y) = \mathcal{Z}^{-1}(\varphi, \varphi) R(x, y). \quad (4.61)$$

With this approach it is possible to construct an iterative algorithm which converges to the solution Ψ of the BPE by applying the following procedure:

- Make an initial guess φ such that $\Psi = \varphi + \delta\varphi$.
- Evaluate the residual function

$$R(x, y) = \left(\nabla^2 \varphi + \tilde{\lambda}^2 \left[\sqrt{\frac{a_-}{a_+}} e^\varphi - \sqrt{\frac{a_+}{a_-}} e^{-\varphi} \right] \right) / (\varphi, \varphi), \quad (4.62)$$

- Construct the operator \mathcal{Z}

$$\mathcal{Z} = \nabla^2 + \tilde{\lambda}^2 h(\varphi) - \tilde{\lambda}^2 \mathcal{L}(\varphi, \dots), \quad (4.63)$$

- Invert the operator \mathcal{Z} and evaluate

$$v(x, y) = \mathcal{Z}^{-1}(\varphi, \varphi) R(x, y), \quad (4.64)$$

- Find the constant α by evaluating

$$\alpha = \frac{(\varphi, \varphi)}{2(v, \varphi) - (\varphi, \varphi)}, \quad (4.65)$$

- Evaluate the variation $\delta\varphi = \alpha v(x, y)$ and update the initial guess $\varphi + \delta\varphi$.

All the above steps have been iterated until the energy E of the system saturated. This iterative procedure allows a solution to the nonlinear BP equation to be found. However, two things are still missing: the first one is how to choose judiciously the

initial guess φ at the beginning of the iterative cycle, and the second is to find a way to write $\mathcal{L}[\varphi, v] = \mathcal{F}[\varphi] v(x, y)$.

The trial function φ can be chosen by considering the type of solution that needs to be obtained. Therefore, if the dipole/monopole/diagonal dipole solution to the BP equation is being sought, then the most natural initial guess is given by the dipole/monopole/diagonal dipole solution of the linearised BP equation. While the first two type have been described by Taylor *et al.* in [114], the diagonal dipole has not been taken into account. This class of solutions plays an important role in the dynamics of point vortices which will be investigated in the next Chapter. The BP equation will be solved in the domain $[-\sqrt{\Lambda}, \sqrt{\Lambda}] \times [-1/\sqrt{\Lambda}, 1/\sqrt{\Lambda}]$ which reduces to $[-1, 1] \times [-1, 1]$ in the case of the square. Explicitly, for the monopole the initial guess is given by

$$\varphi_M(x, y) = \frac{16A\lambda^2}{\pi^2} \sum_{n,m=1}^{+\infty} \frac{\sin(nX_M) \sin(mY_M)}{nm(\lambda^2 - (m^2\pi^2/\Lambda L_x^2 - n^2\pi^2\Lambda/L_y^2))}, \quad (4.66)$$

where

$$X_M = \frac{\pi}{L_x} \left(x - \sqrt{\Lambda} \right), \quad Y_M = \frac{\pi}{L_y} \left(y - \frac{1}{\sqrt{\Lambda}} \right), \quad (4.67)$$

and $A = 0.02$ is a constant which fixes the maximum amplitude of the initial guess and $L_x = L_y = 2$. For the dipole, the initial guess is given by

$$\varphi_D(x, y) = A \sin(X_D) \sin(Y_D), \quad (4.68)$$

where

$$X_D = \frac{\pi x}{\sqrt{\Lambda}}, \quad Y_D = \frac{\pi}{2} \left(\sqrt{\Lambda}y - 1 \right), \quad (4.69)$$

and for the diagonal dipole

$$\varphi_{DD}(x, y) = \varphi_D(x, y) + A \sin(X_{DD}) \sin(Y_{DD}), \quad (4.70)$$

where

$$X_{DD} = \frac{\pi}{2} \left(\frac{x}{\sqrt{\Lambda}} - 1 \right), \quad Y_{DD} = \pi \sqrt{\Lambda}y. \quad (4.71)$$

In the following the attention is given on writing the new operator $\mathcal{F}[\varphi]$ such that $\mathcal{L}[\varphi, v] = \mathcal{F}[\varphi] v(x, y)$.

Each term of $\mathcal{L}[\varphi, v]$, apart from the constant term, is of the form

$$\langle f, v \rangle g(x, y) = \frac{g(x, y)}{\mathcal{D}} \int_{\mathcal{D}} f(\tilde{x}, \tilde{y}) v(\tilde{x}, \tilde{y}) d\tilde{x} d\tilde{y} \quad (4.72)$$

CHAPTER 4. MEAN-FIELD THEORY OF VORTEX GAS IN BOUNDED GEOMETRIES

Numerically, the integral of the above quantity is evaluated by replacing the double integral by a double summation over the nodes x_i and y_j , $i, j = 0 \dots, N$

$$\langle f, v \rangle \sim \sum_{i=0}^N \sum_{j=0}^N f(x_i, y_j) v(x_i, y_j) w_{x_i} w_{y_j} \equiv \sum_{i=1}^N \sum_{j=1}^N f_{i,j} v_{i,j} \mathcal{W}_{i,j}, \quad (4.73)$$

where w_{x_i} and w_{y_j} are the weights associated to each node and for brevity $\mathcal{W}_{i,j} = w_{x_i} w_{y_j}$. The quantity given by Eq. (4.72) can be written in terms of a matrix product as follows

$$\begin{pmatrix} f_{1,1}\mathcal{W}_{1,1}g_{1,1} & \cdots & f_{1,N}\mathcal{W}_{1,N}g_{1,1} & f_{2,1}\mathcal{W}_{2,1}g_{1,1} & \cdots & f_{N,N}\mathcal{W}_{N,N}g_{1,1} \\ f_{1,1}\mathcal{W}_{1,1}g_{1,2} & \cdots & f_{1,N}\mathcal{W}_{1,N}g_{1,2} & f_{2,1}\mathcal{W}_{2,1}g_{1,2} & \cdots & f_{N,N}\mathcal{W}_{N,N}g_{1,2} \\ \vdots & \vdots & \vdots & \vdots & \vdots & \vdots \\ f_{1,1}\mathcal{W}_{1,1}g_{1,N} & \cdots & f_{1,N}\mathcal{W}_{1,N}g_{1,N} & f_{2,1}\mathcal{W}_{2,1}g_{1,N} & \cdots & f_{N,N}\mathcal{W}_{N,N}g_{1,N} \\ f_{1,1}\mathcal{W}_{1,1}g_{2,1} & \cdots & f_{1,N}\mathcal{W}_{1,N}g_{2,1} & f_{2,1}\mathcal{W}_{2,1}g_{2,1} & \cdots & f_{N,N}\mathcal{W}_{N,N}g_{2,1} \\ \vdots & \vdots & \vdots & \vdots & \vdots & \vdots \\ f_{1,1}\mathcal{W}_{1,1}g_{N,N} & \cdots & f_{1,N}\mathcal{W}_{1,N}g_{N,N} & f_{2,1}\mathcal{W}_{2,1}g_{N,N} & \cdots & f_{N,N}\mathcal{W}_{N,N}g_{N,N} \end{pmatrix} \begin{pmatrix} v_{1,1} \\ \vdots \\ v_{1,N} \\ v_{2,1} \\ \vdots \\ \vdots \\ v_{N,N} \end{pmatrix}$$

By writing each term of the operator $\mathcal{L}[\varphi, v]$ (4.72) in this form, it is possible to write Eq. (4.58) as Eq. (4.59) and find the solution $v(x, y)$. The BP equation is then solved on a Chebyshev grid consisting of 33×33 points. The use of a Chebyshev grid has the advantage that it alleviates the so called *Runge phenomenon* [117] which results in spurious oscillations of smooth functions near boundaries. The Chebyshev grid resolves this problem by using a non-uniform grid [117]. For a given number of points N the Chebyshev nodes are defined on the interval $[-1, 1]$ by the following relation

$$x_i = \cos\left(\frac{i\pi}{N}\right), \quad i = 0 \dots N \quad (4.74)$$

and they can be visualized as the projection of equispaced points on the upper half of the unit circle onto the interval $[-1, 1]$ (see Fig. (4.5)). Numerical details on the construction of the discrete Laplace operator on a Chebyshev grid used in Eq. (4.62), and on the weights w_{x_i} and w_{y_j} used in Eq. (4.73) can be found in [117].

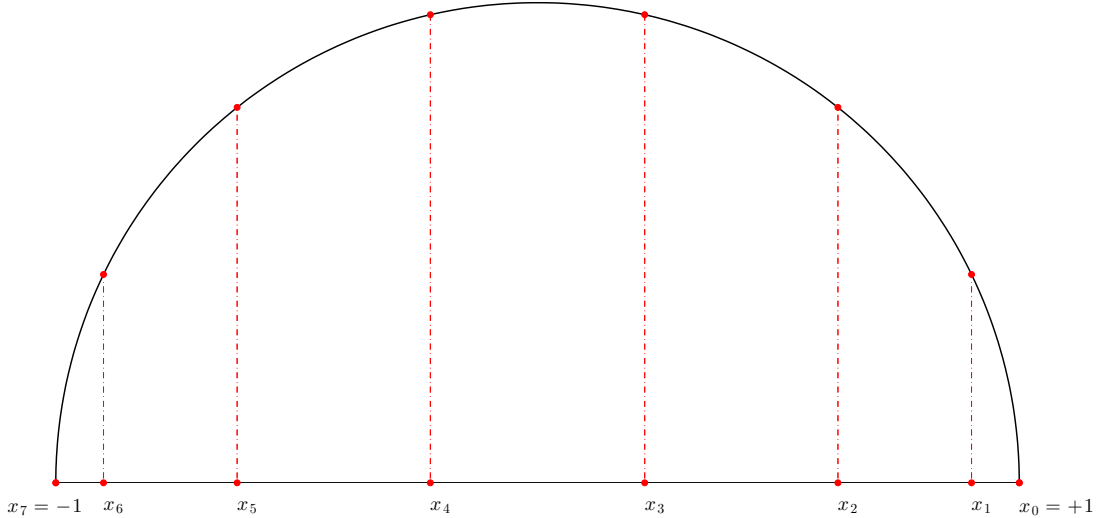


Figure 4.5: Chebyshev nodes in the interval $[-1, 1]$: the nodes are more dense near the endpoints.

4.4 Solutions of the Boltzmann-Poisson Equation in the Squared Domain

In the previous section a solution procedure was presented for finding solutions of the BP equation. In this section the solutions obtained in a squared domain will be presented. The BP equation was solved in a squared domain for different values of the parameter $\tilde{\lambda}^2$ for the following families of solutions: monopole, dipole and diagonal dipole. Results are presented in Fig. (4.6) where the energy \hat{E} given by Eq. (4.14) and the entropy per vortex \hat{S} given by (4.20) are evaluated for each solution in each family. For the three type of solutions, the parameter $\tilde{\lambda}^2$ runs between $\tilde{\lambda}^2 = 3$ and $\tilde{\lambda}^2 = 11.5$ with steps of 0.5. According to the mean-field theory, all the solutions presented are local maxima of the entropy. The classification shown in Fig. (4.6) reveals that in the squared domain, the global maxima corresponds to the monopole, for any value of the non dimensional energy \hat{E} . This result, which was predicted in the linear theory (4.2), is still valid in the full non linear theory. An important result, which improves the result given by Taylor *et al.* [114], is given by the comparison between the dipole (blue curve) and diagonal dipole (red curve): the diagonal dipole is more favourable than the dipole. This result will turn out to be crucial in understanding the dynamics of point vortices which will be assessed in the next chapter.

Examples of vorticity fields associated to different solutions of the BPE in the square are given in Fig. (4.7). In the dipole and diagonal dipole cases, the vorticity is distributed symmetrically whereas for the monopole the distribution is asymmetric: nega-

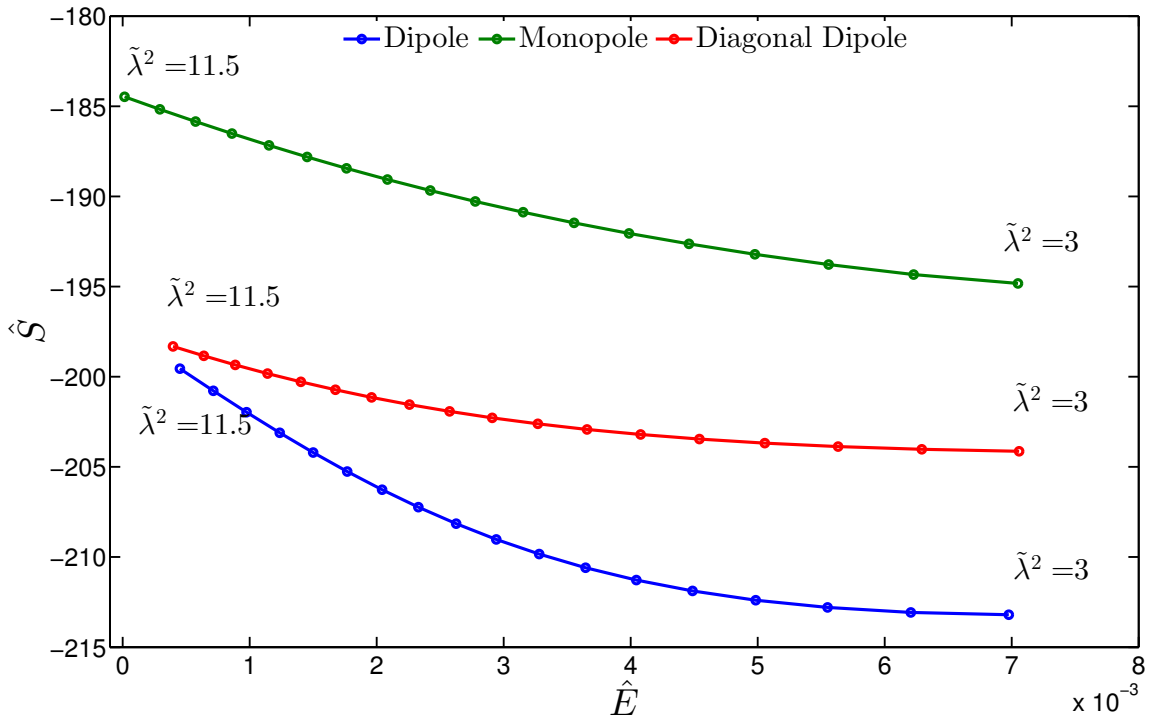


Figure 4.6: Branches related to the solutions of Eq. (4.46) for different values of $\tilde{\lambda}^2$ in the square with $L_x = L_y = 2$. The monopole (green curve) has the highest entropy followed by the diagonal dipole (red curve). Values of $\tilde{\lambda}^2$ are indicated at the beginning and at the end of each branch and each circle refers to an increment of 0.5 in its value.

tive vorticity is located in the center of the domain surrounded by the positive vorticity which extends to the four corners of the domain. It should be remarked that if the doubly period domain would have been considered, the maximum entropy configuration would have been the dipole as shown in [124] and [71]. The particular range of values

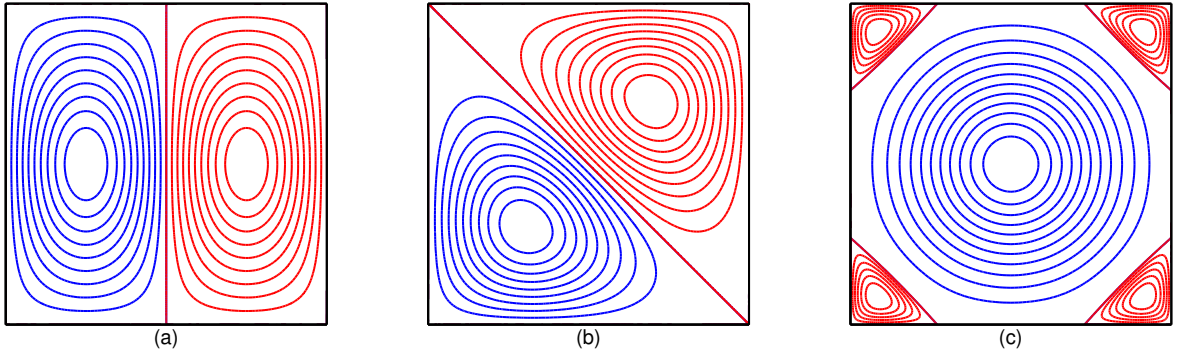


Figure 4.7: Contour plots for the dipole *a*), the diagonal dipole *b*), and for the monopole *c*). These solutions have been obtained by solving the BPE for $\tilde{\lambda}^2 = 9$: the blue line corresponds to a region where the streamfunction is negative while the red lines represents a region where the streamfunction is positive.

of $\tilde{\lambda}^2$ considered in Fig. (4.6) have been selected for two main reasons. The first reason is related to the number of Chebyshev nodes used during the numerical evaluation of the solutions of the BP equation. Small values of the parameter $\tilde{\lambda}^2$ correspond to highly localised vorticity distributions. In fact, for values smaller than $\tilde{\lambda}^2 = 3$, the localisation of the vorticity field degraded the numerical accuracy of the solution unless the resolution is increased. The trend of the error as a function of the parameter $\tilde{\lambda}^2$ is shown in Fig. (4.8) where the error increases as $\tilde{\lambda}^2$ decreases. The error has been evaluated by considering the degree of convergence that can be achieved with the iterative method. In particular the following norm is evaluated

$$Error = \left| \nabla^2 \Psi + \frac{\lambda^2}{2} \left[\frac{e^\Psi}{\langle e^\Psi \rangle} - \frac{e^{-\Psi}}{\langle e^{-\Psi} \rangle} \right] \right|, \quad (4.75)$$

where Ψ is the numerical solution obtained.

The second reason is related to the fact that for large values of $\tilde{\lambda}^2$, the final configurations corresponds to streamfunctions with a high number of zeros as in the case of the monopole solutions for the linear BP equation presented in Fig. (4.3). It can be shown [16] that these configurations have higher energies and therefore, are less favourable. As a consequence, their entropy is lower than the entropies of the solutions with fewer zeros and for this reason values of $\tilde{\lambda}^2 \geq 12$ have not been considered.

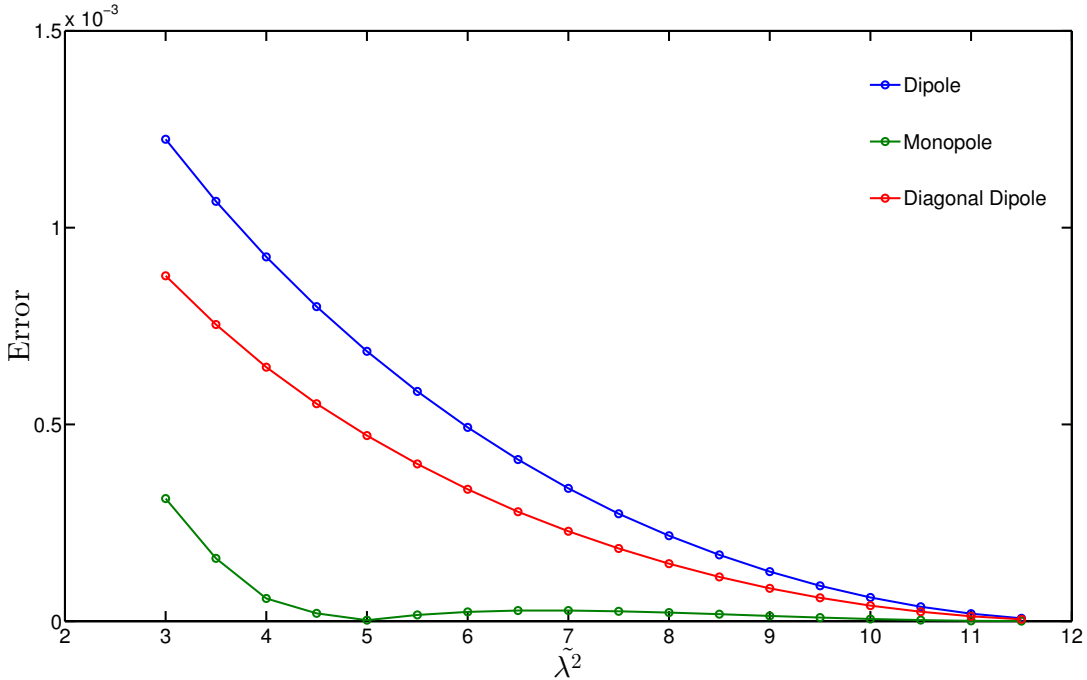


Figure 4.8: Variation of error as a function of $\tilde{\lambda}^2$ for different solution branches in the squared domain. The error increases as $\tilde{\lambda}^2$ decreases: this is due to the localised solution to the BP equation for small values of $\tilde{\lambda}^2$.

4.5 Solutions of the Boltzmann-Poisson Equation in the Rectangular Domain

In the previous section, the entropy \hat{S} for the monopole, dipole and diagonal dipole was evaluated in the square. According to the linear theory high entropy states correspond to the monopole configuration. Motivated by the linear analysis that shows that as the aspect ratio is increased the different solution branches cross at around $\Lambda_c \sim 1.122$, the same analysis has been performed in the rectangle with an aspect ratio $\Lambda = 1.5$, keeping the area fixed. The branches for this geometry are shown in Fig. (4.9). The first difference between the square (4.6) and the rectangle, is the absence of the branch related to the diagonal dipole. In fact by starting the initial guess that corresponds to the diagonal dipole the algorithm always converged to a dipole. It suggests that for this particular geometry, the diagonal dipole is no longer a stationary point for the entropy. The other difference is given by the role of the dipole and the monopole solutions. In this case the dipole configurations are global maxima for the entropy whereby the monopole structures are local maxima so the roles of these two families have been interchanged. This behaviour is consistent with the predictions obtained from the linear theory.

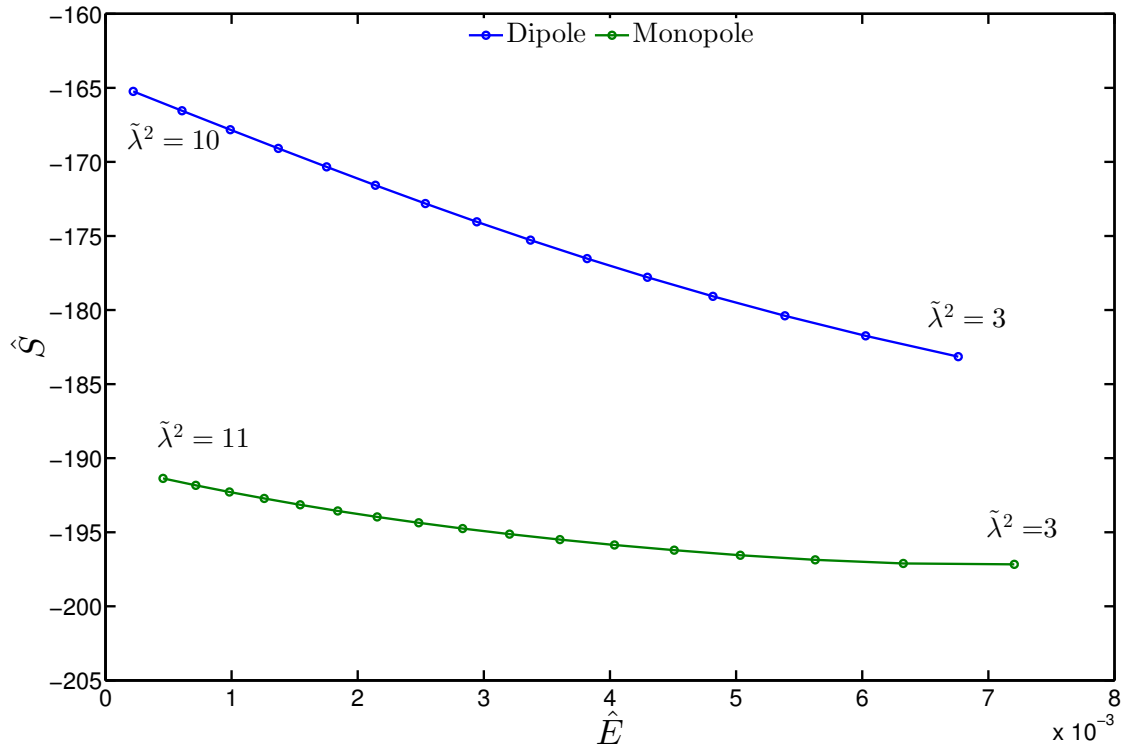


Figure 4.9: Branches related to the solutions of the Eq. (4.46) for different values of $\tilde{\lambda}^2$ in the rectangle with aspect ratio $\Lambda = 1.5$: the higher value for the entropy is achieved by the dipole (blue curve).

For reasons similar to these discussed for the square, the range of the values of the parameter $\tilde{\lambda}^2$ has been restricted to be between $\tilde{\lambda}^2 = 3$ and $\tilde{\lambda}^2 = 10$ for the dipole and $\tilde{\lambda}^2 = 3$ and $\tilde{\lambda}^2 = 11$ for the monopole. As with Fig. (4.8), norm of the error for the solutions in the rectangular domain presented in Fig. (4.10) shows that for small values of the parameter $\tilde{\lambda}^2$ the error increases.

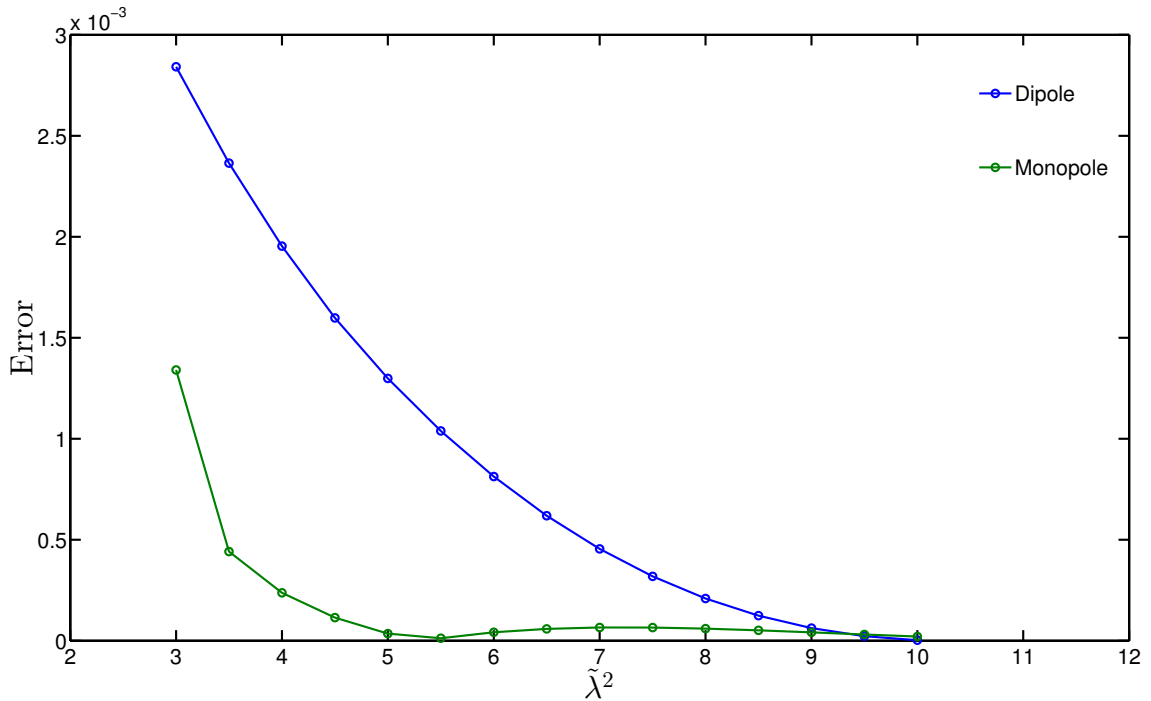


Figure 4.10: Variation of error as a function of $\tilde{\lambda}^2$ for different solution branches in the rectangular domain. The error increases as $\tilde{\lambda}^2$ decreases: this is due to the localised solution to the BPE for small values of $\tilde{\lambda}^2$.

4.6 Solutions of the Boltzmann-Poisson as a Function of the Aspect Ratio

The analysis performed in the previous two sections showed that the values of the entropy \hat{S} depends on the aspect ratio Λ . In order to complete this analysis, the BP equation has been solved for different values of the aspect ratio Λ and the same analysis on the solutions has been performed. Figure (4.11) shows the variation of the entropy \hat{S} for the dipole and the monopole as a function of the aspect ratio Λ . Figure (4.11) *a*) shows branches of the dipolar solutions as a function of the aspect ratio Λ . As the aspect ratio increases, the entropy of these type of solutions increases. Figure (4.11) *b*) shows branches of the monopolar solutions as a function of the aspect ratio Λ and in

this case the entropy decreases as the aspect ratio increases. Figure (4.11) *c*) combines all the branches for the two types of solutions for different values of the aspect ratio Λ . In this analysis the numerical values of the parameter $\tilde{\lambda}^2$ have been restricted to be between $\tilde{\lambda}^2 = 3$ and $\tilde{\lambda}^2 = 9$.

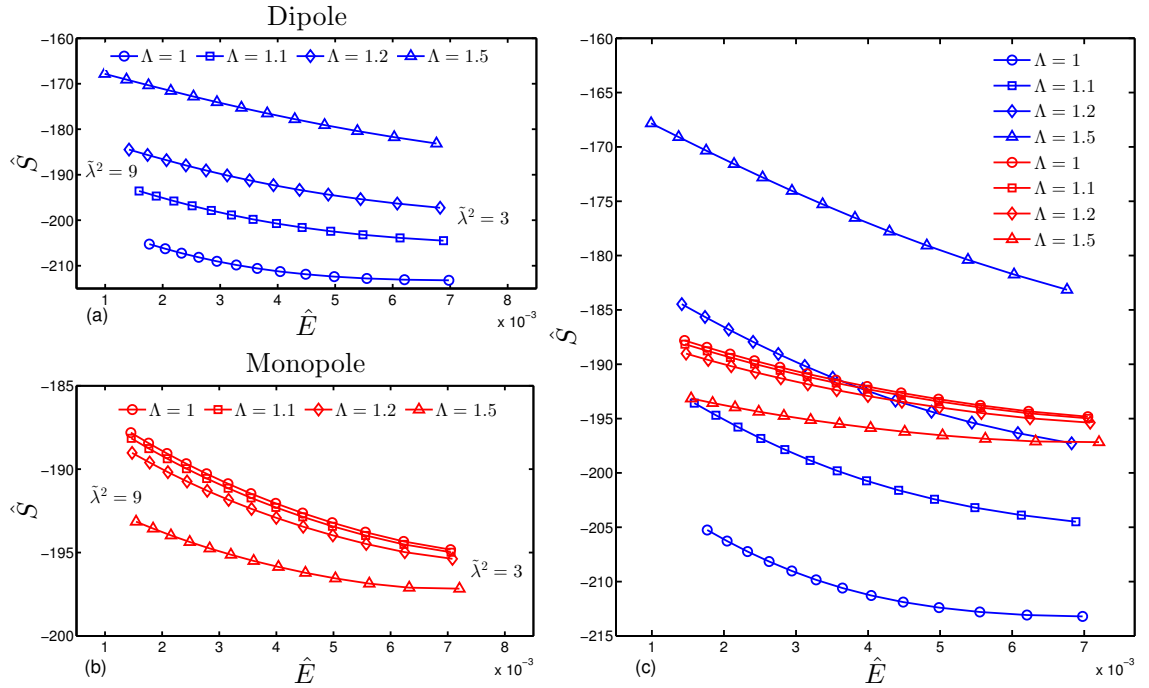


Figure 4.11: Branches related to the solutions of the BP equation (4.17) as a function of the aspect ratio Λ for the dipole *a*) and for the monopole *b*) for different values of the parameter $\tilde{\lambda}^2$. In Fig. *c*) the graphs presented in *a*) and *b*) are compared.

4.7 Role of the Angular Momentum

The classification of solutions of the BP equation presented in §4.4 and §4.5 revealed the crucial role of the geometry with respect to the configuration with higher entropy. In the squared domain the monopole is the solution which is the global maxima for the entropy, followed by the diagonal dipole and by the dipole. On the other hand, by changing the domain into a rectangle with aspect ratio $\Lambda = 1.5$, the maximum entropy is achieved by the dipole configuration while the monopole corresponds to a local maxima. This feature has an important effect to a measurable quantity which is the angular momentum: in fact, the angular momentum L of a flow described by a

streamfunction Ψ is given by (see Eq. (2.138))

$$L = 2 \int_{\mathcal{D}} \Psi dx dy = 2\mathcal{D}\langle \Psi \rangle, \quad (4.76)$$

where the density $\rho = 1$. In the rectangular geometry the higher entropy state is associated with a configuration described by a streamfunction Ψ such that $\langle \Psi \rangle = 0$ hence, to a zero value of the angular momentum L . On the other hand, in the squared geometry, the maximum entropy state is achieved by the monopole. In this case the streamfunction Ψ is such that $\langle \Psi \rangle \neq 0$ and, as a consequence, it is possible to associate to this configuration a nonzero angular momentum.

The acquisition of an angular momentum in the case of a non-neutral configuration of point vortices is not surprising: however, the studied system is composed of an equal number of positive and negative point vortices. This spontaneous acquisition of an angular momentum by a neutral vortex gas it has been investigated in classical fluid in [33]. This behaviour is predicted by the mean-field theory but for our knowledge has never been demonstrated directly by considering the dynamics of point vortices. In the next chapter, the dynamics for a system composed by an equal number of point vortices in a squared and rectangular domain will be described. The aim will be to test to what extent the predictions of the theory that have been obtained assuming large N apply to a dynamical simulation consisting of around 100 vortices which is achievable in current experiments on Bose-Einstein condensates.

Chapter 5

Point Vortex Dynamics in the Square and the Rectangle

In the previous Chapter the solutions to the Boltzmann-Poisson (BP) equation for the streamfunction ψ for a neutral vortex gas consisting of two species of vortices have been considered. Solutions for both a squared domain with sides $L_x = L_y = 2$ and in a rectangle with sides $L_x = 2\sqrt{\Lambda}$ and $L_y = 2/\sqrt{\Lambda}$ where $\Lambda = L_x/L_y = 1.5$ have been presented. In particular, two type of solutions have been investigated and classified in terms of their energy and entropy: the solutions for which ψ has a zero mean value and those for which their mean value is non-zero. Example of the first kind of solutions are given by the dipole and the diagonal dipole and in the second case an example is given by the monopole. This analysis revealed the presence of two configurations which maximise the entropy of the system: the monopole in the square and the dipole in the rectangle.

Since the BP equation has been derived in the framework of a microcanonical approach, and since in the point vortex model (PVM) the total number of vortices and the total energy \mathcal{H} are conserved, it will be interesting to confirm the predictions given from the mean-field-theory to see whether for which the long term dynamics of point vortices in the square reveals a monopole structure but a dipole configuration in the rectangle.

Another interesting aspect to study is the transition of the vortex gas from the positive temperature to the negative temperature regime and the formation of large coherent structures as the system evolves deeply into the negative temperature regime. Unfortunately, the PVM does not allow this scenario to occur: the reason lies in the fact that in the transition from the positive to the negative temperature regime, the energy of the system must increase but in this model the energy is a constant of motion.

CHAPTER 5. POINT VORTEX DYNAMICS IN THE SQUARE AND THE RECTANGLE

Therefore, without modelling additional physical processes that prevent the energy to change, the energy can not vary and the clustering can never occur, unless the vortices are initialised from the beginning to correspond to a negative temperature state. This problem can be resolved by adopting a proposal put forward in [107] by T. Simula *et al*, whereby an annihilation parameter δ is introduced to remove vortices with opposite sign in the dynamics. The physical motivation for introducing this annihilation mechanism is that in superfluids, vortices are topologically stable excitations that can annihilate with antivortices when they pass near one another. The annihilation of vortices with opposite sign reduces the number of vortices, it keeps the system neutral, and it increases the energy per vortex of the vortex gas. As a consequence, the system migrates into the negative temperature regime and the study of the transition between these two regimes can be performed. This mechanism permits the study of how clustering of vortices spontaneously occurs and it helps in understanding the role played by the geometry in the dynamics and in the formation of coherent structures. The starting point to describe the dynamics of point vortices is to derive the Hamiltonian for the considered geometry: as already discussed in §2.5 the derivation of the Hamiltonian \mathcal{H} in the presence of boundaries can be very complicated. This Chapter, is organised as follows. In §5.1, the dynamics of a neutral vortex gas and the transition between the positive and the negative temperature regime is investigated in two geometries: the square and the rectangle. The idea is to confirm the results given by the energy-entropy analysis in the square and the rectangle given in §4.4 and §4.5, respectively . In particular, it will be shown that in the square the vortices tend to gather together forming a monopole and in the rectangle they form a dipole. In §5.2 a qualitative analysis of the angular momentum in the square and the rectangle will be presented. In §5.3 will be presented a thorough comparison between results from point vortex dynamics and solutions of the BP equation. This will involve the construction of smooth vorticity fields from the discrete representation provided by point vortices. These results will bridge the gap between the statistical mechanical and dynamical approach to the problem. In §5.4 a quantitative analysis on the angular momentum will be given. Finally, in section §5.5 the analysis on the dynamics of point vortices in the square and the rectangle where annihilations on the boundaries can occur will be presented. This additional type of annihilation allows the system to become non neutral and hence, it will be shown that in both geometries the system naturally evolves towards a monopole configuration.

5.1 Point Vortex Dynamics

The aim of this section is to investigate the dynamics of a neutral system composed of point vortices in the square and in the rectangle with aspect ratio $\Lambda = L_x/L_y = 1.5$: the first case is studied in §5.1.1 while the second is investigated in §5.1.2. In these two geometries random initial configurations are generated and the long term dynamics is studied by integrating the equation of motion (2.79) where the Hamiltonian \mathcal{H} is given by Eq. (2.124) and adding an annihilation parameter between vortices with opposite circulation to the dynamics. Particular attention will be given to the structures in which the vortices can arrange themselves and if they coincide with the structures which have been presented in §4.4 and §4.5 based on the BP equation. If this is the case, then the behaviour of the vortices can be explained in terms of maximum entropy principle which produces different outcomes in the square and in the rectangle as already discussed in the previous Chapter. Analysis on the results will be performed by invoking ergodicity thereby allowing ensemble averages to be replaced by time averages. Hence, a time average of point vortex positions is then generated from intervals of the same length during the dynamical runs for both geometries. An example on how this time averaging allows more well desired structures to be calculated is illustrated in Fig. (5.1). This shows how superpositions of point vortices from two instantaneous, not necessary consecutive, configurations leads to more well desired clusters. This approach can

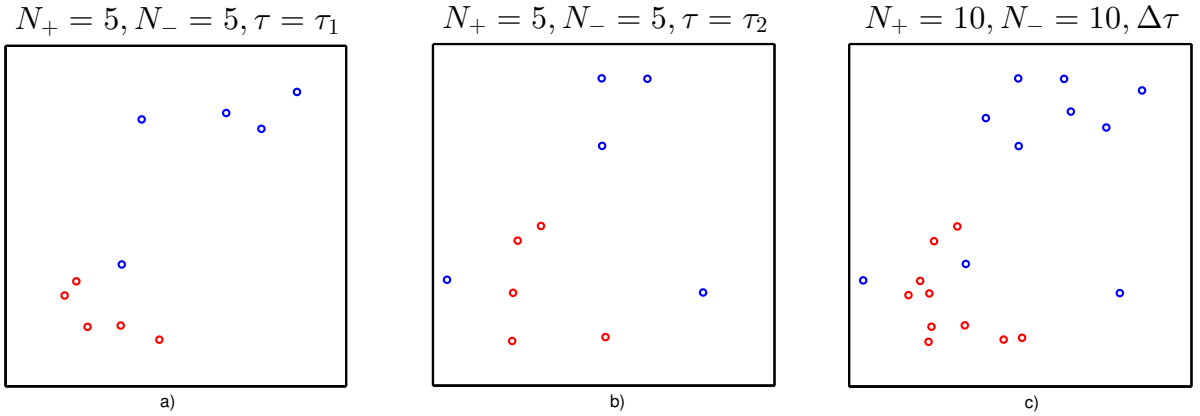


Figure 5.1: Figures a) and b) show two configurations at τ_1 and τ_2 respectively and the resulting ensemble is given by Fig. c) on the right: the red and blue circles represent the vortices with positive and negative circulation respectively.

be easily extended to an arbitrary number of configurations, giving the possibility of creating ensembles with a large number of point vortices. The method which will be adopted to study the vortex dynamics in a statistical sense, is to generate ensembles

from the dynamics and to evaluate their time-averaged streamfunction ψ .

5.1.1 Dynamics in the Square

In this subsection the dynamics of a neutral vortex gas in the square with sides $L_x = L_y = 2$ is investigated. In order to do so, the equations of motion (2.79) where the Hamiltonian is given by Eq. (2.124) for a system composed of $N^+ = 60$ and $N^- = 60$ vortices with circulation $\gamma_\pm = \pm 1$ are numerically solved with the built-in ODE45 MATLAB function [105] based on an adaptive 4th-5th order Runge-Kutta scheme with a maximum time step $\tau = 0.005$. An annihilation parameter $\delta = 0.01$ is added to the dynamics: when the distance between vortices of opposite circulation becomes less than δ , a pair will be removed from the system. The statistical weight analysis performed in §3.2.1 helps in generating an initial condition whose energy lies in the positive temperature regime. Figure (5.2) shows the statistical weights in the square for neutral configurations of point vortices composed by a different number of vortices N indicated in the legend. The statistical weights immediately identify the regions for which the temperature of the vortex gas is positive or negative, depending on the slope of the tangent to the graphs (see Eq. (3.5)).

The initial configuration has been randomly generated and its energy is evaluated by using Eq. (2.124) and it is given by $\mathcal{H}_{in} = -0.13$: this value corresponds to an energy of a vortex gas with a positive temperature. The energy of the initial configuration is represented by the vertical dotted line in Fig. (5.2). The inset figure shows the positions of the initial configuration with vortices with positive circulation (red circles) and negative circulation (blue circles) and its corresponding streamfunction normalised by the number of vortices ψ/N . By looking at the contour plot the absence of clusters of like signed vortices becomes evident and it is the signature of a perfectly mixed configuration, typical of a system in a positive temperature regime. The streamfunction ψ has been generated from knowledge of the instantaneous positions of the vortices and by using Eq. (2.128). The configuration has been generated by imposing two constraints $\delta_V = 0.08$ and $\delta_B = 0.12$ on the positions of vortices. The reason for the first constraint lies in the fact that if vortices are too close at the beginning of the simulation, a large number of pairs will be removed due to the annihilation parameter δ . By imposing this constraint this possibility is avoided and allows the system to smoothly migrate into the negative temperature regime due to the chaotic vortex dynamics. The second constraint δ_B prevents the initial vortex positions from being unrealistically close to the boundaries. This constraints help in generating realistic initial configurations for the study of the dynamics of a vortex gas in two-dimensional Bose-Einstein condensates

[103] where annihilation on the boundaries can also occur. This problem will be investigated in more details in Chatper §6. By solving the equation of motions (2.79) together with the annihilation parameter δ imposed between pairs with opposite circulation, the total number of vortices in the system is gradually lost whilst remaining neutral. However, the energy per vortex is seen to increase. Figure (5.3) shows the number of vortices as a function of time τ during the dynamics. It can be seen that the number

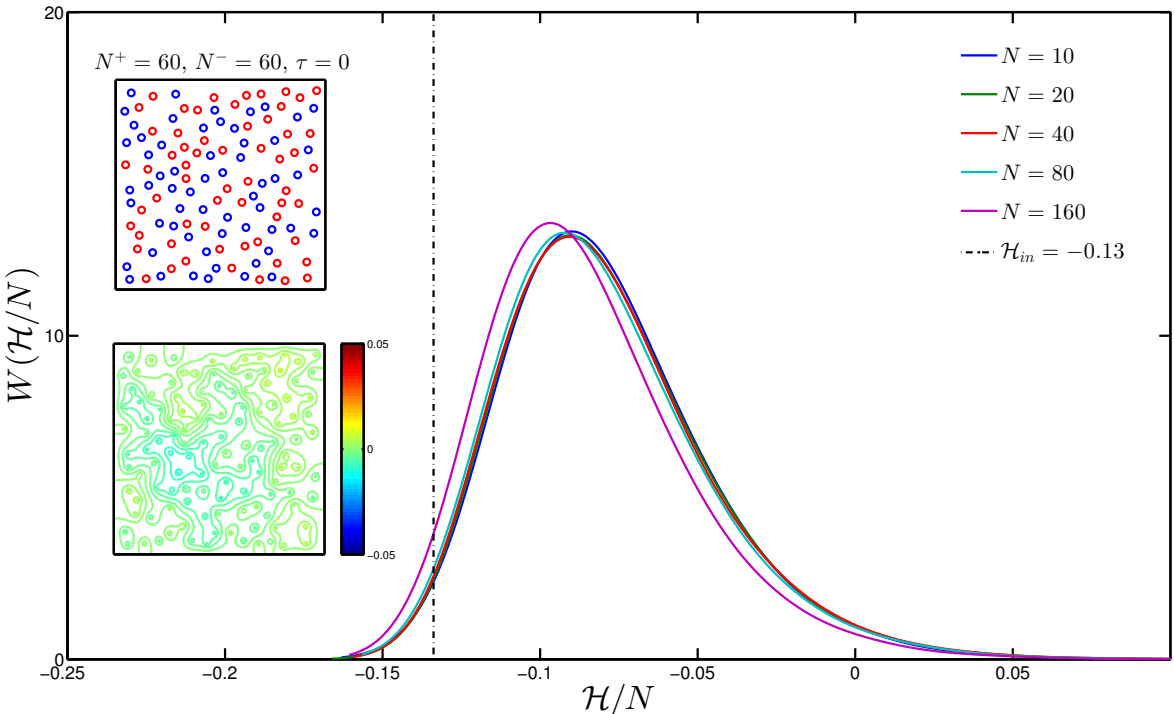


Figure 5.2: Statistical weights in the square for neutral systems of point vortices composed of a different total number of vortices N : the vertical dotted line represents the energy of the initial configuration. On the left the configuration (upper figure) in which the red and the blue circles represent the vortices with positive and negative circulation respectively. The figure below is the corresponding contour plot for the streamfunction per vortex ψ/N . All the random configurations have been generated by imposing a minimum distance $\delta_V = 0.08$ between each vortex and a minimum distance $\delta_B = 0.12$ between the vortices and the boundaries.

of vortices reduces from $N = 120$ to $N = 42$ in the total running time ($\tau = 25$ which corresponds to 50,000 iterations) and by $\tau \sim 5$ the initial number of vortices is halved. In addition, after $\tau = 13.2$ the process of annihilation slows down dramatically and it can be inferred that the system is reaching a *quasi-equilibrium* regime.

During the entire dynamics short time intervals have been considered and in these windows different time-averaged streamfunctions per vortex ψ/N have been evaluated: examples of the streamfunction over three time intervals are shown in Fig. (5.3) (in-

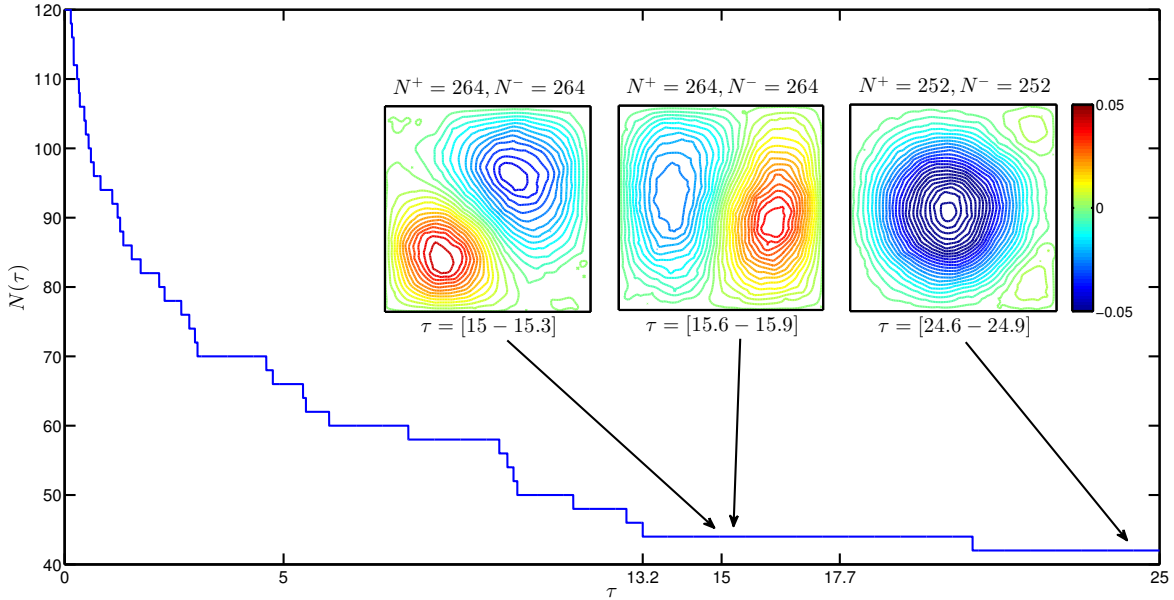


Figure 5.3: Number of vortices as a function of time in the square. The contour plots represent the streamfunction per vortex ψ/N for three different time intervals during the dynamics. Indicated below each inset is the interval used to generate the averaged streamfunctions while the number of positive and negative vortices used in the averaging is indicated above each inset.

set figures). This shows the presence of different structures at different stages in the dynamics which correspond to the same structures predicted in §4.2: the dipole, the diagonal dipole and the monopole. This idea of generating time-averaged streamfunctions over certain intervals can be performed systematically. Starting from $\tau = 13.2$, when annihilations almost stop, the averaged streamfunctions are evaluated over time intervals of $\Delta\tau = 0.3$ in duration. The results of this analysis are presented in Fig. (5.4) where each figure represents the averaged streamfunction per vortex ψ/N . The colors refer to the same colorbar of Fig. (5.3) and Fig. (5.2). Since the number of vortices does not change in time each averaged streamfunction was evaluated from a total of $N=528$ vortex positions.

By looking at Fig. (5.4), it is possible to identify time intervals in which the vortices form a dipole ($\tau = [15.6 - 15.9]$ for example), diagonal dipole ($\tau = [16.8 - 17.1]$ for example), and monopole ($\tau = [17.7 - 18]$ for example). These configurations correspond to the flows studied in §4 and classified in terms of their energy and entropy in §4.4. Figure (5.4) shows also another interesting fact: although the entropy of the dipole is lower than the entropy of the diagonal dipole (Fig. (4.6)) the system bounces between these two configurations. For example the system can be found in the diagonal dipole configuration in the interval $\Delta\tau = [14.1 - 14.4]$, then in a lower entropy configuration

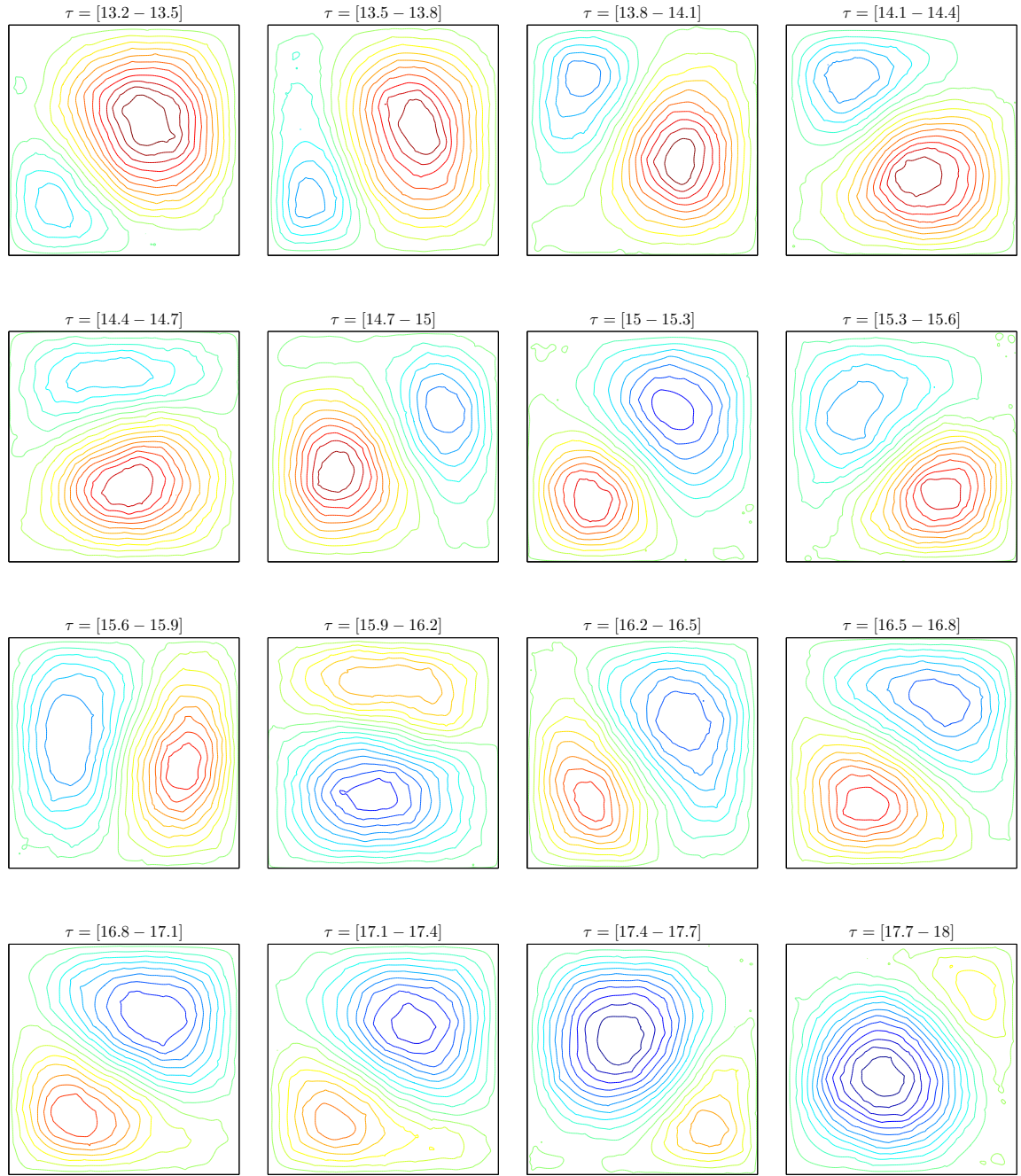


Figure 5.4: Contour plots of the streamfunction per vortex ψ/N evaluated over different time intervals in the square: the total number of vortices used in the averaging in each case and the interval from which the plots have been evaluated are indicated above each figure. All plots were generated from a total of $N^+ = N^- = 264$ vortices. The colors of the contour plots refer to the same colorbar as in Fig. (5.3) and Fig. (5.2).

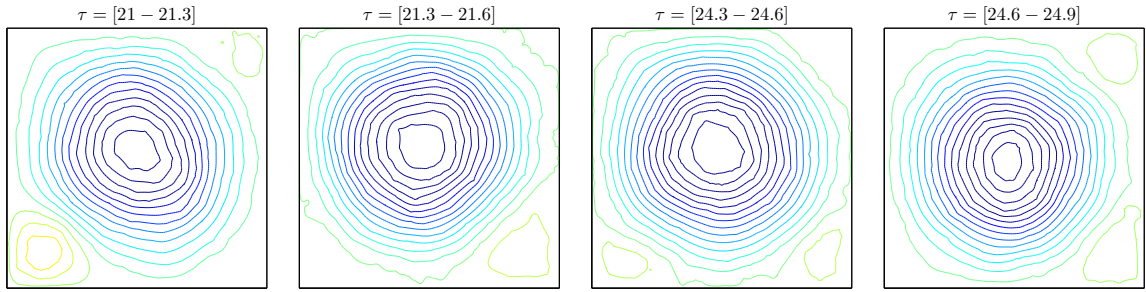


Figure 5.5: Contour plots of the streamfunction per vortex ψ/N evaluated over different time intervals in last part of the dynamics in the square: the total number of vortices used in the averaging in each case and the interval from which the plots have been evaluated are indicated above each figure. All plots were generated from a total of $N^+ = N^- = 252$ vortices. The colors of the contour plots refer to the same colorbar as in Fig. (5.3) and Fig. (5.2).

in the interval $\Delta\tau = [14.4 – 14.7]$ and then again in a higher entropy configuration in the interval $\Delta\tau = [15 – 15.3]$ and so on. In other words, the system is free to explore all the possible configurations in this particular stage of the dynamics. However, among all the possible configurations, the monopole has the highest entropy in the square and it is achieved for the very first time at $\tau = 17.7$ (see last contour plot of Fig. (5.4)): the negative charges occupy the centre of the domain and the positive charges occupy the four corners. This configuration, which first appears at $\tau = 17.7$, lasts until the end of the simulation at $\tau = 25$. Figure (5.5) provides four contour plots of four different averaged streamfunctions evaluated over different time intervals (indicated above each figure) during the latter stages of the simulation. It has to be remarked that during the whole dynamics, it has not been possible to find any other structure (for example the quadrupole). According to the linear study performed in §4.2, the corresponding streamfunctions have many zeros and a lower entropy and therefore they are less favourable. This first qualitative analysis confirms the predictions of the mean-field theory. When the system is not deeply into the negative temperature regime, it explores all possible microstates which can be local maxima for the entropy. However, the long term dynamics is governed by the maximum entropy principle which causes the vortices of the same charge to gather together and to occupy the centre of the square while the charges with opposite circulation tend to occupy the four corners.

5.1.2 Dynamics in the Rectangle

The squared domain is now stretched into a rectangle with sides $L_x = 2\sqrt{\Lambda}$ and $L_y = 2/\sqrt{\Lambda}$ where $\Lambda = L_x/L_y = 1.5$ is the aspect ratio. This choice modifies the shape of the domain but it preserves its volume. Since the phase space of a two dimensional vortex gas coincides with the physical space, the phase space of the rectangle is equal to the phase space of the square. The initial configuration has been randomly generated

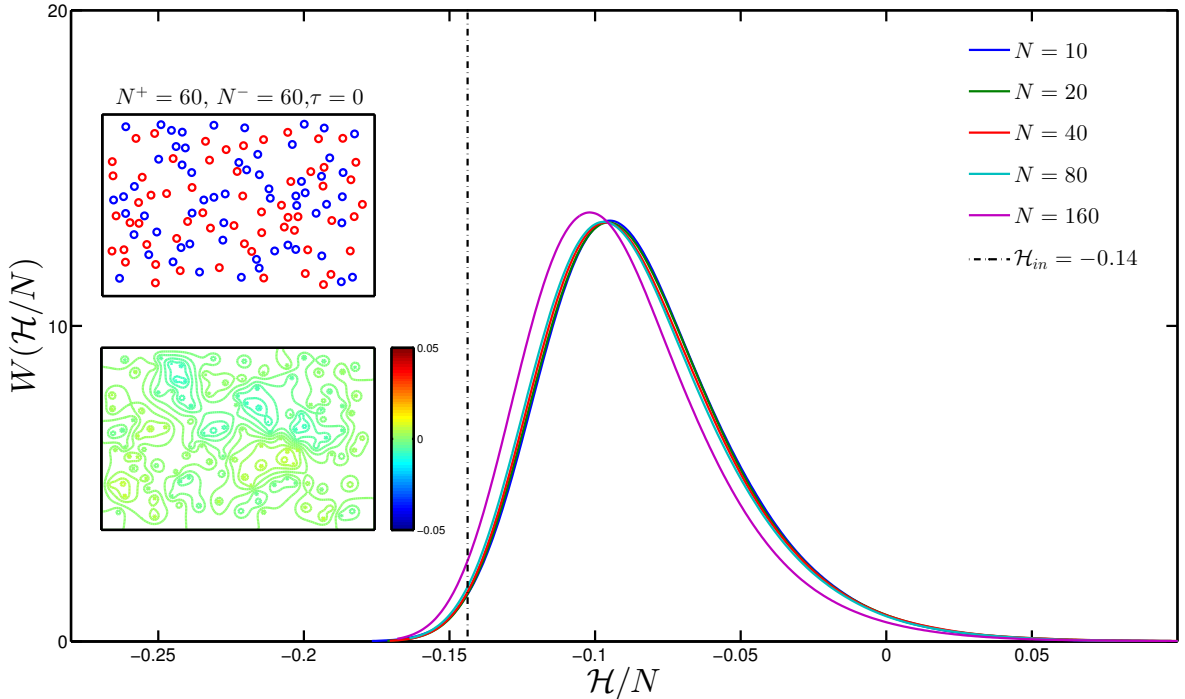


Figure 5.6: Statistical weights in the rectangle for neutral systems composed of different number of vortices N : the vertical dotted line represents the energy of the initial configuration. On the left the configuration (upper figure) in which the red and the blue circles represent the positive and negative vortices. The figure below is the corresponding contour plot for the streamfunction per vortex ψ/N . All the random configurations have been generated by imposing a minimum distance $\delta_V = 0.08$ between each vortex and a minimum distance $\delta_B = 0.12$ between the vortices and the boundaries.

and its energy is evaluated by using (2.124) and it is given by $\mathcal{H}_{in} = -0.14$: this value corresponds to an energy of a vortex gas with a positive temperature. The energy of the initial configuration is represented by the vertical dotted line in Fig. (5.6). The inset figures show the positions of the initial configuration with vortices with positive circulation (red circles) and negative circulation (blue circles) and its corresponding instantaneous streamfunction per number of vortices ψ/N . As before the contour plot demonstrates the lack of clustering of like signed vortices in the initial

condition which is the signature of a perfect mixed configuration, typical of a system in a positive temperature regime. Once the dynamics starts, the system is smoothly driven into the negative temperature regime due to annihilations. The number of vortices as a function of time is presented in Fig. (5.7). The decaying rate of the vortices is compatible with the result for the square. Figure (5.7) also shows four

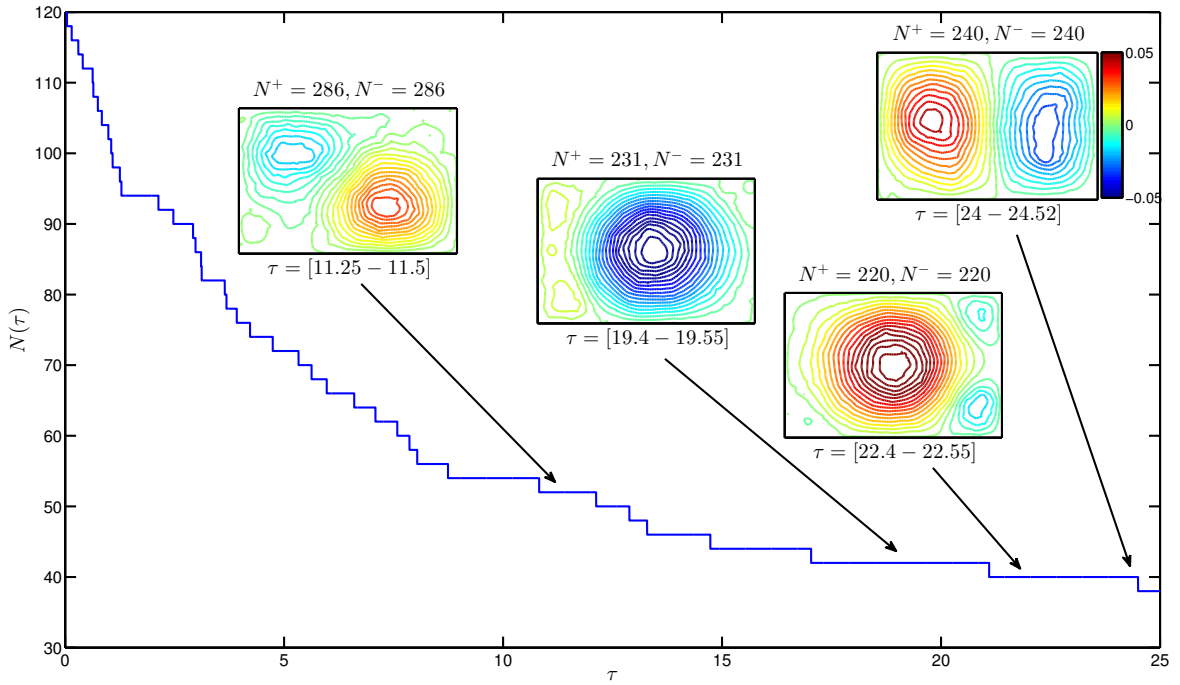


Figure 5.7: Number of vortices as a function of time in the rectangle. The contour plots represent the streamfunction per vortex ψ/N for four different time intervals during the dynamics. Indicated below each inset is the interval used to generate the averaged streamfunctions while the number of positive and negative vortices used in the averaging is indicated above each inset.

contour plots for the streamfunction per vortex ψ/N of four averaged streamfunctions generated over different time intervals during the dynamics: in particular intervals in which the system is in the diagonal dipole, monopole and dipole configuration have been found. The diagonal dipole has been found in a single interval $\Delta\tau = 0.25$ and it has not been possible to find any other interval in which the system is in the same configuration. This is consistent with the fact that in the rectangle it was not possible to find diagonal dipole solutions to the BP equation as shown in Fig. (4.5). The other inset figures show a dipole and two monopole configurations where negative vortices occupy the centre of the domain (interval $\tau = [19.4 - 19.55]$) or where positive vortices are in the centre of the rectangle (interval $\tau = [22.4 - 22.55]$).

Starting from the beginning of the simulation, averaged streamfunctions constructed

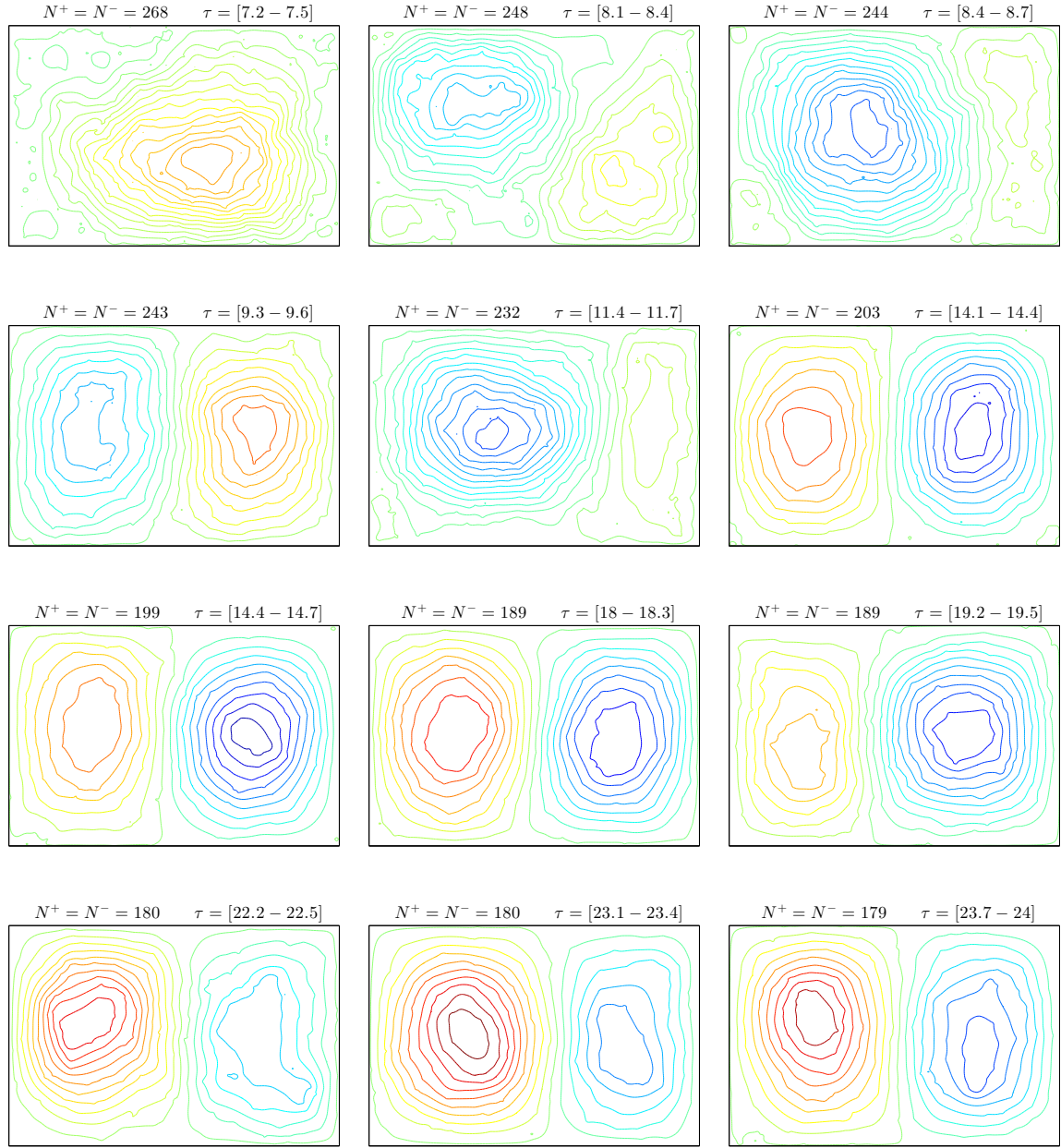


Figure 5.8: Contour plots of the streamfunction per vortex ψ/N evaluated over different time intervals in the rectangle: the total number of vortices used in the averaging in each case and the interval from which the plots have been evaluated are indicated above each figure. The colors of the contour plots refer to the same colorbar as in Fig. (5.3) and Fig. (5.2).

CHAPTER 5. POINT VORTEX DYNAMICS IN THE SQUARE AND THE RECTANGLE

over time intervals $\Delta\tau = 0.3$ from a different total number of vortices have been generated during the dynamics. Figure (5.8) shows contour plots of these streamfunctions over the duration of the simulation. Above each figure is indicated the window in which the plot has been generated. Since the annihilations do not stop during the dynamics, different number of vortices have been used within each time interval which are shown above each contour plot. In this set of possible configurations the monopole does not seem to occur so often and, if it occurs, it does not last for long time intervals. The reason is due to the fact that in the considered rectangle, the value of the aspect ratio is much greater than the critical value $\Lambda_C = 1.122$ [71] and therefore, the monopole is strongly suppressed. In the early stage of the dynamics the system can be found in a monopole configuration which is a local maximum for the entropy. However, when the point vortices arrange themselves in a dipole configuration, the global maximum for the entropy is achieved and therefore the dipole configuration persists until the end of the simulation at $\tau = 25$, as shown in Fig. (5.8). Hence, the predictions of the theory given by the BP equation have also been confirmed for the rectangle.

The conclusions at this stage are that the predictions of the mean-field theory are confirmed for both the considered geometries. When the system of point vortices is driven into the negative temperature regime there are two possible outcomes, depending on the considered geometry: in the case of the square, the vortices tend to form a monopole structure while for the rectangular domain the dipole is the most probable configuration. As already pointed out in §4.7 the streamfunction ψ related to a possible configuration of point vortices can be either $\langle \psi \rangle \neq 0$ or $\langle \psi \rangle = 0$, where $\langle \dots \rangle$ denotes the spatial average. Since the angular momentum L of the system is given by Eq. (4.76), by changing the geometry from a rectangle to a square, the system spontaneously acquires a non zero value for the angular momentum L . This concludes the analysis of the dynamics of a neutral system composed of point vortices in the square and the rectangle. During their dynamics the point vortices are free to explore all the possible configurations subjects to the instantaneous energy constraint imposed by the Hamiltonian of the system. Some configurations are local maxima for the entropy while others are global maxima for the entropy. It has been shown that the long time dynamics is such that the configurations which maximise the entropy are always achieved. In the case of the square this configuration is given by the monopole and in the case of the rectangle it is given by the dipole. In the next section the qualitative analysis of the angular momentum in both geometries is presented.

5.2 Angular Momentum

In §2.5.3 it has been shown that the angular momentum L evaluated with respect to the point (x_0, y_0) of a distribution of N point vortices each with circulation γ_i located at (x_i, y_i) , $i = 1, \dots, N$ in a bounded domain \mathcal{D} is given by the sum of a volume term, indicated with L_V , given by

$$L_V = -\frac{\rho}{2} \sum_{i=1}^N \gamma_i [(x_i - x_0)^2 + (y_i - y_0)^2], \quad (5.1)$$

and a boundary term L_B , given by

$$L_B = -\frac{\rho}{2} \oint_{\partial\mathcal{D}} [(x - x_0)^2 + (y - y_0)^2] (-v, u) \cdot d\mathbf{n}, \quad (5.2)$$

where $d\mathbf{n}$ is the normal vector to the boundary $\partial\mathcal{D}$. The volume term L_V depends exclusively on the positions of the vortices and their circulation, while the boundary term L_B requires the knowledge of the value of the components of the velocity Eq. (2.135) on the boundary $\partial\mathcal{D}$. However, the boundary term L_B can be evaluated indirectly since the total angular momentum is related to the streamfunction of the distribution of vortices, via

$$L = 2\rho \int_{\mathcal{D}} \psi dx dy, \quad (5.3)$$

and therefore,

$$L_B = 2\mathcal{D}\rho\langle\psi\rangle - L_V, \quad (5.4)$$

where $\langle \dots \rangle$ represents the spatial average and $\rho = 1$ is taken as the superfluid density.

Hereafter, the point (x_0, y_0) is chosen to be the center of the domain for the square and the rectangle. Before describing the trend of the angular momentum in the square and in the rectangle, it is important to note that in the case of a perfectly symmetric configuration the total angular momentum is identically zero. This is immediate by looking at Eq. (5.3). This fact can be used to describe and characterise the spatial configuration of a distribution of point vortices by looking at the graph of the total angular momentum L as a function of time. If it presents a large number of zeros then the system is passing through symmetric configurations which can be either a dipole, a diagonal dipole, a quadrupole, etc... On the other hand, the lack of zeros in the values of L reflects an asymmetric configurations such as the monopole. In the next two subsections, the qualitative analysis of the angular momentum in the square and in the rectangle will be presented.

5.2.1 Angular Momentum in the Square

By considering the positions of the point vortices during their dynamics in the square, it is possible to evaluate the angular momentum as a function of time during the whole dynamics. Figure (5.9) shows the total angular momentum L , the volume term L_V and the boundary term L_B given by Eqs. (5.3), (5.1), and (5.4), respectively as a function of time for the dynamics in the square. Aside from the initial time, the graph

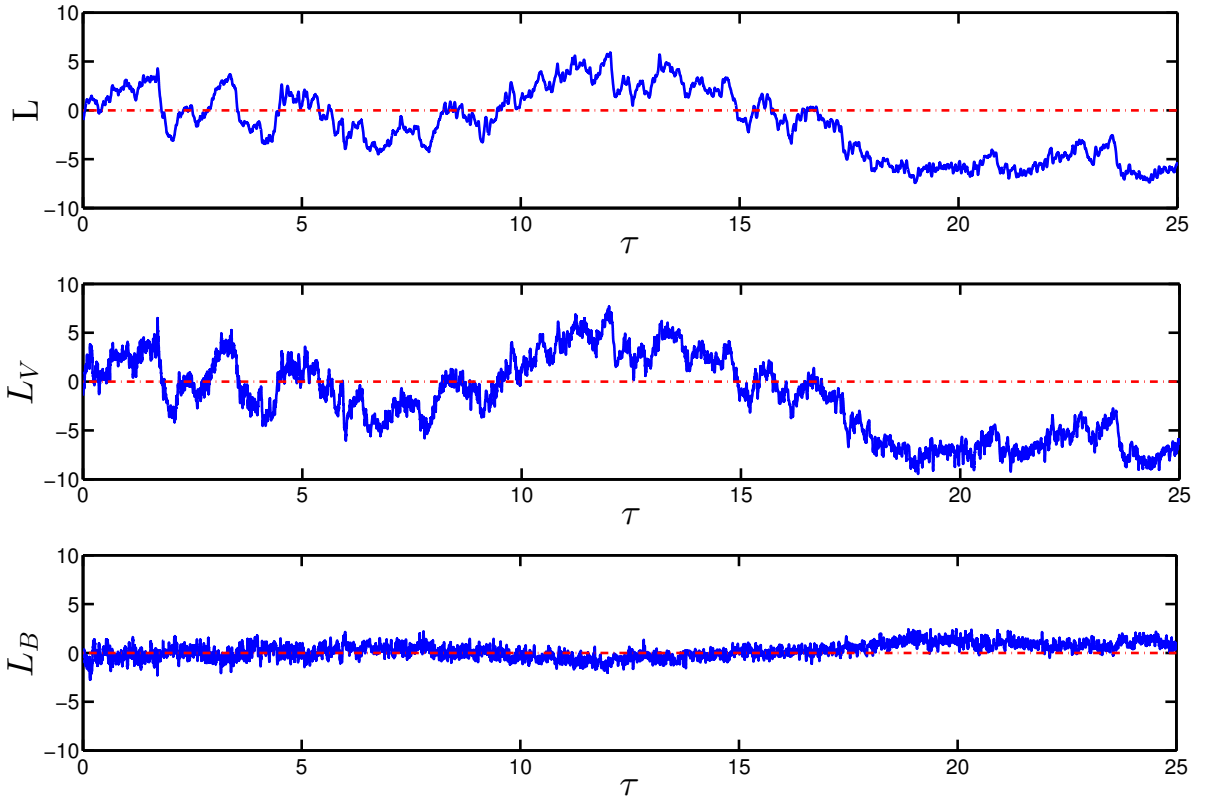


Figure 5.9: From the top to the bottom: total angular momentum L , volume term L_V and boundary term L_B evaluated in the square during the dynamics. The red dotted line represents the zero.

of the angular momentum L (upper figure) in Fig. (5.9) clearly shows very few zeros: this is a signature of an asymmetric configuration such as a monopole. Fig. (5.10) shows L as a function of time and also four contour plots for the averaged streamfunction over four different time intervals generated during the dynamics.

The contour plots have been generated in the interval indicated above each figure. The presence of different structures during the dynamics has been widely described in §5.1.1 and Fig. (5.10) shows how these different configurations are associated with different values of L . When $L = 0$ then $\langle \psi \rangle = 0$ and $L \neq 0$ implies $\langle \psi \rangle \neq 0$ where

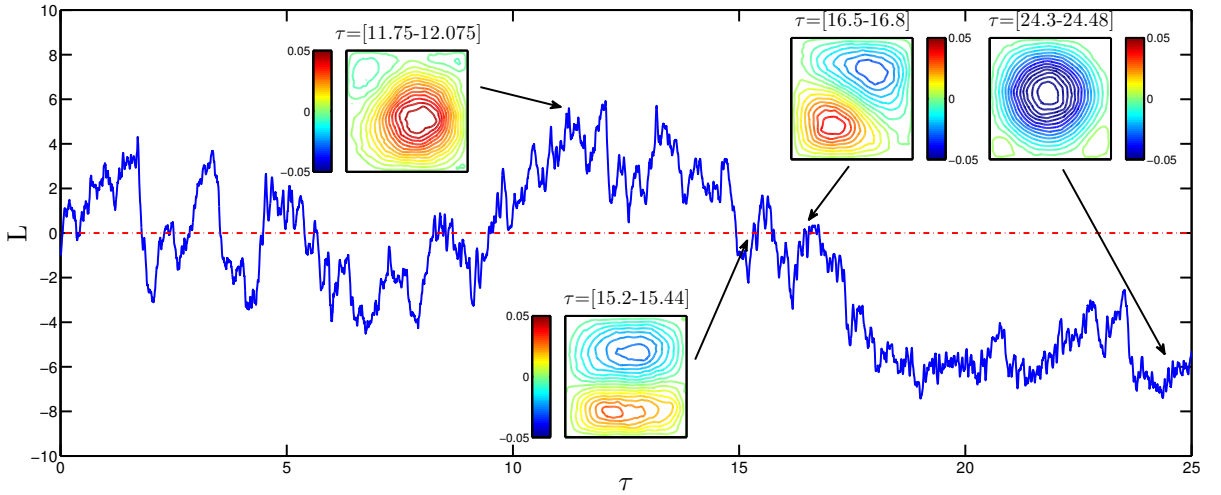


Figure 5.10: Graph of the total angular momentum L as a function of time in the square: the inset figures are the streamfunction per vortex ψ/N for different time intervals generated during the dynamics. The interval from which the plots have been evaluated are indicated above each figure. The red dotted line represents the zero.

$\langle \dots \rangle$ denotes the usual spatial average. It should be remarked that some of these configurations can last for only short time intervals.

5.2.2 Angular Momentum in the Rectangle

By changing the aspect ratio of the domain to $\Lambda = 1.5$, the maximum entropy state is achieved by a symmetric configuration and hence, the trend of the angular momentum L as a function of time is expected to coincide with zero. In the case of the rectangle, the graph of the the total angular momentum L , the volume term L_V and the boundary term L_B given by Eqs. (5.3), (5.1), and (5.4), respectively as a function of time are shown in Fig. (5.11). The trend of the total angular momentum during the dynamics of the point vortices in the rectangle reveals the expected trend. The behaviour is clearly completely different from the previous case: here the graph oscillates throughout the simulation from positive to negative values of L but never deviates from extended periods from zero. Figure (5.12) shows the plot of the total angular momentum L in the rectangle with three example of averaged streamfunctions per vortex ψ/N for different time intervals. Two of them show configurations close to a monopole although they are less well defined and they do not persist for very long. The other one is a dipolar configuration. The monopoles are present in intervals where the angular momentum has a peak while the dipoles can be found in intervals where the values of L is close to zero.

The analysis of the angular momentum clearly shows two different behaviours whether the square or the rectangle is considered. In the first case, the system naturally evolves to a configuration with a non zero angular momentum and a consequent significant deviation from zero in the graph of L , while in the rectangle the system evolves towards a dipolar configuration which can be revealed by the extended deviations during which L is approximately zero

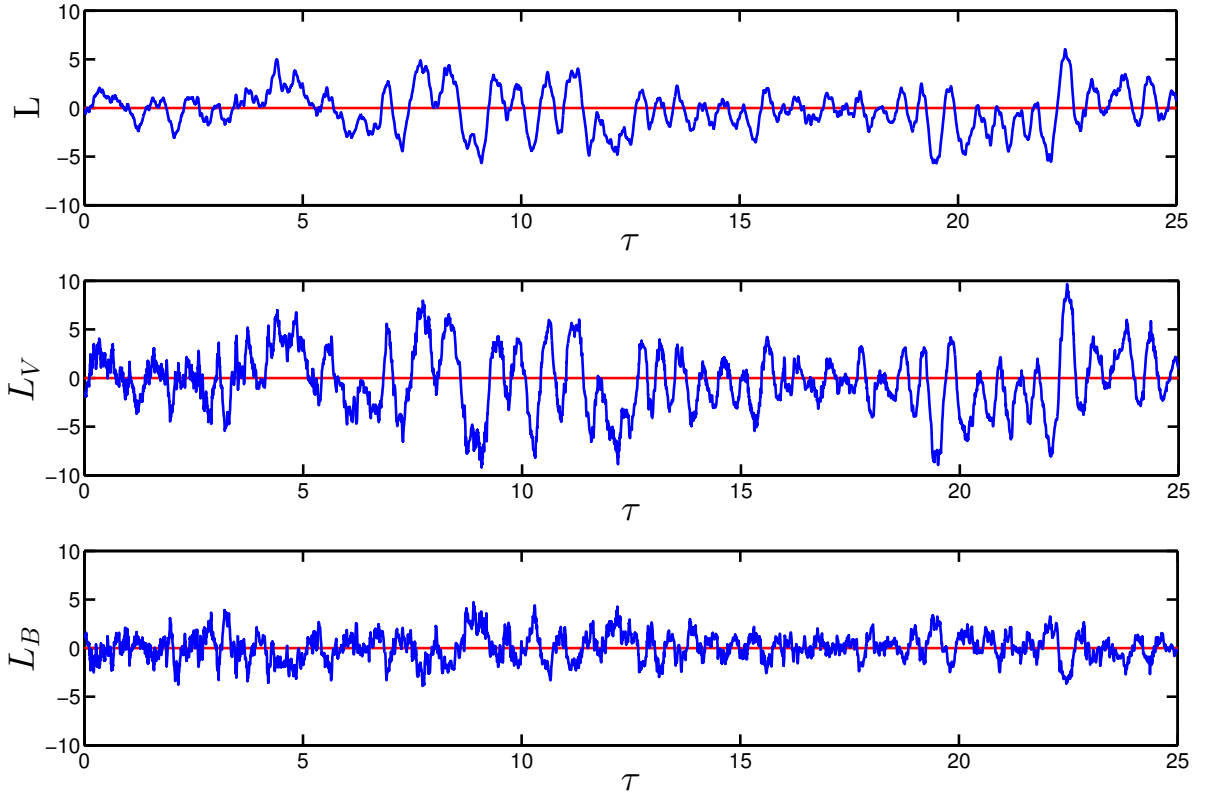


Figure 5.11: From the top to the bottom: total angular momentum L , volume term L_V and boundary term L_B in the rectangle. The red dotted line represents the zero.

5.3 Entropy analysis for the point vortex dynamics

In the previous two sections a qualitative analysis to the dynamics of point vortices and to the trend of the angular momentum in the square and the rectangle was presented. Moreover, by using a time sequence of vortex positions within particular intervals, the system was found in configurations where vortices arrange themselves into a dipole, diagonal dipole or monopole in the square and in a monopole or dipole in the rectangle. The aim of this section is to evaluate the non-dimensional energy \hat{E} given

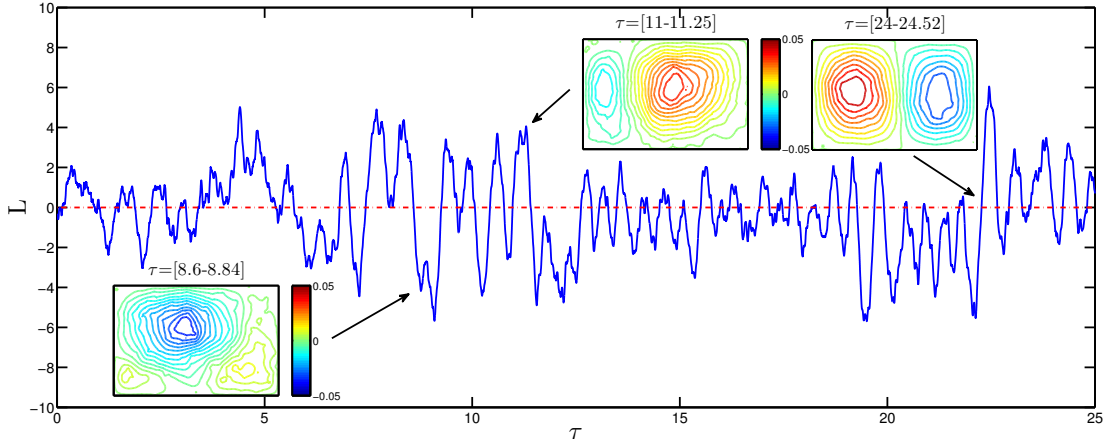


Figure 5.12: Graph of the total angular momentum L as a function of time in the rectangle: the inset figures are the streamfunction per vortex ψ/N for different time intervals generated during the dynamics. The interval from which the plots have been evaluated are indicated above each figure. The red dotted line represents the zero.

by Eq. (4.14) and the non-dimensional entropy \hat{S} given by Eq. (4.16) for these configurations identified from the dynamical simulations. In other words, the main objective of this section is to classify these structures based on their non-dimensional energy and entropy as was previously done in §4.4 and §4.5 for the solutions of the BP equation. The values of \hat{E} and \hat{S} computed from the dynamical run will also be compared with the values already shown in Figs. (4.6) and (4.9) obtained from the solutions of the BP equation.

In order to perform this analysis it is necessary to reconstruct, starting from the positions of the vortices, the streamfunction ψ and the positive and the negative vorticity fields ω^\pm required to evaluate the entropy of each configuration. This section is divided into four subsections which will culminate in the comparison of the entropies of the solutions of the BP equation and the dynamical simulations of point vortices. This section is organised as follows. In subsection §5.3.1 the problem of generating the ensembles for the dipole, the diagonal dipole and the monopole in the square and for the monopole and the dipole in the rectangle is discussed. In the subsection §5.3.2 a mathematical method which allows for the construction of the smooth vorticity fields ω_+ and ω_- , corresponding to the vorticity fields generated by the positive and negative vortices respectively, starting from the positions of the point vortices is presented . Finally in subsection §5.3.4 the comparison between the non-dimensional entropy computed from the dynamical simulations of point vortices in the square and the rectangle and the solutions of the BP equation will be presented.

5.3.1 Generating the ensembles

Ensembles in the square

Since the point vortices spend most of the time in the monopole configuration during their dynamics, it is straightforward to identify a long enough time interval from which an ensemble for the monopole in the square can be reconstructed based on the assumption of ergodicity. The situation is different for the dipole and diagonal dipole since they emerge over shorter time intervals. This can be seen by looking at the contour plots presented in Fig. (5.4) which show fewer configurations in which the system can be found in the dipole or diagonal dipole state. One of the main challenges associated with generating an ensemble is to extract sufficiently many positions related to the same macroscopic configuration during the dynamics. For example, the configurations in the intervals $\tau = [15.6 - 15.9]$ and $\tau = [15.9 - 16.2]$ (see Fig. (5.4)) are both in the dipole configuration but the first one has a vertical orientation and the second is horizontally orientated. Although the two ensembles represent a dipole, it is not possible to consider all these configurations to generate an ensemble in which the dipole is vertically oriented. However, this problem can be overcome by noticing that the system is symmetric under rotations: the configurations in the interval $\tau = [15.9 - 16.2]$ can be rotated by 90° clockwise and all the configurations in the whole interval $\tau = [15.6 - 16.2]$ can be used to generate an ensemble for a vertically orientated dipole. Therefore, by appropriately rotating the positions of the vortices extracted from the dynamics, a large number of configurations where the system is in a dipole configuration with the negative charges on the left and the positive charges on the right can be generated.

In the following a vertically orientated dipole will be generated and the time intervals which have been used to generate it correspond to $\tau = [13.2 - 14.1]$, $\tau = [14.1 - 14.7]^R$, $\tau = [14.7 - 15.6]^R$, $\tau = [15.6 - 15.9]$, $\tau = [15.9 - 16.2]^R$ and $\tau = [17.1 - 17.7]^R$ where the superscript R means that the vortex positions have been rotated. The number of configurations in which the system can be found in a diagonal dipole and monopole are enough to generate an ensemble with a large number of vortices. In particular for the diagonal dipole, the configurations are those in the intervals $\tau = [14.8 - 15.3]$ and $\tau = [16.2 - 17.4]$ (see Fig. (5.4)). Finally, for the monopole, the positions are taken from the final stages of the dynamics in the interval $\tau = [20 - 25]$. Figure (5.13) shows the superposition of all vortex positions within each ensemble corresponding to dipole (left), the diagonal dipole (centre) and the monopole (right) in the square. The ensemble for the dipole, the diagonal dipole and the monopole contains $N = 8580$, $N = 8360$ and $N = 8502$ vortices, respectively.

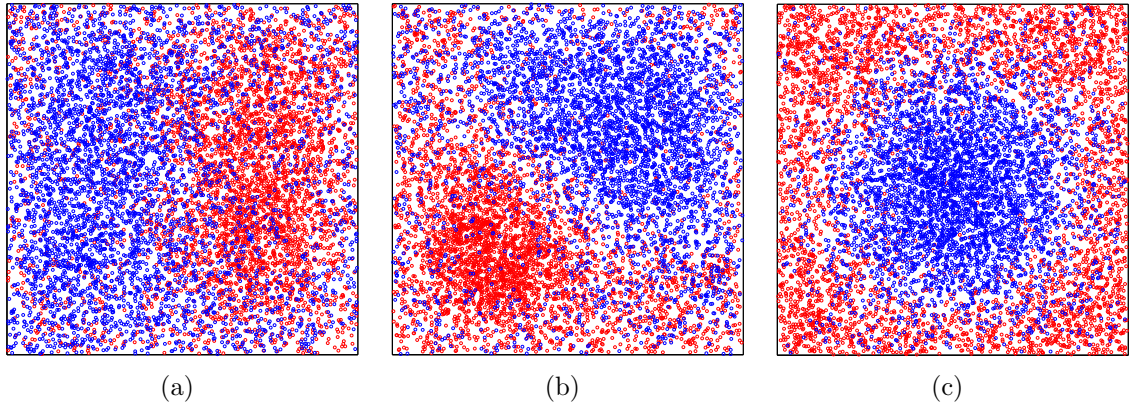


Figure 5.13: Ensembles for the dipole (a), diagonal dipole (b) and monopole (c) in the square: the number of vortices in each ensemble is $N = 8580$, $N = 8360$ and $N = 8502$ respectively. The red and the blue dots represent the vortices with positive and negative circulation respectively.

Before proceeding, it is important to establish if the ensembles which have been generated can be used and studied in a statistical sense. In particular, it is important that the generated ensembles do not contain strong local spatial correlations: an example is given by Fig. (5.14(a)) and Fig. (5.14(b)). The frame on the left is taken at $\tau_1 = 20$, the frame in the centre after 10 iterations at $\tau_2 = 20.005$ and the resulting ensemble is given on the right. In the first two frames the position of a positive vortex is indicated with a yellow circle: the distance travelled by the vortex is not enough to avoid small scale correlations in the resulting vorticity field ω^- generated by considering the resulting ensemble (figure on the left). The same problem can also be noticed for the negative charges indicated by the orange circles. These correlations are not seen in Fig. (5.14(b)) where the time interval between the two configuration is $\Delta\tau = 0.025$ which corresponds to 50 iterations. In this case the positive and negative vortices are well separated and from the ensemble it is not possible to deduct any correlation in the vortex positions.

These considerations lead to the conclusion that for an ensemble generated over smaller time intervals, the individual instantaneous vortex configurations can be more strongly correlated and the problem discussed above can become more pronounced. Therefore, the ensemble corresponding to the monopole in the square or the ensemble corresponding to the dipole in the rectangle which are generated from a large number of time intervals are less susceptible to this problem.

In order to understand the problem, imagine that the available set of data consists on N_C configurations during the dynamics at time $\tau_1, \tau_2, \dots, \tau_{N_C}$ and the number of

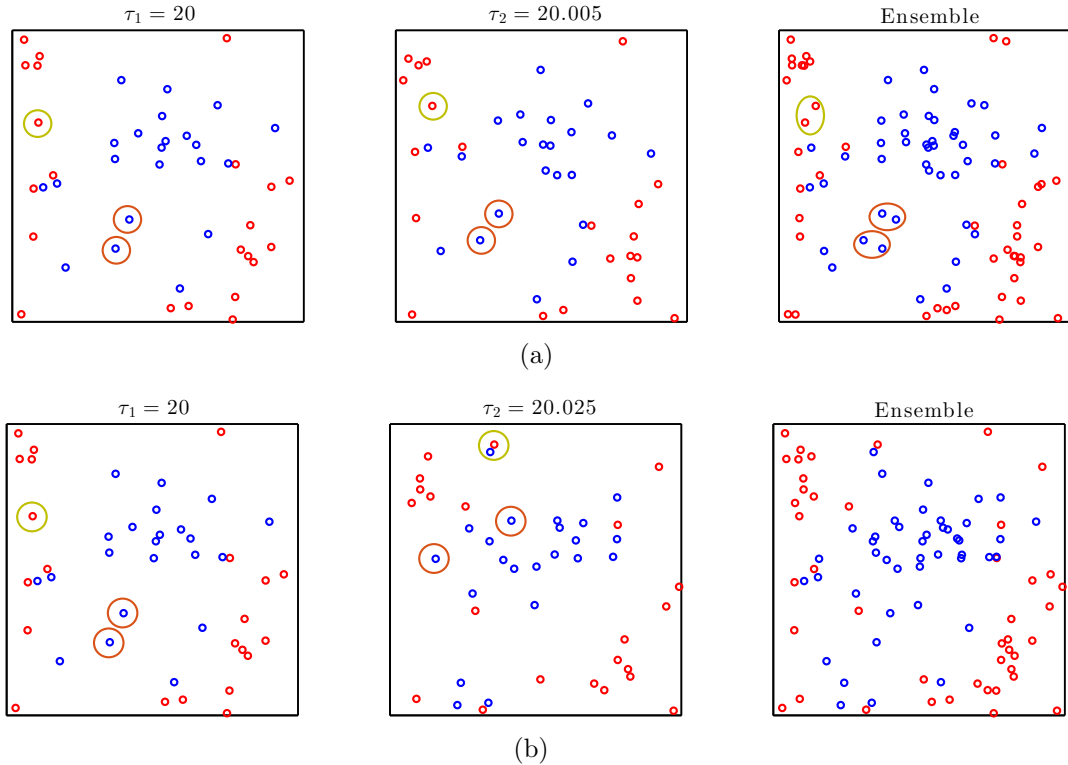


Figure 5.14: On the left, positions of the vortices at initial time $\tau = 20$: the yellow and orange circles represent a positive and two negative vortices respectively. In the centre, the position of the vortices after $\Delta\tau = 0.005$ (upper figure) and after $\Delta\tau = 0.025$ (lower figure). On the right, the resulting ensembles: in the lower image the separation between the vortices at time τ_1 and τ_2 is enough to avoid spatial correlations which will affect the resulting vorticity fields. In the upper image the separation of the vortices is not enough to avoid any spatial correlation.

CHAPTER 5. POINT VORTEX DYNAMICS IN THE SQUARE AND THE RECTANGLE

vortices at each time is $N_v(\tau_i)$. Hence, it is possible to generate an ensemble with $N = \sum_i^{N_C} N_v(\tau_i)$ vortices. However, by considering all the positions, the vortices will not have travelled enough in order to guarantee a good separation between the positions at any time τ_i and τ_{i+1} (see Fig. (5.14)). This raises the following questions: "what is the mean separation of all vortices in the ensembles given in Fig. (5.13)?", "Is this distance enough to ensure the absence of spatial correlations in the ensemble?". In the case of the diagonal dipole in the square, the set of data consists of $N_C = 3402$ configurations and in order to have an ensemble with $N \sim 8000$ vortices a maximum time interval of $\Delta\tau = 0.009$ is required. By considering two configurations separated by this interval, it is possible to consider the separation of the i -th vortex at time τ_1 and time τ_2 , indicated by $|\Delta z_i|$, which is given by

$$|\Delta z_i| = |z_i(\tau_2) - z_i(\tau_1)|, \quad (5.5)$$

where $z_i(\tau_1)$ and $z_i(\tau_2)$ are the positions of the i -th vortex after an interval $\Delta\tau = 0.009$. The mean separation between all vortices in the sample is given by

$$|\Delta z| \equiv \frac{1}{N_v} \sum_{i=1}^{N_v} |\Delta z_i|, \quad (5.6)$$

which, in the case of the diagonal dipole gives $|\Delta z| \sim 0.29$, roughly a seventh of the side of the squared domain. The result of this analysis for the diagonal dipole is shown in Fig. (5.15) (figure in the centre). In this analysis only two configurations separated by $\Delta\tau = 0.009$ have been considered. In each figure the x -axe refers to a particular vortex (the first 22 red are those with positive circulation and the last 22 blue are those with negative circulation) and the dots represent the separation of the i -th vortex after the time $\Delta\tau$. In the case of the dipole $\Delta\tau = 0.009$, for the diagonal dipole $\Delta\tau = 0.0185$ and for the monopole $\Delta\tau = 0.025$. The horizontal dotted line indicates the mean value given by Eq. (5.6) of the separation of all the vortices. These results show that the minimum separation occurs for the diagonal dipole and it is $\Delta z \sim 0.29$.

This suggests that the distance travelled by vortices is a function of the scale of the large structures (assumed to be of the order of the domain size); it is nevertheless sufficiently large when an ensemble consisting of many instantaneous configurations is used.

In the case of the dipole and the monopole, the set of data consists in $N_C = 7502$ and $N_C = 10000$ configurations respectively. In order to have an ensemble with $N \sim 8000$ vortices a maximum time interval of $\Delta\tau = 0.0185$ for the dipole and $\Delta\tau = 0.025$ for the

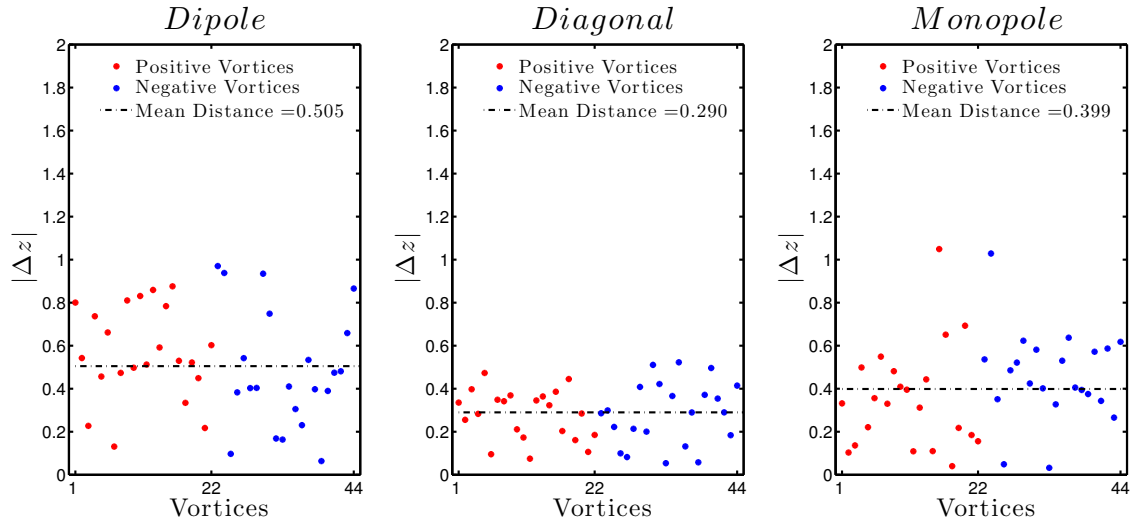


Figure 5.15: Mean distance between two instantaneous configurations of vortices for the dipole, diagonal dipole and monopole in the square: each dot in the above figures represents the separation $|\Delta z|$ of each vortex after an amount of time $\Delta\tau$. In the case of the dipole $\Delta\tau = 0.009$, for the diagonal dipole $\Delta\tau = 0.0185$ and for the monopole $\Delta\tau = 0.025$. The red and the blue dots represent the positive and negative vortices respectively.

monopole are required. The separation given by Eq. (5.6) between two configurations for the dipole is given by $|\Delta z| \sim 0.399$ and for the monopole by $|\Delta z| \sim 0.505$ (see Fig. (5.14)).

Ensembles in the rectangle

In the case of the rectangle, the symmetry argument does not hold any more, and hence, the only possibility is to find the system in the appropriate configuration and construct the ensemble. In the case of the dipole, the configurations have been considered in the interval $\tau = [20 - 25]$. Regarding the monopole the following intervals have been chosen: $\Delta\tau = [11.5 - 12.5]$ and $\tau = [19.25 - 19.6]$. Using these intervals it has been possible to create two ensembles (for the monopole and the dipole shown in Fig. (5.16)) containing more than $N = 8000$ vortices. The mean separation analysis about the mean separation between all vortices given by Eq. (5.6) was repeated for the rectangle and can be visualised in Fig. (5.17) for both ensembles of Fig. (5.16). For the monopole the number of configurations correspond to $N_C = 2700$ while $N_C = 10000$ for the dipole. A time interval of $\Delta\tau = 0.012$ between the two configurations is required to generate an ensemble which contains around $N \sim 8000$ vortices for the monopole, while for the dipole the interval is given by $\Delta\tau = 0.025$. For these values, the minimum mean

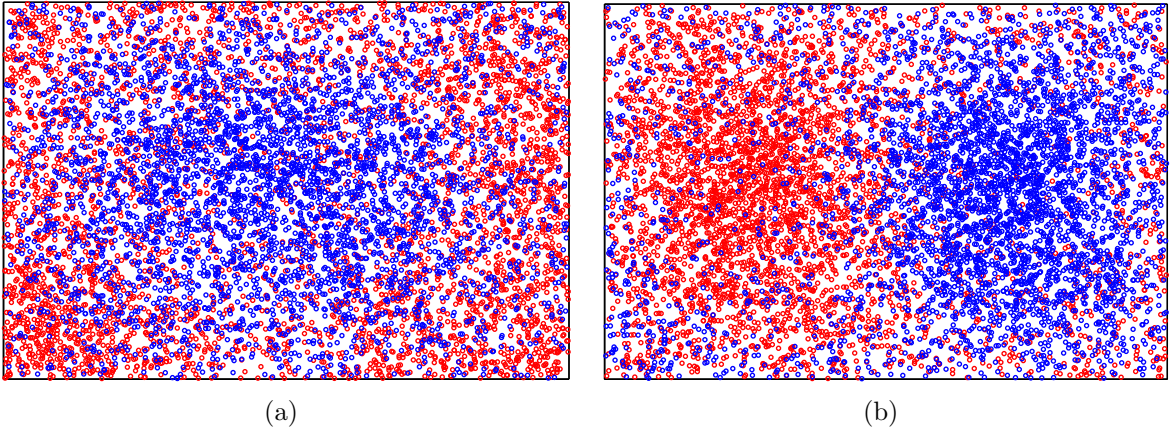


Figure 5.16: Ensembles for the monopole (*a*) and the dipole (*b*) in the rectangle: the number of vortices in each ensemble are $N = 8022$ and $N = 8086$ respectively. The red and the blue dots represent the vortices with positive and negative circulation respectively.

separation between all vortices occurs for the monopole and it is $\Delta z \sim 0.211$. The fact that the minimum mean distance occurs for the monopole is perfectly reasonable due to the limited number of configurations.

5.3.2 Lamb-Oseen Vortex in a Box

The main result of the previous subsection is given by the ensembles in the square and the rectangle: in particular ensembles for the dipole, the diagonal dipole and the monopole in the square and for the monopole and the dipole in the rectangle have been generated and they are shown in Fig. (5.13) and Fig. (5.16), respectively. In this subsection the problem of recovering a smooth vorticity field from these ensembles will be presented.

In the framework of the statistical mechanics, if a domain \mathcal{D} is divided into a large number of cells with size h^2 , an important concept is played by the *macrostate* which has been introduced in §3.2. In the case of point vortices, the macrostate is defined by the number of positive and negative vortices in each cell. This uncertainty can be represented by smearing the vorticity of each vortex using a characteristic "core size" that is of the order of the side of the cell and hence, only the information about the distribution of vortices in each cell h . Therefore, the vorticity field generated by a point vortex given by Eq. (2.65) can be approximated by a smooth two dimensional Gaussian distribution with standard deviation σ given by Eq. (2.111). This smearing procedure is similar to that adopted in §3.2.1 when the statistical weights for different number of

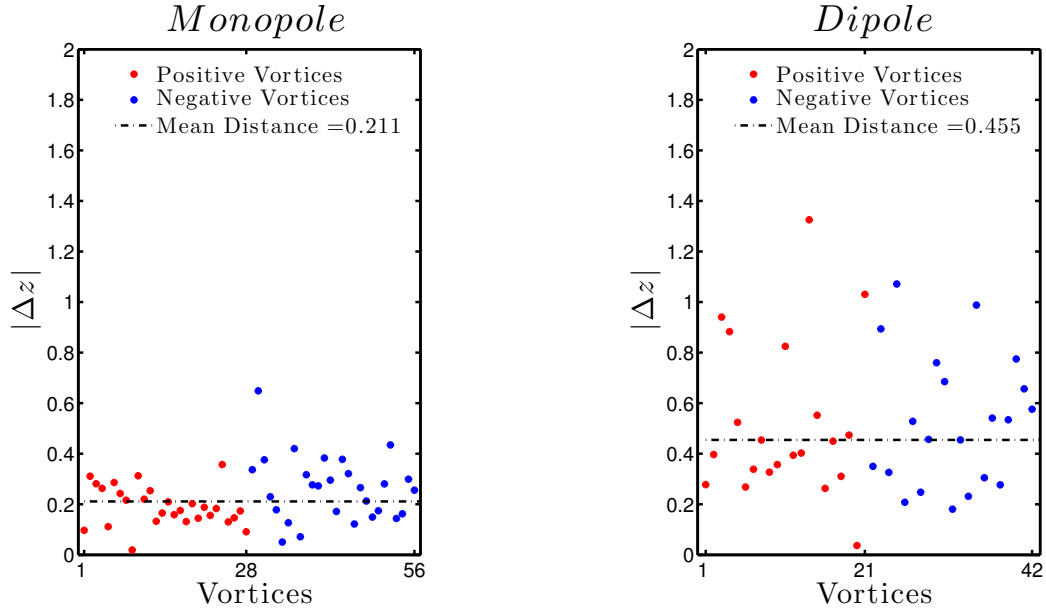


Figure 5.17: Mean separation between two instantaneous configurations of vortices for the monopole and the dipole in the rectangle: each dot in the above figures represents the separation $|\Delta z|$ of each vortex after an amount of time $\Delta\tau$. In the case of the monopole $\Delta\tau = 0.012$ and for the dipole $\Delta\tau = 0.025$. The red and the blue dots represent the positive and negative vortices respectively.

vortices were generated. In that case, the statistical weights were approximated by a one dimensional Gaussian kernel given by Eq. (3.22). Now a two dimensional Gaussian kernel is required and it is given by

$$GK_{2D}(r; \sigma) = \frac{1}{2\pi\sigma^2} e^{-\frac{r^2}{2\sigma^2}}, \quad (5.7)$$

where the parameter σ is the standard deviation and $r = \sqrt{x^2 + y^2}$ is the distance between the point vortex position and a generic point in the domain. This expression is analogous to the expression for the vorticity field corresponding to the *Lamb-Oseen* vortex [102] located at the centre of an infinite domain for which the vorticity field is given by

$$\omega(r, t) = \frac{\gamma_0}{4\pi\nu t} e^{-r^2/4\nu t}, \quad (5.8)$$

where $\sigma = \sqrt{2\nu t}$ and γ_0 is the circulation of the point vortex. This vorticity profile arises as an exact solution of the Navier-Stokes equation with an initial vorticity corresponding to that of a point vortex in the presence of a dissipative term ν

$$\frac{\partial\omega}{\partial t} = \nu\nabla^2\omega, \quad \omega(r; t=0) = \gamma_0\delta(r). \quad (5.9)$$

CHAPTER 5. POINT VORTEX DYNAMICS IN THE SQUARE AND THE RECTANGLE

Comparing Eqs. (5.8) and (5.7), the standard deviation of a two dimensional Gaussian kernel can be associated with the viscous term such that $\nu = \sigma^2/2t$.

When a bounded domain is considered, these results that hold for an unbounded domain need to be modified. In a bounded region the solution to Eq. (5.9) is no longer given by Eq. (5.8). In addition, in a bounded domain, the initial condition $\omega(r; t = 0) = \gamma_0\delta(r)$ needs to be modified. In other words the representation of the Dirac delta function as having the property

$$\int_{-\infty}^{+\infty} \int_{-\infty}^{+\infty} f(\mathbf{y})\delta(\mathbf{x} - \mathbf{y})d\mathbf{y} = f(\mathbf{x}), \quad (5.10)$$

must be modified for the particular type of boundary conditions to be used. For these reasons, in the following the solution of Eq. (5.9) in a rectangular region will be derived and a representation of the Dirac delta function in a bounded domain will be given.

The starting point will be to consider a rectangular region with sides L_x and L_y in which a single vortex with circulation γ_0 is placed at (x_0, y_0) . The vorticity field $\omega(x, y)$ is required to satisfy the following boundary conditions

$$\begin{aligned} \omega(x = 0, y) &= \omega(x = L_x, y) = 0, \\ \omega(x, y = 0) &= \omega(x, y = L_y) = 0. \end{aligned} \quad (5.11)$$

The equation (5.9) can be solved by using the method of separation of variables and hence, the vorticity field is assumed to take the form

$$\omega(x, y, t) = X(x)Y(y)T(t). \quad (5.12)$$

Substituting Eq. (5.12) into Eq. (5.9), and dividing both sides by $X(x)Y(y)T(t)$, gives

$$\frac{T'(t)}{T(t)} = \nu \frac{X''(x)}{X(x)} + \nu \frac{Y''(y)}{Y(y)}, \quad (5.13)$$

which can be split into three ordinary differential equations

$$X'' - \lambda_1 X = 0, \quad Y'' - \lambda_2 Y = 0, \quad T' - \nu(\lambda_1 + \lambda_2)T = 0, \quad (5.14)$$

where two constants λ_1 and λ_2 have been introduced. The first two equations for $X(x)$ and $Y(y)$ have the same form and, hence, only one needs to be solved and then the

result can be immediately applied to the other. The equation for the function $X(x)$ is

$$X'' - \lambda_1 X = 0, \quad (5.15)$$

and, depending on the sign of the eigenvalue λ_1 , it admits three different types of solution.

If $\lambda_1 = 0$ the equation simply becomes

$$X'' = 0, \quad (5.16)$$

and its solution is given by $X(x) = Ax + B$. By imposing the boundary conditions (5.11) the only possible solution is the constant zero solution which has no physical meaning.

If $a^2 = \lambda_1 > 0$ then the solution to Eq. (5.15) is given by

$$X(x) = A \cosh(ax) + B \sinh(ax), \quad (5.17)$$

In this case, the boundary conditions (5.11) at $x = 0$ and $x = L_x$, imply $A = 0$ and $B = 0$ respectively which gives rise to a trivial solution. Hence, the last possibility is $a^2 = -\lambda_1 > 0$ for which the solution to Eq. (5.15) is given by

$$X(x) = A \cos(ax) + B \sin(ax). \quad (5.18)$$

Applying the boundary conditions (5.11) at $x = 0$

$$X(x) \Big|_{x=0} = A \cos(ax) + B \sin(ax) \Big|_{x=0} = A, \quad (5.19)$$

which imposes $A = 0$. The other boundary condition at $x = L_x$ is given by

$$X(x) \Big|_{z=L_x} = B \sin(ax) \Big|_{z=L_x} = B \sin(aL_x) = 0, \quad (5.20)$$

which implies the existence of an infinite set of eigenvalues and eigenfunctions given by

$$a = \frac{n\pi}{L_x}, \quad \sin\left(\frac{n\pi x}{L_x}\right). \quad (5.21)$$

Recalling $a^2 = -\lambda_1 > 0$, the final results for $X(x)$ and $Y(y)$ are given by

$$\begin{aligned}\lambda_{1,n} &= -\frac{n^2\pi^2}{L_x^2}, & X_n(x) &= \sin\left(\frac{n\pi x}{L_x}\right), \\ \lambda_{2,m} &= -\frac{m^2\pi^2}{L_y^2}, & Y_m(y) &= \sin\left(\frac{m\pi y}{L_y}\right).\end{aligned}\quad (5.22)$$

The solution to the differential equation for the function $T(t)$ is straightforward to obtain and is given by

$$T(t) = e^{\nu t(\lambda_{1,n} + \lambda_{2,m})t} = e^{-\nu t(n^2\pi^2/L_x^2 + m^2\pi^2/L_y^2)}. \quad (5.23)$$

The final solution to Eq. (5.9) is therefore given by Eq. (5.12) in terms of a double infinite series due to the two sets of eigenfunctions and eigenvalues

$$\omega(x, y, t) = \sum_{n,m=1}^{+\infty} C_{n,m} e^{-\nu t(n^2\pi^2/L_x^2 + m^2\pi^2/L_y^2)} \sin\left(\frac{n\pi x}{L_x}\right) \sin\left(\frac{m\pi y}{L_y}\right), \quad (5.24)$$

where the coefficients $C_{n,m}$ need to be evaluated by considering the initial condition. The first step to evaluating the coefficients $C_{n,m}$ in Eq. (5.24), is to consider the solution (5.24) at the initial time $t = 0$, multiplying it by $\sin(n'\pi x/L_x)$ and $\sin(m'\pi y/L_y)$ where n', m' are non zero integers, and integrating it over the domain L_x, L_y . By using the following property

$$\int_0^{L_x} \sin\left(\frac{n\pi x}{L_x}\right) \sin\left(\frac{n'\pi x}{L_x}\right) dx = \frac{L_x}{2} \delta_{n,n'}, \quad (5.25)$$

the integration of the right hand side of Eq. (5.24) gives

$$C_{n',m'} \frac{L_x L_y}{4}. \quad (5.26)$$

It is important to notice that the boundary conditions (5.11) are equivalent to the configuration described in §2.5.2 where the presence of two infinite sets of images mimics the walls of the rectangular box with sides L_x and L_y . Therefore, the configuration in which a single vortex is placed in a box, is equivalent of a doubly infinite set of periodic images along the x and the y axes (with periodicity $2L_x$ and $2L_y$) with the circulations equivalent to that discussed in §2.5.2.

The periodic distribution of vortices which needs to be considered is shown in Fig. (5.18) in complete analogy to the arguments presented in §2.5.2. This fact is extremely

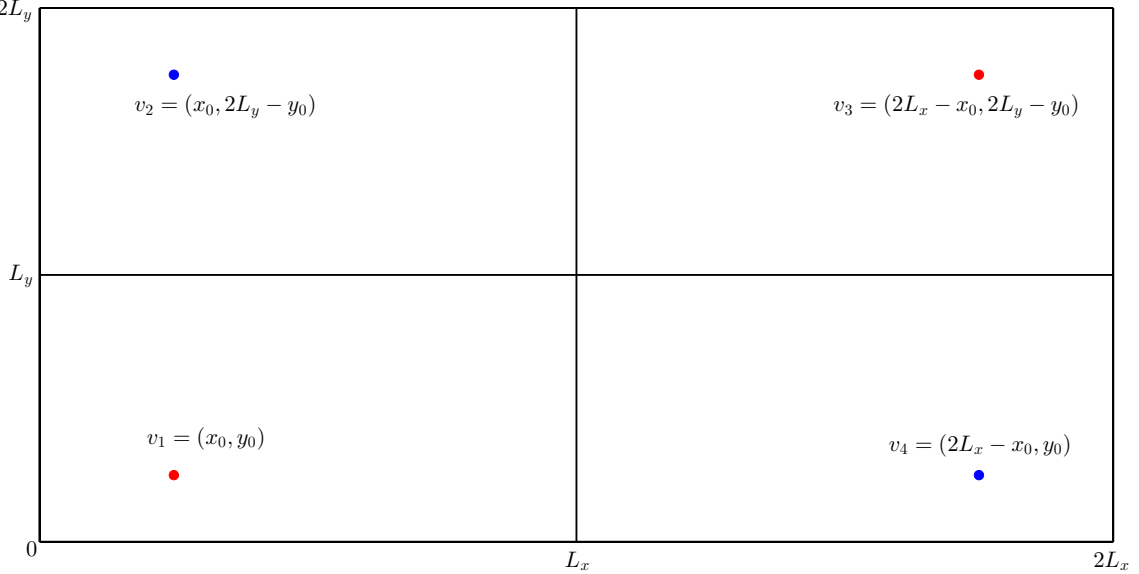


Figure 5.18: Configuration which automatically satisfies the boundary conditions given by (5.11): the real vortex v_1 and its three images v_2 , v_3 and v_4 which made up a periodic cell. The two sets of images continue along the x and the y directions by periodically repeating this periodic cell. If v_1 has positive circulation then so does the image v_3 while the other two vortices have a negative circulation.

useful because there exists a periodic representation of Dirac's delta function, the so called *Dirac's comb* [68] given by

$$\sum_{m_1=-\infty}^{+\infty} \delta(x - x_0 - 2m_1 L) = \frac{1}{2L} + \frac{1}{L} \sum_{n=1}^{+\infty} \cos \left(\frac{n\pi(x - x_0)}{L} \right), \quad (5.27)$$

where $2L$ is the period along x and x_0 is the position of the charge. This representation can be easily extended in two dimensions. Therefore, the initial condition associated with the vorticity field generated by the configuration of point vortices shown in Fig.

(5.18) (which continues periodically along x and y) can be described by

$$\begin{aligned}
 \tilde{\omega}(x, y) = & \gamma_0 \sum_{\substack{m_1=-\infty \\ m_2=-\infty}}^{+\infty} \delta(x - x_0 + 2m_1 L_x) \delta(y - y_0 + 2m_2 L_y) \\
 & - \gamma_0 \sum_{\substack{m_1=-\infty \\ m_2=-\infty}}^{+\infty} \delta(x - (2L_x - x_0) + 2m_1 L_x) \delta(y - y_0 + 2m_2 L_y) \\
 & + \gamma_0 \sum_{\substack{m_1=-\infty \\ m_2=-\infty}}^{+\infty} \delta(x - (2L_x - x_0) + 2m_1 L_x) \delta(y - (2L_y - y_0) + 2m_2 L_y) \\
 & - \gamma_0 \sum_{\substack{m_1=-\infty \\ m_2=-\infty}}^{+\infty} \delta(x - x_0 + 2m_1 L_x) \delta(y - (2L_y - y_0) + 2m_2 L_y). \tag{5.28}
 \end{aligned}$$

Now the vorticity $\tilde{\omega}(x, y)$, which represents the condition at initial time, must be multiplied by $\sin(n'\pi x/L_x)$ and $\sin(m'\pi y/L_y)$ where n', m' are non zero integers, and integrated over the domain with sides L_x and L_y . Hence, the contributions given by the charges v_2, v_3 and v_4 indicated in Fig. (5.18) must be taken into account. In order to do so, it is useful to consider the following integral

$$I = \gamma_0 \sum_{m_1=-\infty}^{+\infty} \int_0^{L_x} \delta(x - (2L_x - x_0) + 2m_1 L_x) \sin\left(\frac{n'\pi x}{L_x}\right) dx, \quad n' \neq 0, \tag{5.29}$$

where n' is any non-zero integer. By performing the change of variable $\tilde{x} = 2L_x - x$, I becomes

$$I = \gamma_0 \sum_{m_1=-\infty}^{+\infty} \int_{L_x}^{2L_x} \delta(-\tilde{x} + x_0 + 2m_1 L_x) \sin\left(2n'\pi - \frac{n'\pi \tilde{x}}{L_x}\right) d\tilde{x}, \tag{5.30}$$

and since the Dirac delta function is an even function, $\delta(x) = \delta(-x)$, the integral becomes

$$I = -\gamma_0 \sum_{m_1=-\infty}^{+\infty} \int_{L_x}^{2L_x} \delta(x - x_0 + 2m_1 L_x) \sin\left(\frac{n'\pi x}{L_x}\right) dx. \tag{5.31}$$

This property shows that the integral over the domain $[0, L_x] \times [0, L_y]$ of the second term of Eq. (5.28) multiplied by $\sin(n'\pi x/L_x)$ and $\sin(m'\pi y/L_y)$ is equivalent to integrating the first term of (5.28) multiplied by $\sin(n'\pi x/L_x)$ and $\sin(m'\pi y/L_y)$ over the interval $[L_x, 2L_x] \times [0, L_y]$. By applying the same property to the other terms, the integral of

the vorticity at the initial time $\tilde{\omega}(x, y)$ given by (5.28) is given by

$$\begin{aligned} I_{\tilde{\omega}} &= \int_0^{L_x} \int_0^{L_y} \tilde{\omega}(x, y) \sin\left(\frac{n'\pi x}{L_x}\right) \sin\left(\frac{m'\pi y}{L_y}\right) dx dy, \\ &= \gamma_0 \sum_{m_1=-\infty}^{+\infty} \int_0^{2L_x} \delta(x - x_0 + 2m_1 L_x) \sin\left(\frac{n'\pi x}{L_x}\right) dx \times \\ &\quad \times \gamma_0 \sum_{m_2=-\infty}^{+\infty} \int_0^{2L_y} \delta(y - y_0 + 2m_2 L_y) \sin\left(\frac{m'\pi y}{L_y}\right) dy, \end{aligned} \quad (5.32)$$

where $n', m' \neq 0$. Inserting in the above expression the representation of the Dirac delta function (5.27) along both x and y directions and using

$$\begin{aligned} \frac{1}{L_x} \int_0^{2L_x} \sum_{n=1}^{+\infty} \cos\left(\frac{n\pi(x - x_0)}{L_x}\right) \sin\left(\frac{n'\pi x}{L_x}\right) dx dy &= \sin\left(\frac{n'\pi x_0}{L_x}\right), \\ \frac{1}{L_y} \int_0^{2L_y} \sum_{m=1}^{+\infty} \cos\left(\frac{m\pi(y - y_0)}{L_y}\right) \sin\left(\frac{m'\pi y}{L_y}\right) dx dy &= \sin\left(\frac{m'\pi y_0}{L_y}\right), \end{aligned} \quad (5.33)$$

gives the final result

$$I_{\tilde{\omega}} = \gamma_0 \sin\left(\frac{n'\pi x_0}{L_x}\right) \sin\left(\frac{m'\pi y_0}{L_y}\right). \quad (5.34)$$

Finally the coefficients can be evaluated by equating Eqs. (5.34) and (5.26) and they are given by

$$C_{n', m'} = \frac{4\gamma_0}{L_x L_y} \sin\left(\frac{n'\pi x_0}{L_x}\right) \sin\left(\frac{m'\pi y_0}{L_y}\right), \quad (5.35)$$

which can be substituted into Eq. (5.24) in order to obtain the final solution for a single vortex with circulation γ_0 located at (x_0, y_0) . If there are N^\pm charges of strength γ_\pm , then the positive and the negative vorticity for this distribution is given by

$$\begin{aligned} \omega^+(x, y) &= \sum_{n, m=1}^{+\infty} C_{n, m}^+ e^{-\nu t(n^2\pi^2/L_x^2 + m^2\pi^2/L_y^2)} \sin\left(\frac{n\pi x}{L_x}\right) \sin\left(\frac{m\pi y}{L_y}\right), \\ \omega^-(x, y) &= \sum_{n, m=1}^{+\infty} C_{n, m}^- e^{-\nu t(n^2\pi^2/L_x^2 + m^2\pi^2/L_y^2)} \sin\left(\frac{n\pi x}{L_x}\right) \sin\left(\frac{m\pi y}{L_y}\right), \end{aligned} \quad (5.36)$$

where the coefficients are given by

$$C_{n, m}^\pm = \frac{4}{L_x L_y} \sum_{i=1}^{N^\pm} \gamma_i \sin\left(\frac{n\pi x_i}{L_x}\right) \sin\left(\frac{m\pi y_i}{L_y}\right). \quad (5.37)$$

CHAPTER 5. POINT VORTEX DYNAMICS IN THE SQUARE AND THE RECTANGLE

From the positive and negative vorticity, it is also possible to derive the streamfunction for the distribution of vortices. In fact, the streamfunction can be decomposed as follows

$$\psi^\pm(x, y) = \sum_{n,m=1}^{+\infty} A_{n,m}^\pm \sin\left(\frac{n\pi x}{L_x}\right) \sin\left(\frac{m\pi y}{L_y}\right), \quad (5.38)$$

and differentiating the above quantity twice with respect to x and y gives

$$\begin{aligned} \frac{\partial^2 \psi^\pm}{\partial x^2} &= - \sum_{n,m=1}^{+\infty} A_{n,m}^\pm \frac{n^2 \pi^2}{L_x^2} \sin\left(\frac{n\pi x}{L_x}\right) \sin\left(\frac{m\pi y}{L_y}\right), \\ \frac{\partial^2 \psi^\pm}{\partial y^2} &= - \sum_{n,m=1}^{+\infty} A_{n,m}^\pm \frac{m^2 \pi^2}{L_y^2} \sin\left(\frac{n\pi x}{L_x}\right) \sin\left(\frac{m\pi y}{L_y}\right). \end{aligned} \quad (5.39)$$

By using the relation between the vorticity and the equation for the streamfunction (2.54), the positive and negative vorticity contributions to the streamfunction are given by Eq. (5.38) where the coefficients are

$$A_{n,m}^\pm = \frac{C_{n,m}^\pm e^{-\nu t(n^2 \pi^2 / L_x^2 + m^2 \pi^2 / L_y^2)}}{\left(\frac{n^2 \pi^2}{L_x^2} + \frac{m^2 \pi^2}{L_y^2}\right)}, \quad (5.40)$$

and the coefficients $C_{n,m}^\pm$ are given by Eq. (5.37). The vorticity fields given by Eq. (5.36) and the streamfunction given by Eq. (5.38) can be readily generated from knowledge of the positions of the vortices: therefore, once this quantity has been calculated, Eq. (3.41) for the entropy S and Eq. (2.61) for the energy E are straightforward to calculate. However, two important points regarding the results need to be considered: firstly the vorticity fields given by Eq. (5.36) and the relative streamfunctions given by Eq. (5.38) depend on a free parameter σ (the core size), secondly the solutions are expressed in terms of a double summation over the indices n and m . These two observations give raise the following questions: "What is the *right* value for σ ?" How many terms in the double summation need to be retained to obtain an accurate approximation?"

An answer to the first question necessitates a more systematic study and it will deferred to the next subsection §5.3.1. Regarding the other question a numerical analysis can be performed and it will be explained in the following.

The first task is to determine an appropriate number of meshgrid points for the vorticity and the streamfunctions: for this purpose meshgrids with 64×64 , 128×128 and 256×256 points are now considered. The number of points should be enough to solve

the vortex core. Since in the square with sides $L_x = L_y = 2$, the minimum value for the vortex core can be estimated approximately by $\sigma = L_x/64 \sim 0.03$, for this analysis a value of $\sigma = 0.05$ is chosen. By fixing the value of σ , the positive and negative vorticity fields given by Eq. (5.36) are constructed and their integral over the domain are evaluated. For a distribution consisting of N^+ vortices with circulation $\gamma_+ = +1$ and N^- vortices with circulation $\gamma_- = -1$ these integrals are equal to the total positive and total negative circulation given by $N^+\gamma_+$ and $N^-\gamma_-$, respectively. Figure (5.19) shows the value of the total positive (figure on the left) and negative (figure on the right) circulation for the initial configuration in the square as a function of the number of modes for three different meshgrids indicated in the legend.

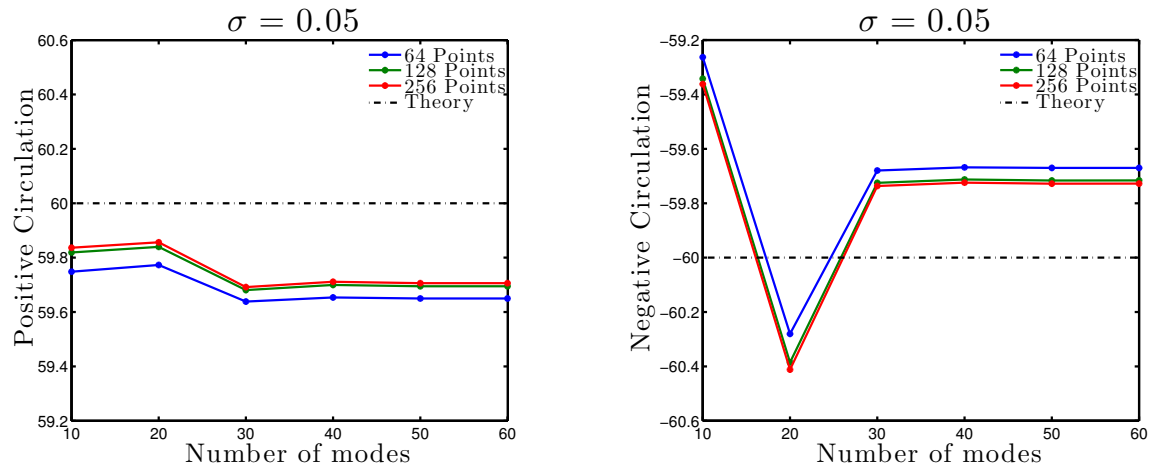


Figure 5.19: Positive (left) and negative (right) circulation for the initial condition as a function of the number of modes m and n and for different meshgrids indicated in the legend. The size of the Gaussian kernel is $\sigma = 0.05$.

Figure (5.19) shows the positive (on the left) and the negative (on the right) values of circulation for the initial condition (see Fig. (5.20) on the left) in the square as a function of the number of modes for different meshgrids. This analysis shows that the circulation does not vary significantly when the number of modes is greater than $n = m = 40$ and that there is not much to gain by increasing the resolution from a grid of 128×128 points to a grid of 256×256 points. For this reason in the following the vorticity fields and the streamfunctions given by Eqs. (5.36) and (5.38) will be evaluated with $n = m = 50$ modes on a 128×128 equispaced meshgrid. Figure (5.19) also shows that the total circulation is not conserved: this is due to the fact that the parameter $\sigma = \sqrt{2\nu t}$, which represents the width of the Gaussian curve, is equivalent to the effect of a diffusive process in time.

Clearly, the values for the positive and negative circulation shown in Fig. (5.19) are

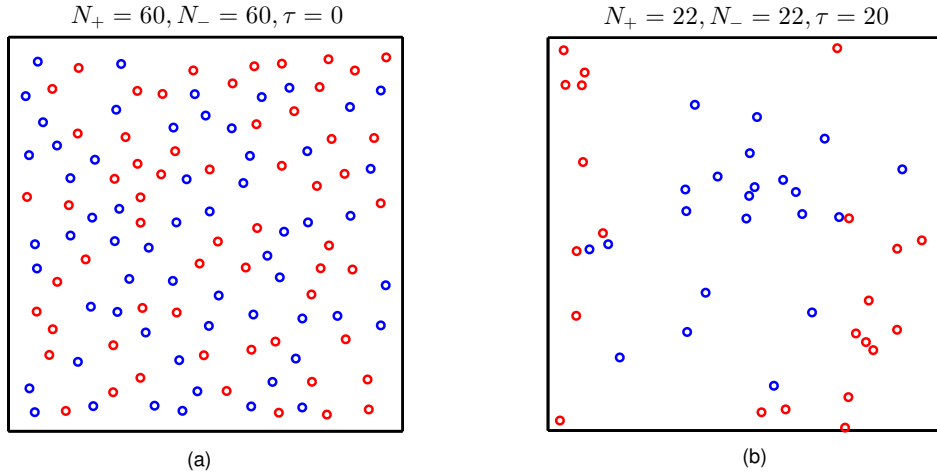


Figure 5.20: Configuration at initial time (on the left) and at later time $\tau = 20$ (on the right): the asymmetric distribution of vortices in the latter configuration causes more loss in the positive circulation (see Fig. (5.21) on the right) due to the positions of the positive vortices near the boundary.

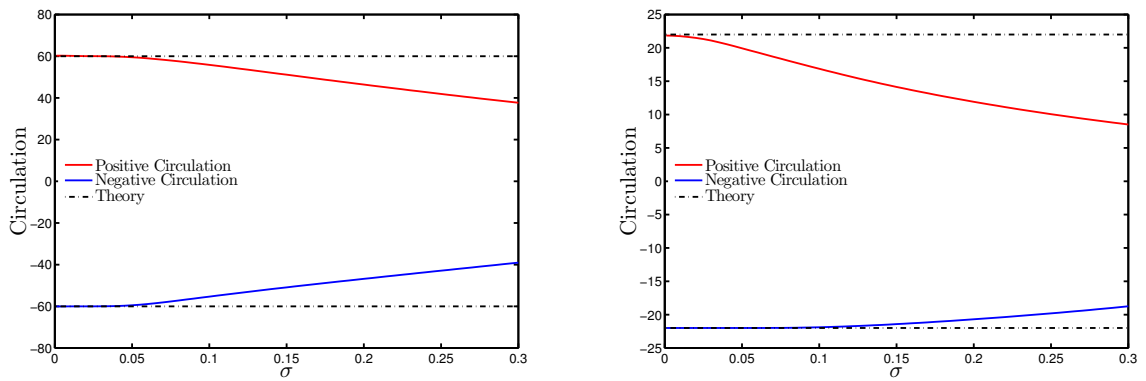


Figure 5.21: Positive and negative circulation for the initial condition (on the left) and at later time $\tau = 20$ (on the right) as a function of the radius σ . The positive circulation in the figure on the right decreases more rapidly as σ increases, due to the positions of the positive vortices being located close to the boundaries. The configurations at the initial time and at $\tau = 20$ are shown in Fig. (5.20).

not the expected values which are given by ± 60 . This situation worsen when vortices of one charge are near the boundaries as in the case of the monopole shown in Fig. (5.20) on the right. The evaluation of the total positive and negative circulation for different values of the parameter σ is presented in Fig. (5.21): the loss in the positive circulation is bigger than the loss in the negative circulation since the positive vortices are closer to the boundaries (Fig. (5.20)). To overcome this problem, the vorticity fields given by Eq. (5.8) are normalised such that their integral over the domain \mathcal{D} is always equal to $N^+ \gamma_+$ for the positive component and $N^- \gamma_-$ for the negative component.

In conclusion, for a given ensemble, the positive and negative vorticity fields will be generated by using Eq. (5.36) where the coefficients are given by Eq. (5.37). These vorticity fields are then normalised such that

$$\int \omega^\pm dx dy = N^\pm \gamma_\pm. \quad (5.41)$$

This provides a smoothed vorticity field which decays to zero on the boundaries but for which the circulation of both the positive and negative charges is always conserved. In the following subsection a method to identify an optimal value of the parameter σ for the ensembles in the square and the rectangle will be discussed.

5.3.3 Entropy Evaluation

In the previous subsection the derivation of the smooth vorticity fields and the streamfunction given by Eqs. (5.36) and (5.38) for a distribution of point vortices has been presented. It has been also pointed out respectively that these quantities depend on a free parameter σ which represents the size of the vortex core. In this subsection it will be shown that the optimal value for the parameter σ is related to the total number of vortices contained in the ensemble.

In §3.3 the entropy for a system composed of N_+ point vortices with positive circulation γ_+ and N_- point vortices with negative circulation γ_- in a domain \mathcal{D} was derived and is given by

$$S[\omega_a] = -k_B \sum_{a=\pm} \int_{\mathcal{D}} \frac{\omega_a}{\gamma_a} \log \left(\frac{\omega_a \mathcal{D}}{\gamma_a N_a} \right) dx dy \quad (5.42)$$

where ω_\pm are the positive and negative vorticity fields. In order to understand the role of the parameter σ , a system composed of vortices with opposite circulation is considered. If the vortices have opposite circulation and they are close enough and their vorticity field is approximated with a large value of σ (much larger than the mutual distance between the two vortices) the net result is that the region in which

CHAPTER 5. POINT VORTEX DYNAMICS IN THE SQUARE AND THE RECTANGLE

the vortices are located has zero total vorticity. On the other hand, if they have the same circulation, then the vorticity in the region will be doubled. Now if instead of two vortices, an ensemble is considered, it is clear that for a very large value of σ all the vortices will overlap creating a neat zero vorticity in the domain. On the other hand, for a very small value of σ the vorticity fields resemble more closely to a superposition of Dirac delta functions, thereby reducing mixing from occurring between vortices. It is reasonable that a good range of values for σ must allow the vortices of the same circulation to overlap enough but not too much: enough to create regions where vortices form coherent structures, but not too much otherwise the positive and negative large structures will cancel each other. The most appropriate values of σ are therefore expected to correspond to a range in which the positive and negative vorticity fields are not too sensitive to the value of σ chosen. In other words, an intermediate range of scales are sought, small enough not to affect the large scale structures but large enough such that the vorticity fields are sufficiently smooth. Such a range is expected to be identifiable in the case of an ensemble with a very large total number of vortices. For this reason different ensembles, each with a different total number of vortices, have been generated for the dipole, the diagonal dipole, and the monopole in the square, and for the monopole and dipole in the rectangle. The positive and negative vorticity fields were then generated by using Eq. (5.36) and then the total entropy per vortex $|S/N|$ was evaluated where S is given by Eq. (5.42). The results of this analysis is presented below.

Entropy evaluation for the ensembles in the square

In the case of the dipole in the square, ensembles with $N = 44$, $N = 220$, $N = 836$, $N = 2156$, $N = 4532$ and $N = 8580$ vortices have been created, and the absolute value of the entropy per vortex $|S/N|$ of all these ensembles has been evaluated. The results are shown in Fig. (5.22) on a log log scale: on the left it is possible to notice that the curves tend to converge to a flatten region as the number of vortices increases. On the right, a zoom in the region where the curves tends to a straight horizontal line is shown. The linear interpolation of $|S/N|$ for $N = 8580$ and $0.035 \leq \sigma \leq 0.07$ gives a slope of 0.094 which confirms that the entropy for this range of values does not change significantly. The range of values for σ has been determined by considering the slope of the interpolant of $|S/N|$ for different ranges of σ and considering the range which corresponds to the lowest value of the slope. These results illustrate that as the number of vortices in the ensemble is increased a well-defined intermediate range can be identified such that the evaluation of the entropy becomes essentially independent

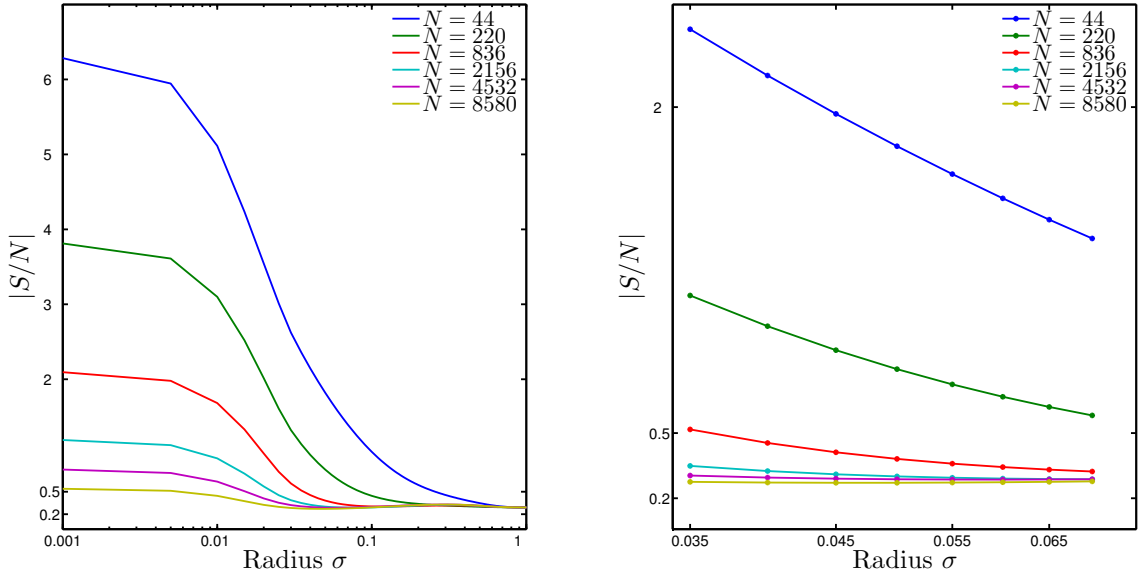


Figure 5.22: On the left, the absolute value of the entropy per number of vortices $|S/N|$ as a function of σ . Results correspond to the dipole in the square generated from different ensembles (each with different amount of vortices indicated in the legend) presented in a log log scale. On the right the results are presented for the range of the values of the parameter σ for which the entropy remains almost constant.

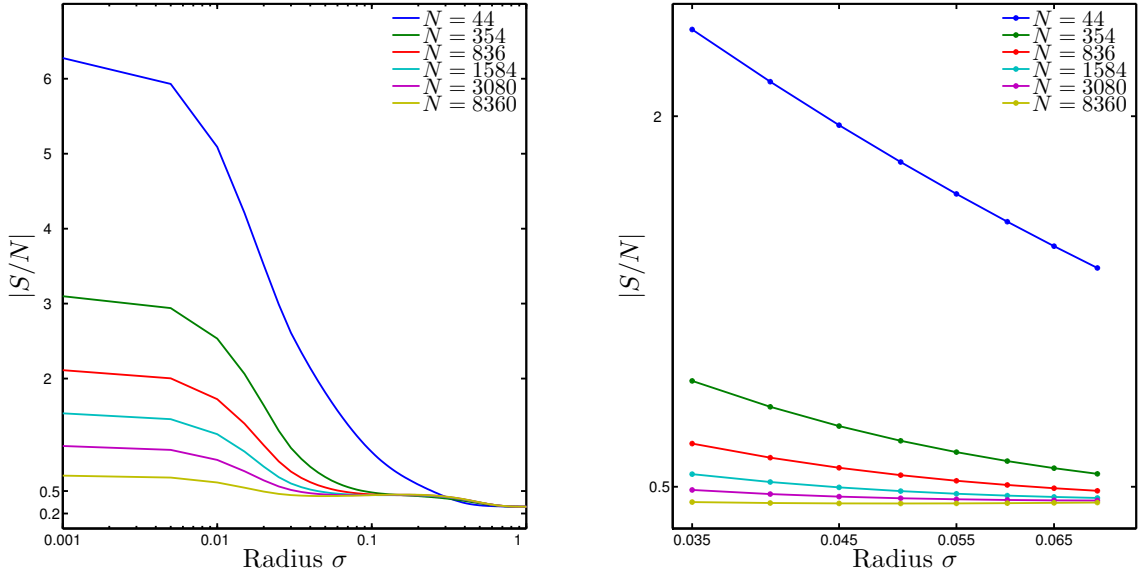


Figure 5.23: On the left, the absolute value of the entropy per number of vortices $|S/N|$ as a function of σ . Results correspond to the diagonal dipole in the square generated from different ensembles (each with different amount of vortices indicated in the legend) presented in a log log scale. On the right the results are presented for the range of the values of the parameter σ for which the entropy remains almost constant.

of σ .

The same analyses has been performed for the diagonal dipole and the monopole in the square and the results are shown in Figs. (5.23) and (5.24).

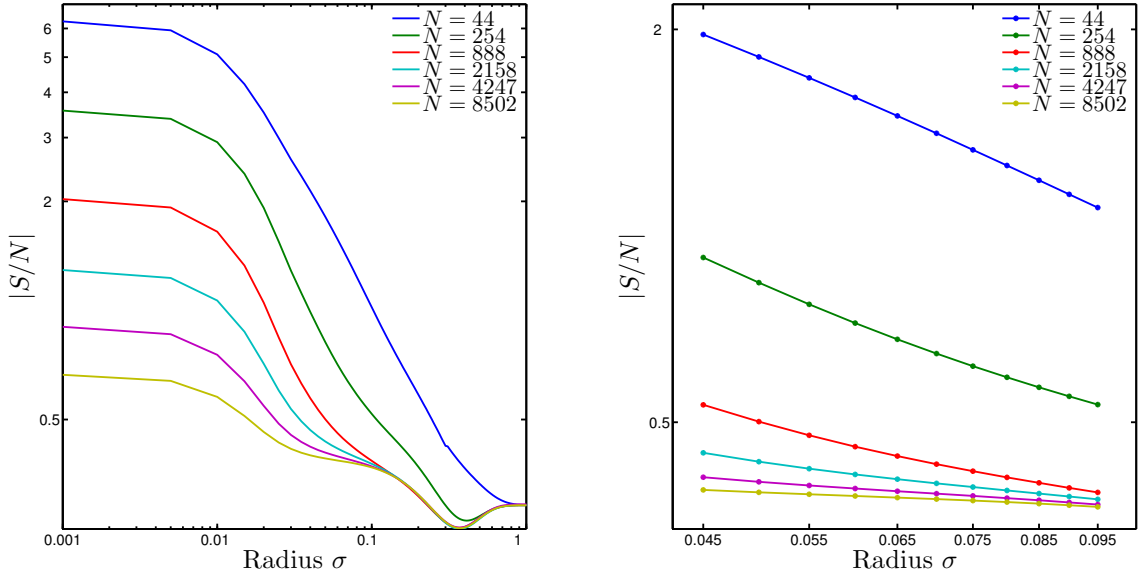


Figure 5.24: On the left, the absolute value of the entropy per number of vortices $|S/N|$ as a function of σ . Results correspond to the monopole in the square generated from different ensembles (each with different amount of vortices indicated in the legend) presented in a log log scale. On the right the results are presented for the range of the values of the parameter σ for which the entropy remains almost constant.

For the diagonal dipole configuration, the interval of the radius is $0.035 \leq \sigma \leq 0.07$ and for the monopole it is $0.045 \leq \sigma \leq 0.095$. For both cases, ensembles up to $N \sim 8000$ have been used as shown in Figs. (5.23) and (5.24). The linear interpolation of the absolute value of the entropy per vortex $|S/N|$ give the values for the slope of -0.014 for the diagonal dipole and -0.44 for the monopole.

This concludes the entropy analysis in the square for the dipole, the diagonal dipole and the monopole: in all cases it has been possible to identify a range of values for the free parameter σ for which the entropy does not vary significantly.

Entropy evaluation for the ensembles in the rectangle

In the case of the rectangle the same procedure has been performed for the monopole and the dipole and the results are shown in Figs. (5.25) and (5.26). In both figures, the absolute value of the entropy per vortex $|S/N|$ for ensembles made of different numbers of vortices (figure on the left) and the region in which $|S/N|$ does not change significantly (figure on the right) are plotted.

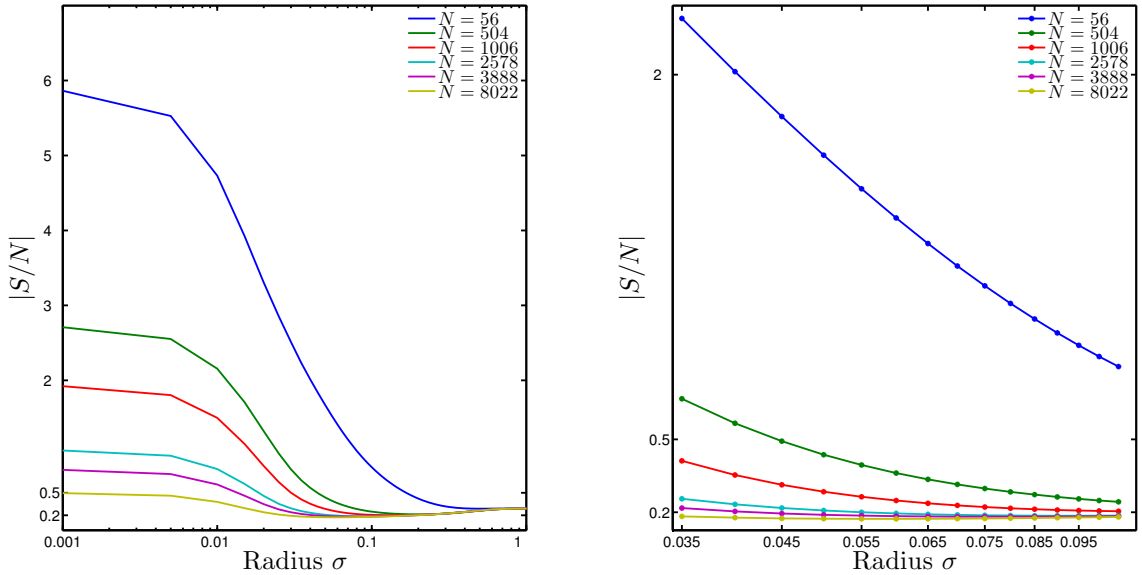


Figure 5.25: On the left, the absolute value of the entropy per number of vortices $|S/N|$ as a function of σ . Results correspond to the monopole in the rectangle for different ensembles (each with different amount of vortices indicated in the legend) in a log log scale. On the right the values of the parameter σ for which the entropy remains almost constant.

For the monopole, ensembles with $N = 56$, $N = 504$, $N = 1006$, $N = 2578$, $N = 3888$ and $N = 8022$ vortices have been considered. For the ensemble with $N = 8022$ vortices, the range of σ for which the entropy $|S/N|$ does not change significantly is given by $0.035 \leq \sigma \leq 0.105$ and for this set of values the slope of the interpolant of $|S/N|$ is given by 0.035. For the dipole, ensembles with $N = 40$, $N = 282$, $N = 844$, $N = 2050$, $N = 4062$ and $N = 8086$ vortices have been considered. For the ensemble with $N = 8086$ vortices, the range of σ is given by $0.04 \leq \sigma \leq 0.085$ and for this set of values the slope of the interpolant of $|S/N|$ is given by -0.022.

The analysis of the entropy for the monopole and the dipole in the rectangle concludes the analysis of the entropy. For all the ensembles in the square (Fig. (5.13)) and in the rectangle (Fig. (5.16)) an interval of values for the free parameter σ has been found. In the following subsections, a quantitative analysis of the entropy for the dipole, the diagonal dipole and the monopole in the square and for the monopole and the dipole in the rectangle will be presented. Moreover, the comparison between these values and the values obtained from the solutions of the BP equation in §4.4 and §4.5 will be given.

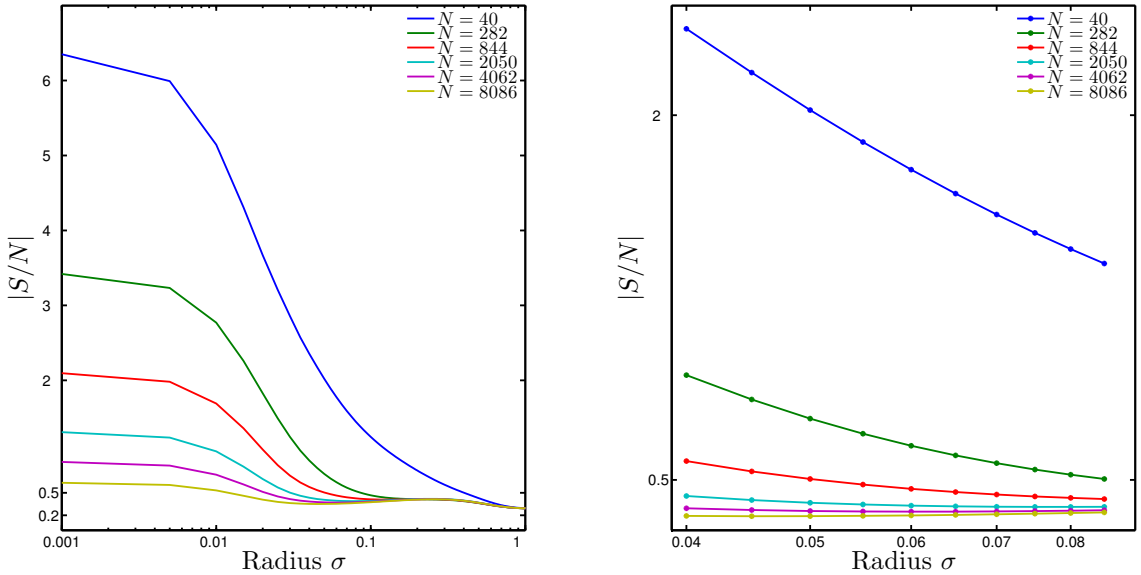


Figure 5.26: On the left, the absolute value of the entropy per number of vortices $|S/N|$ as a function of σ . Results correspond to the dipole in the rectangle for different ensembles (each with different amount of vortices indicated in the legend) in a log log scale. On the right the values of the parameter σ for which the entropy remains almost constant.

5.3.4 Entropy Comparison

In the previous subsection, the values for the parameter $\sigma = \sqrt{2\nu t}$ for all the ensembles in the square and the rectangle have been found. As a consequence, it is now possible to use Eqs. (5.36) and (5.38) and evaluate the smoothed vorticity fields and the corresponding streamfunction. This allows the evaluation of the non-dimensional entropy \hat{S} and the non dimensional energy \hat{E} for these configurations in order to compare these results with the results presented in §4.4 and in §4.5 obtained from the BP equation.

In the following the vorticity fields are normalised according to

$$\int_{\mathcal{D}} \omega^{\pm} dx dy = \pm N^{\pm}, \quad (5.43)$$

where the number of positive and negative vortices has been arbitrarily chosen $N^{\pm} = 60$. The procedure to evaluate the non-dimensional entropy \hat{S} for a configuration can then be obtained as follows:

- Fix a value for the parameter σ and evaluate the streamfunction ψ_{σ} given by Eq. (5.38), and the positive and negative vorticity fields ω_{σ}^{\pm} given by Eq. (5.8) for the configuration under examination.

- Evaluate the energy E_σ and the non-dimensional energy \hat{E}_σ

$$E_\sigma = \frac{1}{2} \int_{\mathcal{D}} \psi_\sigma \omega_\sigma dx dy, \quad \hat{E}_\sigma \equiv \frac{E_\sigma}{4\rho N^2 \gamma^2}. \quad (5.44)$$

- For that value of \hat{E} , identify the value of $\tilde{\lambda}^2$ by looking at Fig. (4.6) for the square or Fig. (4.9) for the rectangle which corresponds to the configuration under investigation.
- Once $\tilde{\lambda}^2$ has been identified, consider the corresponding solution to the BP equation Ψ , evaluate the terms a_\pm and the inverse temperature β

$$a_\pm = \frac{1}{\mathcal{D}} \int e^{\pm\Psi} dx dy, \quad \beta = -\frac{\tilde{\lambda}^2}{\sqrt{a_+ a_-}} \frac{\mathcal{D}}{N \rho \gamma^2}. \quad (5.45)$$

- Consider the smoothed streamfunction ψ_σ evaluated at the first step and generate the non-dimensional stramfunction $\Psi_\sigma = \rho \beta \gamma \psi_\sigma$ where $\rho = 1$.
- Evaluate the terms

$$A_\pm^\sigma = \mathcal{D} \left(\int_{\mathcal{D}} e^{\mp\Psi_\sigma} dx dy \right)^{-1}, \quad a_\pm^\sigma = \frac{1}{\mathcal{D}} \int_D e^{\pm\Psi_\sigma} dx dy, \quad \lambda^2 = \tilde{\lambda}^2 \frac{\sqrt{a_+^\sigma a_-^\sigma}}{2}. \quad (5.46)$$

- Evaluate the non-dimensional entropy \hat{S}_σ

$$\hat{S}_\sigma = -\frac{1}{2} \log (A_+^\sigma A_-^\sigma) - 8\lambda_\sigma^2 \mathcal{D} \hat{E}_\sigma. \quad (5.47)$$

For each ensemble in the square and in the rectangle, a range of values of the parameters σ has been found and this will correspond to a range of values in the $\hat{E} - \hat{S}$ plane. In what follows, this analysis will be performed on the ensembles in the square and in the rectangle which have been constructed in §5.3.1.

Entropy comparison in the square

Having established a suitable range of values for the parameter σ for the dipole, the diagonal dipole and the monopole in the square and by following the procedure previously explained it is possible to classify the ensembles based on their energy and entropy. For the dipole, the diagonal dipole and the monopole in the square, the ranges of values of the parameter σ are given by $0.035 \leq \sigma \leq 0.07$, $0.035 \leq \sigma \leq 0.07$, and

$0.045 \leq \sigma \leq 0.095$ respectively. Therefore, following the aforementioned procedure, the non-dimensional energy \hat{E} of each configuration and for all the values of σ can be evaluated and the results are shown in Fig. (5.27). In each figure, the blue curve represents the non-dimensional energy \hat{E}_σ and the red dotted line is the mean value \bar{E} whose numerical value is indicated in the legend.

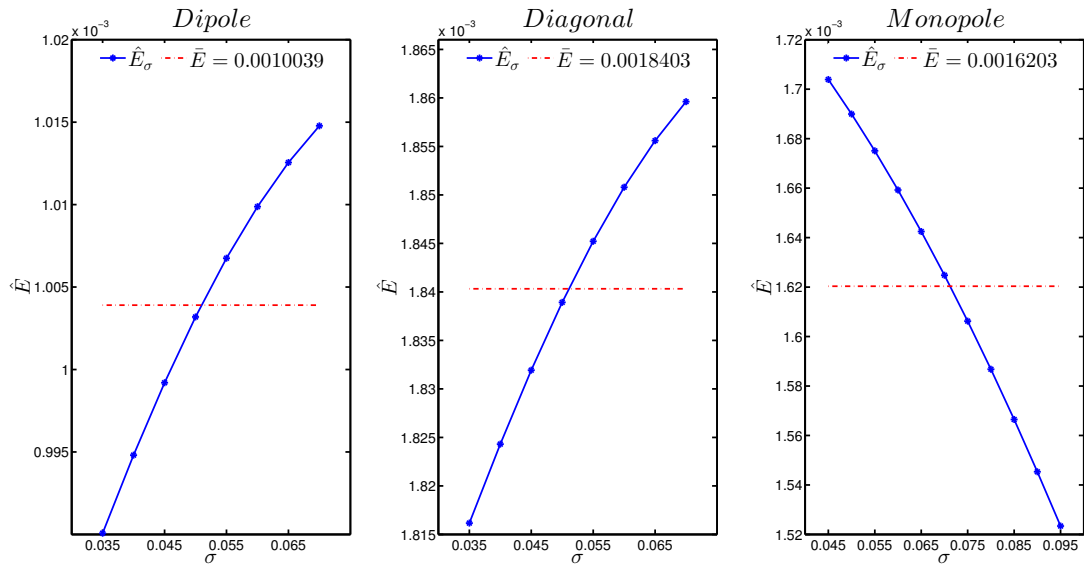


Figure 5.27: Non dimensional energy \hat{E}_σ (blue curve) as a function of the parameter σ and its mean value \bar{E} (red dotted line) for the dipole (left), diagonal dipole (centre) and the monopole (right) in the square.

These values can now be compared with respect to the solution branches of the BP equation as illustrated in Fig. (5.28). The range of values of \hat{E} for all the three ensembles are compatible with the range of the energy of the solutions of the BP equation. For the diagonal dipole and the monopole, the value of the mean energy lies in between the values of $\tilde{\lambda}^2 = 8.5$ and $\tilde{\lambda}^2 = 9$. For the dipole, this value is very close to $\tilde{\lambda}^2 = 10.5$.

Having identified the values of $\tilde{\lambda}^2$, the inverse temperature β needs to be evaluated. For the diagonal dipole and the monopole, the solutions Ψ to the BP equation for $\tilde{\lambda}^2 = 8.5$ and $\tilde{\lambda}^2 = 9$ have been used to evaluate the terms a_\pm in the expression for the inverse temperature given by Eq. (5.45) and then their mean value have been considered. As for the dipole, this quantity has been evaluated by considering only the solution Ψ for $\tilde{\lambda}^2 = 10.5$. The values for the inverse temperature β are

$$\beta_{dipo} = -0.4298, \quad \beta_{diago} = -0.4242, \quad \beta_{mono} = -0.3987. \quad (5.48)$$

Knowledge of the inverse temperature β for all the ensembles, allows the non-dimensional streamfunction $\Psi_\sigma = \rho\beta\psi_\sigma$ and the corresponding terms A_\pm^σ , a_\pm^σ and λ_σ^2 , to be evalu-

ated for each value of the parameter σ . The values of \hat{S}_σ as given by Eq. (5.47) for the dipole, the diagonal dipole and the monopole in the square are presented in Fig. (5.28). This provides a direct comparison between the non-dimensional entropy for the solutions of the BP equation and the ensembles generated from the dynamics of point vortices (indicated with PV in the legend). The figures *b*, *c* and *d*) show the magnified plots of the values of the non-dimensional energy and the non-dimensional entropy for all the values of σ per each ensemble.

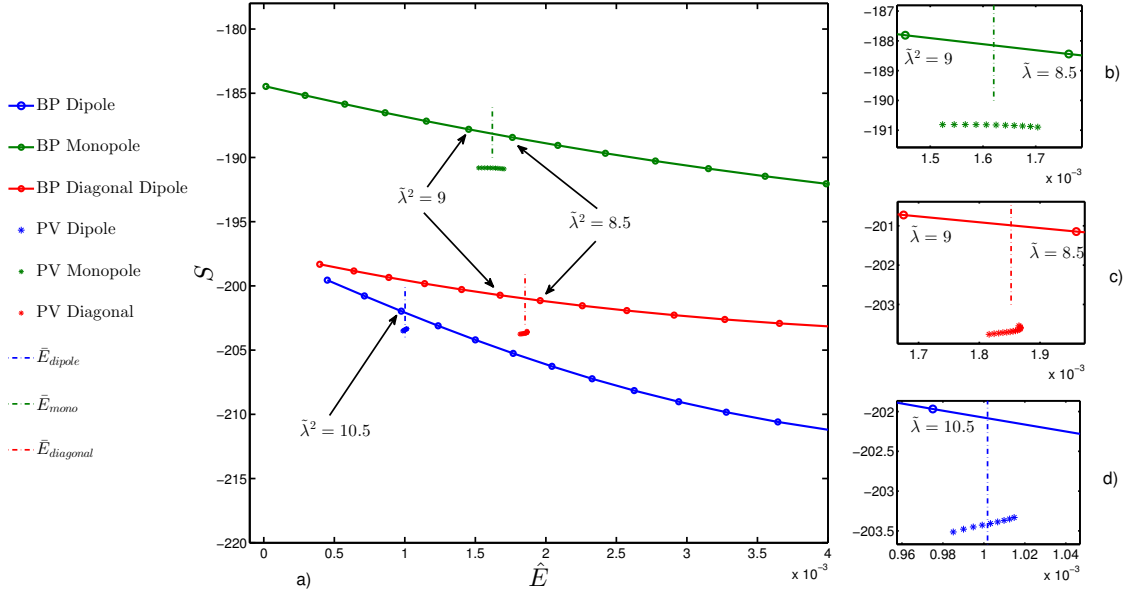


Figure 5.28: Energy-entropy comparison between the results obtained from the solutions of the BP equation and those obtained from the ensembles (PV) in the square. Included on the right three magnified plots for the dipole *d*), the diagonal dipole *c*) and the monopole *b*): in each figure each marker represents the energy \hat{E}_σ and the entropy \hat{S}_σ for each value of the parameter σ .

It can be seen from Fig. (5.28) that the dipole and the diagonal dipole configurations have a substantial difference in energy. However, their entropy is very similar. This suggests that the ensemble for the dipole may not coincide with the equilibrium states established at later time in the simulation. On the other hand, the important fact is given by the difference in entropy between the diagonal dipole and the monopole. Both configurations have a similar energy while the difference in their entropy is comparable to that obtained from solutions of the BP equation. This reinforces the premise on which the statistical mechanical approach is build on: the monopole observed during the dynamical simulations corresponds to a higher entropy state. A quantitative comparison of the values of the non-dimensional entropy for the dipole in the square obtained from

the solution of the BP equation and point vortex dynamics gives

$$\hat{S}_{BP} = -201.968, \quad \hat{S}_{PV} = -203.4001. \quad (5.49)$$

\hat{S}_{BP} is the non-dimensional entropy for the solution found for $\tilde{\lambda}^2 = 10.5$ while the second is the mean value of the non-dimensional entropy evaluated after averaging over all values of the parameter σ for the dipole. The comparison between these two values can be expressed in terms of the percentage error [59] defined by

$$PE(x_{PV}, x_{BP}) = \frac{|x_{BP} - x_{PV}|}{x_{BP}} \times 100\%, \quad (5.50)$$

where the value x_{BP} is the theoretical value obtained from the solution of the BP equation and x_{PV} is the value obtained from the point vortex dynamics. For the values given by Eq. (5.49), the percentage error is given by

$$PE_{dipo} = -0.7\%. \quad (5.51)$$

In the case of the diagonal dipole, the values of the non-dimensional entropy are given by

$$\hat{S}_{BP} = -200.9365, \quad \hat{S}_{PV} = -203.7106, \quad (5.52)$$

where \hat{S}_{BP} is computed from the averaging over the values of \hat{S} obtained from the solution for $\tilde{\lambda}^2 = 8.5$ and $\tilde{\lambda}^2 = 9$. In this case, the percentage error is given by

$$PE_{diago} = -1.4\%. \quad (5.53)$$

In the case of the monopole, the values of the non-dimensional entropy are given by

$$\hat{S}_{BP} = -188.1261, \quad \hat{S}_{PV} = -190.8353, \quad (5.54)$$

where \hat{S}_{BP} is computed from the averaging over the values of \hat{S} obtained from the solution for $\tilde{\lambda}^2 = 8.5$ and $\tilde{\lambda}^2 = 9$. In this case, the percentage error is given by

$$PE_{mono} = -1.4\%. \quad (5.55)$$

From this analysis it can be inferred that the difference in entropy between the results obtained from the ensembles is compatible with the result obtained from the solutions of the BP equation, with a maximum error of 1.4%.

These results concludes the analysis of the entropy for the dipole, diagonal dipole and monopole in the square. In the following part, a similar analysis to the ensembles in the rectangle will be presented.

Entropy comparison in the rectangle

The procedure to classify the ensembles based on their non-dimensional energy \hat{E} and entropy \hat{S} explained at the beginning of this subsection is now applied to the ensembles in the rectangle shown in Fig. (5.16). The non-dimensional energy \hat{E}_σ as a

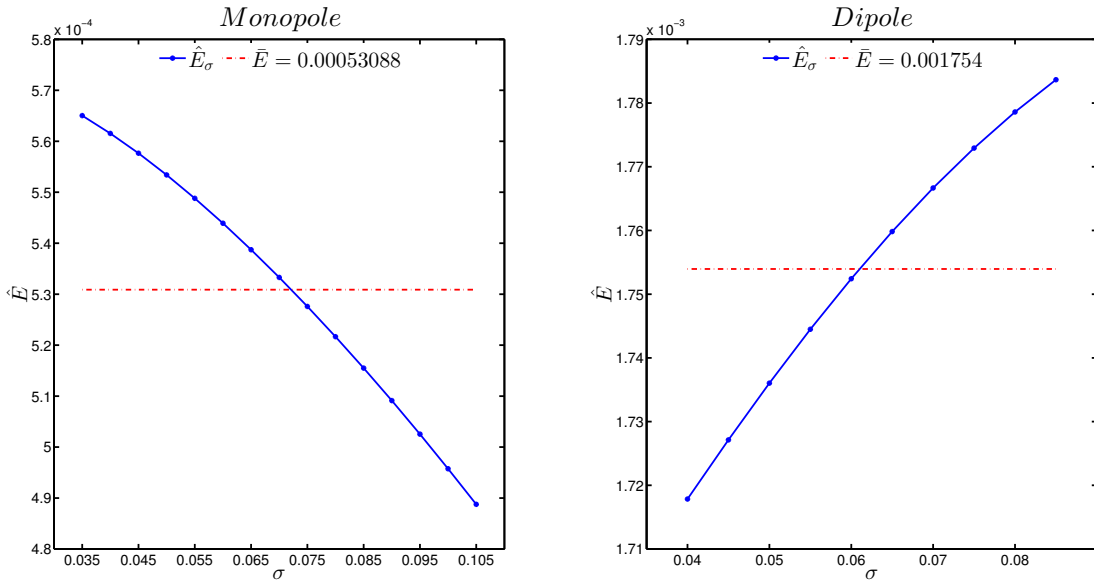


Figure 5.29: Non dimensional energy \hat{E}_σ (blue curve) as a function of the parameter σ and its mean value \bar{E} (red dotted line) for the monopole (left), and the dipole (right) in the rectangle. In the legend the mean values are indicated.

function of the radius σ has been evaluated for the monopole and dipole in the rectangle and are shown in Fig. (5.29). The blue line in each figure represents the value of the energy as a function of σ and the red dotted line is the mean value whose numerical value is indicated in the legend. The values of energies for the two configurations are compatible with the range of energies obtained from the solutions of the BP equation: by looking at Fig. (5.30) it is clear that the energy of the monopole is equivalent to the energy of the monopole solution of the BP equation corresponding to $\tilde{\lambda}^2 = 11$ while for the dipole its energy corresponds to the dipole solution of the BP equation with $\tilde{\lambda}^2 = 8$. The corresponding values for β are then given by

$$\beta_{mono} = -0.4004, \quad \beta_{dipo} = -0.3565. \quad (5.56)$$

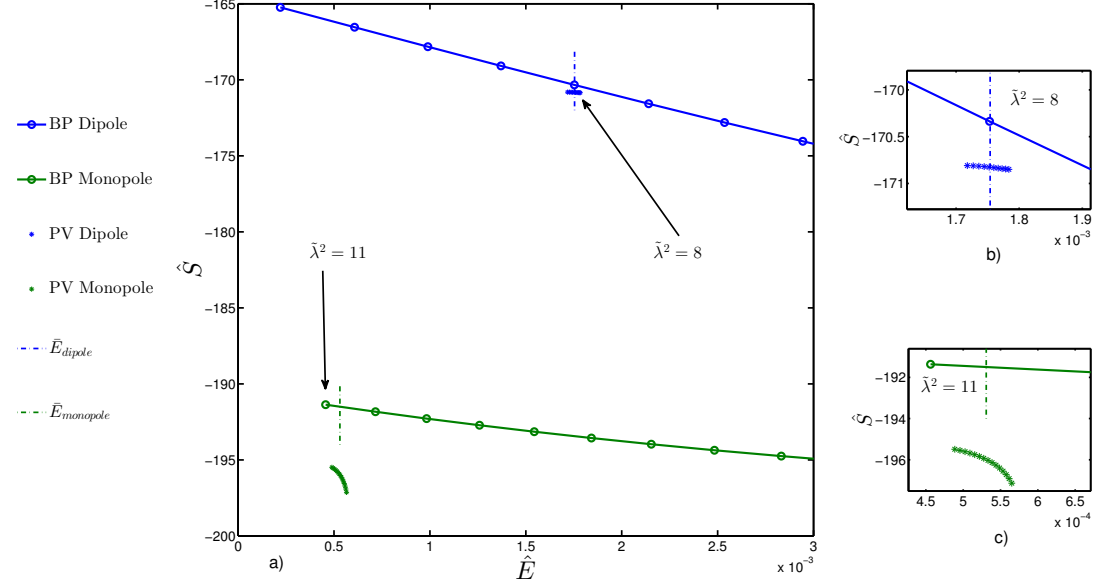


Figure 5.30: Energy-entropy comparison between the results obtained from the solutions of the BP equation and those obtained from the ensembles (PV) in the rectangle. On the right two magnified plots for the the monopole *c*) and the dipole *b*): in each figure each marker represents the energy \hat{E}_σ and the entropy \hat{S}_σ for each value of the parameter σ .

A comparison of the non-dimensional entropy \hat{S}_σ computed from the ensembles with solutions of the BP equation is shown in Fig. (5.30). The figures on the right show magnified plots of the non-dimensional energy and non-dimensional entropy for different values of the core size σ for the monopole *c*) and the dipole *b*). As expected from the result of §4.5 the dipole corresponds to a higher entropy configuration than the monopole which is now also confirmed by direct point vortex simulations. Now the percentage error between the values of the entropy obtained from the solutions of the BP equation and the values obtained from the ensembles is evaluated for the monopole and the dipole. For the monopole these values are given by

$$\hat{S}_{BP} = -191.368, \quad \hat{S}_{PV} = -196.1323, \quad (5.57)$$

where \hat{S}_{BP} is the non-dimensional entropy for the solution found for $\tilde{\lambda}^2 = 11$ while \hat{S}_{PV} is the mean value of the non-dimensional entropy for all values of the parameter σ for the monopole. In this case the value of the percentage error is given by

$$PE_{mono} = -2.5\%. \quad (5.58)$$

For the dipole the non-dimensional entropies are given by

$$\hat{S}_{BP} = -170.3366, \quad \hat{S}_{PV} = -170.8288, \quad (5.59)$$

where \hat{S}_{BP} is the non-dimensional entropy for the solution found for $\tilde{\lambda}^2 = 8$ and where \hat{S}_{PV} the second is the mean value of the non-dimensional entropy for all values of the parameter σ for the dipole. In this case the value of the percent error is given by

$$PE_{dipo} = -0.3\%. \quad (5.60)$$

It can be concluded that the values obtained by analysing the ensembles are compatible with the results obtained from the solutions of the BP equation with a maximum error of 2.5%.

5.4 Analysis of the Angular Momentum

In the previous section the non-dimensional energy \hat{E} and entropy \hat{S} of ensembles in the square and the rectangle have been evaluated. This analysis allowed the comparison between the theoretical values given by the solutions of the BP equation and the ensembles generated from the dynamics of the point vortices. Moreover, good agreement with the result obtained in §4.7 has been found. In this section the comparison of the values of the angular momentum associated to the solutions of the BP equation and to the ensembles will be performed.

In §4.7 the spontaneous acquisition of angular momentum by a flow was described and it occurs when the vortices organise themselves in an asymmetric configuration for which $\langle \psi \rangle \neq 0$. The qualitative analysis on the trend of the angular momentum has been presented in §5.2.1 and §5.2.2 for the square and the rectangle respectively. These analyses confirmed that when the system is in a monopole configuration, the value of L is non-zero and for any symmetric configuration (dipole or diagonal dipole) the value of the angular momentum is close to zero.

In order to evaluate the normalised angular momentum , it is useful to recall the non-dimensional linearised energy \hat{E}_{lin} given by Eq. (4.23) introduced in §4.2 and the non-dimensional angular momentum \tilde{L}

$$\hat{E}_{lin} = \frac{\lambda^2 \mathcal{D}}{2} [\langle \Psi^2 \rangle - \langle \Psi \rangle^2], \quad L = 2\mathcal{D}\langle \Psi \rangle. \quad (5.61)$$

The normalised angular momentum was introduced in §2.5.3 and it is the value of

the angular momentum divided by the maximum value accessible for the system; this corresponds to the angular momentum that the system will have if it would rotate as a solid body. The normalised angular momentum is therefore given by Eq. (2.143)

$$\hat{L} = \frac{L}{L_{Max}} = \frac{2\mathcal{D}\langle\Psi\rangle}{\sqrt{\hat{E}_{lin}\mathcal{I}}}, \quad (5.62)$$

where \mathcal{I} is the moment of inertia of a rectangular body given by Eq. (2.140). By substituting Eq. (2.140) into the above equation, the non-dimensional normalised angular momentum becomes

$$\hat{L} = 4\sqrt{\frac{3}{\lambda^2\mathcal{D}}} \left[\left(\frac{L_x L_y}{L_x^2 + L_y^2} \right) \left(\frac{\langle\Psi\rangle^2}{\langle\Psi^2\rangle - \langle\Psi\rangle^2} \right) \right]^{1/2} \quad (5.63)$$

It is clear from this formula that \hat{L} vanishes if $\langle\Psi\rangle = 0$ while $\hat{L} \neq 0$ when $\langle\Psi\rangle \neq 0$. With these definitions a comparison between the value of \hat{L} associated to the solutions of the BP equation and to the ensembles in the square and the rectangle will now be performed.

Angular momentum in the square

It has been shown that for the diagonal dipole and the monopole, the value of the mean non-dimensional energy \hat{E} lies in between the values of $\tilde{\lambda}^2 = 8.5$ and $\tilde{\lambda}^2 = 9$ and for the dipole, this value is very close to $\tilde{\lambda}^2 = 10.5$. In the case of the monopole, starting from the solutions Ψ of the BP equation for $\tilde{\lambda}^2 = 8.5$ and $\tilde{\lambda}^2 = 9$, it is possible to evaluate λ^2 by using Eq. (5.46) and hence to evaluate the non-dimensional normalised angular momentum \hat{L} for these solutions. For the dipole and the diagonal dipole, the theoretical values are zero due to the fact that in this case $\langle\Psi\rangle = 0$.

For any given ensemble in the square, a range of σ has been found in §5.3.3. Moreover, for each value of the parameter σ , it is possible to consider the non-dimensional streamfunction $\Psi_\sigma = \rho\beta\gamma\psi_\sigma$ where ψ_σ can be evaluated by Eq. (5.38). Therefore, for each streamfunction Ψ_σ , the value of \hat{L} can be evaluated: the results are shown in Fig. (5.31).

For all the plots in Fig. (5.31), the blue markers represent the values of \hat{L}_σ obtained from the ensembles (indicated with Ensembles PV in the legend) as a function of the parameter σ and the dotted blue line represents the mean value. In the case of the monopole (figure on the right) there are also two dotted lines: the red and the green lines correspond to the value of the \hat{L} for the solution of the BP equation for $\tilde{\lambda}^2 = 9$ and

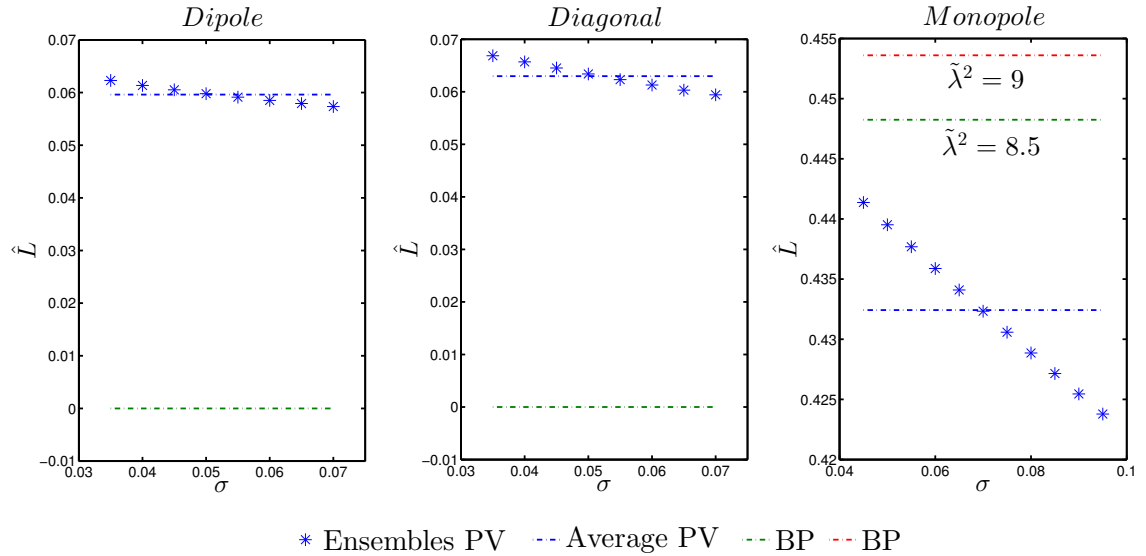


Figure 5.31: Non-dimensional normalised angular momentum associated to the ensembles in the square: the dipole (left), the diagonal dipole (centre) and monopole (right). The blue dotted lines represent the mean value of each configuration and the green dotted line the values of \hat{L} associated to the solutions of the BP equation. In the case of the monopole there are two values: one related to the solution for $\tilde{\lambda}^2 = 9$ and the other one for $\tilde{\lambda}^2 = 8.5$.

$\tilde{\lambda}^2 = 8.5$ respectively. The numerical mean values of the angular momentum obtained from the ensembles are given by

$$\hat{L}_{dipo} = 0.0596, \quad \hat{L}_{diago} = 0.0629, \quad \hat{L}_{mono} = 0.4324, \quad (5.64)$$

while the values obtained from the solutions of the BP equation are given by

$$\hat{L}_{dipo} = \hat{L}_{diago} = 0, \quad \hat{L}_{mono}^{8.5} = 0.4482, \quad \hat{L}_{mono}^9 = 0.4536, \quad (5.65)$$

where the superscripts 8.5 and 9 refer to the values of $\tilde{\lambda}^2$ for the monopole configuration. In analogy to the errors computed for non-dimensional entropy \hat{S} the percentage error between the theoretical values (taken from the solutions of the BP equation) and the values of \hat{L} obtained from the ensembles in the square are evaluated. In particular for \hat{L} obtained from the solutions of the BP equation, the mean value of $\hat{L}_{mono}^{8.5} = 0.4482$ and $\hat{L}_{mono}^9 = 0.4536$ has been used and in this case the percentage difference between this value and \hat{L}_{mono} is given by

$$PE_{mono} = 4.3\%. \quad (5.66)$$

CHAPTER 5. POINT VORTEX DYNAMICS IN THE SQUARE AND THE RECTANGLE

Unfortunately, for the dipole and the diagonal dipole the percent difference can not be evaluated since the theoretical value is zero. However, the maximum absolute error in this case is 6%.

From this analysis it can be inferred that the values found starting from the solutions of the BP equation and the ensembles generated during the dynamics of the point vortices, are in good agreement with a maximum error of 6%.

Angular momentum in the rectangle

The same analysis is now performed for the ensembles in the rectangle. In this geometry, the two ensembles have a non-dimensional energy which corresponds to the solutions of the BP equation for $\tilde{\lambda}^2 = 11$ for the monopole and $\tilde{\lambda}^2 = 8$ for the dipole. The results for \hat{L} as in the case for the square are shown in Fig. (5.32). The numerical mean values of \hat{L} obtained from the ensembles are given by

$$\hat{L}_{mono} = 0.3696, \quad \hat{L}_{dipo} = 0.0298, \quad (5.67)$$

while the values obtained from the solutions of the BP equation are given by

$$\hat{L}_{mono} = 0.3844, \quad \hat{L}_{dipo} = 0. \quad (5.68)$$

The percentage error in the case of the monopole is equal to

$$PE_{mono} = 3.8\%. \quad (5.69)$$

For the dipole the absolute error is approximately 3%.

From this analysis it can be inferred that the values found starting from the solutions of the BP equation and the ensembles generated during the dynamics of the point vortices, are in good agreement with a maximum error of 4.3%.

5.5 Annihilation with the Boundaries

In §5.1 the dynamics of point vortices has been studied in the square and the rectangle where annihilations between vortices with opposite circulation can occur. The annihilation which has been manually introduced in the dynamics, allowed the system to migrate into the negative temperature regime always preserving its neutrality. However, in physical systems such as a Bose-Einstein condensate, the point vortices can also annihilate at the boundaries. This additional effect can cause the system to become

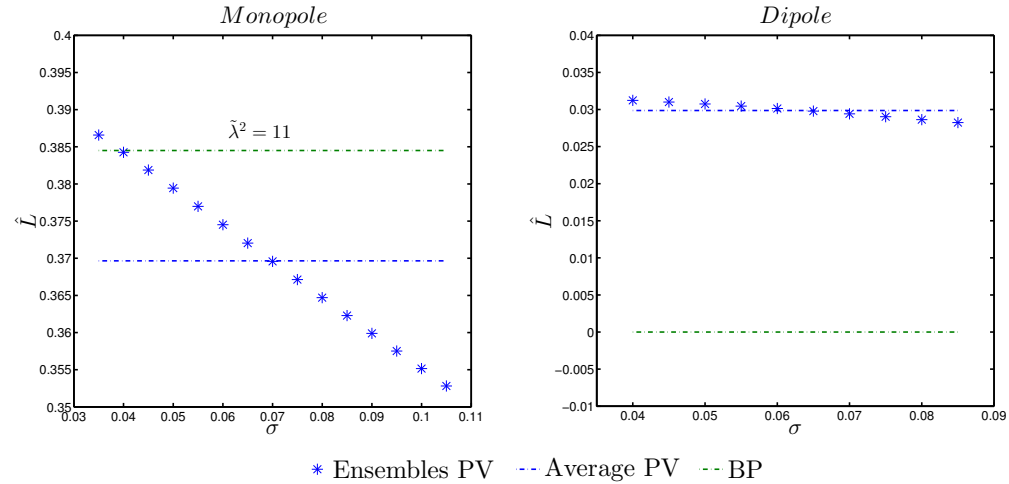


Figure 5.32: Non-dimensional normalised angular momentum associated to the ensembles in the rectangle: the monopole (left) and the dipole (right). The blue dotted lines represent the mean value of each configuration and the green dotted line the values of \hat{L} associated to the solutions of the BP equation.

non-neutral resulting in an asymmetry in the number of charges. The result in the long term dynamics is that the system can become polarised and this may favour the emergence of a large monopole configuration. As a consequence, the angular momentum can be altered by the polarised state of the vortices. The analysis of the angular momentum for a system where the annihilation includes pairs of opposite circulation as well as between vortices and the boundaries is now presented in the square and the rectangular domain.

The same initial conditions used in §5.1 for the dynamics of point vortices in the square and the rectangle are now considered. In order to study the differences in the dynamics of the vortices in these systems, the equation of motion (2.79) are numerically integrated and two annihilation parameters have been added to the dynamics. The first one is the usual annihilation parameter between vortices with opposite circulation $\delta = 0.01$ and the second one is the parameter which takes into account the annihilation between the vortices and the boundaries $\delta_{\text{bound}} = \delta/2 = 0.005$. The reason for this choice of values lies in the fact that the boundary is generated by the presence of an image of the opposite sign. Hence, this value is the analogue of the annihilation parameter δ between vortices of opposite sign inside the domain. In the case being considered, the system develops a strong asymmetry in the number of vortices, due to the annihilation of the vortices at the boundaries. For both the square and the rectangle, majority of decay occurs with the negative vortices and therefore, the final configurations present a large number of positive vortices which occupy the centre of

CHAPTER 5. POINT VORTEX DYNAMICS IN THE SQUARE AND THE RECTANGLE

the domain in a monopole configuration. The asymmetry in the number of vortices can be quantified by evaluating the polarisation P defined as

$$P(N^+, N^-) = \frac{N^+ - N^-}{N^+ + N^-}, \quad (5.70)$$

where N^\pm are the number of positive and negative vortices. Figure (5.33) shows the graph of the number of positive (blue curve) and negative (green curve) vortices in the square a) and in the rectangle b) as a function of time τ . The inset figures show the vortex configurations when the system is polarised due to the annihilation between the vortices and the boundaries. It is worth noticing that the process of polarisation takes place earlier in the rectangle. This behaviour can be explained by noticing that the value of the perimeter of the rectangle is larger than the perimeter of the square with a consequent higher probability of annihilation between vortices and the boundaries in the rectangle. As a consequence, for both the rectangle and the square, the system acquires a positive value for the total angular momentum L . The evaluation of L by using Eq. (5.3) during the dynamical simulations for both the square and the rectangle is presented in Fig. (5.34). As already discussed in §5.2, the graph of the angular momentum as a function of time can be used to describe the configuration which the system is exploring. At early times, when a large number of annihilations occur, both systems seem to do not develop a strong asymmetry in the number of vortices as shown in Fig. (5.33). This is also confirmed from the trend of the angular momentum and, in particular, by the presence of few zeros in both graphs at the beginning of the dynamics. The zeros of the angular momentum L correspond to symmetric spatial configurations of positive and negative vortices, which can take place if the system is not strongly polarised. However, if the long term dynamics is investigated, this asymmetry becomes more pronounced: the systems become strongly polarised and they acquire a well defined value of the angular momentum L . This fact follows by the lack of zeros in the graph of the angular momentum shown in Fig. (5.34) and it is confirmed by the asymmetric vortex configurations presented in Fig. (5.33). The inset figures represent the configuration and the corresponding contour plot of the streamfunction at $\tau = 6$ for both the square and the rectangle: they both reveal the monopole configuration where the positive charges tend to occupy the centre of the domain.

This brief analysis shows that when the system is non neutral, it will naturally evolve towards a monopole configuration with a consequent acquisition of angular momentum L . However, it can not be inferred that this is the only possible outcome: during the dynamics the symmetry in the number of vortices can also be restored due to

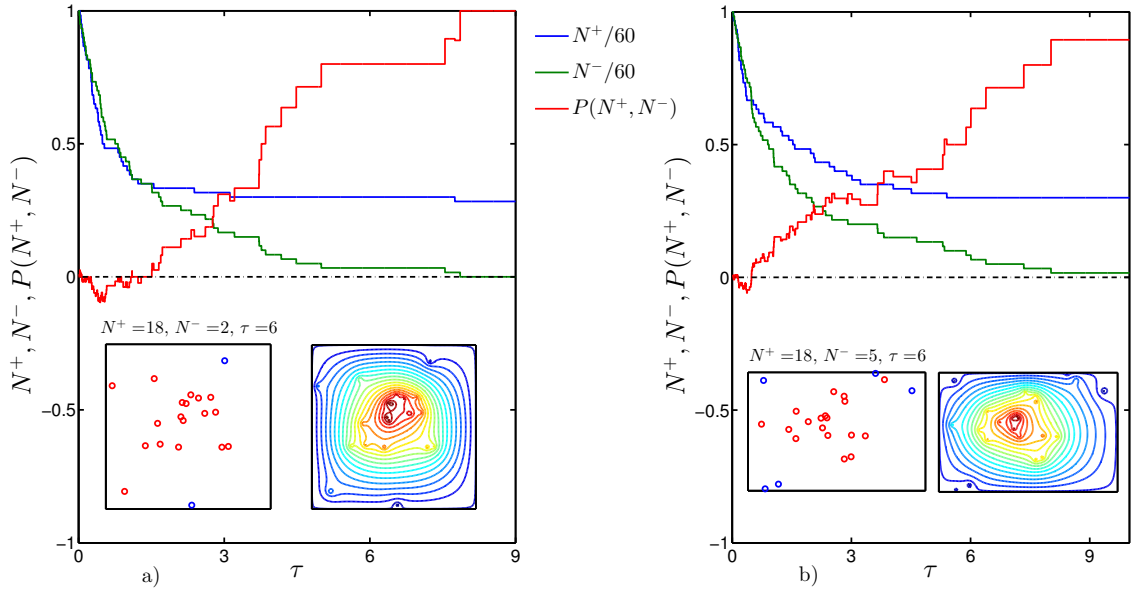


Figure 5.33: Normalised number of positive (blue curve) and negative (green curve) vortices in the square *a*) and in the rectangle *b*). The normalisation is given by the initial number of vortices $N^\pm = 60$. The red curve represents the polarisation $P(N^+, N^-)$ and the black dashed line represents the zero. The inset figures show the vortex positions and the corresponding streamfunction ψ . Above each configuration the number of positive and negative vortices are indicated.

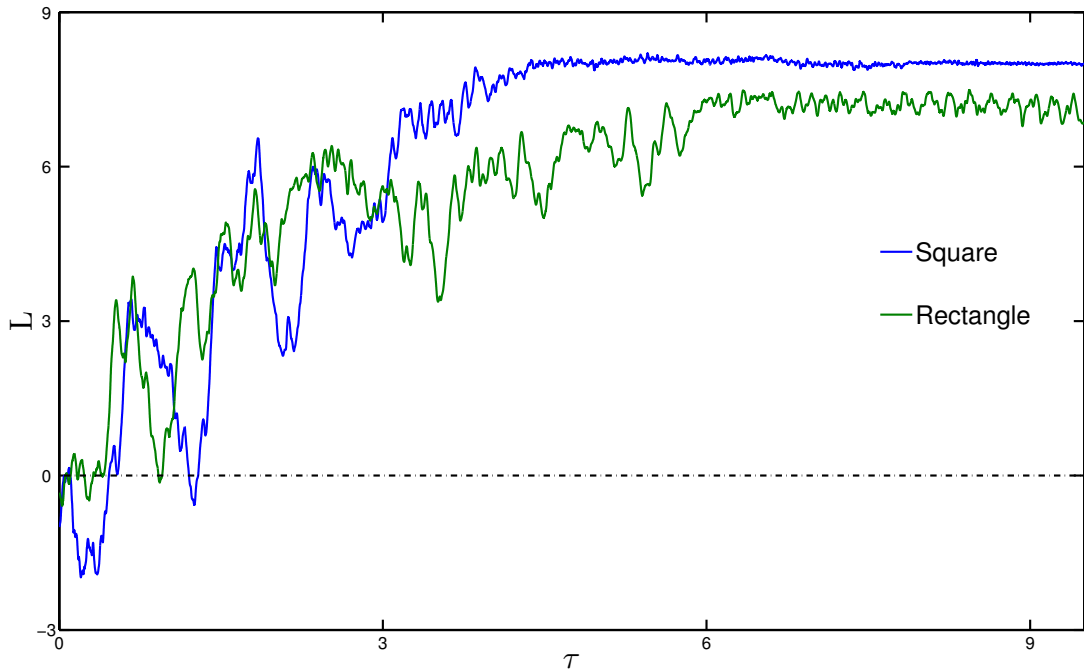


Figure 5.34: Total angular momentum in the square (blue curve) and in the rectangle (green curve).

CHAPTER 5. POINT VORTEX DYNAMICS IN THE SQUARE AND THE RECTANGLE

the annihilation on the boundaries. In other words, the annihilation parameter δ_{bound} , which is the cause of the asymmetry in the number of vortices, can act on the remaining charges and push the system again in a neutral configuration. It has to be remarked that this is a possibility which here has not been tested. A possible way to demonstrate this scenario requires the study of a large number of simulations and determine the number of cases in which the symmetry is naturally restored.

Chapter 6

Gross-Pitaevskii Simulations in the Square and the Rectangle

In the previous Chapter, the dynamics of point vortices in the square and the rectangle was investigated by using the point vortex model (PVM). For both geometries, the averaged streamfunctions correspond to the solutions of the Boltzmann-Poisson (BP) equation found in §4.4 and §4.5. The aim of this Chapter is to demonstrate that the same predictions apply to the dynamics of quantised vortices in Bose-Einstein condensates (BEC). An important difference between the dynamics of point vortices and the dynamics in the Gross-Pitaevskii (GP) model is given by the fact that in the latter, the annihilation process is permitted to occur by the underlying macroscopic theory without the need for any phenomenological modelling. Moreover, there are two types of annihilation: annihilation between vortices and antivortices and annihilation of vortices at the boundaries. As a consequence of the latter type, the system can develop asymmetries in the number of positive and negative vortices and become polarised. This process was investigated in §5.5 when the effects of the annihilation of vortices at the boundaries were manually included in the dynamics of point vortices. In order to describe the dynamics of quantised vortices in a two-dimensional BEC, the two dimensional GP equation (2.14) presented in §2 will be numerically solved in the square, and in the rectangle with aspect ratio $\Lambda = 1.5$.

6.1 Gross-Pitaevskii Equation in Two Dimensions

In the laboratories, BECs are trapped in confined regions of the space by using trapped harmonic-oscillator potentials with frequencies ω_x , ω_y , and ω_z . If $\omega_z \gg \omega_x \approx \omega_y$ and $\mu \ll \hbar\omega_z$ then the dynamics along z -direction is frozen and the condensate is

considered quasi two-dimensional. Motivated by [84], [?], and [?] the condensate is assumed to contain $N = 5 \times 10^5$ atoms of ^{87}Rb ($m = 1.4273 \times 10^{-25}\text{kg}$) trapped along the z -direction with a tight harmonic oscillator trap with frequency $\omega_z = 2\pi \times 1440$ Hz. In this case, the two-dimensional condensate wavefunction $\phi(x, y)$ can be written as

$$\phi(x, y) = \frac{1}{\sqrt{2\pi a_z}} \int \phi_{3D}(x, y, z) e^{-z^2/a_z^2} dz, \quad a_z = \sqrt{\frac{\hbar}{m\omega_z}} = 2.84\mu\text{m}. \quad (6.1)$$

Therefore, by setting $V_{ext} = 0$, the three-dimensional GP equation given by Eq. (2.14) reduces to [92]

$$i\hbar \frac{\partial \phi(x, y, t)}{\partial t} = -\frac{\hbar^2}{2m} \nabla^2 \phi(x, y, t) + g_{2D} |\phi(x, y, t)|^2 \phi(x, y, t), \quad (6.2)$$

where g_{2D} is the coupling constant in two spatial dimensions given by

$$g_{2D} = g \sqrt{\frac{m\omega_z}{2\pi\hbar}}, \quad g = \frac{4\pi\hbar^2 a_s}{m}, \quad (6.3)$$

and a_s is the s -wave scattering length. For these parameters, the healing length ξ at $z = 0$ is given by

$$\xi = \frac{\hbar L}{\sqrt{2mg_{2D}N}} = 0.284\mu\text{m}. \quad (6.4)$$

The extent of the square box potential along x and y is assumed to correspond to $L^2 \sim 72\mu\text{m}^2$. These values ensure the possibility of having a BEC which can contain many well-separated vortices. Equation (6.2) can be written in non-dimensional form by scaling space, time, and the wavefunction as follows

$$t \rightarrow \frac{2mL^2}{512^2\hbar}t, \quad x \rightarrow \frac{L}{512}x, \quad y \rightarrow \frac{L}{512}y, \quad \phi \rightarrow \sqrt{N}\phi, \quad (6.5)$$

which can be inserted into Eq. (6.2) in order to obtain

$$i\frac{\partial \phi}{\partial t} = -\nabla^2 \phi + \tilde{g} |\phi|^2 \phi, \quad (6.6)$$

where $\tilde{g} = 2mg_{2D}N/\hbar^2 = 93367$. The non-dimensional GP equation given by Eq. (6.6) is then numerically solved on a 512×512 grid by using a symmetric Strang Splitting method of order 2 [57] with a timestep of $\Delta t = 0.1$. As in the previous Chapter, the sides of the rectangular domain are given by $L_x = 512\sqrt{\Lambda}$ and $L_y = 512/\sqrt{\Lambda}$ in order to ensure the area remains constant. Moreover, motivated by [50], the condensate is assumed in an optical square box potential which is simulated by imposing reflec-

tive boundary conditions on the condensate wavefunction $\phi(x, y, t)$. These boundary conditions are simulated by using a discrete cosine transform in the Strang Splitting method.

The initial condition for the GP simulation is generated by considering a particular realisation of the position of the vortices used in §5.1.1 for the square and in §5.1.2 for the rectangle. The phase field $\varphi(x, y)$ and the density field $\phi(x, y)$ are generated as follows

$$\varphi(x, y) = \pm \sum_{k=1}^{N^\pm} \arctan \left(\frac{y - y_k^\pm}{x - x_k^\pm} \right), \quad \phi(x, y) = e^{i\varphi(x, y)}, \quad (6.7)$$

where $N^+ = 60$ and $N^- = 60$ are the number of vortices with positive and negative circulation located at (x_k^\pm, y_k^\pm) . The density field is then relaxed through integration of the GP equation in imaginary time to give the desired initial distribution of vortices. During the dynamics, the position of the vortices are identified numerically by using a method developed by Villois *et al* in [2]. Information about the circulation of each vortex can not be extracted by evaluating the vorticity field. In fact, for the GP model $\boldsymbol{\omega} = \nabla \times \mathbf{v}$ is identically zero apart from the core of the vortex where it is given by a Dirac delta. Rather, the sense of circulation of each vortex can be identified by considering the value of the *pseudo-vorticity* $\boldsymbol{\omega}_{ps}$ defined by

$$\boldsymbol{\omega}_{ps} = \frac{1}{2} \nabla \times \mathbf{j}, \quad \mathbf{j} = \rho \mathbf{v} = \frac{\hbar}{2i} (\phi^* \nabla \phi - \phi \nabla \phi^*), \quad (6.8)$$

where ϕ^* is the complex conjugate of ϕ , $\rho = m|\phi|^2$ is the density, and \mathbf{v} is given by Eq. (2.30). This quantity, is finite at the position of each vortex but rapidly decays to zero outside the healing layer. Moreover, its sign determines the sense of the circulation of the vortex [26]. Knowledge on the positions of the vortices and their circulation are then used to generate the streamfunction ψ of the flow by using Eq. (2.128). This allows time averaged streamfunctions to be evaluated within the desired time intervals.

6.2 Dynamics in the Square

The same initial condition as the one presented in §5.1.1 is now generated in a square with sides $L_x = L_y = 512$ and it is shown in Fig. (6.1). Figure *a*) shows the density field $|\phi|^2$ where the vortices correspond to localised depletions in the density field. Figure *b*) is the corresponding pseudo-vorticity field $\boldsymbol{\omega}_{ps}(x, y)$. The red and the blue dots correspond to the positions of positive and negative circulation, respectively. The non-dimensional GP equation (6.2) is then integrated in time. As the annihilation processes

reduces the number of vortices the vortex gas migrates into the negative temperature regime. The graph related to the number of vortices and antivortices as a function of time is presented in Fig. (6.2). In contrast to the PVM, in this case annihilation can also occur to the boundaries and therefore, the system can become polarized where the polarisation of the system is given by Eq. (5.70). Figure (6.2) shows the total number

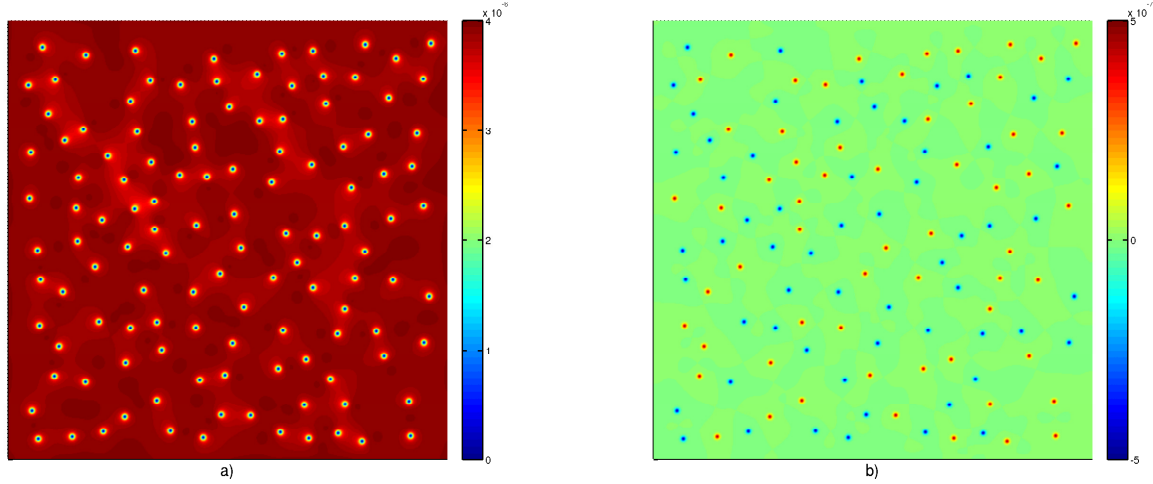


Figure 6.1: Initial condition for the GP simulation in the square: Fig. *a*) is the density field $|\phi|^2$ and, *b*) is the corresponding pseudo-vorticity field ω_{ps} . The red and blue dots represent the vortices and antivortices, respectively.

of vortices and antivortices (blue and green curve respectively) as a function of time τ in unit of $t_v = L^2/|\gamma|$ where $L^2 = 512^2$ is the size of the domain and $|\gamma| = 4\pi$ is the value of the circulation given by Eq. (2.37) in terms of the non-dimensional units defined by Eqs. (6.5). The red curve corresponds to the polarisation given by Eq. (5.70). The curves are normalised by the initial number of positive and negative vortices. Knowledge of the positions and the number of vortices and antivortices permits the evaluation of the time-averaged streamfunction per vortex. The time-averaged streamfunctions of the dipole, diagonal dipole and monopole found during the dynamics are presented in Fig. (6.3). These configurations coincide with those found in §5.1.1 and, therefore, they can also be explained in terms of high entropy states. It is important to point out, as observed in the point vortex simulation, that the monopole configuration appears at later time when the system is deeply into the negative temperature regime. Once the monopole configuration takes place, the positive vortices are closer to the boundaries and therefore the system is more likely to become negatively polarised. In other words, the process of the formation of the monopole can be divided into two stages. At first, the monopole appears because the configuration maximises the entropy. After

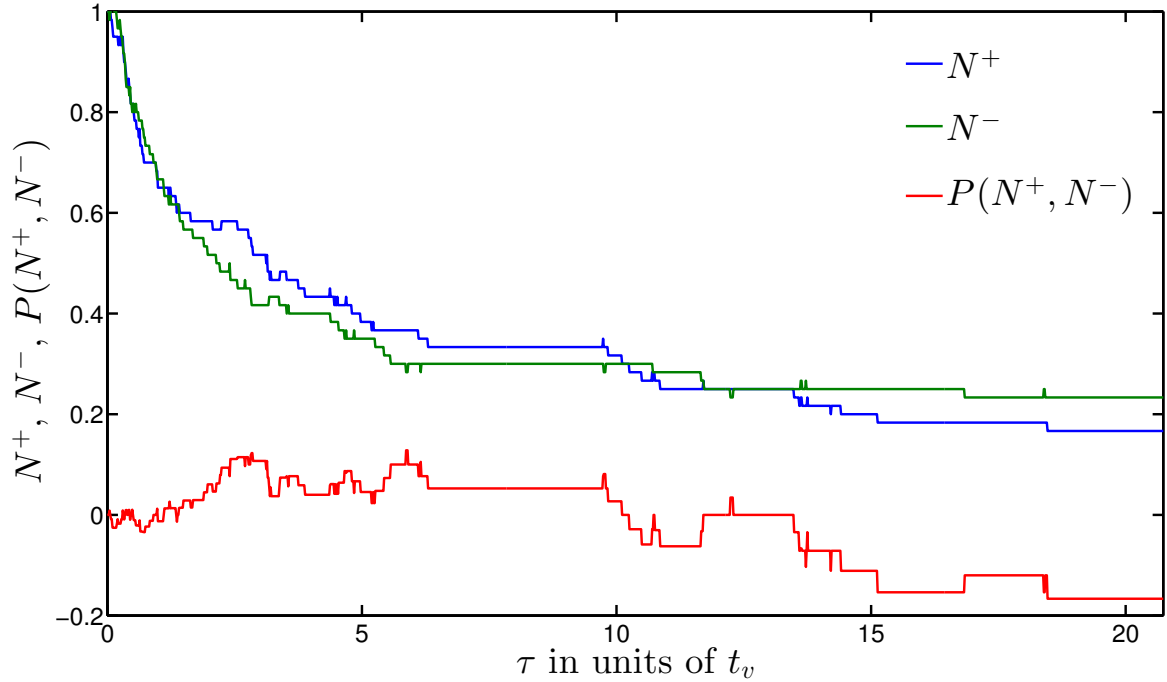


Figure 6.2: Number of vortices (blue curve), antivortices (green curve) and polarisation (red curve) as a function of time τ in units of t_v during the GP simulation in the square. The discrepancy in the number of positive and negative vortices gives raise to a negative polarisation P .

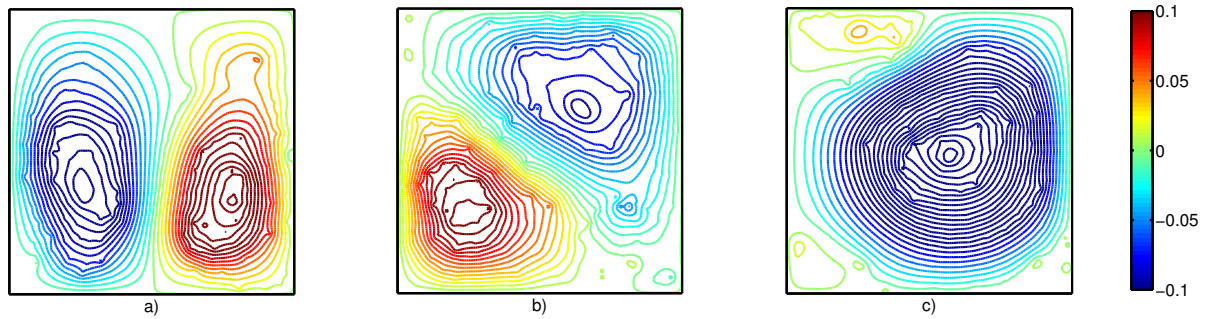


Figure 6.3: Averaged streamfunction per total number of vortices $\psi/(N^+ + N^-)$ in the square for three configurations in which the system is found during the dynamics. For the dipole *a*) the averaging interval corresponds to $\tau \in [11.5t_v - 12.95t_v]$, for the diagonal dipole *b*) it corresponds to $\tau \in [10.06t_v - 10.49t_v]$, and for the monopole *c*) it corresponds to $\tau \in [18.4t_v - 18.7t_v]$.

this process takes place, the annihilation of the vortices closer to the boundaries will increase the difference between vortices and antivortices as described in §5.5. Therefore, at long times, the emergence of the monopole will favour the formation of a polarised gas. The analysis of the angular momentum L given by Eq. (5.3) is presented in Fig. (6.8). The green curve presents a similar behaviour to the curve presented in Fig. (5.10). It is interesting the presence of few zeros around $\tau \sim 10t_v$ related to symmetric configurations, followed by a slow process of developing a non-zero angular momentum. In this case the system slowly evolves toward the monopole configuration which maximises its entropy. These results lead to the conclusion that the predictions of the mean-field BP theory apply also to a Bose gas governed by the GP equation. In particular, all the structures investigated in §4.4 and revealed during the dynamics of point vortices in §5.1.1, have also been found in the context of the GP model in the early stage of the dynamics. At later time, when the vortex gas becomes strongly polarised due to the annihilations of vortices at the boundaries, the results are consistent with the case studied in §5.5 where the PVM with the additional annihilation parameter of vortices at boundaries was considered.

6.3 Dynamics in the Rectangle

The square is now stretched into a rectangle with sides $L_x = 512\sqrt{\Lambda}$ and $L_y = 512/\sqrt{\Lambda}$. The same initial condition as the one presented in §5.1.2 is generated and it is shown in Fig. (6.4). Figure *a*) shows the density field $|\phi|^2$ where the vortices correspond

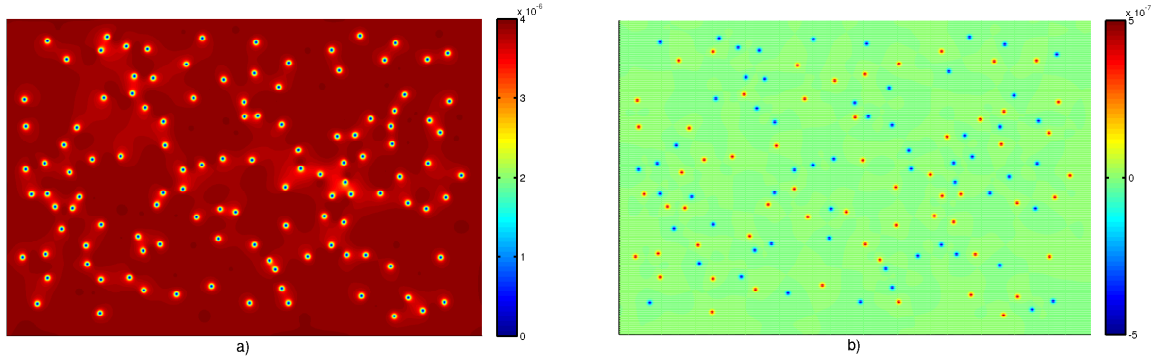


Figure 6.4: Initial condition for the GP simulation in the rectangle with aspect ratio $\Lambda = 1.5$: Fig. *a*) is the density field $|\phi|^2$ and, *b*) is the corresponding pseudo-vorticity field ω_{ps} . The red and blue dots represent the vortices and antivortices, respectively.

to localised depletions in the density field. Figure *b*) is the corresponding pseudo-

vorticity field $\omega_{ps}(x, y)$. Similarly to §6.2 the annihilation process reduces the number of vortices and the vortex gas migrates into the negative temperature regime. The number of positive and negative vortices during the dynamics is presented in Fig. (6.5). The figure shows also the polarisation given by Eq. (5.70) (red curve). In the first half

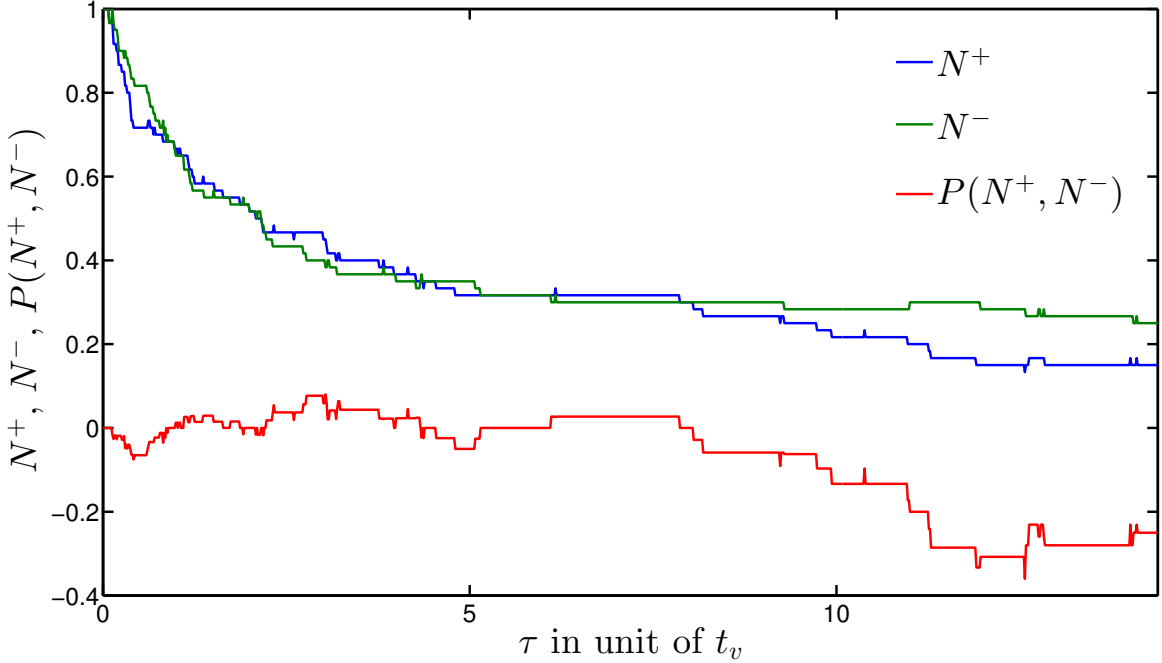


Figure 6.5: Number of vortices (blue curve), antivortices (green curve) and polarisation (red curve) as a function of time τ in units of t_v during the GP simulation in the rectangle. The discrepancy in the number of positive and negative vortices gives raise to a negative polarisation P .

of the simulation, averaged streamfunctions reveal the presence of monopoles as shown in Fig. (6.6). However, the system gradually evolves towards the maximum entropy configuration as the vortices arrange themselves in a dipole as shown in Fig. (6.7) *a*). However, at later time the system can be found again the a monopole configuration as shown in Fig. (6.7) *b*). The occurrence of the monopole configuration at later time can be understood in terms of the polarisation which is more important in the rectangle rather than in the square. Since the rectangle has a larger perimeter than the square, the system tends to annihilate more vortices at the boundaries which causes the system to become more polarised. The difference in the number of positive and negative vortices favours the formation of a monopole configuration as already discussed in the case of a strongly polarised gas in §5.5. The analysis of the angular momentum L given by Eq. (5.3) is presented in Fig. (6.8). The blue curve presents the same oscillating behaviour described in §5.2.2 for the PVM. However, around $\tau \sim 10t_v$ the system which

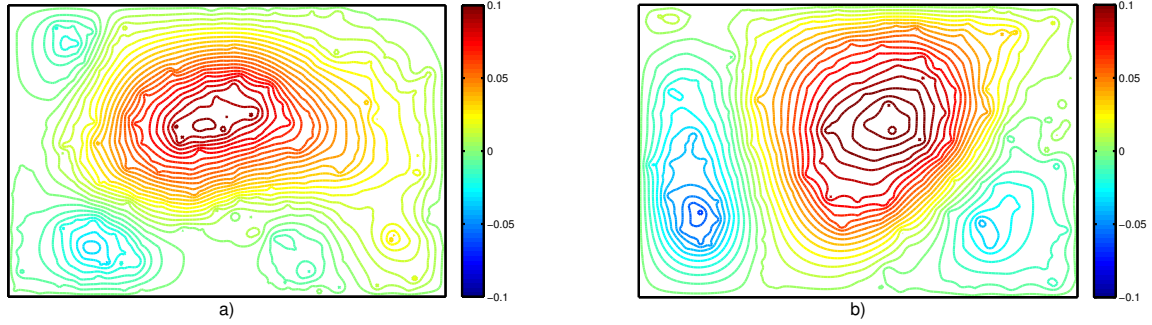


Figure 6.6: Averaged streamfunctions per total number of vortices $\psi/(N^+ + N^-)$ in the rectangle during the first half of the GP simulation. Both images show the presence of a monopole at different stage during the dynamics. The averaging interval of the configuration *a*) corresponds to $\tau \in [2.44t_v - 2.58t_v]$ while for *b*) it corresponds to $\tau \in [6.61t_v - 6.84t_v]$.

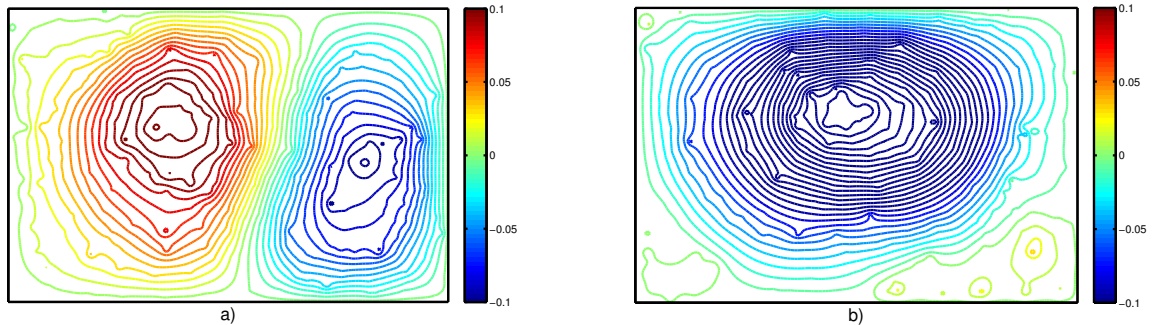


Figure 6.7: Averaged streamfunctions $\psi/(N^+ + N^-)$ in the rectangle during the GP simulations in the second half of the dynamics: on the left the dipole configuration and on the right the monopole is caused by a strongly polarised system. The averaging interval of the configuration *a*) corresponds to $\tau \in [8.77t_v - 9.2t_v]$ while for *b*) it corresponds to $\tau \in [12.65.61t_v - 13.23t_v]$ when the system is strongly polarised.

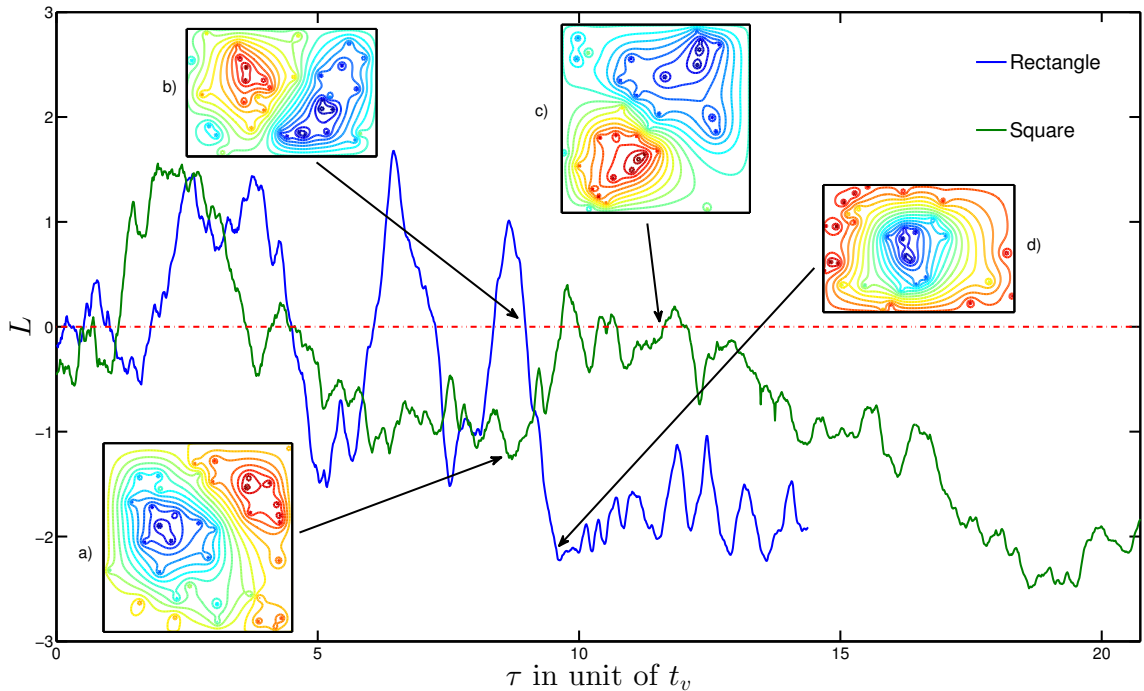


Figure 6.8: Graph of the total angular momentum L as a function of time τ in unit of t_v in the square and in the rectangle: the inset figures are the streamfunction per vortex $\psi/(N^+ + N^-)$ for different instantaneous configurations during the dynamics. Figures a) and c) show the streamfunction in the square of an asymmetric and symmetric configuration during the dynamics. Figures b) and d) show the streamfunction of a symmetric and an asymmetric configuration in the rectangle, respectively. The colors of the contour plots refer to the same colorbar shown in Fig. (6.6) and the red dotted line represents the zero.

is found in a monopole configuration (see inset Fig. (6.8) *d*) becomes strongly polarised and the vortices rearrange themselves in a monopole configuration with a consequent non-zero value of the angular momentum L . Therefore, it has been shown that the results obtained by using the GP model are consistent with the theoretical predictions given by the mean-field BP equation presented in §4.5. These results can therefore be explained in terms of high entropy states. Moreover, in the long term dynamics, the annihilation of vortices at the boundaries gives rise to a strongly polarised vortex gas with a consequent formation of a large monopole structure in agreement with the result presented in §5.1.2.

This concludes the analysis of the dynamics of quantum vortices in a BEC by using the GP model. Numerical simulations in the square and in the rectangle with $\Lambda = 1.5$ revealed that the monopole in the square and the dipole in the rectangle represent the maximum entropy states in good agreement with the solutions of the BP equation presented in §4.4 and §4.5. Moreover, these results are in agreement with the results which have been obtained in §5.1.1 and §5.1.2 by using the PVM . However, at later time in the dynamics, the vortex gas becomes strongly polarised. Independently of the geometry, according to the results presented in §5.5 for the PVM, the system is then found in a monopole configuration. The analysis of the angular momentum L in both geometries provides an additional evidence on the similarities between the dynamics of quantised vortices in the GP model and point vortices in the PVM. The analysis of the angular momentum in the GP simulations are consistent with the results obtained for the PVM in §5.2 in the the early stage of the dynamics. Moreover, later in the dynamics when the system becomes strongly polarised, the formation of a monopole generates a nonzero angular momentum according to the results obtained in §5.5 when the effects of the annihilations at the boundaries were introduced in the PVM.

Chapter 7

Conclusions

In this work the relaxation of a two-dimensional Bose gas has been studied in a squared and a rectangular domain by using both the point vortex model and the Gross-Pitaevskii model. Moreover, in order to explain the results obtained from the numerical simulations, a mean-field theory for a vortex gas has been developed.

In the first part of this work, attention was given to developing a mean-field theory of a neutral vortex gas based on a statistical mechanical approach. By assuming the maximum entropy principle, it was possible to derive the Boltzmann-Poisson equation whose solutions represent all possible configurations of vortices which are local maximisers of the entropy. It was shown that nontrivial solutions to this equation exist only if the absolute temperature of the vortex gas is negative. These solutions correspond to configurations in which point vortices with the same sign tend to cluster and form large coherent structures. Moreover, due to the nature of the long-range interaction between point vortices, these nontrivial configurations depend on the shape of the domain. The Boltzmann-Poisson equation was solved in the square and in the rectangle for two specific families of solutions: those with a streamfunction that has a spatial average value that is either zero or nonzero. Among the former, emphasis was given to the dipole and the diagonal dipole while for the latter emphasis was given to the monopole. Analysis of these solutions in terms of their entropy and energy has been carried out showing that the maximum entropy solutions in the square are given by the monopole and in the rectangle are given by the dipole. An important difference between these solutions is given by the property that those whose spatially averaged value of the streamfunction is nonzero correspond to configurations with a nonzero value of the angular momentum.

The second part of this work focused on the study of the dynamics of a neutral system composed by point vortices in the square and in the rectangular domain by using the point vortex model. Since the predictions of the mean-field theory are valid

in the negative temperature regime, the transition from the positive to the negative temperature states was also investigated. Therefore, by starting from a vortex gas in the positive temperature regime, and by adding to the dynamics a mechanism of annihilation between point vortices of opposite sign, the system migrates from the positive to the negative temperature regime, allowing the study of the transition between these two regimes. A study on the dynamics of point vortices in the square and the rectangle revealed that their dynamics can be explained in terms of the Boltzmann-Poisson theory. By assuming these systems to be ergodic, time averaging of vortex positions during the numerical simulations revealed the presence of the dipole, the diagonal dipole, and the monopole in the square, and the monopole and the dipole in the rectangle. In order to compare the difference in entropy between these states, ensembles of point vortices for the dipole, diagonal dipole, and monopole in the square and for the monopole and the dipole in the rectangle have been generated from the dynamical runs. A procedure to generate smoothed vorticity fields from these ensembles was then presented allowing the energy and entropy to be evaluated and compared with the theoretical values. This analysis showed two important results. Firstly, in perfect agreement with the mean-field theory, the high entropy states in the square and in the rectangle are given by the monopole and the dipole, respectively. Secondly, the difference in entropy between for the configurations in the square and the rectangle are compatible with the theoretical values. Therefore, it has been shown that the dynamics of point vortices and the formation of clusters of like-signed vortices can be explained in terms of high entropy states. Furthermore, the values of the angular momentum for these ensembles have been evaluated and the results compared with the theoretical predictions showing good agreement. In addition, the dynamics of point vortices has been investigated also for a non-neutral vortex gas. In this case, an additional mechanism which allows vortices to annihilate at the boundaries has been introduced to the point vortex model. With this additional mechanism, dynamical simulations showed that, independent of the geometry, the vortex gas spontaneously evolves towards a monopole configuration with a consequent nonzero value for the angular momentum.

Finally, the relaxation of a system composed of quantised vortices in a Bose-Einstein condensate has been investigated in the same geometries by using the Gross-Pitaevskii model. In this model vortices can either annihilate with vortices of the opposite sign or at the boundaries and, therefore, the vortex gas can become polarised. In order to compare the dynamics of such a system with the results obtained with the point vortex model, the same initial configuration of vortices has been used in the square and in the rectangle. For both geometries the dynamics showed two behaviours depending on the

CHAPTER 7. CONCLUSIONS

polarisation of the vortex gas. In the early stages of the dynamics, when the polarisation of the system is negligible, time averaging of vortex positions in both geometries revealed the presence of the same structures found in the point vortex model and predicted by the mean-field theory for a neutral system. Remarkably, in perfect agreement with the results found previously, the monopole in the square and the dipole in the rectangle appeared during the late stages of the dynamics. Therefore, the formation of the monopole in the square and the dipole in the rectangle, can be explained in terms of high entropy states. However, waiting even longer, the polarisation is seen to become more important. It was shown that, independent of the geometry, the system spontaneously evolves towards a monopole configuration with a consequent nonzero value of the angular momentum. Moreover, it has been shown that the process of polarisation appears earlier in the rectangle than in the square. Such a difference has been explained in terms of the higher probability of annihilation of vortices at the boundaries due in the rectangle to its larger perimeter.

Bibliography

- [1] B. P. Anderson A. C. White and V. S. Bagnato. Vortices and turbulence in trapped atomic condensates. *Proceedings of the National Academy of Sciences of the United States of America*, 111:4719–4726, 2014.
- [2] Giorgio Krstulovic Hayder Salman Alberto Villois, Davide Proment. Vortex filament tracking method in the gross-pitaevskii model. 2016.
- [3] J.F. Allen and A. D. Misener. Flow of liquid helium ii. *Nature*, 141:75–75, 1938.
- [4] B. P. Anderson, P. C. Haljan, C. E. Wieman, and E. A. Cornell. Vortex precession in bose-einstein condensates: Observations with filled and empty cores. *Phys. Rev. Lett.*, 85:2857–2860, Oct 2000.
- [5] M. H. Anderson, J. R. Ensher, M. R. Matthews, C. E. Wieman, and E. A. Cornell. Observation of bose-einstein condensation in a dilute atomic vapor. *Science*, 269(5221):198–201, 1995.
- [6] arXiv:1405.0992.
- [7] arXiv:1607.00092.
- [8] P. Attard. *Non-equilibrium Thermodynamics and Statistical Mechanics: Foundations and Applications*. Oxford University Press, 2012.
- [9] Vanderlei Bagnato and Daniel Kleppner. Bose-Einstein condensation in low-dimensional traps. *Phys. Rev. A*, 44:7439–7441, Dec 1991.
- [10] Vanderlei Bagnato, David E. Pritchard, and Daniel Kleppner. Bose-einstein condensation in an external potential. *Phys. Rev. A*, 35:4354–4358, May 1987.
- [11] G. K. Batchelor. *An Introduction to Fluid Dynamics*. Cambridge University Press, 2000. Cambridge Books Online.

BIBLIOGRAPHY

- [12] Natalia G Berloff. Pad approximations of solitary wave solutions of the grosspi-taevskii equation. *Journal of Physics A: Mathematical and General*, 37(5):1617, 2004.
- [13] Proukakis N. P. Berloff N. G., Brachet M. Modeling quantum fluid dynamics at nonzero temperatures. *Proceedings of the National Academy of Sciences of the United States of America*, 111(Suppl 1):4675–4682, 2014.
- [14] T. P. Billam, M. T. Reeves, B. P. Anderson, and A. S. Bradley. Onsager-kraichnan condensation in decaying two-dimensional quantum turbulence. *Phys. Rev. Lett.*, 112:145301, Apr 2014.
- [15] N. N. Bogoliubov. On the theory of superfluidity. *J. Phys. USSR*, 11(23), 1947.
- [16] D. L. Book, Shalom Fisher, and B. E. McDonald. Steady-state distributions of interacting discrete vortices. *Phys. Rev. Lett.*, 34:4–8, Jan 1975.
- [17] Bose. Plancks gesetz und lichtquantenhypothese. *Zeitschrift fr Physik*, 26(1):178–181, 1924.
- [18] Ashton S. Bradley and Brian P. Anderson. Energy spectra of vortex distributions in two-dimensional quantum turbulence. *Phys. Rev. X*, 2:041001, Oct 2012.
- [19] D. I. Bradley, D. O. Clubb, S. N. Fisher, A. M. Guénault, R. P. Haley, C. J. Matthews, G. R. Pickett, V. Tsepelin, and K. Zaki. Decay of pure quantum turbulence in superfluid $^3\text{He-B}$. *Phys. Rev. Lett.*, 96:035301, Jan 2006.
- [20] D. Brown. *The Chemical Bond in Inorganic Chemistry*. Oxford University Press, 2016.
- [21] Oliver Bhler. Statistical mechanics of strong and weak point vortices in a cylinder. *Physics of Fluids*, 14(7), 2002.
- [22] Alessandro Campa, Thierry Dauxois, and Stefano Ruffo. Statistical mechanics and dynamics of solvable models with long-range interactions. *Physics Reports*, 480(36):57 – 159, 2009.
- [23] Antoine Campagne, Basile Gallet, Frdric Moisy, and Pierre-Philippe Cortet. Direct and inverse energy cascades in a forced rotating turbulence experiment. *Physics of Fluids*, 26(12), 2014.

BIBLIOGRAPHY

- [24] L. J. Campbell, M. M. Doria, and J. B. Kadtke. Energy of infinite vortex lattices. *Phys. Rev. A*, 39:5436–5439, May 1989.
- [25] L.J. Campbell and Kevin O’Neil. Statistics of two-dimensional point vortices and high-energy vortex states. *Journal of Statistical Physics*, 65(3-4):495–529, 1991.
- [26] Robert M. Kerr Katepalli R. Sreenivasan Cecilia Rorai, Jack Skipper. Approach and separation of quantum vortices with balanced cores. 2014.
- [27] P. H. Chavanis and J. Sommeria. Classification of self-organized vortices in two-dimensional turbulence: the case of a bounded domain. *Journal of Fluid Mechanics*, 314:267–297, 5 1996.
- [28] P. H. Chavanis and J. Sommeria. Classification of self-organized vortices in two-dimensional turbulence: the case of a bounded domain. *Journal of Fluid Mechanics*, 314:267–297, 5 1996.
- [29] Pierre-Henri Chavanis. *Statistical Mechanics of Two-Dimensional Vortices and Stellar Systems*. Springer Berlin Heidelberg, Berlin, Heidelberg, 2002.
- [30] Pierre-Henri Chavanis. Statistical mechanics of two-dimensional point vortices: relaxation equations and strong mixing limit. *The European Physical Journal B*, 87(4):1–24, 2014.
- [31] F. Chevy, K. W. Madison, V. Bretin, and J. Dalibard. Interferometric detection of a single vortex in a dilute bose-einstein condensate. *Phys. Rev. A*, 64:031601, Aug 2001.
- [32] J. P. Christiansen. Proceedings of the conference on the numerical simulation of plasmas (4th). 1970.
- [33] H. J. H. Clercx, S. R. Maassen, and G. J. F. van Heijst. Spontaneous spin-up during the decay of 2d turbulence in a square container with rigid boundaries. *Phys. Rev. Lett.*, 80:5129–5132, Jun 1998.
- [34] S. L. Cornish, N. R. Claussen, J. L. Roberts, E. A. Cornell, and C. E. Wieman. Stable ^{85}Rb bose-einstein condensates with widely tunable interactions. *Phys. Rev. Lett.*, 85:1795–1798, Aug 2000.
- [35] F. Dalfovo, A. Lastri, L. Pricauzenko, S. Stringari, and J. Treiner. Structural and dynamical properties of superfluid helium: A density-functional approach. *Phys. Rev. B*, 52:1193–1209, Jul 1995.

BIBLIOGRAPHY

- [36] K. B. Davis, M. O. Mewes, M. R. Andrews, N. J. van Druten, D. S. Durfee, D. M. Kurn, and W. Ketterle. Bose-einstein condensation in a gas of sodium atoms. *Phys. Rev. Lett.*, 75:3969–3973, Nov 1995.
- [37] Malcolm E. Davis and J. Andrew McCammon. Electrostatics in biomolecular structure and dynamics. *Chemical Reviews*, 90(3):509–521, 1990.
- [38] P. Debye and E. Hückel. Zur theorie der elektrolyte. i. gefrierpunktserniedrigung und verwandte erscheinungen. the theory of electrolytes. i. lowering of freezing point and related phenomena. *Physikalische Zeitschrift*, 24:185–206, 1923.
- [39] R.J. Donnelly. *Quantized Vortices in Helium II*. Number v. 2 in Cambridge Studies in American Literature and Culture. Cambridge University Press, 1991.
- [40] S. F. Edwards and J. B. Taylor. Negative Temperature States of Two-Dimensional Plasmas and Vortex Fluids. *Proceedings of the Royal Society of London. A. Mathematical and Physical Sciences*, 336(1606):257–271, February 1974.
- [41] Albert Einstein. *Quantentheorie des einatomigen idealen gases*, pages 261–267. Sitzber. Kgl. Preuss. Akad. Wiss., 1924.
- [42] Richard S. Ellis, Kyle Haven, and Bruce Turkington. Large deviation principles and complete equivalence and nonequivalence results for pure and mixed ensembles. *Journal of Statistical Physics*, 101(5):999–1064, 2000.
- [43] J. G. Esler and T. L. Ashbee. Universal statistics of point vortex turbulence. *Journal of Fluid Mechanics*, 779:275–308, 9 2015.
- [44] J. G. Esler, T. L. Ashbee, and N. R. McDonald. Statistical mechanics of a neutral point-vortex gas at low energy. *Phys. Rev. E*, 88:012109, Jul 2013.
- [45] A.L. Fetter and J.D. Walecka. *Quantum Theory of Many-particle Systems*. Dover Books on Physics. Dover Publications, 2003.
- [46] Richard Feynman, Robert Leighton, and Matthew Sands. *The Feynman Lectures on Physics*, volume 1. Addison-Wesley, Boston, second edition, 1963.
- [47] R.P. Feynman. Chapter {II} application of quantum mechanics to liquid helium. volume 1 of *Progress in Low Temperature Physics*, pages 17 – 53. Elsevier, 1955.
- [48] D. V. Freilich, D. M. Bianchi, A. M. Kaufman, T. K. Langin, and D. S. Hall. real-rime rynamics of ringle vortex lines and vortex dipoles in a bose-einstein condensate. *Science*, 329(5996):1182–1185, 2010.

BIBLIOGRAPHY

- [49] Z. M. Galasiewicz. *Helium 4: The Commonwealth and International Library: Selected Readings in Physics*. Elsevier Science, 2013.
- [50] Alexander L. Gaunt, Tobias F. Schmidutz, Igor Gotlibovych, Robert P. Smith, and Zoran Hadzibabic. Bose-einstein condensation of atoms in a uniform potential. *Phys. Rev. Lett.*, 110:200406, May 2013.
- [51] Axel Griesmaier, Jörg Werner, Sven Hensler, Jürgen Stuhler, and Tilman Pfau. Bose-einstein condensation of chromium. *Phys. Rev. Lett.*, 94:160401, Apr 2005.
- [52] A. Griffin, D.W. Snoke, and S. Stringari. *Bose-Einstein condensation*. Cambridge Univ. Press, Cambridge, 1995.
- [53] E.P. Gross. Structure of a quantized vortex in boson systems. *Il Nuovo Cimento Series 10*, 20(3):454–477, 1961.
- [54] Y. Yasaku H. Shibayama and T. Kuwamoto. Vortex nucleation in boseeinstein condensates confined in a quic trap by topological phase imprinting. *Journal of Physics B: Atomic, Molecular and Optical Physics*, 44(7):075302, 2011.
- [55] D. Ter Haar. *Men of Physics: L.D. Landau. Volume 2: Thermodynamics, Plasma Physics and Quantum Mechanics*. Pergamon, Oxford,UK, 1969.
- [56] H. Helmholtz. Über integrale der hydrodynamischen Gleichungen, welche den Wirbelbewegungen entsprechen. *Journal fr die reine und angewandte Mathematik*, 55:25–55, 1858.
- [57] Thorsten Hohage and Frank Schmidt. On the numerical solution of nonlinear schrödinger type equations in fiber optics. (02-04), 2002.
- [58] S. Inouye, S. Gupta, T. Rosenband, A. P. Chikkatur, A. Görlitz, T. L. Gustavson, A. E. Leanhardt, D. E. Pritchard, and W. Ketterle. Observation of vortex phase singularities in bose-einstein condensates. *Phys. Rev. Lett.*, 87:080402, Aug 2001.
- [59] Cecilia A. Hernndez-Hall Jerry D. Wilson. *Physics Laboratory Experiments*. Cengage Learning, Boston, 2015.
- [60] G. Joyce and D. Montgomery. Negative temperature states for the two-dimensional guiding-centre plasma. *Journal of Plasma Physics*, 10:107–121, 8 1973.

BIBLIOGRAPHY

- [61] G. H. Keetels, H. J. H. Clercx, and G. J. F. van Heijst. Spontaneous angular momentum generation of two-dimensional fluid flow in an elliptic geometry. *Phys. Rev. E*, 78:036301, Sep 2008.
- [62] G.H. Keetels, H.J.H. Clercx, and G.J.F. van Heijst. On the origin of spin-up processes in decaying two-dimensional turbulence. *European journal of mechanics, B/fluids*, 29(1):1–8, 2010. The authors gratefully acknowledge financial support from the Dutch Foundation for Fundamental Research on Matter (FOM), which is financially supported by the Nederlandse Organisatie voor Wetenschappelijk Onderzoek (Netherlands Organization for Scientific Research, NWO). Part of this work was sponsored by the Stichting Nationale Computerfaciliteiten (National Computing Facilities Foundation, NCF) for the use of supercomputer facilities, with financial support from NWO.
- [63] A.I.A. Khinchin. *Mathematical Foundations of Statistical Mechanics*. Dover Books on Mathematics. Dover Publications, 1949.
- [64] Sebastian Kraft, Felix Vogt, Oliver Appel, Fritz Riehle, and Uwe Sterr. Bose-einstein condensation of alkaline earth atoms: ^{40}Ca . *Phys. Rev. Lett.*, 103:130401, Sep 2009.
- [65] R. H. Kraichnan. Inertial Ranges in Two-Dimensional Turbulence. *Physics of Fluids*, 10:1417–1423, July 1967.
- [66] Kazue Kudo and Yuki Kawaguchi. Coarsening dynamics driven by vortex-antivortex annihilation in ferromagnetic bose-einstein condensates. *Phys. Rev. A*, 91:053609, May 2015.
- [67] A. E. Leanhardt, A. Görlitz, A. P. Chikkatur, D. Kielpinski, Y. Shin, D. E. Pritchard, and W. Ketterle. Imprinting vortices in a bose-einstein condensate using topological phases. *Phys. Rev. Lett.*, 89:190403, Oct 2002.
- [68] M. J. Lighthill. *Fourier analysis and generalized functions*. Cambridge University press, 1960.
- [69] C. C. Lin. On the motion of vortices in two dimensions: I. existence of the kirchhoff-routh function. *Proceedings of the National Academy of Sciences of the United States of America*, 27(12):570–575, 1941.

BIBLIOGRAPHY

- [70] Mingwu Lu, Nathaniel Q. Burdick, Seo Ho Youn, and Benjamin L. Lev. Strongly dipolar bose-einstein condensate of dysprosium. *Phys. Rev. Lett.*, 107:190401, Oct 2011.
- [71] T. S. Lundgren and Y. B. Pointin. Non-Gaussian probability distributions for a vortex fluid. *Physics of Fluids*, 20:356–363, March 1977.
- [72] Kobayashi M. and Tsubota M. Kolmogorov spectrum of superfluid turbulence: Numerical analysis of the gross-pitaevskii equation with a small-scale dissipation. *Phys. Rev. Lett.*, 94:065302, Feb 2005.
- [73] M. R. Matthews C. E. Wieman E. A. Cornell M. H. Anderson, J. R. Ensher. Observation of bose-einstein condensation in a dilute atomic vapor. *Science*, 269(5221):198–201, 1995.
- [74] S. R. Maassen, H. J. H. Clercx, and G. J. F. van Heijst. Self-organization of quasi-two-dimensional turbulence in stratified fluids in square and circular containers. *Physics of Fluids*, 14(7), 2002.
- [75] M. R. Matthews, B. P. Anderson, P. C. Haljan, D. S. Hall, C. E. Wieman, and E. A. Cornell. Vortices in a bose-einstein condensate. *Phys. Rev. Lett.*, 83:2498–2501, Sep 1999.
- [76] J. Maurer and P. Tabeling. Local investigation of superfluid turbulence. *EPL (Europhysics Letters)*, 43(1):29, 1998.
- [77] B.E. McDonald. Numerical calculation of nonunique solutions of a two-dimensional sinh-Poisson equation. *Journal of Computational Physics*, 16(4):360 – 370, 1974.
- [78] N. D. Mermin and H. Wagner. Absence of ferromagnetism or antiferromagnetism in one- or two-dimensional isotropic heisenberg models. *Phys. Rev. Lett.*, 17:1307–1307, Dec 1966.
- [79] S. Middelkamp, P. J. Torres, P. G. Kevrekidis, D. J. Frantzeskakis, R. Carretero-González, P. Schmelcher, D. V. Freilich, and D. S. Hall. Guiding-center dynamics of vortex dipoles in bose-einstein condensates. *Phys. Rev. A*, 84:011605, Jul 2011.
- [80] J. Miller. Statistical mechanics of euler equations in two dimensions. *Phys. Rev. Lett.*, 65:2137–2140, Oct 1990.

BIBLIOGRAPHY

- [81] G. Modugno, G. Ferrari, G. Roati, R. J. Brecha, A. Simoni, and M. Inguscio. Bose-einstein condensation of potassium atoms by sympathetic cooling. *Science*, 294(5545):1320–1322, 2001.
- [82] A. Naso, H. P. Chavanis, and B. Dubrulle. Statistical mechanics of two-dimensional euler flows and minimum enstrophy states. *The European Physical Journal B*, 77(2):187–212, 2010.
- [83] Sergey Nazarenko and Miguel Onorato. Freely decaying turbulence and bose-einstein condensation in gross-pitaevski model. *Journal of Low Temperature Physics*, 146(1):31–46, 2007.
- [84] T. W. Neely, A. S. Bradley, E. C. Samson, S. J. Rooney, E. M. Wright, K. J. H. Law, R. Carretero-González, P. G. Kevrekidis, M. J. Davis, and B. P. Anderson. Characteristics of two-dimensional quantum turbulence in a compressible superfluid. *Phys. Rev. Lett.*, 111:235301, Dec 2013.
- [85] T. W. Neely, E. C. Samson, A. S. Bradley, M. J. Davis, and B. P. Anderson. Observation of vortex dipoles in an oblate bose-einstein condensate. *Phys. Rev. Lett.*, 104:160401, Apr 2010.
- [86] Paul K. Newton. *The N-vortex problem : analytical techniques*. Applied mathematical sciences. Springer, New York, 2001.
- [87] Ryu Numasato and Makoto Tsubota. Possibility of inverse energy cascade in two-dimensional quantum turbulence. *Journal of Low Temperature Physics*, 158(3):415–421, 2009.
- [88] Kiyomi Okamoto and Atsuhiro Kitazawa. Quantum phase transition of s=12 trimerized {XXZ} spin chain in magnetic field. *Physica B: Condensed Matter*, 281282:840 – 841, 2000.
- [89] L. Olivares-Quiroz and V. Romero-Rochin. On the order of bec transition in weakly interacting gases predicted by mean-field theory. *Journal of Physics B: Atomic, Molecular and Optical Physics*, 43(20):205302, 2010.
- [90] L. Onsager. Statistical hydrodynamics. *Il Nuovo Cimento Series 9*, 6(2):279–287, 1949.
- [91] C. J. Pethick and H. Smith. *BoseEinstein Condensation in Dilute Gases*. Cambridge University Press, second edition, 2008. Cambridge Books Online.

BIBLIOGRAPHY

- [92] L.P. Pitaevskii and S. Stringari. *Bose-Einstein Condensation*. International Series of Monographs on Physics. Clarendon Press, 2003.
- [93] Y. B. Pointin and T. S. Lundgren. Statistical mechanics of twodimensional vortices in a bounded container. *Physics of Fluids (1958-1988)*, 19(10), 1976.
- [94] N. P. Proukakis and B. Jackson. Finite-temperature models of boseeinstein condensation. *Journal of Physics B: Atomic, Molecular and Optical Physics*, 41(20):203002, 2008.
- [95] Matthew T. Reeves, Thomas P. Billam, Brian P. Anderson, and Ashton S. Bradley. Inverse energy cascade in forced two-dimensional quantum turbulence. *Phys. Rev. Lett.*, 110:104501, Mar 2013.
- [96] F. Reif. *Fundamentals of statistical and thermal physics*. McGraw-Hill series in fundamentals of physics. McGraw-Hill, 1965.
- [97] Lewis Fry Richardson. *Weather Prediction by Numerical Process*. Cambridge University Press, second edition, 2007. Cambridge Books Online.
- [98] B. D. Ripley. The second-order analysis of stationary point processes. *Journal of Applied Probability*, 13(2):255–266, 1976.
- [99] A. Robert, O. Sirjean, A. Browaeys, J. Poupard, S. Nowak, D. Boiron, C. I. Westbrook, and A. Aspect. A bose-einstein condensate of metastable atoms. *Science*, 292(5516):461–464, 2001.
- [100] R. Robert. A maximum-entropy principle for two-dimensional perfect fluid dynamics. *Journal of Statistical Physics*, 65(3):531–553, 1991.
- [101] R. Robert and J. Sommeria. Statistical equilibrium states for two-dimensional flows. *Journal of Fluid Mechanics*, 229:291–310, 08 1991.
- [102] P. G. Saffman. *Vortex Dynamics*. Cambridge University Press, 1993. Cambridge Books Online.
- [103] H. Salman and D. Maestrini. Long-range ordering of topological excitations in a two-dimensional superfluid far from equilibrium. 2015.
- [104] Kai Schneider and Marie Farge. Final states of decaying 2d turbulence in bounded domains: Influence of the geometry. *Physica D: Nonlinear Phenomena*, 237(1417):2228 – 2233, 2008. Euler Equations: 250 Years OnProceedings of an international conference.

BIBLIOGRAPHY

- [105] L. F. Shampine and M. W. Reichelt. The matlab ode suite. *SIAM Journal on Scientific Computing*, 18(1):1–22, 1997.
- [106] B. W. Silverman and P. J. Green. *Density Estimation for Statistics and Data Analysis*. Chapman and Hall, London, 1986.
- [107] Tapio Simula, Matthew J. Davis, and Kristian Helmerson. Emergence of order from turbulence in an isolated planar superfluid. *Phys. Rev. Lett.*, 113:165302, Oct 2014.
- [108] Audun Skaugen and Luiza Angheluta. Vortex clustering and universal scaling laws in two-dimensional quantum turbulence. *Phys. Rev. E*, 93:032106, Mar 2016.
- [109] H. Eugene Stanley. Turbulence: The legacy of A. N. Kolmogorov. *Journal of Statistical Physics*, 88(1):521–523, 1997.
- [110] Simon Stellmer, Meng Khoon Tey, Rudolf Grimm, and Florian Schreck. Bose-einstein condensation of ^{86}Sr . *Phys. Rev. A*, 82:041602, Oct 2010.
- [111] Simon Stellmer, Meng Khoon Tey, Bo Huang, Rudolf Grimm, and Florian Schreck. Bose-einstein condensation of strontium. *Phys. Rev. Lett.*, 103:200401, Nov 2009.
- [112] Araki T., Tsubota M., and S. K. Nemirovskii. Energy spectrum of superfluid turbulence with no normal-fluid component. *Phys. Rev. Lett.*, 89:145301, Sep 2002.
- [113] Yosuke Takasu, Kenichi Maki, Kaduki Komori, Tetsushi Takano, Kazuhito Honda, Mitsutaka Kumakura, Tsutomu Yabuzaki, and Yoshiro Takahashi. Spin-singlet bose-einstein condensation of two-electron atoms. *Phys. Rev. Lett.*, 91:040404, Jul 2003.
- [114] J. B. Taylor, Matthias Borchardt, and Per Helander. Interacting vortices and spin-up in two-dimensional turbulence. *Phys. Rev. Lett.*, 102:124505, Mar 2009.
- [115] A.C. Ting, H.H. Chen, and Y.C. Lee. Exact solutions of a nonlinear boundary value problem: The vortices of the two-dimensional sinh-Poisson equation. *Physica D: Nonlinear Phenomena*, 26:37 – 66, 1987.
- [116] G. M. Torrie and J. P. Valleau. Electrical double layers. 4. limitations of the gouy-chapman theory. *The Journal of Physical Chemistry*, 86(16):3251–3257, 1982.

BIBLIOGRAPHY

- [117] L.N Trefethen. *Spectral Methods in MATLAB*.
- [118] Tino Weber, Jens Herbig, Michael Mark, Hanns-Christoph Nägerl, and Rudolf Grimm. Bose-einstein condensation of cesium. *Science*, 299(5604):232–235, 2003.
- [119] Angela C. White, Carlo F. Barenghi, and Nick P. Proukakis. Creation and characterization of vortex clusters in atomic bose-einstein condensates. *Phys. Rev. A*, 86:013635, Jul 2012.
- [120] K. C. Wright, L. S. Leslie, and N. P. Bigelow. Optical control of the internal and external angular momentum of a bose-einstein condensate. *Phys. Rev. A*, 77:041601, Apr 2008.
- [121] E. J. Yarmchuk, M. J. V. Gordon, and R. E. Packard. Observation of stationary vortex arrays in rotating superfluid helium. *Phys. Rev. Lett.*, 43:214–217, Jul 1979.
- [122] Yuichi Yatsuyanagi, Yasuhito Kiwamoto, Hiroyuki Tomita, Mitsusada M. Sano, Takeshi Yoshida, and Toshikazu Ebisuzaki. Dynamics of two-sign point vortices in positive and negative temperature states. *Phys. Rev. Lett.*, 94:054502, Feb 2005.
- [123] Tarik Yefsah, Rémi Desbuquois, Lauriane Chomaz, Kenneth J. Günter, and Jean Dalibard. Exploring the thermodynamics of a two-dimensional bose gas. *Phys. Rev. Lett.*, 107:130401, Sep 2011.
- [124] Z. Yin, D. C. Montgomery, and H. J. H. Clercx. Alternative statistical-mechanical descriptions of decaying two-dimensional turbulence in terms of patches and points. *Physics of Fluids*, 15(7), 2003.
- [125] Xiaoquan Yu, Thomas P. Billam, Jun Nian, Matthew T. Reeves, and Ashton S. Bradley. Theory of the vortex-clustering transition in a confined two-dimensional quantum fluid. *Phys. Rev. A*, 94:023602, Aug 2016.
- [126] J. Dalibard Z. Hadzibabic. Two-dimensional bose fluids: An atomic physics perspective. *Rivista del Nuovo Cimento*, 34(6), 2011.

E quindi uscimmo a riveder le stelle.

Inferno, XXXIV, 139

Thence issuing we again beheld the stars.

Inferno, XXXIV, 133